uOttawa

L'Université canadienne
Canada's university

FACULTÉ DES ÉTUDES SUPÉRIEURES ET POSTOCTORALES

uOttawa

L'Université canadienne
Canada's university

FACULTY OF GRADUATE AND POSDOCTORAL STUDIES

Christophe Kinnard

AUTEUR DE LA THÈSE / AUTHOR OF THESIS

Ph.D. (Geography)

GRADE / DEGREE

Department of Geograpghy

FACULTÉ, ÉCOLE, DÉPARTEMENT / FACULTY, SCHOOL, DEPARTMENT

Coupled Sea Ice and Climate Variability from Modern Observations and Proxy Reconstructions

TITRE DE LA THÈSE / TITLE OF THESIS

Bernard Lauriol

DIRECTEUR (DIRECTRICE) DE LA THÈSE / THESIS SUPERVISOR

Christian Zdanowicz

CO-DIRECTEUR (CO-DIRECTRICE) DE LA THÈSE / THESIS CO-SUPERVISOR

EXAMINATEURS (EXAMINATRICES) DE LA THÈSE / THESIS EXAMINERS

Luke Copeland

Michael Sawada

David Fisher

Bruno Tremblay

Gary W. Slater

Le Doyen de la Faculté des études supérieures et postdoctorales / Dean of the Faculty of Graduate and Postdoctoral Studies

COUPLED SEA ICE AND CLIMATE VARIABILITY FROM MODERN OBSERVATIONS AND PROXY RECONSTRUCTIONS

Christophe Kinnard

Department of Geography
University of Ottawa

A dissertation submitted to the School of Graduate and Postdoctoral Studies
in partial fulfillment for the degree of
Doctor of Philosophy in Geography

Examining Board: ***Dr. Luke Copland*** *(Professor of Geography, University of Ottawa),* ***Dr. Michael C. Sawada*** *(Professor of Geography, University of Ottawa),* ***Dr. David A. Fisher*** *(Research Scientist, Geological Survey of Canada). External examiner:* ***Dr. Bruno Tremblay*** *(Professor of Atmospheric and Ocean Sciences, McGill University)*

Advisors: ***Christian M. Zdanowicz*** *(Research Scientist, Geological Survey of Canada),* ***Bernard Lauriol*** *(Professor of Geography, University of Ottawa).*

Your file Votre référence
ISBN: 978-0-494-51801-4
Our file Notre référence
ISBN: 978-0-494-51801-4

ABSTRACT

Coupled climate and sea ice variability in the Arctic was investigated using a combination of modern, historical and proxy observations. In the Canadian Arctic, operational sea ice charts were homogenized into a spatially and temporally consistent gridded dataset. A complete climatic analysis of this dataset revealed the presence of dominant modes of sea ice variability related to driving climate patterns and atmospheric circulation indices such as the North Atlantic Oscillation (NAO) and El Nino Southern Oscillation (ENSO). On a hemispheric scale, the late-summer ice cover extent is decreasing at a much faster rate than the maximum winter ice cover. The disappearing perennial ice is partly replaced by seasonal ice, the areal extent of which has increased steadily over the last century. The enhanced seasonal sea ice freeze-thaw cycle is predicted to increase the salinity of surface waters over continental shelves, thereby enhancing haline convection and ventilation of the deeper Arctic Ocean. Coupled sea ice and climate proxies for the North Baffin Bay region were developed from an existing ice core from Devon Ice Cap and a new ice core from the Prince-of-Wales (POW) Icefield on Ellesmere Island. A sea-salt concentration record from the Devon ice core was found to relate with sea ice concentration in nearby Baffin Bay. The record was used to study past sea ice conditions in Baffin Bay over the last 200 years in relation with temperature proxies (melt %, $\delta^{18}O$). Sea ice extent variations in northern Baffin Bay appear to be mostly dynamically driven, with sea ice decreasing when Nares Strait becomes congested with ice from the Arctic Ocean, and northerly winds advect ice from Baffin Bay southward. A new high-resolution melt record was developed using digital image analysis of the POW ice core. The record was used to show that melting affects the solid

conductivity signal of the core, which compromises dating by seasonal layer counting, and hinders the identification of acidic volcanic horizons. The POW melt record, a proxy for summer warmth, was shown to be site-specific, which may be explained by the close presence of the North Open Water polynya and the peculiar position of the ice cap which rests on the shifting boundary between the maritime climate of Baffin Bay and the drier, colder climate of the high Arctic. The long-term, natural variability of late-summer Arctic sea ice was reconstructed from a network of 68 climate proxies from the circum-Arctic region. The proxy network contains both a temperature and a sea ice signal. Past sea ice extent was reconstructed using multivariate statistical calibration of the network against historical sea ice observations over the last century. The record shows that the decline in sea ice extent of the last two decades is anomalous in the context of the last 900 years. Non-linear processes are responsible for much of the variability in ice extent over the past millennium, and the same processes may be enhancing the greenhouse gas-induced decrease in ice extent currently observed.

RÉSUMÉ

La variation couplée entre le climat et l'étendue des glaces de mer dans l'Arctique a été étudiée au moyen d'observations modernes, historiques et proxy. Des cartes opérationnelles des conditions de glace de mer dans l'Arctique canadien furent assemblées en une base de données spatialement et temporellement homogène. Une analyse climatique complète de cette nouvelle base de données a démontré l'existence de modes dominants de variabilité des glaces de mer, lesquels sont reliés à des patrons de forçage climatique distincts ainsi qu'aux principaux indices de circulation atmosphérique tels que l'oscillation nord-atlantique (NAO) et le phénomène El Niño (ENSO). À l'échelle hémisphérique, l'étendue du couvert de glace estival a connu une retraite plus rapide qu'à la fin de l'hiver, la période d'extension maximale. La fonte progressive du couvert de glace permanent entraîne une augmentation de la production de glace saisonnière, laquelle a connu une croissance constante de son étendue au cours du dernier siècle. Il est prédit que l'accentuation du cycle saisonnier de gel-dégel de la glace de mer entraînera une augmentation de la salinité des eaux de surface au-dessus des plateaux continentaux polaires, ce qui pourrait accroître la convection et la ventilation des eaux profondes de l'Océan Arctique. Des proxies pour la variabilité couplée climat - glace de mer on été développés pour la région de la baie de Baffin à partir d'une carotte de glace provenant de la calotte glaciaire de Devon et d'une nouvelle carotte prélevée sur la calotte Prince of Wales (POW), sur l'île d'Ellesmere. Les concentrations en sels marin mesurées dans la carotte de glace de Devon varient en fonction de l'étendue des glaces de mer dans la baie de Baffin. Les conditions de glace de mer dans la baie de Baffin furent reconstruites pour les 200 dernières années à partir de ce proxy et comparées avec les

variations des proxies de température (% fonte, $\delta^{18}O$). Les variations d'étendue des glaces dans le nord de la baie de Baffin sont principalement causées par des facteurs dynamiques, la glace déclinant lorsque le détroit de Nares devient bloqué par la glace en provenance de l'Océan Arctique, et lorsque que les vents dominant du nord transportent la glace de la baie de Baffin vers le sud. Une nouvelle série à haute-résolution du pourcentage de fonte annuel a été développée à partir de l'analyse d'images digitales de la carotte de glace de POW. Cette série a permis de démontrer que les processus de fonte affectent le signal de conductivité de la carotte de glace, ce qui compromet la datation de la carotte par comptage des cycles glaciochimiques saisonniers, ainsi que l'identification des pics d'acidités d'origine volcanique. Il fût démontré que le pourcentage annuel de fonte sur POW, un proxy pour la température en été, diffère des autres glaciers de l'Arctique. Ceci est expliqué par la proximité de la polynie des eaux du Nord ainsi que par la position particulière de la calotte de glace, qui se situe sur une frontière transitoire séparant le climat maritime de la baie de Baffin et le climat plus froid et sec du Haut-Arctique. La variabilité naturelle à long-terme du couvert de glace estival tardif a été reconstruite à partir d'un réseau de 68 proxies climatiques de la région arctique. Le réseau de proxies contient deux signaux climatiques, l'un relié aux fluctuations de température et l'autre à l'étendue variable des glaces de mer. Les variations passées du couvert de glace de mer furent reconstruites à partir d'une calibration multivariée entre le réseau de proxies et les observations historiques de glace de mer au cours du dernier siècle. La reconstruction démontre que l'étendue des glaces dans l'Arctique depuis les deux dernières décennies est anormalement restreinte dans le contexte des derniers 900 ans. Des processus non linéaires sont responsables de la variabilité du couvert de glace au

cours du dernier millénaire, et ces mêmes processus pourraient amplifier la décroissance récente du couvert de glace causée par l'augmentation des gaz à effet de serre.

ACKNOWLEDGEMENTS

I wish to express my sincere gratitude toward my advisor Dr Christian Zdanowicz for his continuous support over the years. Christian has put great efforts to facilitate my work and expand my scientific network, and this has greatly contributed toward the success of this thesis and my achievement as a scientist. I spent great times exploring remote corners of the Canadian Arctic with Christian and will keep excellent memories of these trips, in addition to an enduring friendship.

I also wish to thank Dr Bernard Lauriol, my co-advisor at the University of Ottawa. Bernard has been supportive of all my endeavours and has always been available whenever I needed help. I keep excellent memories of our field trip to Auyuittuq National Park and our long delay in Broughton Island...

I want to thank my colleagues at the Geological Survey of Canada, who form a small but strong and stimulating core of scientists. I enjoyed greatly there presence over the past years.

I wish to extend my gratitude toward my parents, who have always been pushing me, as well as giving me the mean, to pursue higher education. I guess they just did not expect that it would work so well...

Merci finalement à Anne-Marie, pour ton amour, pour avoir été là et m'avoir épaulé lors des moments plus difficiles. Merci à ma fille Éliane, apparue récemment dans ma vie, et quoique m'ayant privé quelques fois d'un sommeil précieux, ma surtout donné joie et inspiration.

PREFACE

Four chapters of this dissertation were written for publication in peer-reviewed scientific journals, while the fifth chapter is in preparation for publication. I am the first author on all these publications but the research involved collaborations with other scientists.

CHAPTER 2

Kinnard, C., C. M. Zdanowicz, D. A. Fisher, B. Alt, and S. McCourt. 2006a. Climatic analysis of sea ice variability in the Canadian Arctic from operational charts, 1980-2004. *Annals of Glaciology*, 44(1), 391-402.

This chapter investigates recent (1980-2004) sea ice variability in the Canadian Arctic and was published in the Annals of Glaciology. Dr. Bea Alt and Steve McCourt from the Canadian Ice Service provided help in gathering and understanding the sea ice operational charts. The paper benefited from advices and discussions with Dr. C. M. Zdanowicz and Dr. D. A. Fisher from the Geological Survey of Canada (GSC).

CHAPTER 3

Kinnard, C., C. M Zdanowicz, D. A. Fisher, and C. Wake. 2006b. Calibration of an ice-core glaciochemical (sea salt) record with sea ice variability in the Canadian Arctic. *Annals of Glaciology*, 44(1), 383-390.

This chapter presents a 150 year-long sea ice proxy reconstruction for the Baffin Bay region based on sea-salt concentrations measured in an ice core from the Devon ice cap. The paper was published in Annals of Glaciology. Dr. C. P. Wake from University of New-Hampshire, C. M. Zdanowicz and D. A. organized the research project, and the paper benefited from revisions by C. M. Zdanowicz and D. A. Fisher.

CHAPTER 4

Kinnard, C., C. M. Zdanowicz, D. A. Fisher, and R. M. Koerner. 2008a. A changing Arctic seasonal ice zone: Observations from 1870–2003 and possible oceanographic consequences. *Geophysical Research Letters*, 35, L02507, doi:10.1029/2007GL032507.

This chapter investigates the variability of seasonal ice extent in the Arctic and its effect on ocean circulation, over the period of historical observations (1870-2003). The paper was published in Geophysical Research Letters and benefited from fruitful discussions with the late Dr. R. M. Koerner, and from revisions by C. M. Zdanowicz and Dr D. A. Fisher.

CHAPTER 5

Kinnard, C., C. M. Zdanowicz, R. M. Koerner, D. A. Fisher , J. Zheng, M. J. Sharp, L. Nicholson, and B. Lauriol. 2008b. Stratigraphic analysis of an ice core from the Prince of Wales Icefield, Ellesmere Island, Arctic Canada, using digital image analysis: high-resolution density, past summer warmth reconstruction and melt effect on ice core solid conductivity. *Journal of Geophysical Research*, 113, D24120, doi:10.1029/2008JD011083

This chapter presents a new method to derive a high-resolution ice core melt record for the Prince of Wales Icefield (POW), Ellesmere Island, and uses this record to study past summer climate in the North Baffin Bay region. The paper was published in the Journal of Geophysical Research. The POW project was organized by Dr. M. J. Sharp from University of Alberta, Dr C. M. Zdanowicz and Dr. D. A. Fisher. Dr. J. Zheng

(GSC) produced the ECM data. Dr Lindsey Nicholson (UofA) helped to process stratigraphic observations. Dr R. M. Koerner produced the visual stratigraphy. D. A. Fisher produced the ice core timescale. C. M. Zdanowicz, D. A. Fisher and Dr. B. Lauriol (University of Ottawa) provided useful advices and discussions.

CHAPTER 6

Kinnard, C., et al (in preparation). Coupled Arctic climate and sea ice extent over the past millennium reconstructed from terrestrial proxies.

This chapter presents a reconstruction of past Arctic sea ice extent for the last 900 years using terrestrial proxies. The research benefited from advices, discussions and revisions by Dr. C. M. Zdanowicz, Dr. D. A. Fisher and Dr. Elisabeth Isaksson (Norwegian Polar Institute).

APPENDIX 1:

Fisher, D.A., A. Dyke, R. Koerner, J. Bourgeois, **C. Kinnard**, C. Zdanowicz, A. de Vernal, C. Hillaire-Marcel, J. Savelle, and A. Rochon. Natural variability of Arctic sea ice over the Holocene. 2006. *Eos, Transactions, American Geophysical Union*, 87(28), 273-275.

This appendix presents a discussion of recent Arctic sea-ice changes in the context of Holocene (< 10 ka) climate change as observed in various proxy records. My contribution to this article was to provide an analysis and discussion of the recent trends in the Arctic sea-ice cover, using satellite-derived sea-ice concentration fields.

TABLE OF CONTENTS

LIST OF TABLES

LIST OF FIGURES

CHAPTER 1. COUPLED CLIMATE AND ARCTIC SEA ICE VARIABILITY: A REVIEW AND RESEARCH FRAMEWORK

1.1. INTRODUCTION

There is increasing evidence that the Earth's climate is changing under the influence of human activities. The burning of fossil fuels since the beginning of the industrial era has caused a sustained increase in the concentration of atmospheric greenhouse gases (GHG), which is causing global-scale warming of the atmosphere (IPCC, 2007). The Arctic has featured prominently in the debate on global warming, both due to the important role it plays in the global climate system and the anticipation that climate warming will be amplified at high latitudes (Moritz et al., 2002; Serreze and Francis, 2006).

Many studies have documented the recent changes occurring in high-latitude environments (Morison et al., 2000; Overland et al., 2004b; Serreze et al., 2000). These include, among others, increased air temperature and precipitation (ACIA, 2005; Solomon et al., 2007), reduced sea ice thickness and extent (Vinnikov et al., 1999), reduced snow cover on land (Groisman et al., 1994), a decrease in sea-level pressure (Walsh et al., 1996), an increase in cyclone frequency and intensity (Serreze et al., 1997; Zhang et al., 2004), and an increased areal extent and warming of the Arctic Ocean's Atlantic layer (Morison et al., 2000).

The drastic reduction (~ 4% decade^{-1}, Comiso and Nishio, 2008) in sea ice extent over the past 30 years is drawing particular attention, as future losses of ice coverage may trigger further Arctic warming due to the positive ice-albedo feedback mechanism, as well as impact on Arctic ecosystems, indigenous lifestyle and maritime transportation

(ACIA, 2005). Over the past decade there has been a strong research focus on understanding the mechanisms of recent sea ice changes. Sea ice variability arises from a complex interplay between atmospheric and oceanic processes operating at different timescales, and these need to be better understood in order to forecast future Arctic sea ice and climate conditions in a warming world.

Most of the documented changes in Arctic climate are derived from observations collected over the last century. In particular, sea ice observations are scarce and of varying quality before the post-1970 satellite era. While modern observations are extremely valuable for understanding recent climate variability, they are difficult to interpret in the context of longer-term, natural climate variability. For this reason, researchers have used proxies developed from natural climate archives such as ice cores, tree rings, and lake and ocean sediments to reconstruct past climate history (Bradley, 1999). By combining various proxies from several sites, it has been possible to reconstruct key climatic variables such as air temperature and pressure patterns over the past one to two thousand years (North et al., 2006). However, only a few studies to this day have produced pan-Arctic climate reconstructions (D'Arrigo and Jacoby, 1993; Overpeck et al., 1997), while high-resolution (sub-decadal) sea ice reconstructions do not exist at present. Such reconstructions would allow an extension of the observational record and help elucidate the role of natural sea ice variability within the Arctic climate system, as well as assist in forecasting future Arctic climate conditions under global warming scenarios.

1.2. Research objectives

This thesis aims to study coupled climate and sea ice variability in the Arctic using available observations and paleoclimate reconstructions. Existing observational sea ice datasets have been assembled and homogenized and new climate and sea ice proxies have been developed, tested and analyzed to further our comprehension of coupled Arctic climate and sea ice and variability over the recent decades to centuries.

The questions guiding this research are:

(1) How do recent (< 100 yr) changes in Arctic sea ice conditions relate to climate variability, both natural and anthropogenically-forced?

(2) How can we infer past Arctic sea ice history from ice cores and other proxy records?

(3) What was the natural variability of Arctic sea ice cover over the past ~1000 years?

(4) How do recent trends in Arctic sea ice cover and climate observations fit into this longer-term, millennial-scale perspective?

(5) What were the dominant processes that controlled natural sea ice cover variations during the recent (<100 yr) and long-term (~1000 yr) period?

1.3. Study region

The Arctic is dominated by the cryosphere, with sea ice, permafrost, land ice (glaciers, ice caps), as well as river and lake ice being essential components of the physical environment. Traditional boundaries for delineation of the Arctic include the Arctic Circle (66.33°N), the 10°C July isotherm or the northern tree line. Since the focus of the proposed research is on sea ice and related climate variability, the study region is defined as the 'marine Arctic' (Macdonald et al., 2003), which denotes an area that includes

Baffin, Hudson, and James Bays; the Labrador, Greenland, Iceland, Norwegian, and Bering Seas; and the Arctic Ocean (Figure 1.1). This research thesis focuses on three specific areas:

(1) The Canadian Arctic, which includes Canadian waters north of latitude 60°N (Chapter 2 and 3)

(2) The Baffin Bay and Smith Sound area (Chapter 3 and 5)

(3) The entire Arctic region (Chapter 4 and 6)

1.4. THE ARCTIC CLIMATE SYSTEM

The climate of the Arctic may be viewed as a system in which the ocean, atmosphere and cryosphere interact together to produce climate variations. This 'internal variability' occurs at various timescales and takes place independently from changes outside the system. Climate variations also occur when the system responds to changes in boundary conditions, or 'external forcing factors', such as long-term changes in incoming solar radiation, atmospheric GHG concentrations or volcanic aerosol loading. Hence climate change reflects the complex interactions between the internal components of the system as well as their response to external forcing. Isolating and understanding the role of human activities on the whole system, or one of its components such as sea ice, represents a significant challenge which requires a good understanding of the relationships between the different components. The main components of the Arctic climate system are reviewed in the next sections.

1.4.1. Ocean circulation in the Arctic

The Arctic Ocean covers about 11.5 million km^2 and forms the core of the Arctic. Its two principal basins, the Eurasian Basin (Amundsen and Nansen) and Canada Basin, are more than 4000 m deep and almost completely landlocked, while shallower continental shelves around the central basin account for more than half of the Arctic Ocean area (Figure 1.1). The 2600-m deep Fram Strait between Svalbard and Greenland is the main connecting pathway to the Atlantic Ocean, while connection with the Pacific Ocean occurs through the narrow and shallow (45 m) Bering Strait.

Relatively warm, saline waters from the North Atlantic enter the Arctic through Fram Strait via the West Spitsbergen Current, and into the Eastern Barents Sea by way of the Barents Sea trough-flow (Figure 1.2). Waters entering trough the Fram Strait and Barents Sea are important sources of heat and salt for the Arctic Ocean. These waters are then diluted by continental freshwater runoff from large rivers such as the Mackenzie, Yenisei or Ob. The two branches of Atlantic inflow interleave and mix at depths of 200 to 2000 m in the Arctic Ocean because of their high salinity and density. They circulate counter-clockwise around the Arctic sub-basins before eventually exiting the Arctic via Fram Strait as a cold, fresh and dense outflow which becomes North Atlantic deep-water. Relatively warm saline water also flows north via the West Greenland Current into Baffin Bay, where it mixes with Arctic outflow and joins the south-flowing Baffin Current.

Water exchange through the Bering Strait is dominated by the inflow of water from the North Pacific into the Arctic Ocean. It spreads north from Bering Strait to dominate the upper layers of the Chukchi and Beaufort Seas, Canada Basin, and the straits and channels of the Canadian Archipelago. An oceanic front presently located over

the Alpha-Mendeleyev Ridge in the Canada Basin separates the region of Pacific dominance from an "Atlantic domain" in the eastern hemisphere.

The interplay of Atlantic and Pacific influences, the inflow of freshwater from river runoff, and the seasonal cycle of freezing and melting create a layered structure in the Arctic Ocean (Figure 1.2). At the top is a cold halocline layer (0-200 m) of relatively fresh seawater diluted by precipitation, river discharge and ice melt. Beneath this halocline is the warmer Atlantic Layer (~200-900 m), which overlies the cold and dense Arctic Deep Water (~900-3000 m). The surface halocline is a determining condition for the existence of perennial sea ice under the present climate. The salinity gradient in the halocline isolates sea ice from deeper and warmer waters, while the weak temperature gradient minimizes the upward flux of heat.

Surface waters within the Arctic Ocean flow along two main currents: the Beaufort Gyre which flows clockwise in response to prevalent anti-cyclonic wind circulation (Ekman transport), and the Transpolar Drift, which is driven by inflow from the large Siberian rivers and by predominant westerly winds that push Arctic surface waters eastward into the Atlantic. These major currents are largely responsible for interannual sea ice drift patterns.

1.4.2. Arctic atmosphere

The dynamics of the arctic atmosphere are highly influenced by the hemispheric circulation, which itself is closely linked to surface pressure patterns. The dominant features of the Northern Hemisphere (NH) surface pressure field in winter are the oceanic Aleutian and Icelandic Lows, and the continental Siberian High with its extension into the Arctic (the Beaufort High). The sea-level pressure distribution in summer is

dominated by subtropical highs in the eastern Pacific and Atlantic Oceans, with relatively weak gradients in polar and subpolar regions. The semi-permanent Aleutian and Icelandic low-pressure centers both result from, and control, the dominant cyclonic storm tracks which carry heat, momentum, and moisture into the Arctic, and have a significant influence on high-latitude climate (see major wind flow patterns in Figure 1.3).

Variations in the intensity and location of these semi-permanent lows and high-pressure centers are associated with specific modes of atmospheric variability. In the NH, the North Atlantic Oscillation (NAO) describes the interplay between the Icelandic Low and the Azores High, which dominates both the intra-seasonal (month-to-month) and interannual variability in sea-level pressure. In its positive phase (depressed Icelandic Low, intensified Azores High), the westerly winds over the North Atlantic are strengthened and storm tracks are displaced northward. This results in increased poleward advection of warm and moist air into the Eurasian Arctic, while cold northerly winds prevail over the eastern Canadian Arctic (Hurrell, 1995). In its negative phase (shallower Icelandic Low and weaker Azores High), the meridional pressure gradient decreases and the storm tracks are shifted southward, bringing moist air to southern Europe, while a drier and colder climate prevails in northern Europe. Thus oscillations in the NAO index are associated with a temperature seesaw between the Baffin Bay/Davis Strait/Greenland region and the European Arctic (Overland et al., 2004a).

Recently, it has been proposed that the NAO is a local manifestation of a broader, annular pattern of sea-level pressure variability called the Arctic Oscillation (AO, Thompson and Wallace, 1998). The AO is the dominant mode of sea-level pressure variability for the NH and represents the surface manifestation of variations in the

strength of the polar vortex. The AO and NAO indices are highly correlated in winter, indicating the dominance of North Atlantic sea-level pressure variability on the more hemispheric AO pattern. The AO/NAO index was at its most negative in the 1960s. There was a general increasing trend from about 1970 to 1989, when the AO entered a positive phase of unprecedented strength in the last century. This was accompanied by a reduction of sea-level pressure over the Arctic (Walsh et al., 1996) that resulted in weakening of the dominant anticyclonic flow. There is considerable debate about the mechanisms driving the AO/NAO variability (Marshall et al., 2001). It is possible that the added radiative forcing due to rising GHG concentrations may have forced the AO/NAO in a prolonged positive phase, which enhanced Arctic warming. Supporting observations show that the spatial pattern of the recent trend in Arctic surface air temperature (SAT) strongly resembles the SAT signature of the AO (Moritz et al., 2002).

Climate variability in the Pacific Ocean regions also affects the Arctic. Decadal oscillatory changes in sea surface temperature in the northeast Pacific Ocean have been found to result from teleconnections with tropical El Ninõ Southern Oscillation (ENSO) changes, and are represented in a Pacific Decadal Oscillation index (PDO, Mantua and Hare, 2002). The PDO manifests itself as an alternation between warm and cool surface waters in the Pacific Ocean, north of 20° N. During a warm, or positive phase of the PDO, the west Pacific becomes cooler and part of the eastern Pacific Ocean warms, affecting air marine advection patterns in the western Arctic.

1.4.3. Arctic sea ice

Over the last decades, the mean Arctic sea ice extent typically reaches its maximum in early March, covering around 15 million km^2, and decreases to a minimum of ~7 million

km^2 in early September. The multiyear, perennial ice that survives summer melt may be 2-4 m thick, while the first-year, seasonal ice thickness is usually less than 2 m (Serreze and Barry, 2005, p.179). The present sea ice distribution reflects the prevalent atmospheric and ocean currents. For example, the southward, cold East Greenland current favors the expansion and growth of ice along the western coast of Greenland, while the warm inflow from the North Atlantic current limits its expansion into the Norwegian Sea. A similar asymmetry exists in Davis Strait where the relatively warm, north-flowing East Greenland current inhibits ice growth in eastern Davis Strait/Labrador Sea, while the colder south-flowing Baffin current favors the expansion of ice into the western Labrador Sea.

Inter-annual sea ice variability results from complex interactions between oceanic and atmospheric processes. On time scales of days to months, sea ice responds strongly to local and regional wind patterns (Fang and Wallace, 1994; Thorndike and Colony, 1982) On multi-annual to decadal scales, the areal distribution and thickness of sea ice appears to co-vary with the major modes of atmospheric and oceanic circulation (Deser et al., 2002). Notably, the AO explains a significant portion of the recent variability in winter ice extent, which may in turn impact spring-summer ice conditions through ocean-atmosphere heat transfer (Rigor et al, 2002). Such feedback mechanisms make it difficult to isolate causal mechanisms in the ocean-ice-atmosphere system (Mysak and Venegas, 1998).

Sea ice concentration is defined as the percentage of ocean covered by ice within a given area, while sea ice extent is the total ocean area within the ice edge, which is typically delineated by the 15 % ice concentration contour line. High-resolution

measurements of sea ice concentration have been obtained for the past 30 years from passive microwave satellite sensors (Cavalieri et al., 1999; Comiso and Nishio, 2008). A pronounced negative trend of ~3.7 % decade^{-1} in sea ice extent was found for the NH (Cavalieri et al., 2003; Comiso et al., 2008; Parkinson and Cavalieri, 2008). The decrease in ice extent is most evident in summer (-6.2 % decade^{-1}) and fall (-4.2 % decade^{-1}) and most pronounced in the Siberian, Chukchi and Beaufort Seas (see appendix 1). During winter, significant decreases in ice extent have occurred in the Greenland and Barents Sea (Johannessen et al., 2004).

A longer perspective on NH sea ice variability was obtained by merging the recent satellite record with historical observations of sea ice conditions made by ships and early airborne surveys (Walsh and Chapman, 2001). The century-long dataset reveals multi-annual to decadal variability in NH sea ice extent, along with a significant decrease beginning in the early 1950s and lasting until present. Longer indices of regional sea ice extent for the Barents and Greenland Seas (Vinje, 2001; Wallevik and Sigurjónsson, 1998) show that in these regions, the 20th century decrease in ice extent is pronounced in the context of to the last 500 years, but not unprecedented. Polyakov et al. (2003a) have shown that the ice extent in the Russian Arctic marginal seas (Kara, Laptev, Chukchi and East Siberian) exhibits significant multi-decadal variability which may hinder the detection of long-term trends and mask the influence of recent climate warming on ice extent. In the Greenland and Barents Sea, Divine and Dick (2006) also found multidecadal oscillations in ice extent, but superimposed on a nearly continuous decline since 1750 AD.

1.4.4. The coupled Arctic climate system

Arctic climate variability exhibits spatial coherence, especially at decadal to multi-decadal time scales (Overland et al., 2004b; Polyakov and Johnson, 2000; Venegas and Mysak, 2000). The major Arctic climate variables such as wind, air and sea temperature, precipitation, snow and ice cover, and river discharge appear to co-vary to some degree as part of internal modes of Arctic climate variability. The low-frequency (>10 year) variability observed in many climatic variables, such as the NAO/AO index, suggests an important influence of oceanic and/or cryospheric processes on the variability of this coupled system. Sea ice is perhaps the most important component with the potential to respond to, and impact on, the Arctic climate system, because it is strongly coupled to atmospheric and oceanic processes. In chapter 6 this coupling between sea ice and climate was exploited to reconstruct past sea ice extent using proxies reflecting climate variables known to drive and/or respond to changes in sea ice conditions.

1.5. MULTIPROXY CLIMATE RECONSTRUCTIONS OVER PAST MILLENNIA

Much effort has been devoted to reconstruct past NH temperatures using multiple proxies (Crowley and Lowery, 2000; D'Arrigo et al., 2006; Esper et al., 2002; Fisher, 2002; Hegerl et al., 2006; Jones et al., 1998; Mann et al., 1998, 1999; Mann et al., 2008; Moberg et al., 2005; Osborn and Briffa, 2006). Various authors have used different proxies and methods with differing results concerning the amplitude of reconstructed temperature changes.

The basic premise behind the multiproxy approach is that large-scale climate patterns may be reconstructed using a sufficiently large and well-distributed network of climate-sensitive proxies, some of which are described in section 1.6.4 (Mann, 2002;

Mann et al., 2005). Each proxy indicator is considered to blend a local climate signal with unrelated variability or stochastic noise (von Storch et al., 2004). The noise is assumed to be independent between the different proxies and is expected to cancel out when combining the proxies together. The question of how many proxies are needed to reconstruct large-scale climate variability depends on both the quality of each proxy (signal-to-noise ratio) and the spatial degree of freedom (number of spatially independent observations) of the targeted climate field (Bradley, 1996; Bretherton et al., 1999; Mann and Rutherford, 2002). Proxies may have different amounts and type of noise, spectral sensitivity to climate, and may suffer from dating uncertainties. For example, isotopic diffusion in ice cores makes $\delta^{18}O$ time series from these cores biased toward low frequencies, while the process of removing the biological growth curve in tree-ring width time series introduces a bias toward high frequencies. By combining several types of proxies, the noise is reduced and the spectral sensitivity widens (Fisher, 2002).

Several approaches have been used to combine proxies. The simplest approach assumes that each proxy predominantly reflects a specific climatic signal, such as air temperature. The proxies are then standardized and averaged, and the resulting spatial mean is scaled to the variance of the target series (e.g. NH temperature, Jones et al., 1998). Unequal weights may also be attributed to proxy series through the use of Empirical Orthogonal Function (EOF) analysis (e.g. Fisher, 2002). This method seeks to extract the common, dominant signal(s) among the proxies, and differs from a simple average of the proxy suite.

More elaborate multivariate statistical techniques have been used for calibrating modern climate observations against a proxy network. The methods are usually based on

linear models such as ordinary least square regression, total least square regression, principal component regression, canonical correlation analysis and partial least square regression (e.g. Cook et al., 1994; Fritts, 1991; North et al., 2006; Rutherford et al., 2005). These methods may be applied to reconstruct a single target series (predictand) such as a hemispheric average temperature (e.g., Hegerl et al., 2006), a climatic index such as the NAO (e.g., Cook et al., 2002), or individual spatial modes of climatic variability (Fritts, 1991; Mann et al., 1998).

NH temperature reconstructions over recent millennia have confirmed the existence of a period of relatively mild climate, called the Medieval Warm Period (MWP), which occurred between 900 to 1300 AD (Jones and Mann, 2004). Climate during those times may have been warmer than today in some regions, but the warmth was asynchronous on a hemispheric scale (Crowley and Lowery, 2000). A period of NH cooling known as the Little Ice Age (LIA) followed until the early to mid-19th century. The precise onset and termination of these two climatic events is debated, and may have varied between regions (Jones and Mann, 2004). The 20th century warming is clearly evident in most proxy records, although there is still debate as to whether the present global temperature rise exceeds previous warm periods such as the MWP (Bradley et al., 2003; Esper et al., 2004; Esper et al., 2005; Jones and Mann, 2004; Soon and Baliunas, 2003). The rate of 20th century warming, however, appears to be anomalous in the context of the past 1000 years, and cannot be explained by natural forcing alone (Barnett et al., 2005).

Many questions remain unanswered concerning the respective influence of natural and anthropogenic forcing on climate. Answering these questions requires a good

understanding of the mechanisms that generate climate variability, and how these respond to external forcing. Notably, the role played by sea ice variability in driving or modulating Arctic and global climate change is poorly known. It has been hypothesized that past rapid climate change events were triggered by abrupt reductions in ice extent (Gildor et al., 2003). Past abrupt sea ice reductions have been modeled (Holland et al., 2006), and one was recently observed when ice extent shrunk by 42 % in September 2007 relative to the past 30 year average (Stroeve et al., 2007). Reconstructing long-term (~1000 years) Arctic sea ice and climate variability may help to unravel the role played by sea ice within the Arctic and global climate system.

1.6. DATA AND METHODS

1.6.1. Field methods

Part of this research project involved the development of a new ice-core climate record from the Prince of Wales Icefield (POW) on Ellesmere Island, Nunavut (Figure 1.1). The POW icefield has a relatively high snow accumulation rate (0.30 m-ice year^{-1}) and is therefore expected to preserve a high-resolution (sub-annual to decadal) record of past climate change for at least the last 1000 years. The proximity of the POW icefield to the North Open Water Polynya and Baffin Bay also make it a good location to investigate potential sea ice proxies (melt %, $\delta^{18}O$, sea salts) in the ice-core record.

The ice-core drilling operation took place in April-May 2005 (see Appendix 2). Two long ice cores, spaced ~1.1 m apart, were recovered using an electro-mechanical drill: the first one reached bedrock at 176.5 m, while the second one reached a depth of 150.7 m. The longest core was used for stratigraphic description as well as stable isotope ($\delta^{18}O$, δH) and ionic chemistry analyses, while the other core is being used in a separate

study on sulphur isotopes by researchers at the University of Calgary. In the field, each core segment was handled with clean plastic gloves and packed in clean plastic bags, and then brought in a separate tent for preliminary measurements. These included stratigraphic descriptions and photography of the cores disposed over a backlit table, as well as electrical conductivity measurements (ECM) of the ice (see Chapter 5). The high ECM resolution (a few mm) allows for precise identification of acidity peaks related to volcanic eruptions, which were used as dating markers.

1.6.2. Laboratory methods

The ice cores were brought back frozen to the Geological Survey of Canada in Ottawa where they were stored in a freezer. One-meter sections of the deeper (176.5-m long) core were cut lengthwise to produce 4.5 x 4.5 x 100 cm segments for high-resolution stable isotope and chemical analyses. Two of the remaining core pieces were combined and cut into ~4.5 cm-long samples to be used for preliminary, lower-resolution measurements of $\delta^{18}O$. The remaining half core segments were stored as an archive.

A continuous ice core melter-sampler system was built based on the design of Osterberg et al (2006) to produce discrete, uncontaminated liquid samples at high-resolution for chemical and isotopic analyses (Appendix 3). Pre-cut rectangular firn/ice core sections were mounted upright in a 1-m pre-cleaned Plexiglas container opened at the bottom so the ice is in contact with the melter head. The latter consists of a nickel plate mounted on a heated aluminum base. The melter plate is 3 mm thick with a series of radiating 200 μm wide slits through which meltwater flows. The slits produce a downward capillary force that prevents wicking of the meltwater into unmelted core, thereby allowing both porous firn and solid ice to be melted and sampled at high

resolution. The melter head splits the meltwater into two channels physically separated by a ridge (1 mm high) on the surface of the plate. Meltwater from the potentially contaminated outer portion of the ice core is directed to the outer channel for stable isotope analysis, and meltwater from the uncontaminated, innermost portion of the ice core is directed to the inner channel for major ion analyses. Water from both channels is pumped by two peristaltic pumps into fractional collectors which count the desired number of water drops per sample and automatically distributes the samples into clean vials. The sampling volume was set to 5 ml for the inner channel, which gave an average sample thickness of 1.3 cm (ice-equivalent density). The inner core samples are currently being analyzed at the University of Alberta for major ions by liquid-phase chromatography, while the outer core samples have been analyzed at the University of Copenhagen for oxygen isotope ratios.

1.6.3. Instrumental Data

A large part of this research involved the use of existing databases of climate observations to study sea ice climate relationships and to calibrate modern sea ice variations against potential sea ice proxies. "Calibration" in this context means the establishment of a quantitative relationship between documented sea ice cover variations and a proxy or combination of proxies. These databases are briefly presented here.

Canadian Ice Service sea ice operational charts

Charts depicting the extent, concentration and type of sea ice present in Canadian waters at a one- to four-week intervals have been produced since 1968 by the Canadian Ice Service (CIS). The original ice charts were recently digitized and merged into a

spatially and temporally consistent gridded database with a spatial resolution of 0.25° x 0.25°. Because the CIS ice charts involve interpretation by an ice analyst, they are better suited for discriminating open water from water pounding at the surface of melting ice, than algorithms used to retrieve sea ice concentrations from satellites (Agnew and Howell, 2003). The ice charts, obtained through collaboration with researchers at the CIS, were interpolated to fill in missing values, and averaged to monthly resolution. They were then used to study recent sea ice variability in the Canadian Arctic for the period 1980-2004 (see Chapter 2). The database was further used to calibrate an ice core sea-salt record from Devon ice cap against sea ice concentration in the Canadian Arctic (see Chapter 3).

National Centers for Environmental Prediction (NCEP) reanalysis data

NCEP gridded climate reanalysis products are available publicly from the Climate Diagnostic Center at the National Oceanic and Atmospheric Administration (CDC-NOAA, www.cdc.noaa.gov/cdc/data.ncep.reanalysis.html). Climate reanalyses use climate observations within a data assimilation model to produce spatially and temporally coherent gridded climate datasets for the period 1948 to present (Kalnay et al., 1996). The NCEP 2.5°× 2.5° grids of monthly surface air temperature (SAT) and sea-level air pressure (SLP) were obtained from CDC. Geostrophic surface wind vectors (*u*- and *v*-winds) were calculated from the SLP grids. Spatial patterns of SAT and SLP were related to the main modes of sea ice variability in the Canadian Arctic derived from analysis of the CIS ice charts (see Chapter 2).

Extended Reconstructed Sea Surface Temperature database (ERSST v.2)

The ERSSR v.2 sea surface temperature (SST) gridded dataset (Smith and Reynolds, 2004) was obtained from the National Climatic Data Center at NOAA (www.ncdc.noaa.gov/oa/climate/research/sst/ersstv2.php), and related to modes of sea ice variability in the Canadian Arctic (Chapter 2). The ERSST dataset was constructed with the most recently available International Comprehensive Ocean-Atmosphere Data Set (ICOADS) SST data, and using improved statistical methods that allow coherent reconstruction from sparse data.

University of Illinois NH sea ice concentrations

Grids of mid-month sea ice concentration for the whole Northern Hemisphere are available from the University of Illinois (http://www.arctic.atmos.uiuc.edu/SEAICE/). The data are mapped on a standard 1×1 degree cylindrical projection, and cover the period 1870-2008. The dataset is a compilation from various sources (historical, airborne and satellite observations) which changed over time, and represents the most complete hemispheric dataset currently available (Walsh and Chapman, 2001; hereafter referred to as WC). It was used to study recent trends in Arctic seasonal ice extent (Chapter 4), and an improved version of the dataset was further used to calibrate a network of potential sea ice proxies in order to reconstruct past Arctic sea ice history (Chapter 6).

Russian Arctic marginal seas ice extent

Total sea ice extent data for the Kara, Laptev, East Siberian and Chukchi Seas over the period 1901-2000 were presented by Polyakov et al (2003a). These authors digitized ice edge positions from operational ice charts compiled and recently released by

the Arctic and Antarctic Research Institute in Saint-Petersburg, Russia. The ice extent time series are available online (http://people.iarc.uaf.edu/~igor/). Observations in the Russian Arctic prior to the satellite era are scarce in the WC dataset. An improved total Arctic ice extent index was derived by replacing the WC ice extent data by those from Polyakov et al (2003a) for the Russian marginal seas. Details of the comparison between these datasets are given in Appendix 4. The new Arctic ice extent index was used in the multiproxy reconstruction of Arctic sea ice extent presented in Chapter 6.

Arctic surface temperature data

Polyakov et al (2003b) compiled sea-level pressure and surface air temperature (SAT) data from weather stations throughout the Arctic. Data from each weather station were downloaded from http://www.frontier.iarc.uaf.edu/~igor/research/data/airtemppres.php, and the same quality-controlled stations used by Polyakov et al (2002) were composited into an Arctic-wide annual temperature index. This index was used to compare against the climate proxy network study in Chapter 6.

1.6.4. Sea ice and climate proxies

Paleoclimate proxies used in high-latitude environments come primarily from glacier ice cores, tree rings, peat bogs, and lake or ocean sediments. In this study, most of the proxies used are derived from glacial cores and a few tree ring and laminated lake sediment records. The snow that is deposited each year on Arctic ice caps contains a variety of environmental signals which may be analyzed at a high temporal resolution (e.g. Bradley, 1999; Legrand and Mayewski, 1997). Published ice-core proxy time series as well as lake sediment records were obtained from the World Data Center for

Paleoclimatology (WDC, http://www.ncdc.noaa.gov/paleo/paleo.html) and the PANGAEA database at the Alfred Wegener Institute (http://www.pangaea.de/), or directly from the original authors. Tree-ring width records from the circum-Arctic region, and processed by the regional curve standardization (RCS) technique to preserve low-frequency variability (e.g. Esper et al, 2002; D'Arrigo et al, 2006), were obtained directly from various authors. The main climate proxies used in this thesis are described next.

Oxygen isotope ratio

The ratio of heavy to light oxygen isotopes in snow ($\delta^{18}O$), expressed as departure from the standard mean ocean water (SMOW), is a first-order proxy for condensation temperature at the deposition site. It is often taken as a proxy for mean annual air temperature, assuming that snow precipitation is more-or-less evenly distributed throughout the year. $\delta^{18}O$-derived temperatures may be biased toward the warm season when precipitation is more abundant. Other factors may influence the $\delta^{18}O$ of snow, such as the distance to the moisture source and the water temperature at the source (Bradley, 1999). For low-elevation ice caps, the varying distance to the sea ice edge may thus influence the $\delta^{18}O$ of snow (Isaksson et al., 2003; Isaksson et al., 2005b).

Melt percentage

The proportion of refrozen meltwater in the total accumulated snow layer (normalized to water equivalent) in a given year or longer time interval (e.g., 5 years) is a direct proxy for summer warmth (Koerner, 1997; Koerner and Fisher, 1990). Koerner (1977) found a significant inverse relationship between summer sea ice extent in the Queen Elizabeth Islands (QEI) and the melt % in an ice core from Devon ice cap. Such a

relationship may indicate reduced sea ice cover due to increased summer warmth and/or a positive feedback from reduced sea ice on surface air temperature.

Glaciochemistry

The concentration of the major soluble ionic species is routinely measured in ice cores. These represent primary or secondary aerosols (or their derivatives) transported and deposited in the ice from relatively distant continental or oceanic source(s). Several factors may cause the concentration of given ionic species to vary, in particular changes in source emissions, atmospheric transport efficiency, and precipitation scavenging rate (Legrand and Mayewski, 1997). Ionic species such as Na^+, Cl^- and Mg^{2+} mainly originate from sea-salt aerosols produced at the sea surface by the breaking of waves by wind (sea spray). In central and northern Greenland ice cores, the changing concentrations of sea-salt ions for the past ~1000 years have been interpreted as resulting primarily from changes in transport efficiency, with colder periods such as the Little Ice Age associated with enhanced transport and deposition of aerosols to the ice cap (Dawson et al., 2003; Fischer et al., 1998; Mayewski et al., 1993; Meeker and Mayewski, 2002; O'Brien et al., 1995). The increased sea salt delivery was explained by an overall enhanced meridional pressure gradient and thus more frequent and intense storms, mainly in the North Atlantic region (Fischer and Mieding, 2005), but perhaps also in the northeastern Pacific region (Fischer, 2001).

A different interpretation of ice core sea-salt variations was proposed in the Canadian Arctic. On Penny and Devon ice caps, which lie at lower elevations and are closer to the sea than central Greenland, inverse correlations were found between ice extent and sea salt concentrations. This suggests that surrounding sea ice cover limits the

delivery of sea salt aerosols to the ice caps, and their concentrations may therefore be used as proxies to infer past sea ice conditions (Grumet et al., 2001; Kinnard et al., 2006b; Murphy, 2000, see Chapter 3). Similar results were also found on the Antarctic Peninsula (Aristarain et al., 2004).

Another potentially useful proxy for sea ice conditions is methanesulfonic acid (MSA) concentration. MSA is a by-product of biogenic dimethyl sulfide (DMS) gas and a proxy for marine biogenic productivity. In polar waters, DMS production is strongly influenced by sea ice coverage and consequently MSA has been used as a sea ice indicator in both the Arctic (Isaksson et al., 2005a; O'Dwyer et al., 2000) and the Antarctic (Curran et al., 2003; Welch et al., 1993).

The concentration of impurities in ice cores may also vary due to changes in precipitation rates between the aerosol source regions and the site of deposition (Hansson, 1995). More efficient removal by precipitation in air masses en route to the ice cap will decrease the residence time of the aerosol and its final concentration at the ice-coring site. This will particularly affect aerosols from very distant sources ($> 10^3$ km).

Tree rings and other proxies

Tree rings series have often been used to reconstruct past high-latitude climates (D'Arrigo and Jacoby, 1993; Fritts, 1991). The most commonly used parameter is the width of the annual growth ring, which typically responds to variations in moisture availability and the length of the growing season. Some long tree-rings series (>1000 yr) exist for Northern Russia, Scandinavia, Canada and Alaska (e.g. D'Arrigo et al., 2006; Esper et al., 2002), and these were used to complement the spatial coverage of ice-core climate proxies for this study. It was hypothesized that trees living close to the coast may

carry a climatic signal that is part of the coupled sea ice climate system, and could therefore be used as potential indicators of past coupled sea ice and climate variability. For example, a long white spruce ring-width series from northwestern Alaska was shown to correlate significantly with sea surface temperature (SST) in the Bering and Chukchi Seas, as well as with the PDO (D'Arrigo et al., 2005). Since sea ice in this area is expected to respond to and impact on SST, such tree ring series could help to extract valuable paleoclimatic information pertaining to sea ice conditions in this area of the Arctic.

Lake sediments contain valuable paleoclimatic information, but may be more difficult to relate to sea ice history since the signal also depends on the properties of the lake catchment. A few high-resolution, temperature-sensitive varve thickness records spanning the last few centuries are available in the Canadian Arctic (Hughen et al., 2000; Moore et al., 2001; Overpeck et al., 1997) and have been included in the multiproxy network for calibration with observed Arctic sea ice extent.

Ocean sediments offer great potential to reconstruct past sea ice history (de Vernal et al., 2005; Fisher et al., 2006), but high-resolution (< 10 yr) records are not yet publicly available. Progress is currently being made to develop direct proxies from ice-rafted debris and micro-organism assemblages (de Vernal et al., 2005; Jensen et al., 2004; Moros et al., 2006).

Figure 1.1. Map of the Arctic (Source: MacDonald et al, 2003)

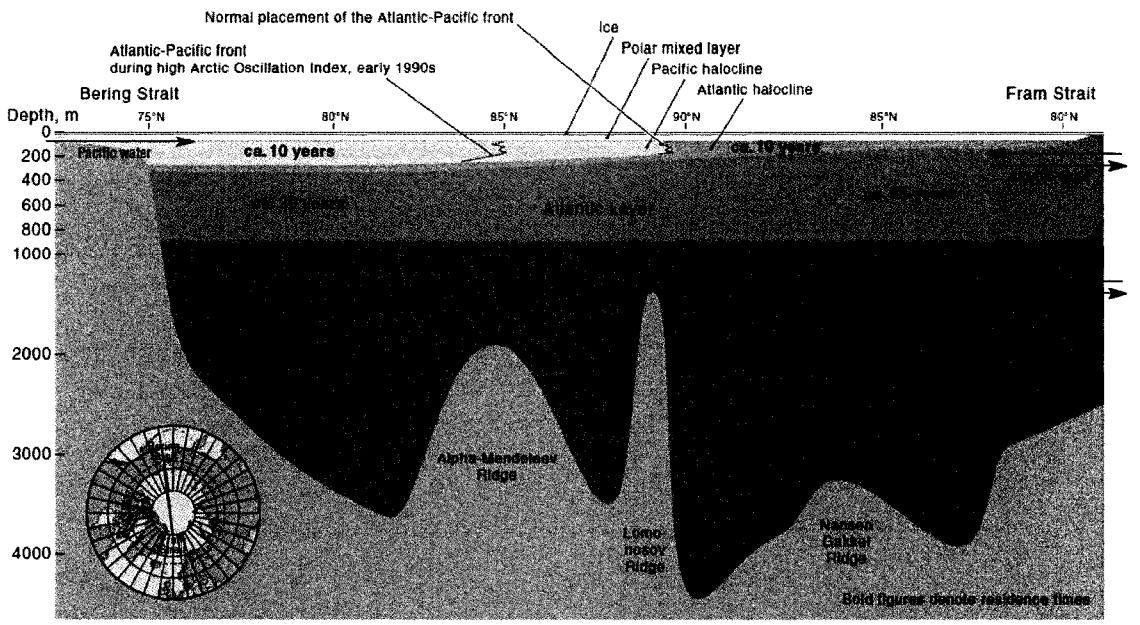

Figure 1.2. The stratification of the Arctic Ocean, showing the polar mixed layer, the Pacific and Atlantic domains of influence and the haloclines. The red lines show the normal placement and the displacement of the Atlantic-Pacific front during the high Arctic Oscillation index of the early 1990s. From Macdonald et al, 2003.

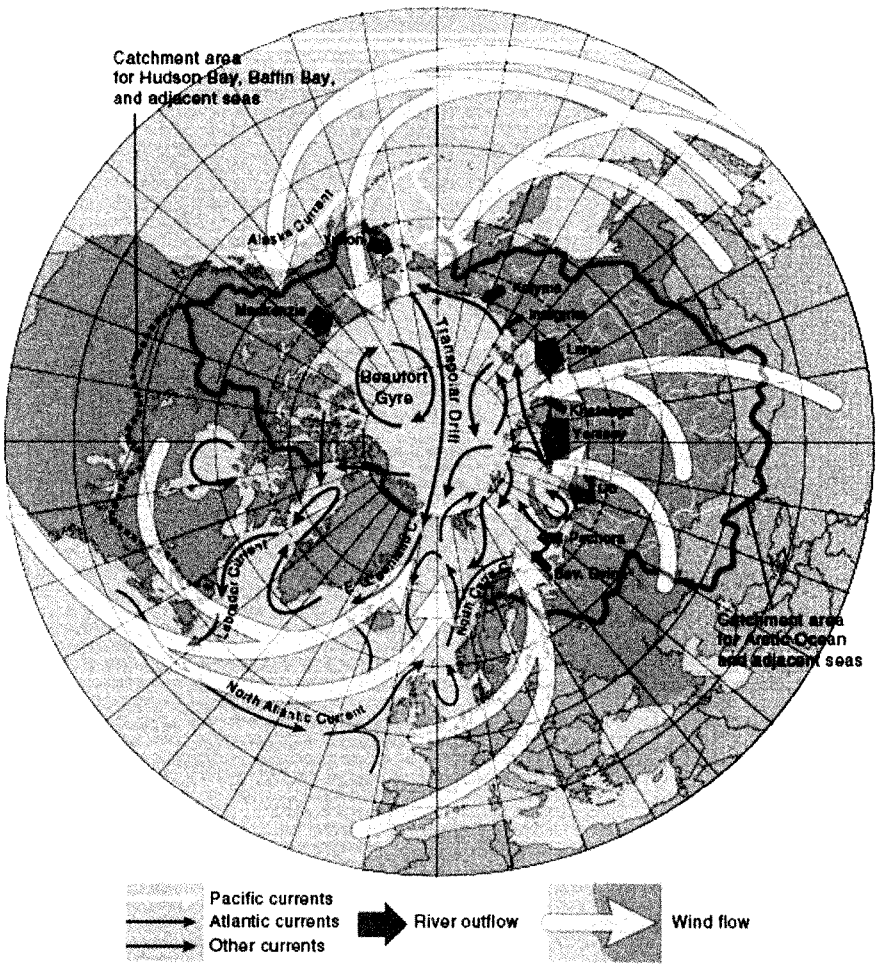

Figure 1.3. Main surface features of atmospheric and oceanic circulation in the Arctic. Source: Macdonald et al, 2003.

CHAPTER 2. CLIMATIC ANALYSIS OF SEA ICE VARIABILITY IN THE CANADIAN ARCTIC FROM OPERATIONAL CHARTS, 1980-2004

Christophe Kinnard[1, 2],

Christian M. Zdanowicz[2]

David A. Fisher[2]

Bea Alt[3]

Steve McCourt[4]

(1) Department of Geography, University of Ottawa

(2) National Glaciology Program, Geological Survey of Canada, Ottawa

(3) Balanced Environment Associates

(4) Canadian Ice Service, Environment Canada, Ottawa

Corresponding author: C. Kinnard

Department of Geography, University of Ottawa, 60 University St, Simard Hall, Ottawa (Ontario), Canada K1N 6N5

Tel.:+1 613 947-5169; fax: + 1 613 562-5145 email: ckinn045@uottawa.ca

Published in: ANNALS OF GLACIOLOGY, VOL. 44, 391-402, 2006

Abstract

We present a complete climatic analysis of sea ice conditions in the Canadian Arctic based on digitized operational charts from the Canadian Ice Service for the period 1980-2004. The seasonal climatology, spatial variance and linear trends in total ice concentrations (CT) were calculated. Maximum reduction rate in CT were found in the Beaufort Sea (> 24% decade^{-1}) and in the Davis Strait/Labrador Sea region (> 18% decade^{-1}) during spring and summer. Empirical orthogonal function analysis (EOF) performed on monthly CT deviations yielded four significant EOF modes explaining 32% of the total variance. The spatial pattern, temporal behavior and seasonality of these four EOF modes are discussed and correlated with fields of sea-level pressure, surface winds, surface air temperature and sea surface temperature monthly anomalies. These results point to the dominant influence of the North Atlantic Oscillation on CT decadal anomalies during the cold season, while climate variability in the Pacific influences CT variations in the Beaufort Sea region during spring-summer.

2.1. INTRODUCTION

Satellite, surface and submarine observations have revealed a significant areal reduction and thinning of Arctic sea ice cover in the past 50 years (Vinnikov et al., 1999). Satellite observations are mostly derived from passive-microwave sensor measurements of total sea ice concentration (CT, see Table 2.1 for a list of acronyms used in the text), available continuously since 1978 (Parkinson et al., 1999). Derived parameters such as total sea ice-covered area and ice extent (total area with CT > 15 %) show a decrease of about 3% per decade for the Northern Hemisphere over this period (Cavalieri et al., 1997; Johannessen et al., 2004). The exact cause of sea ice cover reduction is still a matter of debate, as it could result from complex interactions between marine and atmospheric forcing and feedbacks (e.g. Zhang et al., 2000). However, there is a growing recognition that anthropogenic climate warming since the late 20th century may be partly responsible for the recent decline (Johannessen et al., 2004; Vinnikov et al., 1999). Sea ice response to natural and anthropogenic climate forcing may vary greatly between regions having different ice regimes (Gloersen et al., 1999; Parkinson et al., 1999). For this reason, studies of regional sea ice variability are needed in order to better understand sea ice dynamics and assess potential future changes.

The Canadian Arctic, defined here as including Hudson Bay (HB), the Arctic Archipelago, and the Davis Strait/Labrador Sea region (DS/LS) is made of an intricate network of channels, islands and bays with different and complex ice regimes (Figure 2.1). The projected retreat and possible disappearance of the summer icepack within this century (Vinnikov et al., 1999) could open the way to increased marine shipping via the Northwest Passage. However it has been suggested that a reduction of first year ice

formation could also allow for incursion of more older ice in the Arctic Archipelago, therefore complicating projections of future ice extent in that region (Falkingham et al., 2001; Wilson et al., 2004).

Here we present results of a systematic investigation of recent (25-year) sea ice variability in the Canadian Arctic and related climatic control. For this analysis we use a gridded, high-resolution digital database of sea ice concentration for the period 1980-2004, recently produced by the Canadian Ice Service (CIS) at Environment Canada. This period was chosen because we are interested in the seasonality of recent sea ice changes and ice charts only became available on a year-round basis after 1980.

2.2. DATABASE AND METHODS

2.2.1. Sea ice data

Observations of sea ice conditions have been collected by the CIS since 1968 as an aid to Arctic shipping, using a combination of spaceborne and airborne sensors as well as surface visual observations. These data were first published as regional weekly operational charts in the shipping season only (June to October). Each chart is made of mapped polygons with sea ice CT and information on sea ice type. After 1980, winter charts were produced at 2-4 week intervals and the accuracy of the database improved as the availability and precision of sensors increased and the use of nowcasting techniques (interpolation of missing chart from past ice conditions and present meteorological conditions) decreased. Detailed information on data acquisition, chart preparation procedures and chart accuracy is available in Crocker and Carrieres (2000). The weekly regional charts were recently digitized and merged into a spatially and temporally consistent gridded database with a spatial resolution of 0.25° x 0.25°. Thus pixel size

varies from 16 km X 27.8 km at 55°N to 4 km x 27.8 km at 82°N. Each weekly grid supplies information on sea ice CT data in tenths per grid cell. The CT values are broadly consistent with those obtained form passive microwave sensors, but the CIS database offers a better coverage of transitional periods (freeze-up and break-up) than the microwave sensors, which are biased due to difficulties in discriminating between melting ponds and open water (Agnew and Howell, 2003). For this study, monthly CT averages were calculated over the period 1980-2004 by averaging the weekly ice concentration data on a pixel-by-pixel basis. Monthly averages include three to four weekly charts, except in winter (December-May) when one or two charts were used. If no weekly charts could be found at a particular grid point for a given month, this month was flagged as a missing value. The mean monthly climatology of sea ice CT was calculated by averaging the CT data at each grid point for the entire period of record (1980-2004). Monthly CT anomalies were then computed by subtracting the mean annual cycle from monthly averages. Seasonally-averaged CT values were also calculated for the winter (JFM), spring (AMJ), summer (JAS) and fall (OND) gridded series. Spatial linear trends in monthly CT anomalies and seasonal CT values were determined by least-square regression at each grid point.

The spatio-temporal variability of monthly CT anomalies was investigated by the empirical orthogonal function (EOF) analysis method (Ribera et al., 2001). Briefly, the method "decomposes" the total variance in the CT anomalies into a set of mutually orthogonal eigenvalues and corresponding eigenvectors from the diagonalized covariance matrix of the CT anomalies. Each eigenvector represents a spatial pattern of CT anomalies whose evolution over time is obtained by projecting the eigenvector onto the

original CT series (the expansion coefficients). Each set of eigenvalue, eigenvector and expansion coefficient series therefore defines a mode of sea ice variability which may be linked to a set of natural processes (oceanic or atmospheric). In this study eigenvectors are represented by homogeneous correlation maps between the expansion coefficient series and the original CT data matrix. Significance levels for correlations were determined at each grid point using the method of Sciremammano (1979). The method estimates the large lag standard error:

$$\sigma = \left[N^{-1} \sum_{-N}^{N} C_{xx}(i\Delta t) C_{yy}(i\Delta t) \Delta t \right]^{1/2} \quad (1)$$

where C_{xx} and C_{yy} are the autocorrelation functions for variables X and Y, N is the sample size and Δt is the sampling time interval. σ reflects the interplay between the dominant time scales of the process and the finite record length. For n degree of freedom ($n=1/\sigma^2$) > 10, the 95% level for correlation corresponds to 2.0σ (Sciremammano, 1979). To reduce sampling error at large lags (and small sample size), we used biased estimates for C_{xx} and C_{yy}. This decreases the effect of longer fluctuations, which may be inadequately sampled by short series. However, if the data length N is smaller than the length of a significant low frequency component of X or Y, then σ (and hence confidence levels) may be underestimated. Sea ice typically has long-term (decadal) memory, especially near the ice edge. 25 years of data are sufficient to sample at least two decadal cycles and obtain reasonable estimates of σ, although increasing data length would increase the robustness of σ estimates. The field significance (the minimum number of significant correlations on a grid needed to be significantly different than chance) was tested using the method of Livezey and Chen (1983). Each gridded dataset was correlated

200 times with a gaussian white noise series and the number of significant correlation was recorded each time. The 95% percentile of the distribution was used as the objective criterion for field significance. The minimum number of significant correlations needed for correlation maps between EOFs and climatological fields (see next section) was around 1000 gridpoints, or 10% of the grid. Unless stated otherwise, all correlation maps were found to pass that threshold.

2.2.2. Climatological variables

Monthly averages of sea-level pressure (SLP) and surface air temperature (SAT) from the National Centers for Environmental Prediction (NCEP) reanalysis data (Kalnay et al., 1996) were obtained through the NOAA-CIRES Climate Diagnostic Center. We used monthly sea surface temperature (SST) averages from the Extended Reconstructed SST database (ERSST v.2; Smith and Reynolds, 2004), obtained through the National Climatic Data Center at NOAA. The SLP and SAT data have resolutions of 2.5° x 2.5°, and the SST data have a resolution of 2° x 2°. Mean monthly wind vector components (*u, v*) were calculated from the monthly SLP data as surface geostrophic wind. Geostrophic winds were preferred to surface winds from NCEP because they are less model-dependent (Kalnay et al., 1996) and because, as a rule, sea ice drifts follows geostrophic winds on subannual time scales (Thorndike and Colony, 1982). Monthly anomalies of SLP, SAT, SST, *u*- and *v*-wind components were calculated in the same way as for the CT data.

The relationships between climatic variables and the principal modes of sea ice CT variability were investigated trough the use of heterogeneous correlation maps, defined as the vector of correlation values between the expansion coefficient of a

particular CT EOF mode, and all successive grid point values of a given climatic field (SAT, SLP, SST, *u* and *v*-wind). Correlation maps were prepared at different leads and lags (typically ± 12 months) to explore potential forcing and feedback mechanisms between sea ice and climatic variables. In addition, we used monthly indices of the main atmospheric teleconnection patterns in the Northern Hemisphere (Barnston and Livezey, 1987) obtained from the Climate Prediction Center at NOAA, to investigate potential relationships between sea ice variability and hemispheric modes of atmospheric circulation.

2.3. RESULTS AND DISCUSSION

2.3.1. Sea ice climatology and trends, 1980-2004

Figure 2.2 illustrates the mean seasonal climatology of sea ice CT in the Canadian Arctic for the period 1980-2004. Maximum ice extent occurs in February, with the eastern edge of the icepack located in the DS/LS region. Ice break-up begins in April-May in HB, the Beaufort Sea and the North Open Water polynya (NOW) in North Baffin Bay, while the ice edge in the LS begins to retreat northward. Minimum ice extent is reached in late summer to early fall (August-September) with the ice edge located North of Eastern Parry Channel. Heavy ice concentrations (>80%) remain west of Parry Channel, in McClintock Channel, Committee Bay, and in Nares Strait. Baffin Bay is mostly ice free in summer but light ice (<35%) may remain off the eastern coast of Baffin Island. Ice freeze-up begins in early October in the Archipelago, northern Fox Basin, Baffin Bay and the northwestern part of HB. The remaining southern areas become encumbered with ice moving with ocean currents and weather systems (Canadian Ice Service, 2002).

Maps of seasonal CT standard deviations are presented in Figure 2.3. High (low) standard deviations indicate large (small) year-to-year variability in sea ice CT. The most pronounced variability occurs in winter in the DS/LS region and in summer in the Beaufort Sea. Other areas of significant variability include the coastal regions of North Baffin Bay in spring-summer, and the northwestern and southeastern coasts of HB as well as the DS/LS region in the spring.

Linear trends in monthly CT anomalies for 1980-2004 (Figure 2.4A) reveal maximum ice cover reductions (>8% decade^{-1}) in the Beaufort Sea, DS/LS region, Hudson Strait/Ungava Bay and along the coast of southern Baffin Island. Important reductions also occur in northwestern HB and southern Foxe Basin (4-8% decade^{-1}), while smaller but statistically significant reductions occur in Foxe Basin, Coronation Gulf, Queen Maud Gulf and the Gulf of Boothia (2-4% decade^{-1}). A marked increase in CT occurs off the western coast of Banks Island, in the region of the Cape Bathurst polynya, while local increases are noted in Smith Sound, in Wellington Channel and in the Norwegian Bay area. The total normalized sea ice area (NTA, Figure 2.4B) for the whole Canadian Arctic shows an overall reduction of 3.6% decade^{-1}, consistent with previous findings (Gloersen et al., 1999; Parkinson et al., 1999). However, previous trends calculated from satellite passive microwave sensor data for the period 1978-1996 showed an increase in CT in the DS/LS region (Gloersen et al., 1999), whereas our analysis shows a substantial reduction in this area.

On a seasonal basis, the negative CT trends occur predominantly in spring and summer (Figure 2.5). Maximum reduction occurs in the Beaufort Sea in summer (14 to >24% decade^{-1}). The decrease in the DS/LS region occurs mainly in winter and spring,

with rates over 18% decade^{-1} while the decrease in northwestern HB is mainly in the spring (>12% decade^{-1}) and in summer to a lesser extent. Apart from the negative trend in the DS/LS region (not statistically significant), very little changes are observed during the winter. Maximum reduction rates during spring and summer are consistent with earlier findings (Johannessen et al., 2004; Parkinson et al., 1999; Walsh and Chapman, 2001). Although Arctic multi-year (older) ice cover has been decreasing more rapidly (7-9% decade^{-1}) than the total ice cover in the last 20-22 years (Comiso, 2002), our analysis shows little decrease in ice cover in the Queen Elizabeth Islands (QEI), an area covered year-round predominantly by multi-year ice (Canadian Ice Service, 2002). This confirms results by Agnew et al (2001) and Jeffers et al (2001) who found no statistically significant trends in the maximum amount of summer open water in the QEI for the period 1961-1998.

2.3.2. Spatio-temporal variability of sea ice cover

The four leading EOF modes of sea ice CT were verified to be uncorrelated according to North's *rule of thumb* (North et al., 1982), and together these modes explain 32% of the total variance in monthly CT anomalies. Individually, they explain 12.3%, 9%, 6% and 4.6%, respectively. The first EOF mode (EOF1) identifies a broad area of coherent sea ice cover variability that encompasses HB and the DS/LS region (Figure 2.6). This mode explains up to 25% and 50% of sea ice variance in these two regions, respectively (local variance explained = square of the correlation value). In contrast, EOF2 identifies a dipole pattern of opposition between HB and the DS/LS region, explaining up to 45% and 20% of local sea ice variance, respectively. A secondary positive centre of action is also found in the Beaufort Sea, explaining about 8% of local variance. EOF3 displays an

antiphase pattern between the Beaufort Sea (up to 65% variance explained) and Baffin Bay (up to 29% variance explained). The northwestern part of HB also loads positively in EOF3, but with only 5% of local variance explained. EOF4 shows opposite centres of action in the northern and southern parts of HB, with 25% and 20% of local variance explained, respectively. Weaker negative correlations occur along a narrow band extending south from Davis Strait along the Labrador Coast, while positive correlations are found offshore in the Labrador Sea.

Over time, EOF1 shows both low-frequency (decadal) variability and inter-annual variability, while EOF2, EOF3 and EOF4 mainly display inter-annual variability (Figure 2.7). Spectral analysis revealed that EOF1 has strongest power at ~10 yr period, with a smaller peak at ~1 yr. The temporal variance of EOF2 is spread over a broader spectrum of frequencies but shows maximum power at ~1 yr. EOF3 and EOF4 both have maximum spectral power around ~2.7 yr with smaller peaks at < 1 yr. The seasonality of each EOF mode was investigated by computing the monthly standard deviation of each expansion coefficient series (Figure 2.8). EOF1 is mainly a cold season pattern (November to June). EOF2 has maximum variability in the transition periods (freeze-up in November and melt in June-July). EOF3 is mainly a summer to early-fall pattern (June to October) and EOF4 is mainly an early to mid-summer pattern (May to July).

The variance recovered by the four leading EOF modes is similar to that found from hemispheric sea ice databases (Singarayer and Bamber, 2003). This rather low value implies that: (1) there may be other significant modes of variability which are unresolved by our analysis due to the short period of record and/or (2) that a significant portion of the total variance represents noise. In particular, the inter-channel areas of the QEI are

underrepresented in the first four EOFs. This suggests that sea ice variability in the QEI is localized and shows little connections with the broader areas of open ocean. Also because the channels are 'under sampled' compared to the broader areas of open ocean, their variance is not likely to be captured by the dominant EOFs.

2.3.3. Sea ice-climate relationships

EOF1

Heterogeneous correlation maps between the expansion coefficient series of EOF1 and climatological field anomalies (SLP, SST, SAT, winds) are presented in Figure 2.9. On these maps, large positive (negative) correlation indices denote strong positive (negative) correlations between EOF1 and normalized anomalies of the climatological fields (e.g., SLP). The correlation pattern for SLP anomalies (Figure 2.9A) shows a strong opposition between the Greenland Sea and a latitudinal band stretching along the 40°N parallel from Newfoundland to Western Europe. Highest correlation values occur over Newfoundland (0.32) and the Denmark Strait (-0.39), which is the normal position of the Icelandic Low. This dipole pattern of SLP anomalies resembles the positive phase of the Arctic Oscillation (AO, Thompson and Wallace, 1998), and even more closely the North Atlantic Oscillation (NAO, Hurrell, 1995). This was confirmed by correlating the winter (DJF) portions of the EOF1 and NAO index series, which gave r = 0.54 at lag 0. A weaker but significant negative correlation was also found between EOF1 and the El Niño Southern Oscillation (ENSO) monthly SLP index at lag +3 months (i.e., ENSO leading by three months). These results are consistent with observations by Wang et al (1994) and Mysak et al (1996), who found positive sea ice anomalies in HB and the

Labrador Sea when strong episodes of ENSO occurred in the previous summer and during positive phases of the NAO during winter of the same year.

Changes in the strength and distribution of SLP anomalies may affect sea ice through dynamic (wind) and thermodynamic (air temperature) forcing. The correlation map of EOF1 with wind anomalies (Figure 2.9B) shows that an anomalous cyclonic circulation over Greenland combined with anticyclonic circulation over Newfoundland induces strong northwesterly winds anomalies in the outermost part of the DS/LS region (Figure 2.9B), favouring a southward advection of ice in winter and spring. The northwesterly wind anomalies also cause advection of cold Arctic air into the eastern Canadian Arctic, HB and Labrador Sea, promoting the growth and preservation of positive sea ice anomalies in these areas (Figure 2.9C). The correlation pattern for SAT (Figure 2.9C) is consistent with the spatial signature of a positive NAO, with cold and dry winters in northern Canada and Greenland (Hurrell, 1995). EOF1 also shows strong negative correlations with SST over the North Atlantic region (Figure 2.9D). Lag correlation maps between EOF1 and SST (not shown) show negative SST anomalies appearing in southwestern Greenland one year before the positive CT anomaly develops in the DS/LS and HB regions. The SST anomaly progressively expands eastward into the Norwegian Sea up to 6 months after the CT anomaly, and southward toward the Newfoundland coast where it dissipates 1 to 1.5 years after the CT anomaly. The lag correlation maps between EOF1 and SAT also show strong negative SAT anomalies developing one year before EOF1 but decaying a few months after (not shown). This is in good agreement with recent results showing that decadal cold climatic episodes and positive ice cover anomalies around Greenland and Baffin are accompanied by cold SST

anomalies lasting 1-3 years after the decay of ice cover anomalies (Deser et al., 2002; Rogers et al., 1998).

When normalizing the correlations coefficients by their estimated large-lag standard errors, SAT ($\sigma_{max} = 5.2\sigma$) appears most strongly related to EOF1, followed by SLP and winds ($\sigma_{max} \sim 4.6\sigma$) and SST ($\sigma_{max} = 3.8\sigma$). These results suggest that atmospheric temperatures contribute more to the CT anomalies expressed by EOF1 than dynamic forcing. These conclusions complement recent results by Prisenberg et al (1997) and Deser et al (2002) who found that positive anomalies develop in the DS/LS region in response to anomalous northwesterly winds within the Labrador Sea and offshore flow east of Newfoundland. A subsequent model simulation by Deser et al (2002) suggested, as reported here, a dominance of thermodynamic processes over dynamic mechanisms.

EOF2

Significant but weaker correlations occur between EOF2 and SLP anomalies, with maximum negative polarity over the Labrador Sea (r = -0.21) and maximum positive polarity (r = 0.17) over western and southern North America (Figure 2.10A). Lag correlation maps (not shown) suggest that negative SLP anomalies lead positive EOF2 anomalies by 1-2 months in the DS/LS region, while the smaller positive SLP anomaly appears farther south two months earlier. The associated wind pattern shows northerly wind anomalies over much of the eastern Canadian Arctic, and southeasterly and easterly wind anomalies over Davis Strait (Figure 2.10B). Correlation with SAT shows maximum values over the DS/LS region (r = 0.42) and minimum values (r = -0.25) over eastern Canada/USA (Figure 2.10C). Positive SAT anomalies lead the positive EOF2 anomalies by 3-4 months, gradually expanding over the DS/LS region and dissipating one month

after the CT anomaly, while negative SAT anomalies only appear at lag 0 and dissipate one month after the CT anomaly (not shown). Closer inspection of the expansion coefficient series of both EOF1 and EOF2 (Figure 2.7) reveals that although both series are statistically uncorrelated as a whole, EOF2 includes much of the annual to sub-annual variability of EOF1. Their winter structure is similar, being inversely correlated at r = -0.99. The winter portion of EOF2 is in turn also correlated with the winter NAO, but negatively (r = -0.55). So while EOF1 represents a predominately decadal signal most active during the cold season, EOF2 appears to be an annual-to-sub annual expression of this first mode, which is related to the winter NAO. It is thought that the dipole between the DS/LS region and HB, which is superimposed on EOF1, results from local ice-to-atmosphere feedbacks controlled by the coupled interannual variability of the NAO and ice cover in the DS/LS region. Reduced ice cover in the DS/LS region during a more negative NAO allows for turbulent heat transfer from the ocean to the atmosphere, causing local warming and decreased SLP (Figure 2.10A, C). The fact that the SAT anomalies associated with EOF2 appear 1-2 months before the SLP anomaly supports this idea. The local SLP anomaly induces northerly winds and advection of cold air over part of HB, promoting positive ice anomalies in that region. The reverse process occurs when ice cover increases during winter in the DS/LS region in response to a more positive NAO. This hypothesis is supported by recent results showing high upward turbulent heat flux anomalies occurring in the DS/LS region when negative CT anomalies occur in winter (Deser et al., 2002; Deser et al., 2000). When taking the standard errors of correlation into account, the onshore surface winds and positive temperature anomalies in the DS/LS are the most significant feature associated with EOF2 ($r > 4\sigma$). The SST

pattern of Figure 2.10D, which is only present at lag 0, may represent a direct effect of CT variability associated with EOF2: decreased (increased) SSTs occur in areas of increased (decreased) sea ice cover. Alternatively, the correlation may reflect the effect of the parameterization between SST and sea ice concentration in the ERSST database (Smith and Reynolds, 2004).

EOF3

SLP anomalies associated with EOF3 show a weak dipole with positive polarity over the Arctic Ocean (r = 0.20) and negative polarity over the Bering Sea (r = -0.15) (Figure 2.11A). The positive SLP anomaly developed 3-4 months earlier over the Arctic Ocean, while the negative anomaly over the Bering Sea appeared one month earlier (not shown). The surface wind pattern associated with EOF3 shows anomalous offshore winds along the Beaufort Sea coast and anomalous northerly and southerly winds over Nares Strait and Baffin Island, respectively (Figure 2.11B). Correlation with SAT shows a warming over northwestern North America and cooling over the North Pacific and northwestern USA (Figure 2.11C). The SST pattern shows warming in the Beaufort Sea (Figure 2.11D), which began 3-4 months before the CT anomaly and disappeared 2 months later (not shown). When normalizing the correlation by their standard error, SST appears as the dominant factor ($r = 6\sigma$), followed by wind and SAT ($r = 3.6\sigma$), and SLP ($r = 3.3\sigma$).

The positive CT anomaly in Baffin Bay seems to be a direct result of the anomalous anticyclonic circulation over the Arctic Ocean, which promotes advection of ice into Baffin Bay through Nares Strait (Figure 2.11B). At the same time, the anomalous southerly winds over Baffin Island may restrain the ice from moving south, thereby

maintaining the positive CT anomaly. The most prominent feature of EOF3, however, is the negative CT anomaly off the Beaufort Sea coast (see Figure 2.6C). The anticyclonic SLP anomaly over the Arctic appears to be causing most of the dynamical forcing on sea ice, by inducing offshore wind anomalies which promote export of ice from the Beaufort Sea toward the eastern Arctic (Figure 2.11B). On the other hand, the cyclonic anomaly over the Bering Sea acts as a thermodynamic forcing on sea ice by driving warm Pacific air into the Beaufort Sea and western coast of North America (Figure 2.13B, C). The position of the two centres of SLP variability is typical of late spring to early summer conditions, when the Beaufort High and the Aleutian Low begin to dissipate. Because the SST anomalies are locally restrained to the Beaufort Sea region, they are more likely to act as a positive feedback on SAT and ice cover rather than being the main driver of the CT anomalies. It is likely that preconditioning of the ice pack during spring by enhanced offshore wind and positive temperature anomalies triggered the decrease in CT, with positive SSTs developing simultaneously and further enhancing the decrease in CT through thermodynamic effects.

The SLP and SAT patterns of Figure 2.11 have similarities with the Pacific/North American teleconnection pattern (PNA, Barnston and Livezey, 1987). The PNA is one of the most prominent modes of low-frequency variability in the Northern Hemisphere. Its positive phase is associated with above-average SLP in the vicinity of Hawaii and over the intermountain region of North America, and below-average SLP over the Aleutian Islands and over the southeastern United States. Increased (decreased) SAT occurs over northwestern North America and the North Pacific, respectively. Although the PNA is a natural internal mode of climate variability, it is strongly affected by ENSO, with positive

phases of the PNA being associated with ENSO years (Stocker et al, 2001, p.453). Cross-correlation between EOF3 and the PNA, ENSO (SLP) and Nino3 (SST) indices (Figure 2.12A) revealed a statistically significant relationships with PNA at lag 0 ($r = 0.16$), with ENSO at lag +4 months ($r = 0.22$) and with the Nino3 index at lag +5 months ($r = 0.34$). The better correlation with the Nino3 and ENSO indices indicates that the link between EOF3 and the PNA is mostly due to ENSO fluctuations. The variability of EOF3 over time is dominated by a few high-amplitude events, which are often preceded by an ENSO event (Figure 2.12B). The cross-correlation function with ENSO and Nino3 suggests an oscillation with a period of ~2-4 years, consistent with the time scale of ENSO variations (2-6 years) and with the low-frequency part of EOF3.

The positive SLP anomaly over the Arctic differs from the PNA pattern and suggests an influence from the North Atlantic (Figure 2.11A). A weak but statistically significant negative correlation was found between EOF3 and the monthly NAO index at lag +1 month ($r = -0.16$). However, the largest anomalies in EOF3 occur when NAO- and ENSO events occur simultaneously (Figure 2.12B). The most striking example is the extreme year of 1998 during which the largest ENSO event over the study period occurred in combination with the second largest NAO- event. The amplitude of the CT anomaly appears to depend on the synchronicity of both indices. A weakening of the Beaufort Gyre occurs during winter/spring under a negative NAO regime, which tends to increase ice export from the Beaufort Sea (Kwok, 2000). Thus large negative CT anomalies in the Beaufort Sea result from preconditioning of the ice pack during winter-spring combined with the thermodynamic and dynamic forcing induced by ENSO events. These results complement recent findings by Maslanik et al (1999) who found similar

SLP anomaly patterns from composite charts associated with light ice years in the Beaufort Sea. They suggested that both the NAO and ENSO could have an impact on ice anomalies in the area but found no clear relationships. The present application of the EOF method allowed for the extraction of the variance in the Beaufort Sea region associated with these two modes of climate variability.

EOF4

The SLP pattern associated with EOF4 (Figure 2.13A) shows a weak positive anomaly over central Canada (r = 0.16) resulting in anomalous northwesterly winds over HB, while anomalous southerly winds occur along the eastern coast of Baffin Island in response to a weak decrease in SLP over southern Baffin Island (Figure 2.13B). Similar SAT and SST patterns are found, with increased temperature over the western coast of North America and Bering Sea and reduced temperature over the central North Pacific (Figure 2.13C, D). Decreased SAT also occurs over southern HB (Figure 2.13C). The strongest correlations between EOF4 and SST occurs within HB (r = 0.46), but since these only appear at lag 0, they most likely reflect the effect of the parameterization between SST and sea ice concentration in the ERSST database (Smith and Reynolds, 2004).

The spatial patterns of SLP, SAT and SST are strongly apparent to the East Pacific- North Pacific teleconnection index (EP-NP, Barnston and Livezey, 1987). The EP-NP index is a Spring-Summer-Fall pattern whose positive phase is associated with a southward shift and intensification of the Pacific Jet Stream from eastern Asia to the eastern North Pacific, followed downstream by enhanced anticyclonic circulation over western North America and by enhanced cyclonic circulation over the Eastern United

States. The positive phase of the EP-NP pattern is associated with above-average surface temperatures over the eastern North Pacific and below-average temperatures over the central North Pacific and eastern North America. Maximum correlation between EOF4 and the monthly EP-NP index ($r = 0.21$) occurs when the EP-NP index leads EOF4 by one month. On a seasonal basis, significant correlations were found between EOF4 and the EP-NP index during spring ($r = 0.63$) and summer ($r = 0.57$), in accordance with the seasonality of both EOF4 and the EP-NP index. When scaling all correlations by their standard errors and ignoring the correlation between EOF4 and SST in HB, SST and SAT appear to have a stronger influence on EOF4 ($r = 3\sigma$) than does SLP and winds ($r = 2.5\sigma$). EOF4 thus appears to result from springtime climate variability in the North Pacific region, which induces anomalous anticyclonic circulation over central/western North America. The resulting southward advection of cold arctic air over HB retards ice melt in the spring while the northwesterly winds tend to push the CT anomalies toward the southern portion of HB. The weaker dipole in the DS/LS region may result from the opposition between the southerly winds anomalies along the eastern coast of Baffin Island and the northwesterly wind anomalies over Labrador.

2.4. Summary and conclusions

The analysis of the new CIS digital sea ice database has allowed a thorough and detailed assessment of recent sea ice variability in the Canadian Arctic. The results of our EOF analysis applied on monthly CT anomalies have shown that the principal modes of sea ice variability in the Canadian Arctic have seasonal dependency as well as connections with preferred modes of atmospheric and SST variability. One recurrent aspect of this study is the preponderant influence of the NAO on sea ice variability during the cold season. The

dominant mode of sea ice variability in the Canadian Arctic is a north-south contraction of the ice edge in the DS/LS region (and HB to a lesser extent) during the cold season, which oscillates on a decadal time scale in response to the NAO. This mode most probably reflects the broader, hemispheric-scale seesaw in ice extent between the Greenland Sea and the DS/LS region identified in previous studies (Deser et al., 2000; Partington et al., 2003; Yi et al., 1999) and which occurs in response to decadal variations in the AO/NAO. The seesaw between HB and the DS/LS region captured by EOF2 may represent a more local mode of variability in which inter-annual changes in ice extent in the DS/LS region, possibly driven by the high frequency variations of the NAO (e.g. Marshall et al., 2001), succinctly impact on HB via ice-to-atmosphere feedbacks.

Sea ice variability during the warm season, captured by EOF3 and EOF4, showed connections with climate variability in the Pacific Ocean as well as in the Atlantic sector. The sensitivity of the Beaufort Sea to both Pacific and Atlantic climate variability means that the ice regime may be punctuated by extreme years of negative and positive ice anomaly, as was the case in 1998. The ice regime of the geographically bound HB is more sensitive to springtime climate variability and so was found to respond to the strength and position of the Pacific Jet Stream, as measured by the EP-NP index.

Of the four dominant modes of sea ice variability in the Canadian Arctic, only EOF1 displays a significant negative trend. However, the trend is not a monotonic decrease, being influenced by the low-frequency variability of EOF1. This low frequency component also dominates the total ice area variability (Figure 2.4B). The large negative trends found in the DS/LS region during winter are not statistically significant and result from this low-frequency variability, with sea ice declining since the early 1990s in

response to a decrease in the NAO index. Little or no warming trends have been reported for the eastern Canadian Arctic that could explain the decrease in CT also occurring in that area in the spring, and it is likely that much of the decline also reflects the recent decrease in the NAO index. On the other hand, the strong negative trend found in the Beaufort Sea occurs in accordance with regional and hemispheric SAT trends, which show greatest warming during spring and summer over the western Canadian Arctic over the past 25 years (Johannessen et al., 2004; Zhang et al., 2000). The Beaufort Sea, like the other peripheral seas of the Arctic (Chukchi, East Siberian, Laptev and Kara Sea) appears most sensitive to the recent climate warming, displaying a consistent decline in ice cover over the past 25 years. Conversely, the Canadian Archipelago shows the least change over the past 25 years. It is then possible that this region, with its more complex physiographic and climatic conditions, will experience a slower ice retreat than that predicted for the rest of the Arctic over the next century.

This study has shown that in the Canadian Arctic (HB, DS/LS and the Arctic Archipelago) interannual to decadal variability predominates over long-term trends. Moreover, linear trends calculated over periods of 20-30 years may be highly influenced by low frequency components of sea ice variability. Extrapolation of trends in areas where such low frequency variability prevails is thus unlikely to give reliable estimates of future ice conditions. This highlights the need for longer series of sea ice variability, in order to isolate any trends due to anthropogenic global warming from the decadal sea ice variability present in many regions. In this regard, proxy-based reconstruction of past sea ice variability may help to reach theses objectives (Kinnard et al., 2006b).

Acknowledgements

This study was funded by the Cryosphere System in Canada Project (CRYSYS) at Environment Canada, and the Canadian Foundation for Climate and Atmospheric Sciences (CFCAS). Funding to C.Kinnard by the Natural Sciences and Engineering Research Council of Canada (NSERC) is also appreciated. We thank Adrienne Tivy for her help in accessing the CIS database.

Table 2.1. Definition of acronyms used in the text

Acronym	*Description*
AO	Arctic Oscillation
CIS	Canadian Ice Service
CT	Total ice concentration
DS/LS	Davis Strait / Labrador Sea
ENSO	El Niño Southern Oscillation
EOF	Empirical orthogonal function
EP-NP	East Pacific-North Pacific index
HB	Hudson Bay
NAO	North Atlantic Oscillation
NOW	North Open Water Polynya
NTA	Normalized total ice area
PNA	Pacific/North American teleconnection pattern
QEI	Queen Elizabeth Islands
SAT	Surface air temperature
SLP	Sea level pressure
SST	Sea surface temperature

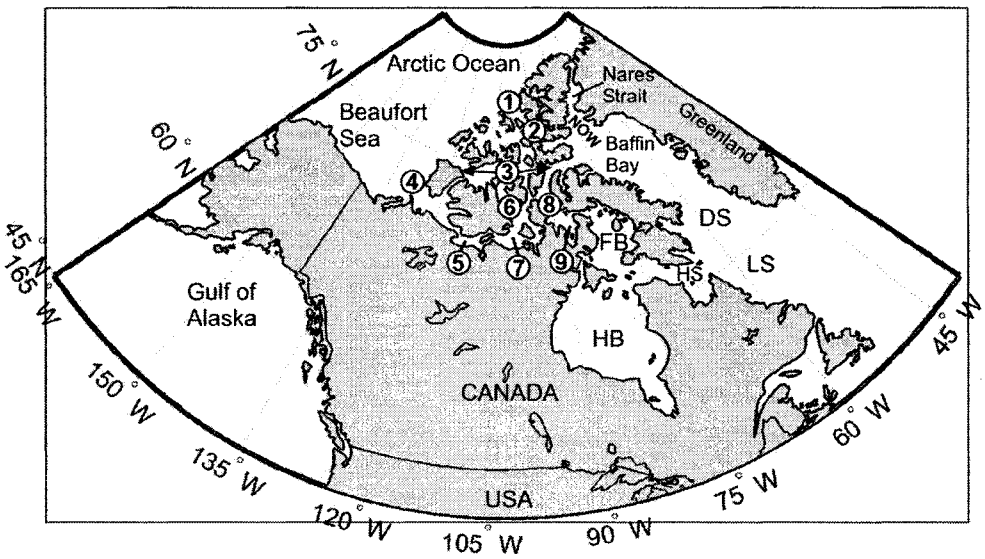

Figure 2.1. Map of the Canadian Arctic showing localities discussed in the text. HB = Hudson Bay, DS = Davis Strait. LS = Labrador Sea, NOW = North Open Water Polynya, FB= Fox Basin, HS = Hudson Strait, 1 = Sverdrup and Peary Channels, 2 = Norwegian Bay, 3 = Parry Channel, 4= Cap Bathurst Polynya, 5 = Coronation Gulf, 6 = M'Clintock Channel, 7 = Queen Maud Gulf, 8 = Gulf of Boothia; 9 = Committee Bay.

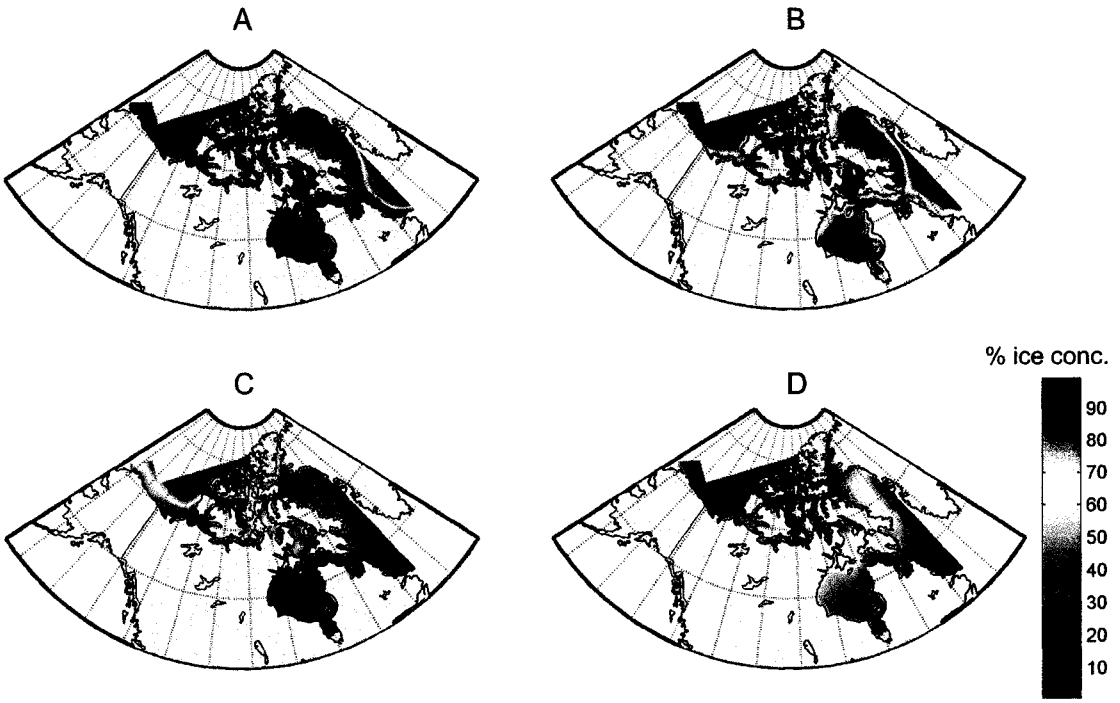

Figure 2.2. Maps of seasonal CT averages for the period 1980-2004. (A) Winter; (B) Spring; (C) Summer; (D) Fall.

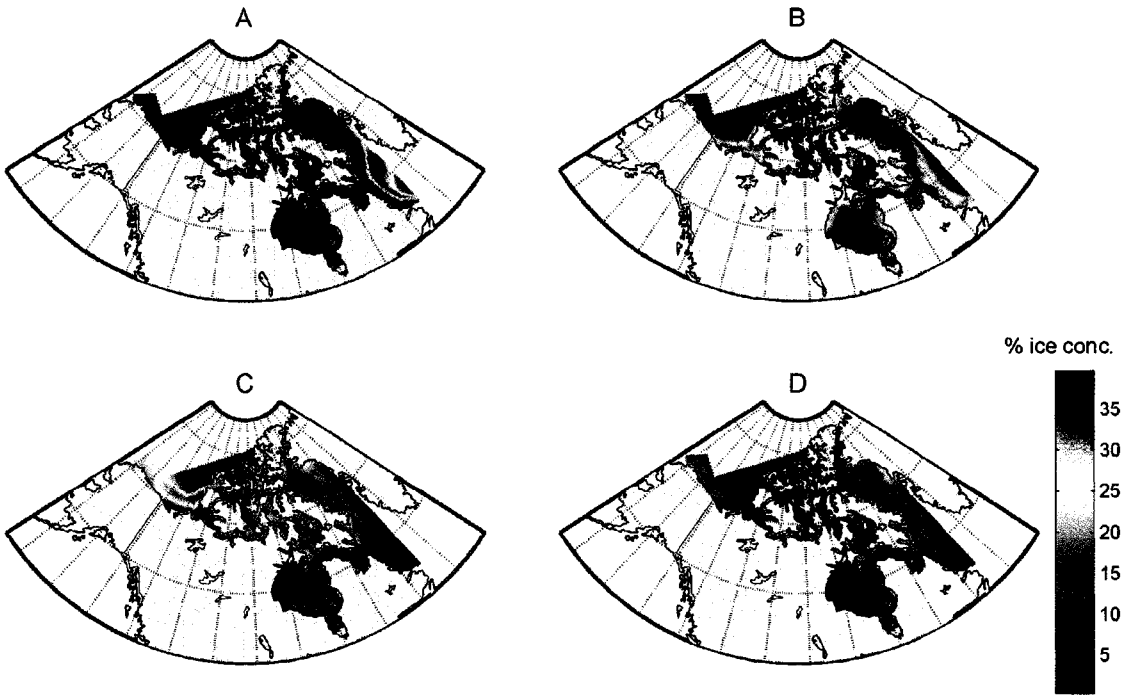

Figure 2.3. Maps of seasonal CT standard deviation for the period 1980-2004. (A) Winter; (B) Spring; (C) Summer; (D) Fall.

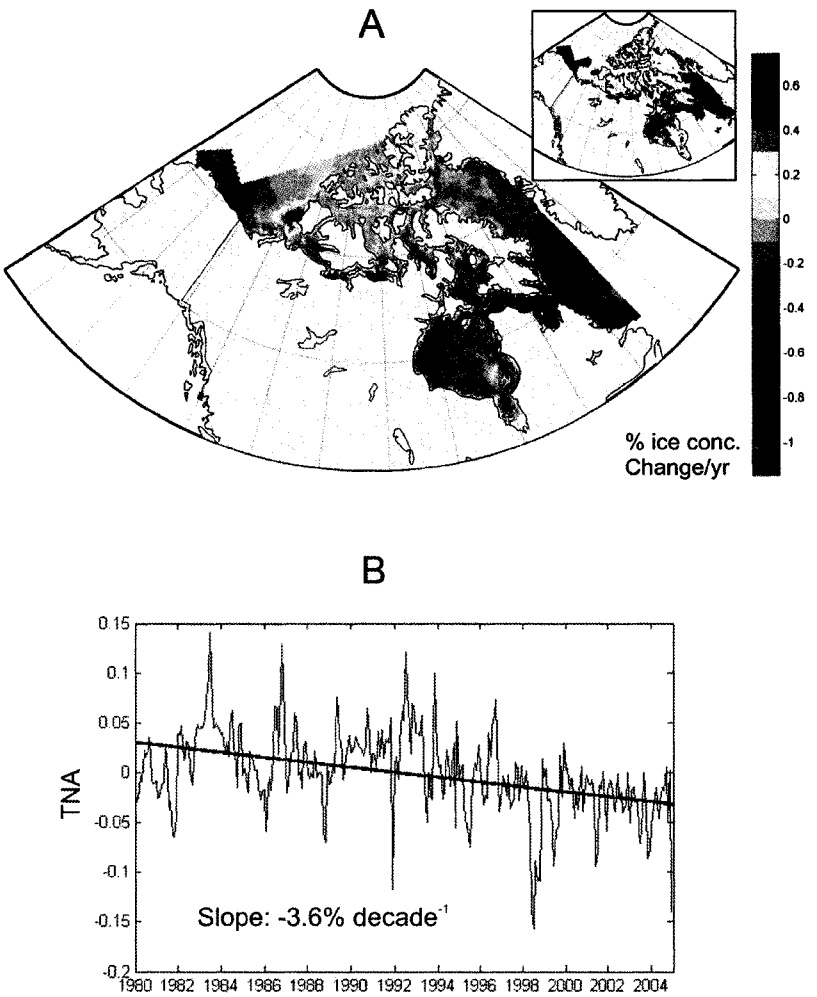

Figure 2.4. (A) Map of linear trends in CT monthly anomalies for the period 1980-2004. Inset shows areas with statistically significant trends ($p < 0.05$); (B) Normalized total ice area (NTA) and corresponding least square linear trend for the whole Canadian Arctic over the period 1980-2004. NTA is calculated by dividing the total ice area by the area covered by all available gridpoints. This minimizes the influence of any missing gridpoint on the calculated ice area.

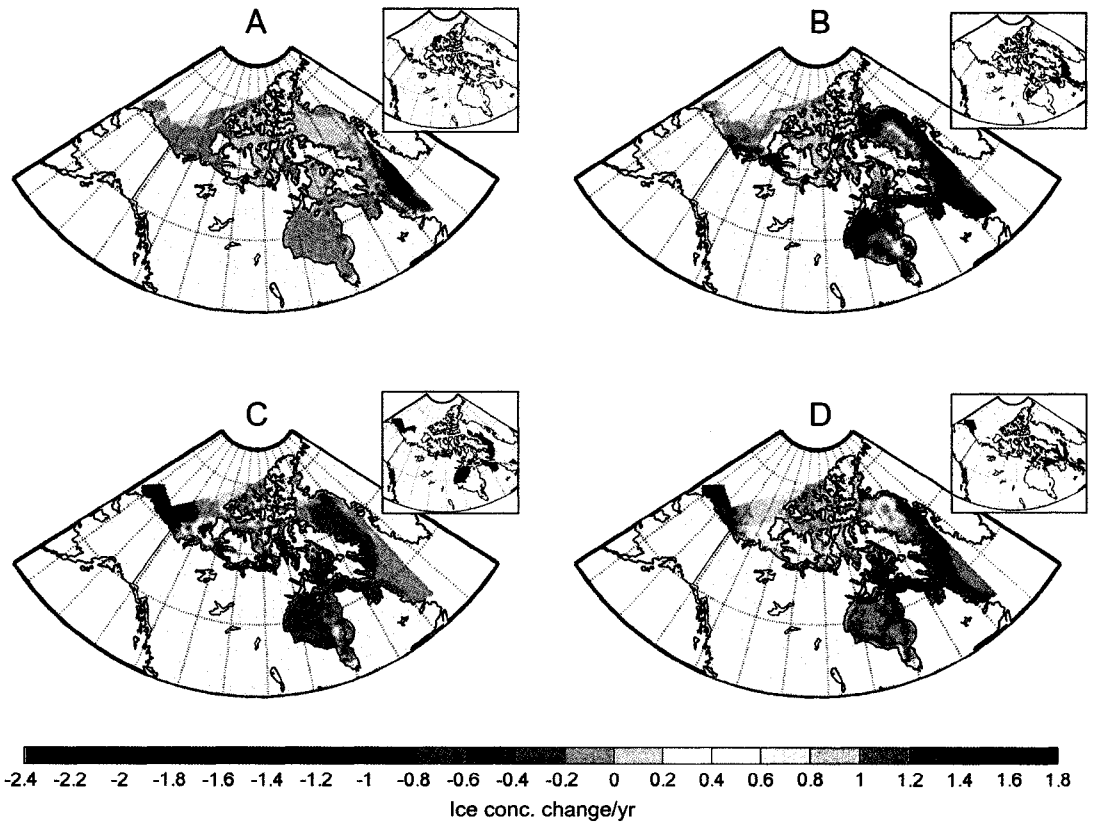

Figure 2.5. Maps of seasonal linear trends in CT. (A) Winter; (B) Spring; (C) Summer; (D) Fall. Insets show areas of statistical significance ($p < 0.05$).

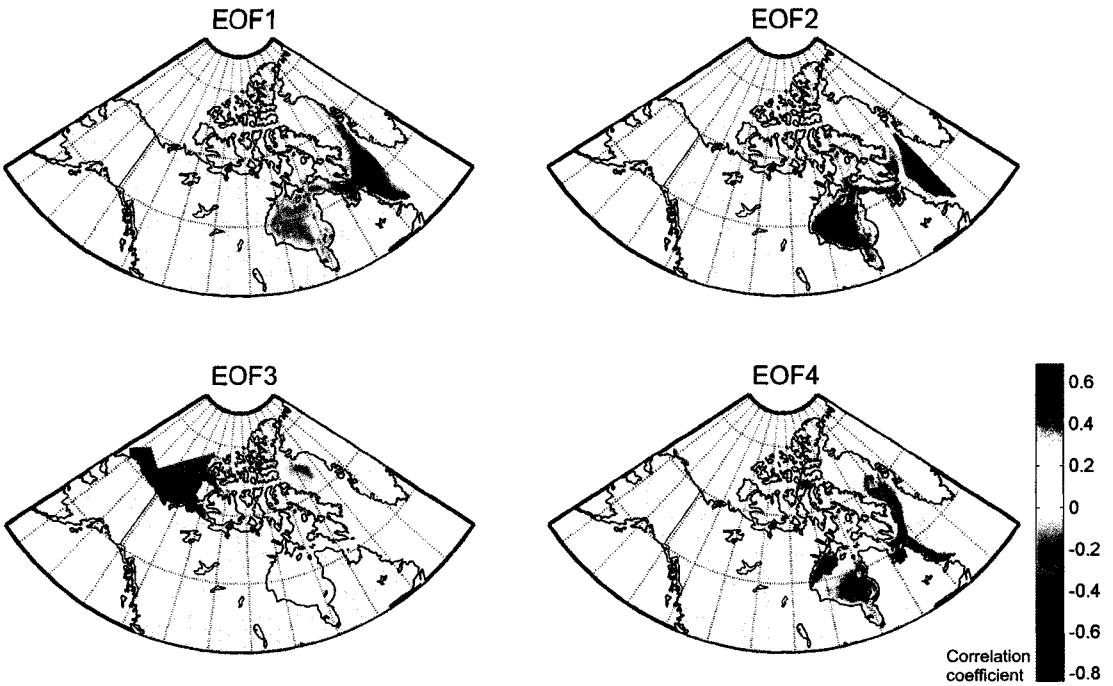

Figure 2.6. Homogeneous correlation maps for the first four EOF modes. Only statistically significant correlations ($p < 0.05$) are shown.

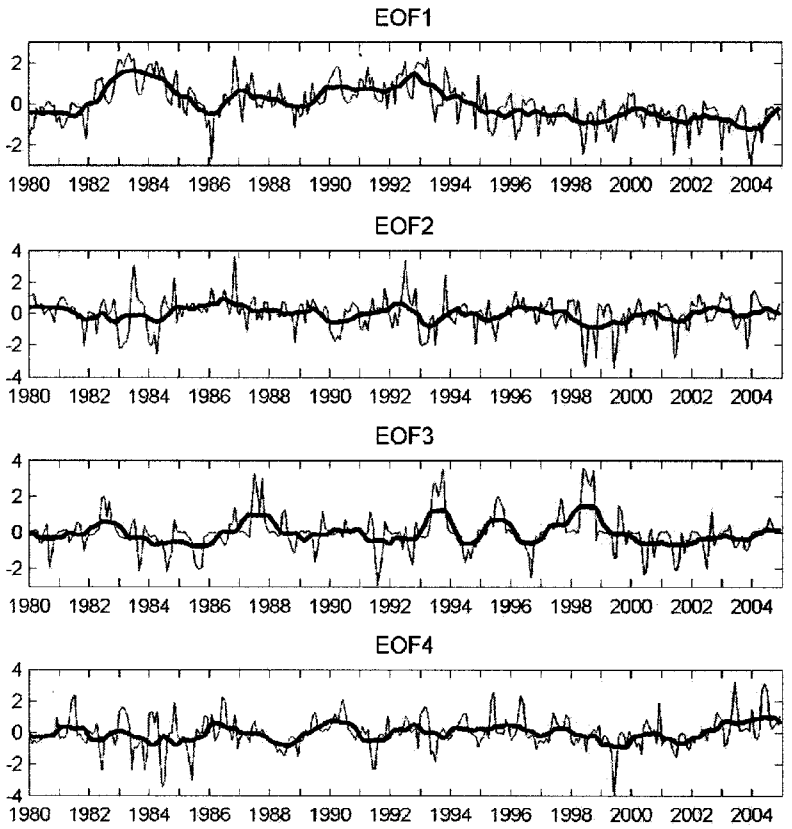

Figure 2.7. Standardized expansion coefficient series for the first four EOF modes. The thick lines represent a 13-point (0.5,1…1,0.5) running mean to highlight inter-annual variability.

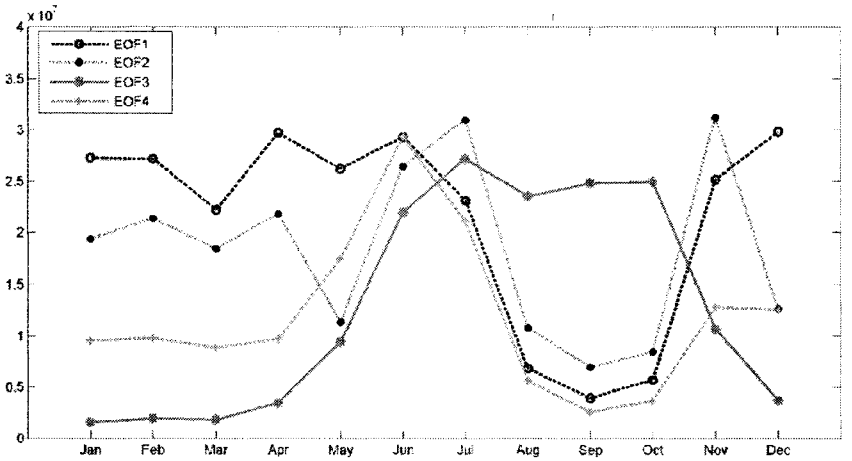

Figure 2.8. Monthly standard deviation for the first four EOF modes.

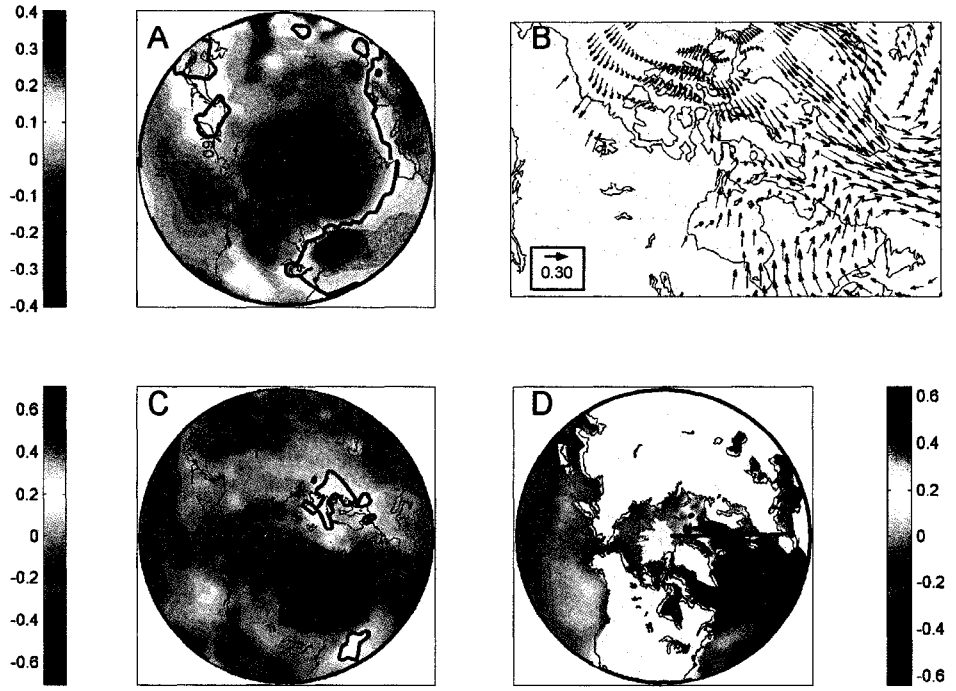

Figure 2.9. Heterogeneous correlation maps (lag 0) between EOF1 and monthly anomalies of (A) SLP; (B) u- and v-wind components; (C) SAT; (D) SST. Color bars and arrow length represent the strength of the correlation coefficient. Black contours delineate areas of statistical significance ($p < 0.05$).

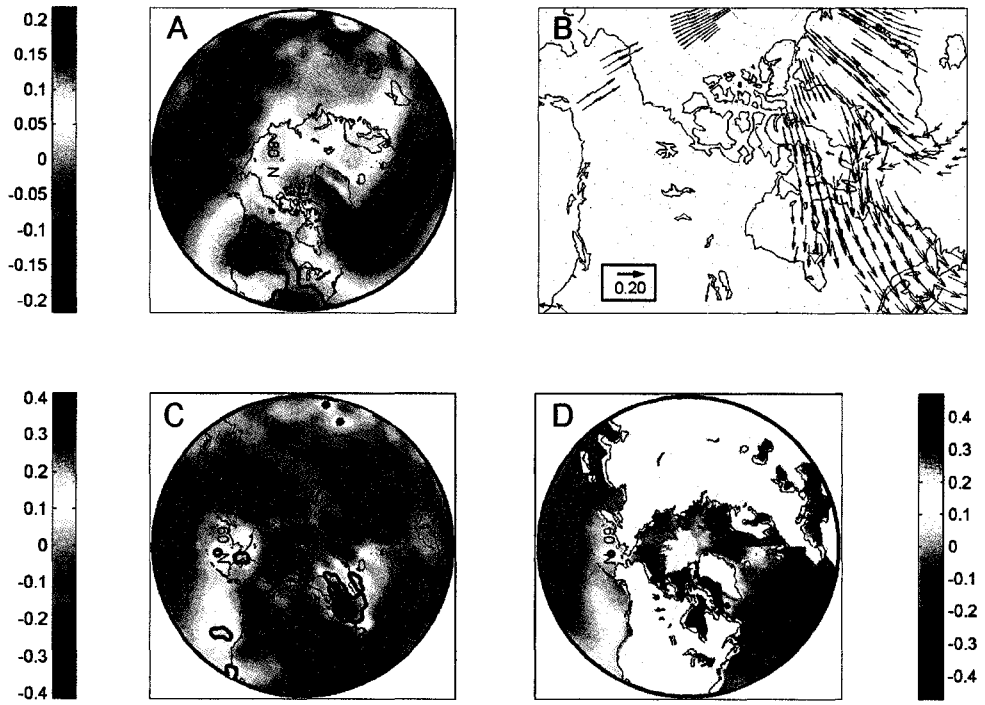

Figure 2.10. Same as Figure 2.9 but for EOF2.

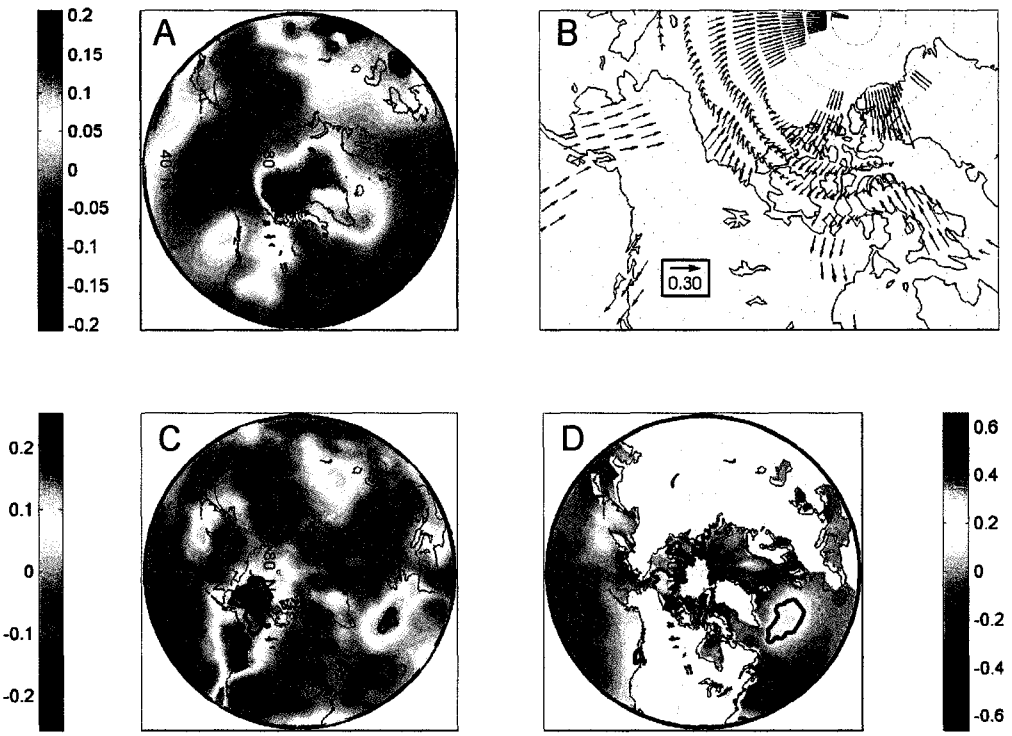

Figure 2.11. Same as Figure 2.9 but for EOF3.

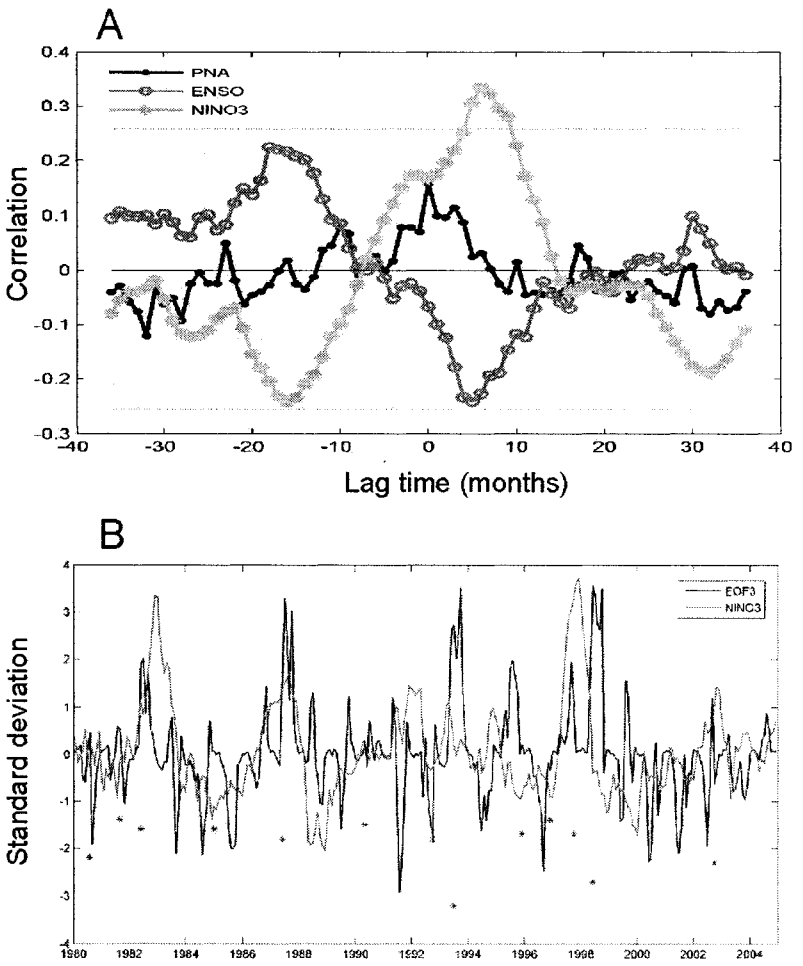

Figure 2.12. (A) Cross-correlation plot between EOF3 expansion coefficients and monthly indices values of the PNA, ENSO and Nino3 indices. Note: El Niño events are defined by a negative ENSO index and positive Nino3 index, while the PNA tends to be inversely correlated with ENSO; (B) Plot of EOF3 expansion coefficients (black line) and Nino3 index (grey line). Black dots represent NAO- events below one standard deviation of the monthly NAO index (only the maximum monthly value within the extreme year is shown).

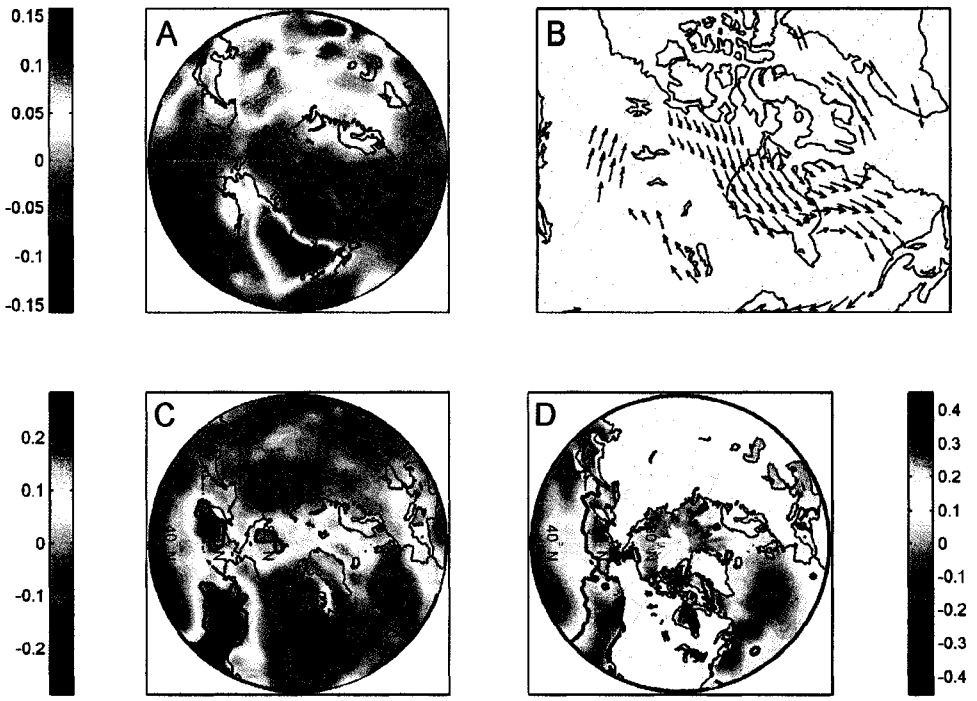

Figure 2.13. Same as Figure 2.9 but for EOF4.

CHAPTER 3. CALIBRATION OF AN ICE-CORE GLACIOCHEMICAL (SEA SALT) RECORD WITH SEA ICE VARIABILITY IN THE CANADIAN ARCTIC

Christophe Kinnard[1, 2]

Christian M. Zdanowicz[2]

David A. Fisher[2]

Cameron P. Wake[3]

(1) Department of Geography, University of Ottawa, Canada.

(2) National Glaciology Program, Geological Survey of Canada, Ottawa, Canada.

(3) Climate Change Research Center, University of New Hampshire, Durham (NH), USA.

Corresponding author: C. Kinnard

Department of Geography, University of Ottawa, 60 University St, Simard Hall, Ottawa (Ontario), Canada K1N 6N5

Tel.:+1 613 947-5169; fax: + 1 613 562-5145 email: ckinn045@uottawa.ca

Published in: ANNALS OF GLACIOLOGY, VOL. 44, 383-390, 2006.

3.1. INTRODUCTION

The past three decades have seen a drastic reduction in Arctic sea ice extent and thickness (Vinnikov et al., 1999). As a consequence there is a pressing interest to: (1) anticipate future ice conditions and their impact on ecosystems and human activities; (2) better understand and predict the effect of a declining sea ice cover on the climate system, as reduced sea ice is expected to reduce Earth's surface albedo. The current decline in ice cover appears to have begun in the early 1960s, in phase with a general increase in air temperature over the Northern Hemisphere. However trends vary spatially as the sea ice response to climate forcing differs between regions. This variability arises from complex interactions between air and sea surface temperatures, winds and ocean currents, and makes it difficult to separate trends due to the recent anthropogenic climate warming from the background, 'natural' variability.

Changes in sea ice cover have been inferred from satellite measurements (e.g. Parkinson et al., 1999) or operational charts (Kinnard et al., 2006a) spanning the last ~30 years. Historical observations, of lesser consistency, have been used to extend the record back 100 years (Walsh and Chapman, 2001), while local indices of sea ice extent have been developed for periods up to 400 years (Kelly et al., 1987). The relatively short instrumental and historical record makes the interpretation of current trends difficult, as our understanding of the natural modes of sea ice variability is limited. Longer proxy record of sea ice cover are therefore needed to help put modern observations in the context of longer-term, natural variability, and forecast future sea ice conditions in a warming climate.

This paper presents results from an ongoing study of past Arctic sea ice variability over the last 1000 years based on ice core records from the Canadian Arctic. Arctic ice caps represent natural archives of past climates, as snow layers deposited annually reflect the state and composition of the atmosphere (see Legrand and Mayewski, 1997, for a review). On Devon ice cap (Figure 3.1), Koerner (1977) found that the percentage of annual snowmelt, as inferred by the thickness of melt-ice layers, was positively correlated with the fraction of open water through the Queen Elizabeth Islands (QEI). Although a potentially useful proxy for past sea ice conditions, the ice-core melt percentage primarily reflects summer temperature forcing, and can therefore not account for sea ice cover variability related, for example, to dynamic motion of the ice pack.

Sea salt aerosols deposited in snow represent another possible indicator of sea ice conditions. These aerosols are emitted when bubbles created by breaking waves burst at the air-sea interface (Blanchard and Woodcock, 1980). The working hypothesis is that an increase (decrease) in open water, or ice-free, area enhances (reduces) the potential emission, transport and deposition of sea salt aerosols on nearby ice caps. Here we use this hypothesis to investigate the relationships between regional sea ice concentrations and the major glaciochemical series in an ice core from the Canadian Arctic.

3.2. Study site and methods

In April-May 1998, a 302-m surface-to-bedrock ice core (D98) was retrieved from the summit region of Devon ice cap on Devon Island (75.32°N, 81.64°W, 1930 m a.s.l., Figure 3.1). The drill site is ~50 km from the coast and has a mean annual air temperature of -23°C. The core was processed and analysed at the Climate Change Research Center of the University of New Hampshire following well-established clean protocols (Murphy,

2000). The data presented here are from the top 52 m-long firn section of the D98 core. This section was sampled at 3 cm intervals, giving an average resolution of 13 samples $year^{-1}$ (see below). The samples were analysed using a Dionex™ suppressed ion chromatograph (IC) for major anions (Cl^-, NO_3^-, SO_4^{2-}) and cations (Na^+, K^+, NH_4^+, Mg^{2+}, Ca^{2+}). Stable isotope ratios for oxygen (expressed as $\delta^{18}O$ relative to SMOW) were determined at the Department of Geophysics of the University of Copenhagen.

In most summers on Devon ice cap some surface melts occurs, and this may alter seasonal signals in the $\delta^{18}O$ and glaciochemical series such that confident resolution of these signals is compromised (Koerner, 1977, 1997). Although no melt percent record is yet available for the D98 core, one was developed for another core (D99) collected a year later from a nearby site. In the D99 record the average melt percentage for the past 1000 years was 10 % but after the 1850s annual rates increased up to 50%, although the mean for 1980-1999 remained only 12%. Studies on Penny ice cap, Baffin Island, have shown that despite intense summer melt there (50% average, sometimes 100%), seasonal glaciochemical cycles are still preserved in the ice, albeit partly obscured by noise (Goto-Azuma et al., 2002; Grumet et al., 1998). We feel reasonably confident that the comparatively lower summer melt rates on Devon ice cap have not altered the D98 chemistry to the point of obliterating meaningful inter-annual variability. Identification of the bomb-produced 1963 tritium peak in the D98 core was used to calculate a mean ice accumulation rate ($\bar{\lambda}$) of 0.245 m yr^{-1} for 1963-1998. Spectral analysis applied to the glaciochemical and $\delta^{18}O$ series also reveal strong periodicities corresponding to ice layer thicknesses of 0.23-0.30 m, which supports the preservation of a seasonal or quasi-seasonal cycle in these series.

Two depth-age relationships were used for the D98 core. The first was developed for the upper 11 m of the core by counting annual peaks in major ionic species and $\delta^{18}O$ values. Annual cycles in Na^+, K^+, Mg^+, Ca^{2+} and Cl^- often show a double concentration peak. These 'doublets' have been observed in snowpit and ice core studies in the Canadian Arctic and were attributed to separate aerosol deposition episodes in late-winter/early spring and fall due to increased storm activity during these time periods (Goto-Azuma et al., 1997; Grumet et al., 1998; Koerner et al., 1999; Sharp et al., 2002). The least negative $\delta^{18}O$ values in the D98 core represent summer precipitation and typically correspond with minima in major ion concentrations, while peaks in these same ions occur on the rising and falling limbs of the $\delta^{18}O$ annual cycle. The year boundary in the core was therefore assigned to the $\delta^{18}O$ maxima and corresponding minima in ionic concentrations, representing the end of summer (August). This time scale covers the period 1980-1997. Despite the relative ease in identifying annual layers in the topmost part of the core, the process remains subjective and is prone to errors of interpretation. We estimate the maximum error for this period to be less than ± 1 yr. The $\overline{\lambda}$ estimated from annual layer counting is 0.257 ± 0.084 m yr^{-1} (1σ). This figure agrees well with that calculated from the 1963 tritium peak, but the standard deviation also points to significant interannual variability (± 33%), part of which may be due to local stratigraphic noise (Fisher et al., 1985).

The second depth-age scale used for the D98 core is based on an ice-flow model (Dansgaard and Johnsen, 1969) 'tuned' using volcanic reference horizons identified from major sulphate peaks in the ice core. Two volcanic events, Katmai (1912 AD, at 25.5 m ice depth) and Laki (1783 AD, at 44.35 m ice depth), provided control points for dating

the topmost 52 m of the core, which is interpreted as representing the accumulation period 1852-1997. The accuracy of this theoretical time scale was estimated to be better than 4.5 yr (see Appendix 5).

The sea ice data used in this study come from the Canadian Ice Service (CIS) weekly operational charts, available year-round since 1980. Each chart supplies total sea ice concentration (CT) in tenths per grid cell on a 0.25° x 0.25° regular grid. The CIS dataset was used because of its high spatial resolution and because it offers a better coverage of transitional periods (ice break-up and ice melt) than ice concentrations derived from passive microwave measurements. The CT data were averaged into annual values, giving 18-year long gridded series of mean annual CT. Full descriptions of the data preparation and homogenization steps are given in Kinnard et al (2006a).

Heterogeneous correlation maps between the D98 glaciochemical time series and the CT series were calculated in order to identify potential relationships between these variables. For the D98 core, annually-averaged ionic concentrations were used because snowfall and aerosol deposition are not evenly distributed through the year, and therefore these series can not be sub-annually resolved with absolute confidence. Significance levels for all correlations were computed by Monte-Carlo simulation. Each time series was randomly re-ordered 200 times and the correlation coefficients (r) re-computed. The 95% significance threshold was determined from the distributions of r, and the procedure was repeated at each grid point of the CT series to obtain a map of significance levels.

3.3. RESULTS

3.3.1. Glaciochemistry

The D98 time series of major ions and $\delta^{18}O$ for the calibration period 1980-1997 are presented in Figure 3.2. Ammonium (NH_4^+) has a more complex origin than other ions and is not discussed in this paper. To investigate the co-variability between various ionic species, an EOF analysis (Ribera et al., 2001) was performed on time series of the seven remaining (standardized) ionic variables for the period 1852-1997 (N = 1546 samples). The estimated standard errors (North et al., 1982) suggest that the first two EOF modes are distinct, the next two may be mixed, and numbers 5 to 7 are distinct from each other but together only account for 8% of the total variance. The two dominant modes, EOF1 and EOF2, account for 55.1% and 21.5% of the total variance, respectively. EOF1 has positive loadings on Mg^{2+} (80.4%), Cl^- (72.7%), Na^+ (71.3%), K^+ (64.7%), and to a lesser extent Ca^{2+} (51.9%) and SO_4^{2-} (37.1%). EOF2 has positive loadings on NO_3^- (73%), SO_4^{2-} (28.7%) and lesser negative loadings on Na^{2+} (19%) (Table 3.1). In coastal environments Na^+, Mg^{2+} and Cl^- deposited in snow are almost entirely derived from sea spray while K^+ and Ca^{2+} may have both a sea salt and crustal (soil dust) origin (Keene et al, 1986). Sulphate (SO_4^{2-}) has multiple sources that include sea spray, marine biogenic emissions, volcanism and, over the last century, industrial pollution (Keene et al., 1986; Legrand and Mayewski, 1997). Here the dominant mode of glaciochemical variability (EOF1) appears to capture primarily a sea salt signal. In contrast, EOF2 is interpreted as representing an Arctic Haze signal, with SO_4^{2-} and NO_3^- concentrations rising since the 1950s (Goto-Azuma and Koerner, 2001).

3.3.2. Correlation with sea ice concentration

Figure 3.3 shows correlation maps between annually-averaged time series of CT, Na^+ and EOF1. The correlation maps between CT, Mg^{2+} and Cl^- (not shown) are similar. Both maps show maximum negative correlations over Baffin Bay ($r_{min} \sim -0.80$) and scattered positive correlations over the Beaufort Sea area, Davis Strait/Labrador Sea area (DS/LS), and Hudson Bay (Figure 3.3). The negative correlations over Baffin Bay between CT and EOF1 are stronger ($r_{min} = -0.85$) and more spatially widespread than for individual sea salt species (e.g., Na^+). Most positive correlations in the DS/LS region are below the 95% significance threshold. These results indicate that the sea salt signal in EOF1 increases mainly when reduced sea ice concentration occur over Baffin Bay, suggesting that sea salt aerosols reaching Devon ice cap originate primarily from that area. EOF1 can then be taken as a proxy indicator of sea ice conditions in the Baffin Bay area.

The seasonality of the CT-EOF1 relationship was investigated by correlating seasonally-resolved (gridded) CT time series with the annually-averaged EOF1 series. Very few significant correlations were found in winter (JFM; Figure 3.4A). However, locally high negative correlations ($r_{min} = -0.81$) were found along the eastern coast of Devon Island, in Lancaster Sound to the south, and also in Prince Regent Inlet, the Gulf of Boothia and Committee Bay (see inset Figure 3.4A). These regions correspond to the location of sea ice leads that form recurrently during winter. The lead systems in Lancaster Sound, Prince Regent Inlet and Committee Bay typically open between November and February in response to ocean and tidal currents (Smith and Rigby, 1981), and may represent locally important sources of sea salt aerosols. Negative correlations between CT and EOF1 in winter were also found in the North Open Water polynya

(NOW, see Figure 3.1), but these are not statistically significant. Although open water conditions are common at the head of Smith Sound in winter, the main area of open water does not begin to expand southward in northern Baffin Bay until May (Smith and Rigby, 1981).

During spring (AMJ) the areas of negative correlation expand over North Baffin Bay, especially its western part (Figure 3.4B). This is consistent with ice break-up which begins there and progresses southward, and with the area of maximum inter-annual variability in spring CT for the Eastern Arctic (Kinnard et al., 2006a). Significant positive correlations are also found in the Kane Basin and Nares Strait between Greenland and Ellesemere Island, as well as in the DS/LS region. These findings suggest that reduced springtime CT in North Baffin Bay tends to occur simultaneously with increased CT in the DS/LS and Nares Strait regions. The mean annual sea level pressure (SLP) pattern for the area shows a trough extending from a quasi-stationary low south of Greenland, and into North Baffin Bay. This pattern results in predominant northerly surface winds over much of Baffin Bay, and southerly winds along the west coast of Greenland, which imparts the typical anticlockwise sea ice gyre motion observed in Baffin Bay (Barber et al, 2001). In years with stronger northerly winds, the flux of ice through Nares Strait may result in the formation of an ice bridge across Smith Sound, slowing or even blocking further ice flux into Baffin Bay (Barber et al., 2001). Stronger northerly winds over Baffin Bay also advect more ice southward into the DS/LS region, which increases open water areas in North Baffin Bay. This scenario appears to be reflected in the positive correlations found between CT and EOF1 in Nares Strait/Smith Sound and the DS/LS region, and in the negative correlations found in Baffin Bay (Figure 3.4B).

During summer (JAS) significant negative correlations (r_{min} = -0.88) are found primarily in central/east Baffin Bay (Figure 3.4C), which coincides with the area of maximum inter-annual CT variability in this season (Kinnard et al., 2006a). While Baffin Bay is typically clear of ice by late August, conditions over the summer may vary from year-to-year depending on air temperature, ocean circulation and antecedent ice conditions (Canadian Ice Service, 2002). The strongest and most spatially extensive negative correlations between CT and EOF1 occur in the fall (OND) over the whole of Baffin Bay (Figure 3.4D). During these months, ice forms in North Baffin Bay and expands southward depending on ocean currents and weather systems (Canadian Ice Service, 2002). We hypothesize that delayed freeze-up or increased southward advection of ice in Baffin Bay are causing the regional negative CT anomaly which anticorrelates with the D98 sea salt record (EOF1).

In order to obtain visual confirmation of the aforementioned correlations, key areas were chosen in the calculated correlation maps (annual and seasonal). Time series of CT for gridpoints showing maximum negative correlations with EOF1 were plotted for each map, as well as other selected CT time series representing areas of widespread negative correlations, for e.g., Baffin Bay (Figure 3.5). Standardized series were used for direct comparison between CT series EOF1. The mean and standard deviation for each extracted CT series are given in Table 3.2, along with their geographic location, and correlation coefficients (r) with EOF1. The highly negative correlations between selected polynya regions and EOF1 during winter arise because of the anomalously low CT of 1992. These conditions (like those in 1981 in the outer Frobisher Bay polynya) may have contributed to a higher-than-average sea salt flux on Devon ice cap. Remarkably, the

most negative correlations between CT and EOF1 during the other seasons also occur in areas with polynyas. These correlations are sometimes surprisingly high, especially during summer and fall (Table 3.2; Figure 3.5). Although not as high, correlations in Baffin Bay do appear in all seasons except winter.

3.4. Discussion

The negative correlation found between Baffin Bay CT and sea salt aerosols in the D98 core (represented by EOF1) is consistent with our hypothesis that reduced sea ice cover leads to greater emission of sea salt aerosols. Increased wind fetch in open water results in more surface waves, which favours sea spray production (Blanchard and Woodcock, 1980). Sea salt particles are typically contained in the coarse mode of the atmospheric aerosol, which limits their atmospheric residence time and potential transport distance (Barrie, 1985). Hence most sea salt aerosols deposited on Devon ice cap are likely to come from nearby, rather than distant, sources. The Cl^-/Na^+ ionic ratio in the uppermost 52 m of the D98 core is 1.07 ± 0.02 (N = 1546; $r^2 = 0.85$). This is close to the seawater ratio of 1.17 (Keene et al., 1986), which suggests that these ions were derived primarily from nearby open water areas, with little fractionation during airborne transport (Legrand and Delmas, 1988). Deviations of the Cl^-/Na^+ ratio from the seawater ratio mostly occurred at low Na^+ concentrations.

An alternative interpretation for the sea ice-sea salt relationship was proposed in Antarctica, where salty "frost flower" crystals formed over polynyas and leads can dominate the sea salt budget in marine aerosols (Rankin et al., 2002). Freezing of highly saline brine below –8°C precipitates mirabilite (sodium sulphate decahydrate), which is strongly depleted in sulphates. A deficit of non-sea salt sulphate ($nssSO_4^{2-}$; sulphate in

excess of the seawater ratio) in snow or ice is then taken as diagnostic of the presence of an important sea ice (frost flower) source for sea salt aerosols. Such a deficit was observed in ice cores from non-coastal Antarctic sites, which led Wolff et al (2003) to propose that sea salt variability at these sites may reflect sea ice production rather than changes in open water area. In our Devon ice cap core, however, the $nssSO_4^{2-}$ content before the pre-industrial era (<1900 AD), calculated using the method of O'Brien et al (1995), is always positive and represents over 90% of the total sulphate load. Hence, we assume that the main source of sea salts is from open water rather than the sea ice surface (Aristarain and Delmas, 2002). However we acknowledge that because $nssSO_4^{2-}$ input from other sources (e.g., marine biota) can be significant, it could mask the diagnostic low SO_4^{2-}signature of aerosols derived from frost flowers. Furthermore, we would expect to find positive correlations between CT and EOF1 if sea salts were mostly produced over newly-formed ice. This is not the case. Instead, the few significant positive correlations were found in areas of predominant old sea ice cover, as discussed earlier.

Our correlation analysis of EOF1 against seasonal CT suggests that local lead and polynya systems may contribute to the annual input of sea salts to Devon ice cap, but that these source areas are spatially restricted. In terms of correlation strength, the relationship between EOF1 and CT in Baffin Bay is similar for the spring, summer and fall seasons. Although maximum open water conditions usually occur in late-August/early September, correlation maps suggest that the most extensive sea salt-producing areas exist between October and December. While the amount of open water may limit the source area for sea salt aerosols, wind patterns and storm trajectories strongly control their delivery to the ice cap. Baffin Bay is an area of intense cyclonic activity, with both cyclogenesis and

cyclolysis occurring regularly (Serreze, 1995). Cyclone intensity throughout the Arctic is greater during the cold months (October-April) than during the warm ones (May-September), with a maximum in February and a minimum in July (Zhang et al., 2004). In Baffin Bay, maximum (minimum) wind speeds occur during winter (summer), while the amount of precipitable water peaks in summer (Barber et al., 2001). Data from automated weather stations maintained on ice caps in the Eastern Canadian Arctic show that most precipitation there falls as snow in the spring and fall seasons (e.g. Sharp et al., 2002), in concurrence with the deposition of sea salt species (Goto-Azuma et al., 1997; Koerner et al., 1999; Sharp et al., 2002). The interplay between moisture availability from open water sources (greatest in summer) and wind transport efficiency (greatest in winter) results in a seasonal cycle of precipitation and sea salt flux that peaks during the transition periods of spring and fall. In particular, the fall months are when the fraction of open water is still great and cyclonic activity most intense, which effectively maximizes emission and dispersal of sea salt aerosols in this season. While the broad zone of negative correlation between annual CT and EOF1 (Figure 3.3) is due mainly to inter-annual changes in fall CT, the area of maximum negative correlation within Baffin Bay is found over its western portion (Figure 3.3), and is due mainly to spring CT variations (Figure 3.4B). Hence, EOF1 appears to reflect the overall CT variability in Baffin Bay during the 'warm' season (spring to fall) with possible year-round influence from leads and polynyas.

Time series of the first mode of glaciochemical variability in the D98 core (EOF1) for the period 1852-1998 are shown on Figure 3.6. Also shown for comparison are ice-core time series of $\delta^{18}O$ (a proxy for regional air temperature) and melt percentage

(a proxy for summer warmth) developed from the same site, and a surface air temperature (SAT) record from Upernavik, Greenland, for 1875-1999 (Polyakov et al., 2003b). Over the 146-yr period considered, EOF1 shows considerable variability at both decadal and interannual scales. It is noteworthy that the EOF1 index generally increased steadily from the early 1950s to the late 1990s, indicating an increasing flux of sea-salt aerosols to Devon ice cap during this period. If our interpretation of the sea ice-sea salt relationship is correct, this trend is consistent with the decline in sea ice extent observed in the Northern Hemisphere since the 1950s (Walsh and Chapman, 2001).

The EOF1 and $\delta^{18}O$ time series show little resemblance on an interannual time scale but appear to be inversely correlated at the decadal time scale (Figure 3.6B). The correlation is low ($r = -0.243$) but significant at the 99% level. The D98 $\delta^{18}O$ record captures some of the low-frequency trends in SAT recorded at Upernavik, Greenland (Figure 3.6D). However, the melt percent record from the D99 core better captures the step-like warming of the early 1920s (Figure 3.6C). There is also little resemblance between the D99 melt record and our sea salt proxy. A similar but more pronounced inverse relationship between $\delta^{18}O$ and sea salt concentrations has been found in Greenland ice cores, and attributed to more efficient sea salt transport during cold periods due to increased storminess (Dawson et al., 2003; Fischer et al., 1998; O'Brien et al., 1995). So while sea salt variability in Greenland ice-cores appears to result primarily from changes in meteorological factors, our analysis suggests that the Devon ice cap sea salt record is more closely linked to changes in regional sea ice cover. It is however expected that our sea ice proxy should also partly reflect the meteorological conditions

driving the sea ice anomalies. A similar interpretation was proposed for the ice-core sea salt record from Penny ice cap, Baffin Island (Grumet et al., 2001).

The lack of positive correlations between our sea salt proxy and the $\delta^{18}O$ and Upernavik SAT series suggests that sea ice cover (CT) in Baffin Bay is not controlled directly and/or uniquely by air temperature. One mechanism already discussed may produce reduced CT under colder conditions: when northerly winds force sea ice to accumulate in Nares Strait, blocking the flux of ice into Baffin Bay while allowing existing ice in the bay to drift southward (Barber et al., 2001). Kinnard et al (2006a) have shown that the dominant mode of variability in monthly CT anomalies is a north-to-south contraction of the ice edge which occurs on a decadal time scale, mainly in response to the North Atlantic Oscillation (NAO). It is hypothesized that increased CT occurs in the DS/LS region and Hudson Bay in response to northerly winds and decreased SAT over the Eastern Arctic during positive phases of the NAO. Enhanced northerly winds advect ice southward during the cold months, and when the ice bridge forms in Nares Strait, open water areas develop in Baffin Bay, resulting in a dipole pattern of sea ice cover with the DS/LS region. An EOF analysis performed on annually-averaged gridded CT series shows a comparable pattern for the dominant mode of sea ice cover variability (not shown).

Polyakov et al (2003b) have shown that SAT measured at Arctic coastal stations since 1875 display considerable interdecadal variability (50-80 yr), which they refer to as the Low-Frequency Oscillation (LFO). The LFO may be linked to slow changes in oceanic thermohaline circulation in the North Atlantic. In its positive phase, the LFO is associated with reduced SLP and SAT and increased wind vorticity over the Baffin Bay

region. The resulting wind stress field tends to increase sea ice mobility and redistribute it more vigorously via the Baffin Bay Gyre. Increased cyclonic activity in the region during the positive phase of the LFO could also increase emissions and transport of sea salt aerosols, especially in the fall when sea ice cover is near its minimum. Thus the LFO may represent one mechanism accounting for decadal co-variability between the D98 EOF1 record and Baffin Bay CT.

3.5. Conclusions

We found a statistically significant inverse relationship between annually-averaged sea salt concentrations (represented by EOF1) in the D98 ice core from Devon Island, and CT in the Baffin Bay area over the period 1980-1997. This relationship is consistent with our hypothesis that reduced sea ice cover expands the source area for sea salt aerosols, thereby allowing for greater emissions and subsequent deposition in snow on the ice cap. The mean Cl^-/Na^+ ratio in the D98 core also indicates that the bulk of sea salt aerosols originate from nearby sources. Our results are in good agreement with those of Grumet et al (2001), who found an inverse correlation ($r = -0.26$, $p < 0.05$) between time series of sea ice cover in Baffin Bay and sea-salt Na^+ in an ice core (P95) from Penny ice cap, Baffin Island, over the period 1901-1990. These authors also found that increased sea salt concentrations in the P95 core resulted from the interplay between reduced sea ice cover in Baffin Bay and increased atmospheric transport associated with a positive NAO index. Murphy (2000) followed the same approach using the D98 core, and found a better correlation with summer sea ice extent in the NOW ($r = -0.46$, $p < 0.05$) but weaker for Baffin Bay ($r = -0.34$, $p < 0.15$). Our own approach differs from these studies in that we used heterogeneous correlation maps of EOF1 and CT to identify regions of greatest sea

ice-sea salt correlations, rather than testing the strength of these correlations over pre-defined regions. Our findings further demonstrate that ice-core glaciochemical proxies can yield meaningful information on past Arctic sea ice conditions and variability at the regional scale. Our sea ice proxy suggests a dominant influence of dynamical factors on the control of sea ice variability in Baffin Bay over the past ~ 150 years.

Acknowledgements

This study was funded by the Cryosphere System in Canada Project (CRYSIS) at Environment Canada, and the Canadian Foundation for Climate and Atmospheric Sciences (CFCAS). Funding to C. Kinnard by the Natural Sciences and Engineering Research Council of Canada (NSERC) is appreciated.

Table 3.1. Results from EOF analysis of glaciochemical data

Variables	*% variance*		*Eigenvectors*	
	EOF1	EOF2	EOF1	EOF2
Na^+	71.3	19.0	33.2	-17.1
K^+	64.7	2.3	31.6	6.0
Mg^{2+}	80.4	3.5	35.3	-7.3
Ca^{2+}	51.9	7.8	28.3	11.0
Cl^-	72.7	16.6	33.5	-16.0
NO_3^-	7.4	73.0	10.7	33.6
SO_4^{2-}	37.1	28.7	23.9	21.1

Table 3.2. Areas of strong correlation (r) between EOF1 and seasonal and annual CT; min. is gridcell with most negative correlation

Period	*Area*	*Mean (% CT)*	*Std (% CT)*	*r*
Winter	*1: Gulf of Boothia*	96.9	0.7	-0.73
	2:East part of Lancaster Sound	96.9	0.5	-0.73
	3 (min): Outer Frobisher Bay polynya	99.8	0.5	-0.81
Spring	*1: Western Baffin Bay*	80.6	11.4	-0.54
	2 (min): South Somerset Island polynya	97.3	6.6	-0.71
Summer	*1: Central Baffin Bay*	23.0	17.0	-0.52
	2 (min): North of Bathurst Island	91.4	8.4	-0.88
Fall	*1: Central Baffin Bay*	69.1	13.0	-0.54
	2: East Lancaster Sound	90.4	6.6	-0.76
	3 (min): Penny Strait polynyas	98.5	1.2	-0.86
Annual	*1(min): North of Bathurst Island*	97.6	2.1	-0.88
	2: Western Baffin Bay	66.4	4.1	-0.71

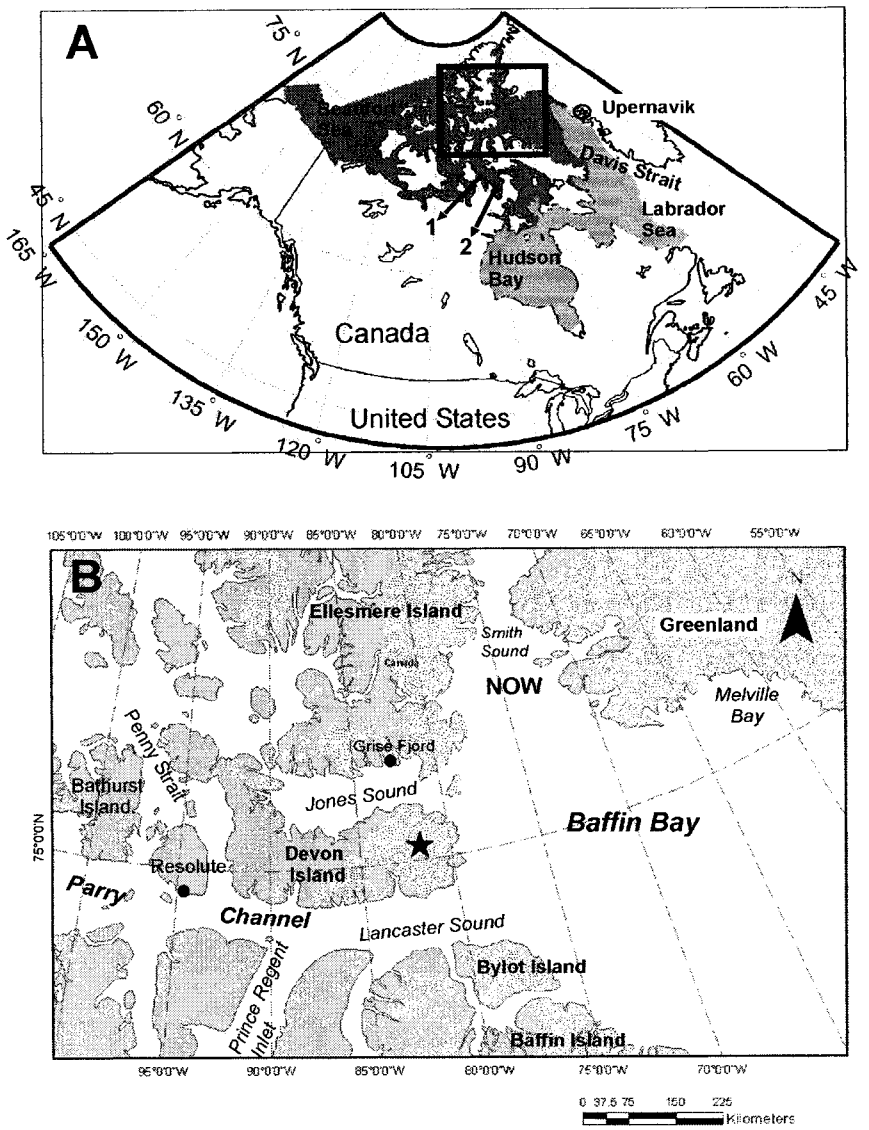

Figure 3.1. (A) Map of study area, showing locations discussed in the text; 1=Gulf of Boothia; 2=Committee Bay. (B) Close-up on the Baffin-Bay region and ice-coring site on Devon ice cap. NOW=North Open Water polynya.

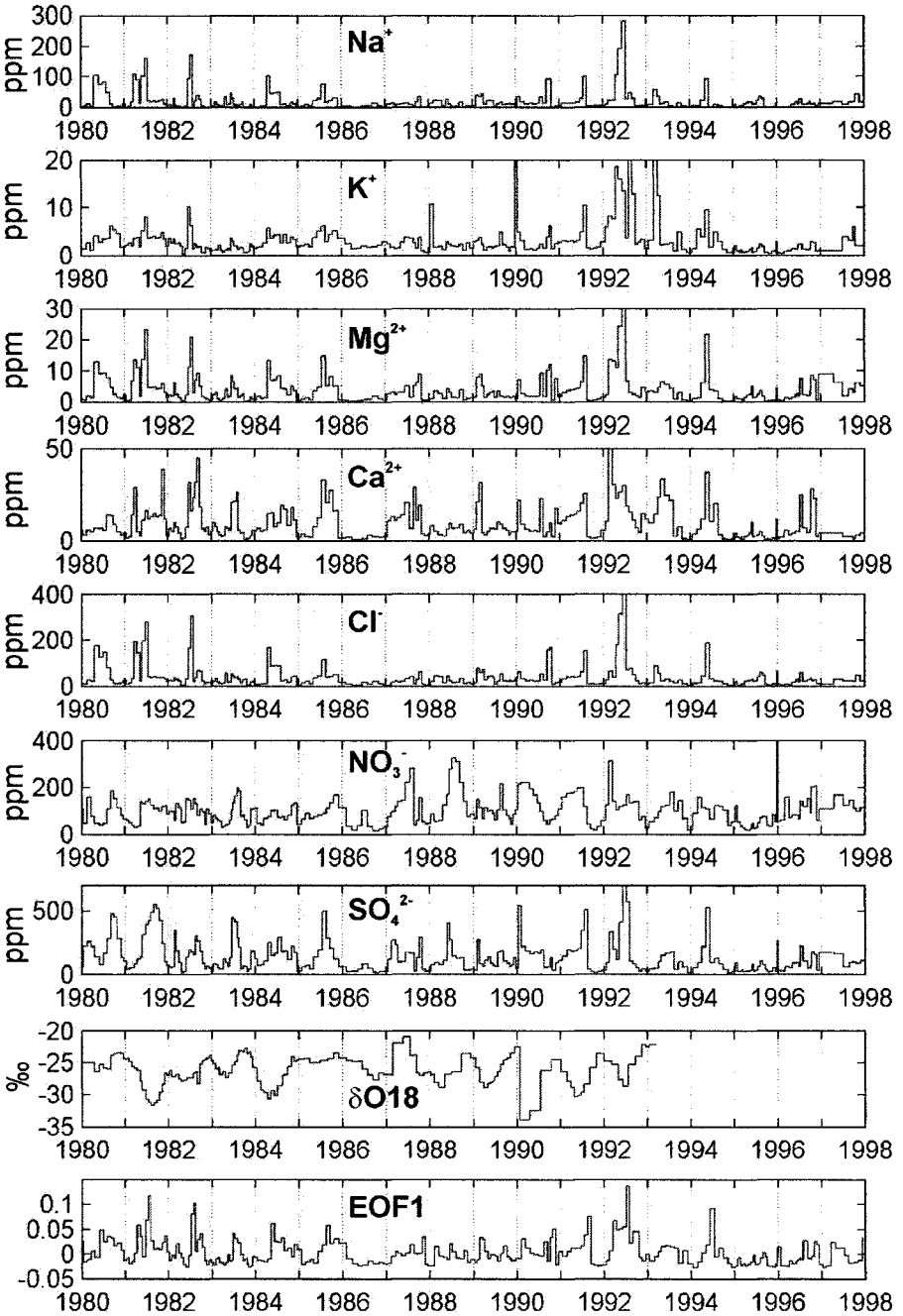

Figure 3.2. Time series of major ions, $\delta^{18}O$ and EOF1 in the D98 ice core for the period 1980-1997.

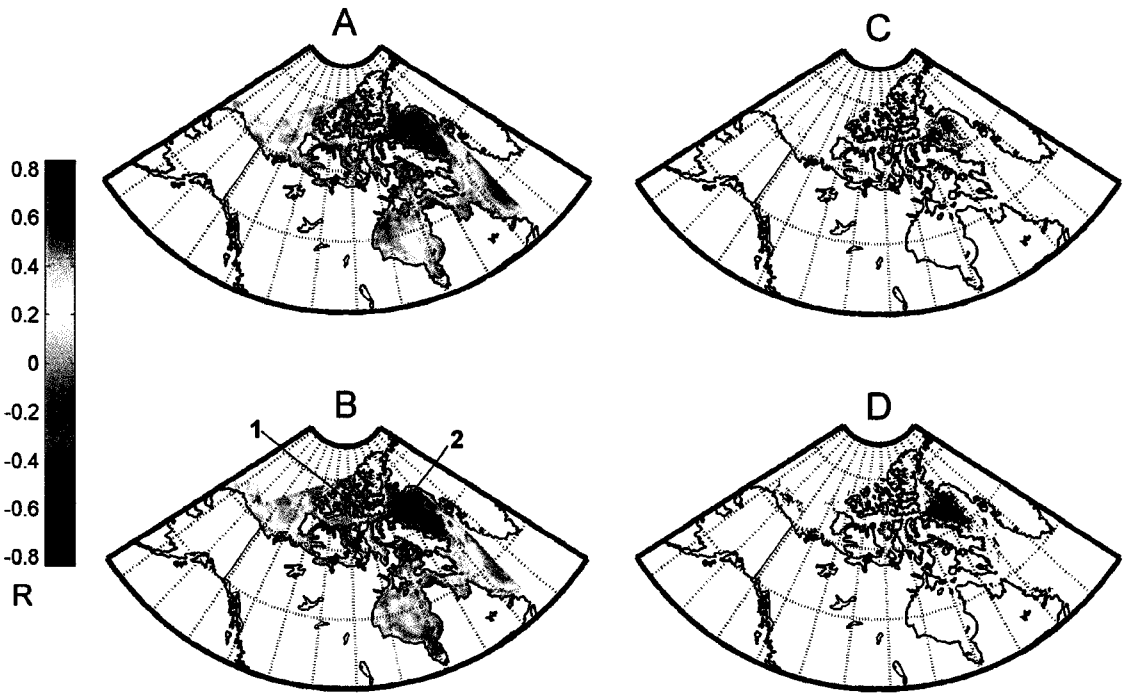

Figure 3.3. Heterogeneous correlation maps between annually averaged series of CT and (A) Na+; (B) EOF1; and corresponding areas of significant correlation ($p<0.05$) for (C) Na+ and (D) EOF1.

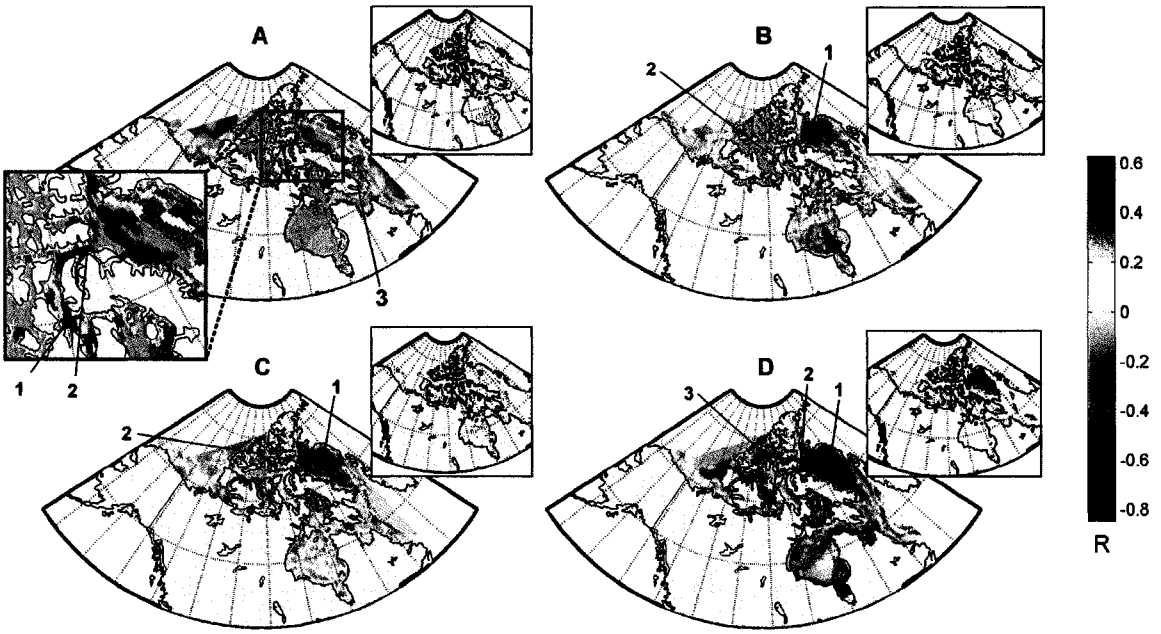

Figure 3.4. Heterogeneous correlation maps between seasonal CT and EOF1 during (A) winter; (B) spring; (C) summer; (D) fall. Insets show areas of 95% statistical significance.

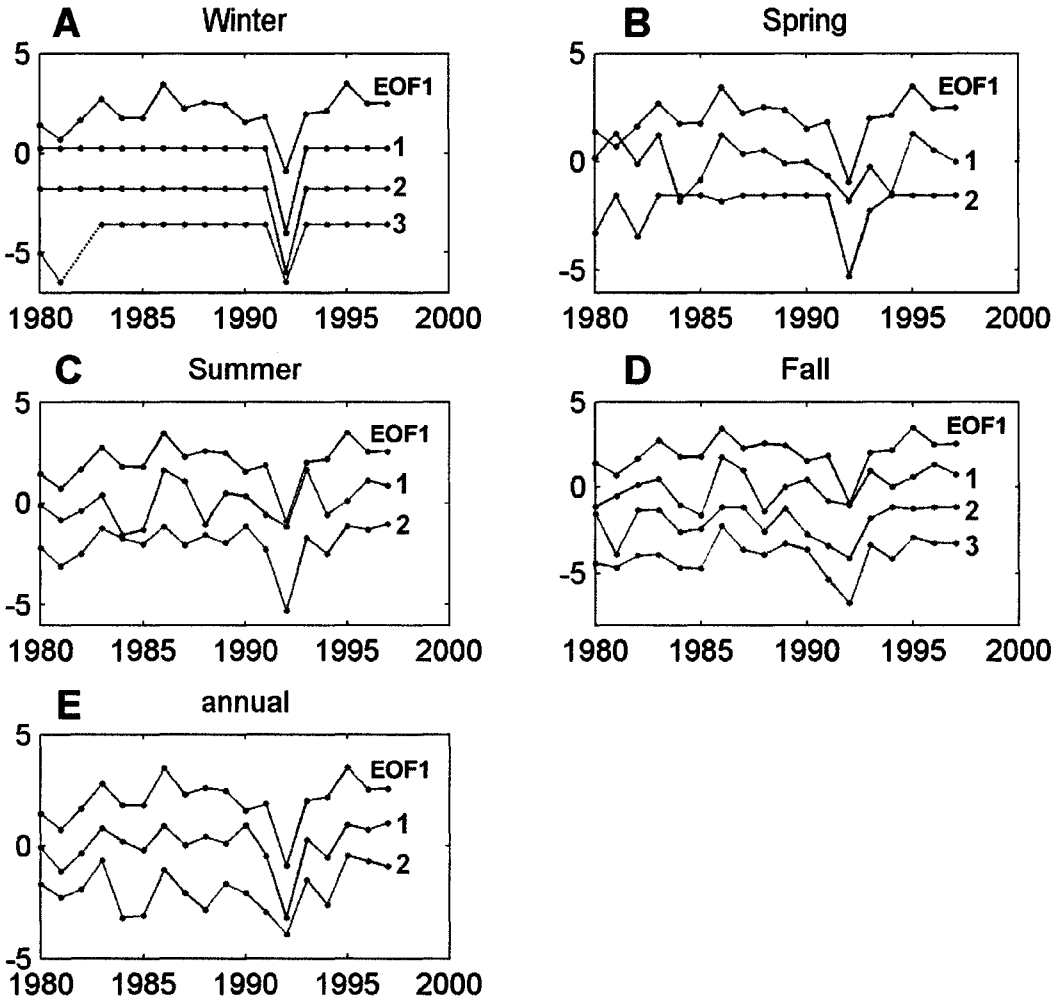

Figure 3.5. Comparison between annually-averaged time series of EOF1 and selected CT series from areas of pronounced negative correlation. Note: EOF1 is inverted for better comparison with CT series. Numbers refer to the corresponding locations on the correlation maps of Figures 3 (annual) and 4 (seasonal).

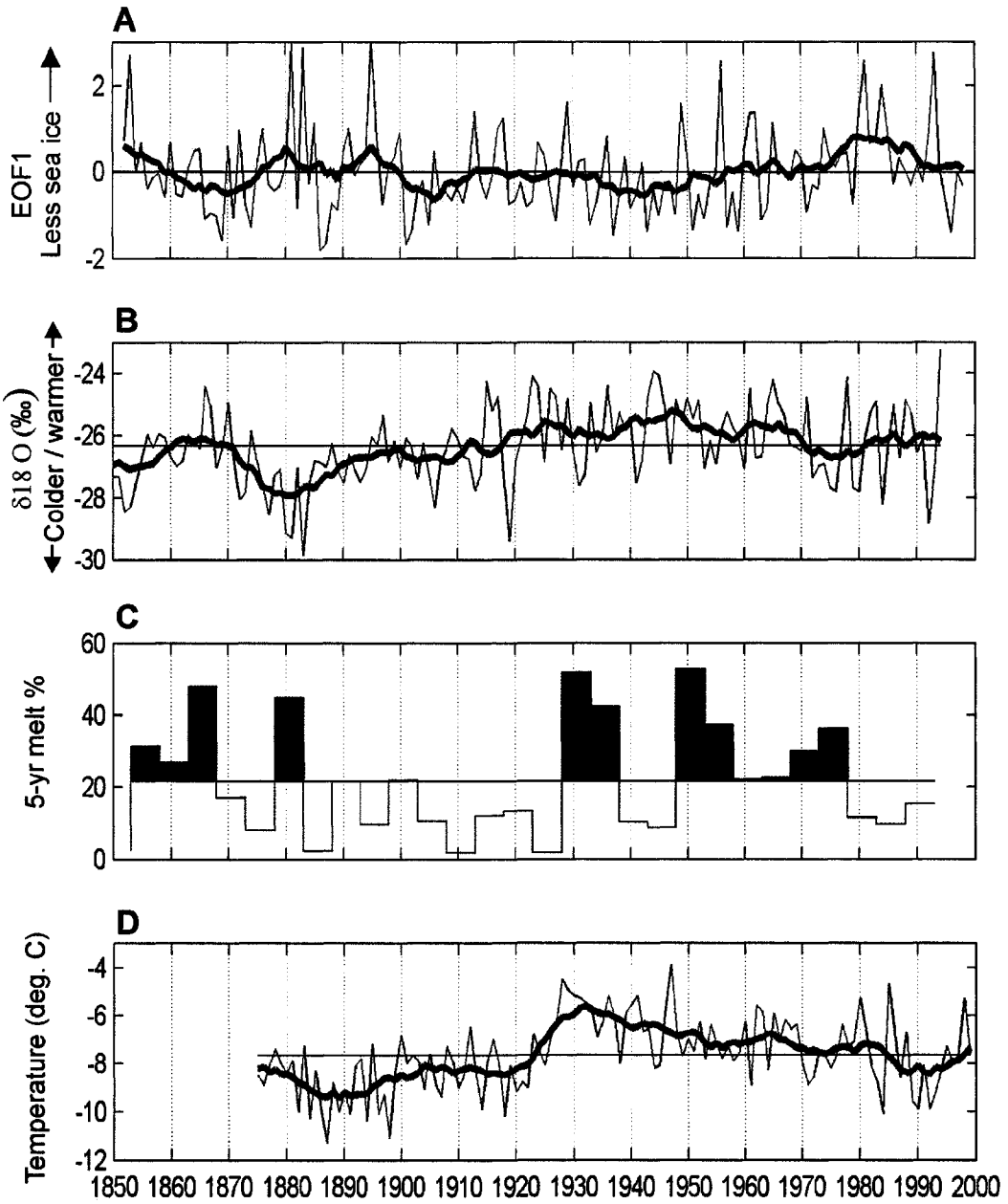

Figure 3.6. (A) Time series of EOF1 for the period 1852-1997. The bold line is an 11-year running mean to highlight decadal variability; (B) same as (A) but for δ18O values; (C) 5-year averages of melt percentages from the D99 core; (D) measured SAT at Upernavik, Greenland, for the period 1875-1999, with 11-year running mean bold line. The black horizontal lines on each graph represent the mean of the series.

CHAPTER 4. A CHANGING ARCTIC SEASONAL ICE ZONE: OBSERVATIONS FROM 1870-2003 AND POSSIBLE OCEANOGRAPHIC CONSEQUENCES

Christophe Kinnard[1, 2]

Christian M. Zdanowicz[2]

Roy. M. Koerner[2]

David A. Fisher[2]

(1) Department of Geography, University of Ottawa, Ottawa, Canada

(2) Geological Survey of Canada, Ottawa, Canada

Index terms: 0750, 1621, 1635, 4532, 4962

Published in: GEOPHYSICAL RESEARCH LETTERS, VOL. 35, L02507, doi:10.1029/2007GL032507, 2008.

Abstract

Changes in the extent of seasonal sea ice were investigated using historical and satellite observations for the period 1870-2003. The seasonal ice zone (SIZ) has been gradually expanding since 1870, with a marked acceleration over the past three decades, and has migrated north to encompass all peripheral Arctic seas. The expansion of the SIZ may be increasing the salinity of the upper Arctic Ocean, consistent with recent observations. The migration of the SIZ over continental shelves may also be enhancing the formation rate and salinity of Arctic deep waters, which are subsequently advected to the convective region of the Greenland-Iceland-Norwegian Sea, thereby influencing the formation of North Atlantic deep waters and related global thermohaline circulation.

4.1. INTRODUCTION

Various studies have reported on the declining Arctic sea ice cover using the recent microwave satellite record available since 1972 (Cavalieri et al., 2003), historical observations (Kinnard et al., 2006a) or a combination of both (Walsh and Chapman, 2001). A consistent observation from these studies is the faster rate of ice extent decline during summer than winter, with recently reported trends of -2.8% and -8.6% per decade for March and September, respectively (Serreze et al., 2007).

Sea ice plays a key role in the surface radiation balance of the Arctic Ocean. A reduced ice cover decreases the surface albedo and allows the ocean to absorb more solar radiation, promoting further ice melt and surface warming. This positive ice-albedo feedback may amplify global warming, and it has been an important incentive for studying recent sea ice changes.

One aspect which has received less attention is the potential change in the extent and configuration of the seasonal ice zone (SIZ) associated with recent ice cover decline. In this paper we use the term "seasonal ice" to designate any ice that melts after the timing of maximum winter extent. This is mainly first-year ice but can include some multiyear ice.

The freeze-thaw cycle which operates within the SIZ plays an important role in the stratification and convection of Arctic Ocean waters (Aagaard and Carmack, 1989). Moreover, exchanges of water masses between the Arctic and the North Atlantic oceans strongly affect the strength of the global thermohaline circulation (THC), which acts as an important climate regulator (Holland et al., 2001). Hence future changes in the characteristics of the SIZ have the potential to impact global climate.

Our objectives here are to quantify the changes in the extent of seasonal ice that have occurred over the period of sea ice observations 1870-2003, and to discuss the potential consequences of these changes on the Arctic Ocean circulation.

4.2. DATA AND METHODS

We use the historical grids of Northern Hemisphere (NH) sea ice cover from the University of Illinois for the period 1870-2003 (Walsh and Chapman, 2001; hereafter termed WC dataset). The grids provide mid-month values of ice concentration (percent ice cover per grid square) on a standard 1×1 degree cylindrical projection. The dataset was compiled from various sources, which vary in quality and availability over time (Walsh, 1978). Reliable ice concentrations are only available from historical sources after 1953, and from satellite imagery since 1972. Prior to 1953, only the ice edge position is reliable. For this reason we used grids of ice extent (i.e. ocean area within the ice edge) to derive the SIZ extent since 1870, but we also calculated the total seasonal ice *area* (sum of concentrations) from satellite-derived time series after 1978 (Cavalieri et al., 2003). The southern Sea of Okhotsk, the Gulf of St-Lawrence and the Baltic Sea were excluded from the analysis as data coverage in these regions is inconsistent in the WC dataset.

We created mid-month ice extent grids for the period 1870-2003 by attributing a value of one (presence of ice) to gridpoints with at least 15% ice concentration and a value of zero (no ice) elsewhere. The threshold of 15% is in accordance with previous studies of ice extent (e.g. Serreze et al., 1997). Grids of maximum annual ice extent were created by assigning, for any given cell, a value of one if ice was present at any time during the year, and a value of zero otherwise. Conversely, in minimum extent grids a value of zero was assigned to cells where open water was present at any time during the

year. Our method differs from the common practice of evaluating minimum and maximum ice extent at fixed dates (typically in September and March). Following Comiso (2002), the minimum ice extent is taken as equivalent to the perennial, predominantly multi-year ice extent. The extent of the SIZ in any given year was then calculated as the difference between the maximum and minimum ice extent grids. Calculated in this manner, the extent of the SIZ approximates the area where new (first year) ice may be produced (e.g. Zhang and Walsh, 2006). This does not take into account ice advection, but this effect may be considered negligible if we assume that during the freezing period, any area from which ice is exported refreezes. Our method may however underestimate the extent of new ice formed over coastal polynyas where continued ice export and refreezing occurs.

Time series of total minimum, maximum and seasonal ice extent were calculated by summing the respective area-weighted gridded fields. In order to examine the spatio-temporal variability of seasonal ice, we calculated anomaly fields of the probability of occurrence of seasonal ice over discrete 20-year time windows. The anomalies are then defined as departures between the 20-year and the 1870-2003 averages.

4.3. TRENDS IN SEASONAL ICE COVER

Figure 4.1 shows the spatial probability of occurrence of the ice edge over the 1870-2003 period. Regions with pronounced meridional contrast in probability (wide color spectrum), such as the Greenland Sea in winter and the Kara Sea in summer, show large temporal changes in ice extent. Time series of minimum and maximum ice extent are shown in Figure 4.2. The maximum extent was relatively stable until the early 1960s, after which a gradual decline is observed. The minimum extent is more variable on inter-

annual to decadal timescales. A declining trend, more pronounced than that of the maximum extent, is apparent after the early 1950s, with a rate increase over the last decade or so.

The total extent of the SIZ is shown in Figure 4.3. Large variability is evident on inter-annual to decadal scales. Overall, the extent of the SIZ has increased over the 1870-2003 period, with the greatest increase occurring after the 1950s, in agreement with the trend in minimum ice extent. Also noteworthy are periods of relative increases in the SIZ extent, in the early 1900s and 1930s. Figure 4.3 also shows the total northern hemisphere SIZ extent and area since 1979, calculated from the NASA team SMMR-SSM/I satellite-derived ice concentrations. Linear trends were computed by ordinary least-square regression with 95% confidence intervals adjusted for autocorrelation in the residuals (Weatherhead et al., 1998), and converted to percent change relative to the 1979-2003 average. Decadal trends for the SIZ extent computed over the 1979-2003 period were $2.14 \pm 1.93 \times 10^5$ km^2 (or $2.6 \pm 2.3\%$) using the WC dataset, and $2.22 \pm 2.15 \times 10^5$ km^2 (or $2.6 \pm 2.5\%$) using the NASA team dataset. Thus the omission of unreliable regions in the WC dataset did not significantly affect the estimated trends, at least over the recent satellite era. When ice concentrations are taken into account, the decadal trend in the SIZ area is $3.42 \pm 2.44 \times 10^5$ km^2 (or $4.1 \pm 2.9\%$), thus more pronounced than for the SIZ extent. This means that a non-negligible amount of seasonal ice forms within the ice edge. Over longer time periods, the SIZ extent exhibits decadal trends of $1.03 \pm 0.91 \times 10^5$ km^2 (or $1.2 \pm 1.1\%$) for 1953-2003, and $0.90 \pm 0.26 \times 10^5$ km^2 (or $1.1 \pm 0.3\%$) for 1870-2003. These results suggest that the increase in the total extent of the SIZ has accelerated during the past 130 years.

In a recent study by Zhang and Walsh (2006), modeled sea ice projections from the Intergovernmental Panel on Climate Change Fourth Assessment Report (IPCC AR4) were synthesized for various global warming scenarios. The prescribed scenarios, taken from the IPCC Special Report on Emission Scenarios (SRES), included: (1) unconstrained emissions leading to an increase in atmospheric CO_2 concentrations to over 800 ppm by the year 2100 (SRES-A2); (2) constrained emissions leading to an increase to 770 ppm (SRES-A1B); and (3) as in SRES-A1B but with a CO_2 increase of 550 ppm (SRES-B1). The authors found that most models predicted an increase in seasonal ice extent over the next century. Their projected trends for the three emission scenarios are shown in Figure 4.3. These were converted to percent change relative to the WC 1979-2003 average for ease of comparison. The steepest projected decadal trend, that of the SRES-A2 scenario ($1.99 \pm 1.47 \times 10^5$ km^2 or $2.4 \pm 2.0\%$), is close to that observed in our study. Hence in the last 24 years the areal extent of the SIZ has increased at a rate comparable to that forecasted under the "worst case" (SRES-A2) scenario. We may conclude that the magnitude and rate of changes in SIZ extent over recent decades are consistent with IPCC AR4.

4.4. SPATIO-TEMPORAL VARIABILITY

Changes in the extent of the SIZ have not occurred equally in space. During the late 19th and early 20th centuries, seasonal ice appeared more frequently than average in the southern portion of the Barents and Greenland-Iceland-Norwegian (GIN) Sea, and less frequently in the Eurasian coastal region, and in Baffin Bay (Figure 4.4; a-c). Beginning in the mid-century the areas of preferred seasonal ice formation shifted north (d-e), closer to the mean long-term position (h). The northward shift accelerated in the early 1970s,

when the decline in sea ice cover intensified and multi-year ice began to melt around the Arctic Ocean to be replaced by first-year ice (f). In the last 13 years there has been an Arctic-wide retreat of the summer ice cover, dominating over the winter decline, which has resulted in a net increase in the extent, and a migration of, the SIZ to the peripheral Arctic seas (g).

4.5. Implications for Arctic Ocean circulation

The change of multiyear to seasonal ice may have strong implications for the energy and freshwater budgets in the Arctic Ocean (Zhang and Walsh, 2006). The influence of freeze-thaw processes on the water properties of the Arctic Ocean is the focus of intense study by oceanographers (e.g. Aagaard and Woodgate, 2001). The freezing of seawater in winter releases salts and forms dense brines which sink and drive haline convection. If seasonal freezing and melting are balanced, this process typically results in shallow convection (~50 m), but this depth may vary spatially according to regional differences in stratification (Aagaard et al., 1985). However because wind-driven ice divergence, freezing and melting rates vary spatially, so does net sea ice production. On a large scale, the Arctic Ocean is an area of net ice production, predominantly balanced by ice export through Fram Strait and melting in the GIN Sea (Steele and Flato, 2000). Hence one might expect that the increased extent of seasonal ice, which is occurring primarily in the Arctic Ocean, should lead to a net salinification of its surface waters, winter ice growth rates and all other fluxes of salt and freshwater being equal. This occurs mainly because ice growth and brine production rates are greater under thin first year-ice (18-70 mm ice/day) than under thicker multi-year ice (~0-4 mm ice/day) (Koerner, 1973). Observations suggest that most of the upper Arctic Ocean has become saltier since the

late 1970s (Swift et al., 2005), even though freshwater fluxes to the Arctic have increased (Peterson et al., 2006). The salinity increase has affected mostly the upper 50 m of the ocean, leading Swift et al. (2005) to suggest that the decreasing perennial ice cover has proportionally increased the area available for new ice formation and brine production. Increased surface salinity was also reported in the upper Eurasian Basin during the early 1990s. This was explained by eastward diversion of Siberian inflow waters (Steele and Boyd, 1998), but also by extensive freezing of open water and thinner ice conditions (Johnson and Polyakov, 2001). In this case, open water conditions resulted from an anomalous atmospheric cyclonic circulation over the eastern Arctic, linked with a more positive North Atlantic Oscillation (NAO), which caused strong southerly winds and ice divergence along the Eurasian coast (Hu et al., 2002). These observations are consistent with our own: over the past three decades the SIZ has expanded in most peripheral Arctic seas and the Eurasian coast, as well as the Chukchi Sea and Baffin Bay, are now prime locations for the formation of seasonal ice (Figure 4.4 f-g).

The influence of ice export rates on the freshwater budget of the GIN Sea and its effect on the global THC have been well studied (Aagaard and Carmack, 1989; Holland et al., 2001; Peterson et al., 2006). However the effect of increased salinification of the Arctic Ocean on water exchanges with the GIN Sea and North Atlantic Ocean is less clear. Two main mechanisms are known to cause thermohaline convection in the Arctic Ocean: boundary current deepening and shelf convection. In the first case the two branches of the North Atlantic current entering the Arctic, the Fram Strait and Barents Sea branches, lose heat by atmospheric cooling and freshen slightly by melting sea ice, ultimately increasing in density, sinking and circulating anti-clockwise around the Arctic

Ocean sub-basins at intermediate depths (~200-1000 m) (Aagaard et al., 1985). In the shelf convection process, brine rejection during ice freezing leads to accumulation of high salinity waters on shelf bottoms, which eventually cascade down the shelf slope as gravity plumes and replenish intermediate and deep (> ~1000m) waters of the Arctic Basin. Shelf convection is most active in areas with frequent ice removal and sustained freezing (Aagaard et al., 1985). Both ventilation processes are affected by sea ice. In particular, shelf-driven ventilation will be enhanced under an accentuated sea ice seasonal cycle. The picture is less clear for boundary currents but as sea ice retreats in the Barents Sea, the density of the Barents troughflow may increase as dilution by ice melt ceases, resulting in even deeper ventilation (Aagaard and Woodgate, 2001). Intermediate waters are well connected with the ventilating regions of the GIN Sea and have relatively short replacement times (10-30 years) compared to deep waters (>100 years), making them susceptible to environmental changes at the surface (Aagaard et al., 1985; Macdonald and Bewers, 1996).

We thus anticipate that the expanding SIZ and its migration to the shelf areas will likely increase the ventilation of intermediate and deep waters of the Arctic Basin. A possible consequence of this could be an increased salinity or advection of Arctic deep/intermediate waters to the convective gyre of the GIN Sea and an increasing contribution of these waters to NADW formation (Aagaard et al., 1991). No convection to the bottom of the GIN Sea has occurred recently and the GIN Sea has gradually been filled with Arctic Ocean deep waters (Meincke et al., 1997; Rudels, 1995). Enhanced ventilation of the Arctic Basin as we evolve toward a summer ice-free Arctic Ocean may then represent a negative feedback on the possible slowing down of the global THC by

freshwater dilution in the GIN Sea. For example, increased ice export from the Arctic under a more positive NAO could result in a freshwater pulse in the GIN Sea, reduced convection and slowing down of the THC, whereas the resulting thinner ice and increased open water conditions in the Arctic Ocean would drive southward advection of deep waters to sustain NADW formation and the global THC. Critical to this discussion is the extent to which shelf-driven convection ventilates the Arctic Ocean, as this remains a debated topic and one that deserves further elucidation (Aagaard and Woodgate, 2001).

4.6. Conclusion

This study has shown that the seasonal ice zone has been gradually expanding since 1870, with a marked increase during the past three decades. This recent increase rate matches model predictions for "worst case" type greenhouse gases emission scenarios. Paleoceanographic evidence for enhanced brine expulsion rates in the western Arctic during the peak warmth of the early Holocene (8-9 ka BP) suggests enhanced seasonal ice formation at the time, and offers a possible analogue for future conditions under a warmer climate (Fisher et al., 2006). The expansion and migration of the SIZ over the Arctic continental shelves is likely to increase the thermohaline ventilation of the Arctic Basin, eventually promoting NADW formation driving the global THC.

Acknowledgements

Financial support to C. Kinnard was provided by the Natural Sciences and Engineering Research Council of Canada.

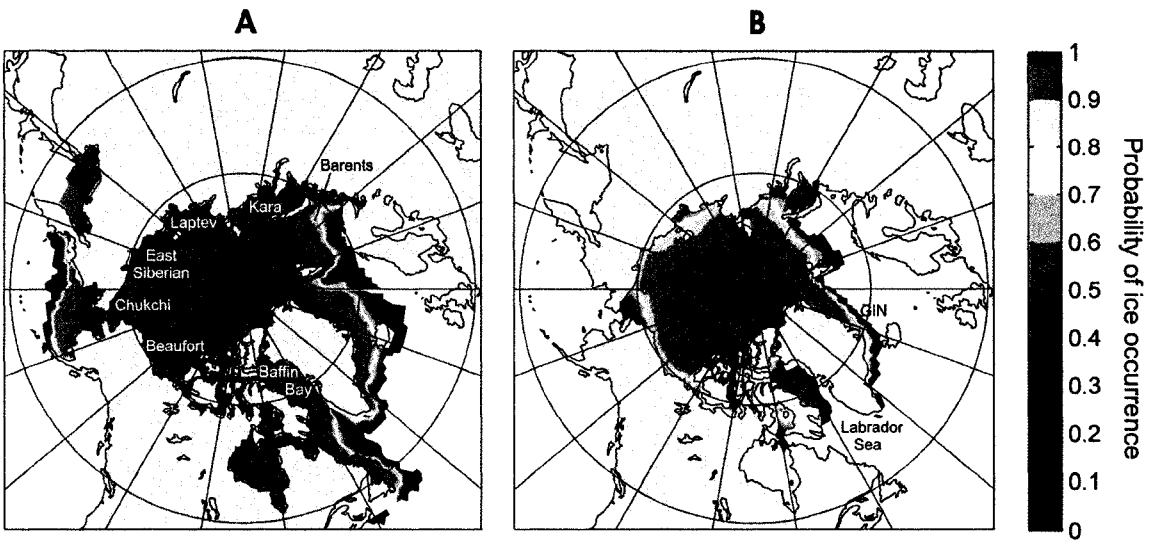

Figure 4.1. Probability of occurrence of the ice edge for (A) maximum and (B) minimum ice extent over the period 1870-2003. Grey areas designate 100% probability.

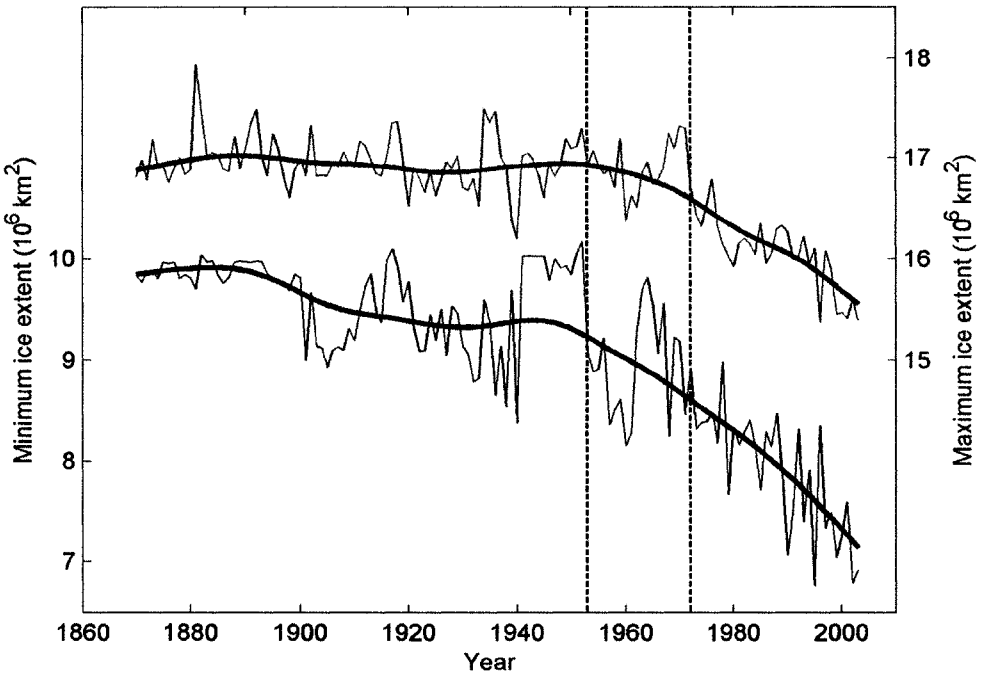

Figure 4.2. Total maximum (green) and minimum (blue) ice extent time series for the period 1870-2003. Thick lines are robust spline functions to highlight low-frequency changes. Vertical dotted lines separate the three periods for which data sources changed fundamentally: (1) 1870-1952: observations of varying accuracy / availability; (2) 1953-1971: generally accurate hemispheric observations; (3) 1972-2003: satellite period - best accuracy and coverage.

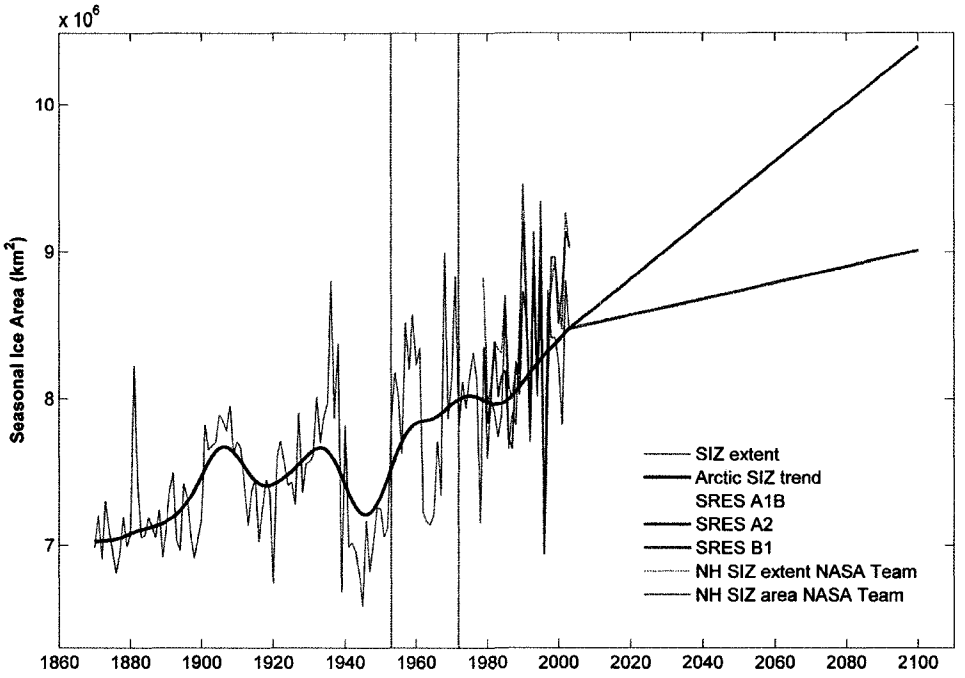

Figure 4.3. Observed and projected total SIZ extent and area. Grey = WC SIZ extent with robust spline fit to highlight trend (black); Dotted pink/blue = NASA team SIZ extent/area; Color lines = projected SIZ extent. Vertical dotted lines are as in Figure 4.2.

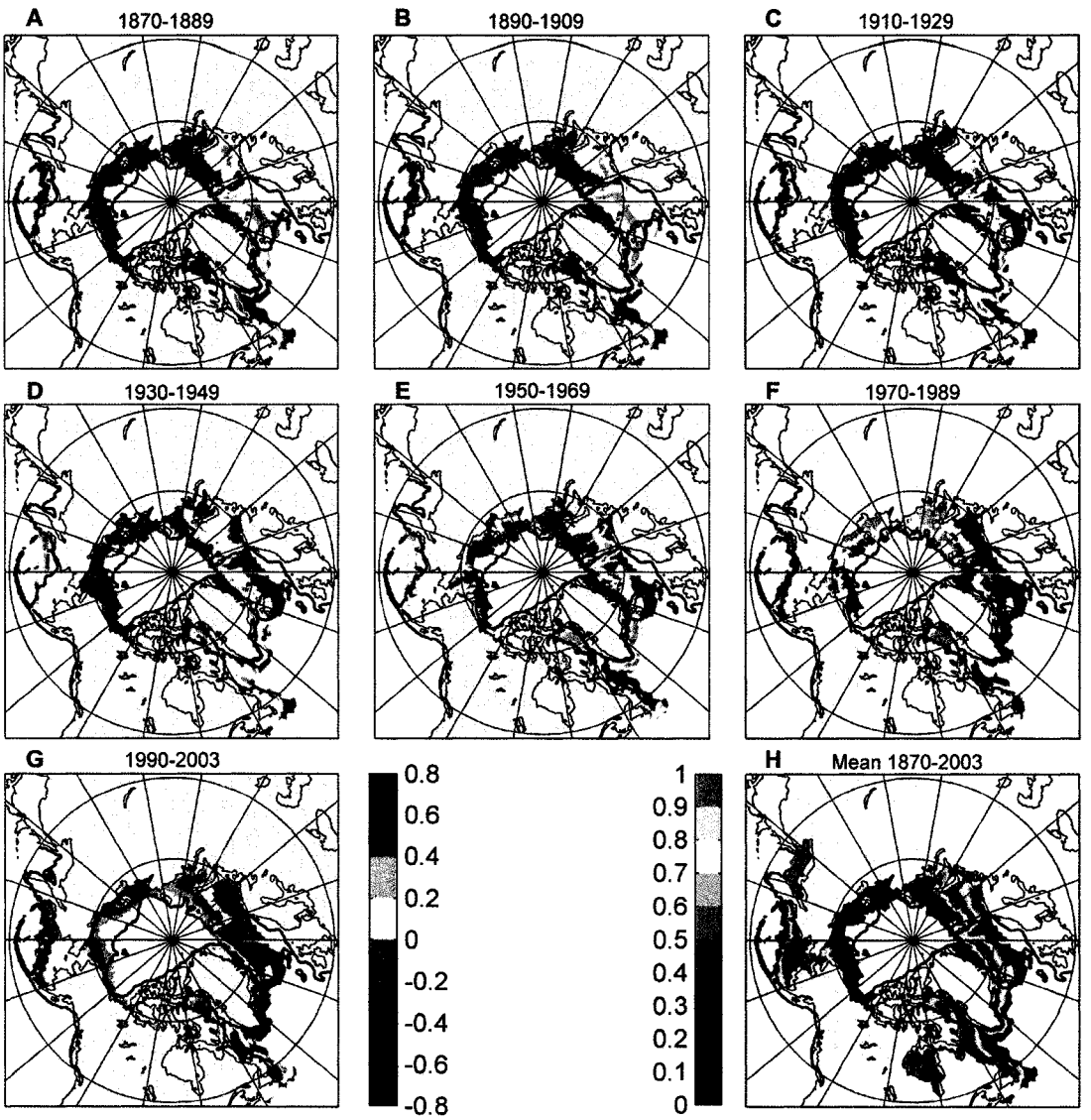

Figure 4.4. Bi-decadal anomalies in the probability of occurrence of seasonal ice. Anomalies (a-g) are relative to the 1870-2003 average probability (h). The thick black line delineates the 500 m bathymetry contour.

CHAPTER 5. STRATIGRAPHIC ANALYSIS OF AN ICE CORE FROM THE PRINCE OF WALES ICEFIELD, ELLESMERE ISLAND, ARCTIC CANADA, USING DIGITAL IMAGE ANALYSIS: HIGH-RESOLUTION DENSITY, PAST SUMMER WARMTH RECONSTRUCTION AND MELT EFFECT ON ICE CORE SOLID CONDUCTIVITY

Christophe Kinnard[1, 2]

Roy. M. Koerner[1, 4]

Christian M. Zdanowicz[1]

David A. Fisher[1]

Jiancheng Zheng[1]

Martin J. Sharp[3]

Lindsey Nicholson[3]

Bernard Lauriol[2]

(1) Geological Survey of Canada, Ottawa, Canada

(2) Department of Geography, University of Ottawa, Ottawa, Canada

(3) Department of Earth and Atmospheric Sciences, University of Alberta, Edmonton, Canada

(4) Deceased 26 May 2008.

Index terms: 3305, 3344, 0724, 0752, 0794

Published in: JOURNAL OF GEOPHYSICAL RESEARCH, VOL. 114, doi:10.1029/2008JD011083, 2009.

Abstract

High-resolution (1 mm) stratigraphic information was derived from digital image analysis of an ice core from the Prince of Wales (POW) Icefield, Central Ellesmere Island, Canada. Following careful image processing, a profile of ice core transmitted light was derived from the greyscale images and used to reconstruct high-resolution density variations for the un-fractured sections of the core. Images were further classified into infiltration and glacier ice using an automatic thresholding procedure, and converted to a high-resolution melt percentage index. The mean annual melt percentage over the last 580 years was 9%, and melting occurred in eight years out of ten. Melting obliterated most of the original depositional sequence, and seasonal density cycles were mostly unrecognizable. The ice core solid conductivity was greater and more variable in melt features than in glacier ice, due to washout of strong acids by meltwater (elution) and chemical enrichment upon refreezing. This hindered the identification of acid volcanic layers and further compromised dating by annual layer counting. Comparison of the melt record with those from other Arctic ice caps shows that the melt-temperature relationship on POW Icefield is site-specific. We speculate that this is due to the peculiar position of the icefield, which rests on the periphery of the Baffin Bay maritime climate zone, and to the proximity of the North Open Water polynya, which control snow accumulation variability on the icefield and affect the melt percentage index.

5.1. INTRODUCTION

Visual stratigraphy is one of the most basic observations made on ice cores recovered from polar ice sheets. The visible layering in polar snow may have a depositional origin, resulting from variations in the precipitation supply and fluctuations in surface meteorological conditions (Langway, 1970). The deposition of dust and pollen at the glacier surface may also form distinctive horizons in polar snow. Post-depositional processes such as the formation of depth hoar, snowmelt and subsequent percolation and refreezing of meltwater also greatly modify the snowpack structure (Koerner, 1997). The preservation at depth of the original depositional sequence will depend on the intensity of these post-depositional processes. For example, in the dry snow zone of Greenland and Antarctica, a high-density wind-packed winter layer typically overlies a lower density, coarse-grained depth hoar layer that formed during the previous summer or fall (Alley et al., 1997). This depth hoar / wind slab couplet forms a seasonal signal which can remain visible at depth, allowing for precise dating of paleoenvironmental records derived from ice cores (Alley et al., 1997; Hawley et al., 2003; Langway, 1970; Meese et al., 1997).

On glaciers where significant melting occurs during summer, the snowpack structure predominantly reflects the effect of melt, and any visible seasonal signal is likely to be partially or completely obliterated. On the other hand, the frequency and thickness of sporadic melt features observed in ice cores, such as ice layers and lenses, constitute useful proxies of past summer warmth (Herron et al., 1981; Kameda et al., 1995; Koerner, 1997; Koerner and Fisher, 1990; Tarussov, 1992).

Early studies in Greenland using ice cores photographed under transmitted light showed the potential for using the optical properties of firn and ice as a tool for

stratigraphic analysis (Langway, 1970). Digital image analysis of sedimentary sequences has often been used in paleolimnology and paleoceanography (e.g. Cooper, 1998; Nederbragt and Thurow, 2004) but its application to ice cores is relatively recent (Hawley et al., 2003; Kaczmarska et al., 2006; Sjögren et al., 2007; Svensson et al., 2005; Takata et al., 2004). In particular, digital image analysis can help to detect stratigraphic features that cannot be identified by the human eye. Optical data have been related to, and used to infer, physical properties of firn cores such as density (Hawley and Morris, 2006; Hori et al., 1999; Sjögren et al., 2007). While sophisticated techniques such as three-dimensional tomography offer promising results (e.g. Kawamura, 1990), simpler imaging systems using charge coupled device (CCD) cameras have also proven useful (Sjögren et al., 2007).

The goal of this study is to derive high-resolution stratigraphic information from a new ice core from the Prince of Wales (POW) Icefield, Arctic Canada, using digital image analysis techniques. In particular, we use image analysis to derive high-resolution ice core density and a stratigraphic summer melt index (Koerner, 1977) in an objective and automated way. This melt index is used to investigate the effect of seasonal melting on the ice core solid conductivity, and to characterize past summer warmth on the POW Icefield over the last 1000 years.

5.2. Field sampling, measurements and core dating

The POW Icefield is located in Central Ellesmere Island, Arctic Canada (Figure 5.1). The surface topography of the icefield is complex, with multiple domes separated by nunataks. During April-May 2005, a 176.5 m-long surface-to-bedrock ice core was retrieved from the summit of one of these domes, using an electro-mechanical drill. The

coring site (78°23.4' N, 80°23.7' W, alt. 1630 m) has a mean annual surface temperature of -20.9 °C based on the 10 m borehole temperature, while the temperature at the bottom of the borehole is -19.6 °C. The accumulation rate, estimated from snow pit stratigraphy and the depth of the Katmai volcanic horizon (1912 AD), is approximately 0.30 m a^{-1} (ice equivalent). The coring site was chosen because of its proximity to Baffin Bay and the North Open Water (NOW) polynya, and the ice cap is expected to contain a record of past climate and sea ice variability for the region. Detailed profiles of stable isotopes (δO_{18} and δD) and major ion concentrations are being developed and will be presented elsewhere.

Both visual and optical stratigraphic observations were conducted in the field. Each core segment recovered had a diameter of 8.3 cm and a maximum length of 100 cm. These were placed on a specially constructed light table made of a closed wooden box with two 34 W fluorescent tubes placed at the bottom (Figure 5.2). A half-cylindrical translucent Plexiglas receptacle was fitted within an opening in the table surface. Visual observations were made with the core segment placed in the receptacle and illuminated from below. For each core, the position and thickness of all visible melt features were recorded visually, and an estimate of the volumetric melt percentage was made for each feature with 10% accuracy. A black cardboard box was then fixed over the light table. Three overlapping images were taken of each core segment from fixed positions (hereafter called scenes 1, 2 and 3) using a Canon PowerShot S50 digital camera attached to a tray that slid along a gap atop the box. The resulting JPEG images are rectangular pixel arrays with 1944 rows and 2592 columns, with the row dimension aligned with the core axis. Each image has three 8-bit (256 tones) color channels (RGB for red, green and

blue) and a resolution of 0.015 cm per pixel. Images were taken in "stitch-assist" mode, which permits visual alignment between overlapping pictures. This mode used a constant focal length of 7.1 mm and aperture value of f2.8, but the exposure time varied automatically between pictures to ensure the best image exposure.

The bulk density of each core segment was measured by the gravimetric method using a top-loading scale with a precision of 0.01 kg. Solid electrical conductivity measurements of the core (ECM, Hammer, 1980) were done by measuring a 1500 VDC current flowing between two brass electrodes that were moved along the core using a custom-built hand-operated device mounted on rails (Zheng et al., 1998).

The present core timescale is derived from a flow model (Dansgaard and Johnsen, 1969) "tuned" using volcanic acid layers detected by the ECM signal (e.g. Fisher and Koerner, 1994). Three eruptions (Katmai, 1912 AD, 1259 AD (possibly El Chichón), and Eldgjá, 934 AD, see Zielinski et al, 1994) were identified, as well as the Pleistocene–Holocene transition where there is a distinctive shutdown of the ECM signal, which was assigned an age of 11 700 BP using the Greenland ice core chronology (Vinther et al., 2006). The timescale was further tuned using a stacked, annually-dated ECM record from Greenland (Vinther et al., 2006). The dating error for this kind of timescale is estimated at 5% (Kinnard et al., 2006b).

5.3. IMAGE PROCESSING

Before applying quantitative analysis, the ice core images were processed to improve image quality and correct radiometric and geometric biases. A brief outline of the processing operations is given here, and a more detailed description is provided online as supplementary material (see appendix 6). First, RGB images were converted to single

channel greyscale images. Because the original JPEG images were not linear with respect to the voltage received by the camera CCD sensors, images had to be 'linearized' using the camera response function, obtained by calibrating the camera against a Kodak grayscale stepchart. The exposure bias resulting from varying the exposure time between images was corrected by tonally registering each linear image against a reference image. This was done by calculating the exposure ratio between each image and the reference, and then multiplying the images by their respective exposure ratio to correct the bias. Uneven background illumination in ice core images occurred due to: (1) vignetting, a common optical defect of camera lenses; (2) interactions of the light source with the box extremities; (3) the cylindrical shape of the cores, which resulted in increased light transmission away from the transverse core axis. The combination of these three factors produced a significant but systematic bias in the background light distribution, which needed to be removed. A data-adaptive procedure was used in which a robust polynomial surface was fitted to each image in order to estimate and remove the uneven background illumination. Finally, a radial pincushion function (Sjögren et al., 2007) was used to remove the geometric ('barrel') distortion, which is another common optical defect of camera lenses.

5.4. Results and discussion

5.4.1. Light intensity and ice density profile

Following image processing, light intensity profiles were produced by averaging intensity values along a 1 cm-wide cross-section at the center of each core image. Intensity profiles from scenes within the same core segment were stitched using reference marks on the light table, and all the core segment profiles were connected together afterwards. The

resulting depth-profile of transmitted light is shown in Figure 5.3a. According to the Beer-Lambert Law, transmittance (T) is a reciprocal exponential function of the sample thickness (x) and the extinction coefficient (K) (e.g. Mellor, 1978).

$$T = \frac{I}{I_0} = e^{-x \cdot K} \tag{1}$$

Intensity variations due to varying core thickness (x) and uneven background illumination were corrected, as well as any bias due to varying exposure and incident light (I_0) (see supplementary material). Random variations in core shape, however, may still add noise to the transmitted light profile. The extinction coefficient K is the fraction of light lost to backscattering and absorption per unit distance within the ice core. Previous studies on the optical properties of snow reported a dependence of K on grain size and density (ρ) (Bohren and Barkstrom, 1974; Kokhanovsky and Zege, 2004; Mellor, 1978; Warren, 1982). Optical theory for snow predicts a negative relationship between K and snow grain size, i.e. light transmission increases with increasing grain size. The association with ρ is more complex, with theory predicting a positive relationship between K and ρ up to ~0.45 g cm^{-3}, after which ice becomes the dominant fraction and the relationship becomes negative (Bohren and Barkstrom, 1974). The minimum bulk ρ for the POW core is close to 0.45 g cm^{-3} (black line, Figure 5.3c). The fact that grain size usually increases with ρ as snow ages makes it difficult to separate the influence of these two variables (Warren, 1982).

An index of core quality (Figure 5.3b), ranging from 0 to 10, was calculated based on the fraction of the core images covered by micro-fractures. These are caused by

mechanical stress during ice drilling. The fractured core sections are unsuitable for stratigraphic analysis, regardless of the method used (automatic or visual).

The mean light intensity profile increases steadily before levelling out at a depth of ~80 m. Because fractures increase light scattering (poor transmission), intensity values for heavily fractured core sections at 76–85 m and beyond 120 m are not reliable. Otherwise the mean intensity profile follows closely that of the measured bulk ρ, although the rate of change in light intensity with depth is different. A scatter plot of mean light intensity against bulk ρ for cores without fractures shows that the relationship does not follow the continuous exponential function predicted by equation 1 (Figure 5.4). Instead, the rate of light intensity change with ice density ($\partial I/\partial \rho$) increases at specific density thresholds, which appear to correspond to different densification stages and mechanisms (Paterson, 1994, p.15). During the first stage ($\rho \leq$ ~0.55 g cm^{-3}), densification is mainly due to settling, which occurs by grain-boundary sliding. $\partial I/\partial \rho$ is small during that stage (Figure 5.4I). In the second stage (ρ = ~0.55–0.73 g cm^{-3}), densification occurs by pressure sintering, with the bounding area between grains increasing by molecular diffusion and internal deformation of crystals. $\partial I/\partial \rho$ increases slightly during that stage (Figure 5.4II). In the third stage (ρ = ~0.73–0.83 g cm^{-3}), the contact area between grains reaches a maximum while further densification occurs by ice creep, and $\partial I/\partial \rho$ increases noticeably (Figure 5.4III). $\partial I/\partial \rho$ increases again sharply around 0.85 g cm^{-3} (Figure 5.4IV), which is close to the pore close-off density (~0.83 g cm^{-3}). Beyond this threshold, air spaces are sealed, the firn has become ice and further densification occurs slowly by ice creep-induced compression of air bubbles. The relationship between I and bulk ρ was modelled by fitting a least-squares piecewise linear

model to the log-transformed I values, with nodes at 0.55, 0.73 and 0.85 g cm^{-3}. In linear space this gives a piecewise exponential function which fits the data well ($r^2 = 0.89$), compared to the expected continuous exponential model (Figure 5.4).

Sjögren et al. (2007) reported an exponential relationship between *reflected* light intensity and ρ similar to that observed here. Hawley and Morris (2006) also compared reflected intensity with density measurements from a neutron-scattering probe in a borehole at Summit, Greenland, and observed a reversal of the relationship between the two variables at ~0.55 g cm^{-3}. The non-linear nature of the relationship between I and ρ confirms that the changing air volume is not the dominant mechanism causing the changes in the light transmission properties of the firn / ice. Because light loss occurs primarily by scattering at ice-air interfaces, the total area of these interfaces per unit volume (A/V) will determine the amount of scattering taking place. An analog measure called the specific surface area (SSA = $A/\rho_i V$, $\rho_i = 0.92$ g cm^{-3}) has been introduced in recent snow studies and was found to relate closely with near-infrared reflectance in surface snow (Domine et al., 2008). The SSA tends to decrease exponentially with increasing ρ but the exact relationship is unclear, and the data reported are only for $\rho <$ 0.5 g cm^{-3} (Domine et al., 2008).Three factors should decrease A/V thereby increasing light transmission: (1) rounding of individual ice particles, since a sphere has the smallest A/V ratio, (2) normal grain-growth processes (bond formation and recrystallization), and (3) rounding and compression of air bubbles within an ice matrix. In densification stage I, settling increases the number of grains per unit volume and hence A/V, and light transmission should decrease as predicted by optical theory for snow with $\rho <$ ~0.45 g cm^{-3}. The observed positive relationship between I and ρ during stages I and II may be

explained by a decrease in A/V due to bond formation. During stage III A/V continues to decrease, as air channels slowly become filled by ice creep and become less tortuous (Gow, 1975). Once pore close-off occurs in stage IV, air is present as irregularly-shaped bubbles which become progressively smaller and more spherical under pressure (Gow, 1969, 1975). Hence while the total density change during that stage is only about 0.09 g cm^{-3}, the concurrent change in microstructure and decrease in A/V strongly affects light transmission.

Assuming that light transmission is related to firn density via the change in ice-air interface area, the modelled relation between mean intensity and bulk density was used to estimate high-resolution proxy density changes for the un-fractured section of the POW core (Figure 5.3c). This approach is similar to that recently used by Sjögren et al. (2007). The high-resolution (5 mm) proxy density profile shows increasing variability near the surface. This is due to the melt conditions at the site that cause refreezing of meltwater and accelerate densification in the upper layers of the icefield. Both the intensity and proxy density profiles were inspected for the presence of possible seasonal cycles, both visually and using wavelet analysis techniques. Some cycles were found in parts of the core where melt was low, but these were too sporadic to be useful for dating purposes. Therefore the original depositional stratigraphy at the POW coring site has been largely obliterated by melt, and optical stratigraphy cannot be used to date the ice core as was done elsewhere (Hawley et al., 2003; Svensson et al., 2005).

5.4.2. Facies classification

Due to the large response of transmitted light to air bubbles, the less bubbly infiltration ice is more transparent than glacier ice, which makes it possible to distinguish melt

features deep in the core. Here the term infiltration ice refers to features (layers, glands, etc.) caused by melting and refreezing. Distinguishing between infiltration ice and glacier ice (or firn) by visual interpretation is a subjective procedure that is prone to interpretation errors. Hence a method that can identify melt features automatically and objectively in an ice core is desirable. In order to distinguish ice facies using transmitted light intensity, we seek an optimal threshold that best discriminates between two populations of pixel intensity. This scheme assumes that the intensity contrast is largest between the two ice facies. This assumption corresponds to visual observations, namely that the contrast between infiltration ice and glacier ice is larger than between other facies, such as depth hoar and wind slab layers. Here we use the minimum error thresholding algorithm (MET) of Kittler and Illingworth (1986), the performance of which has been found to surpass that of many other algorithms in the literature (Sezgin and Sankur, 2004). The MET procedure assumes that the image probability density function $p(I)$, approximated by the intensity histogram, represents a mixed, two-class population of pixels that can be divided into objects (infiltration ice) and background (glacier ice). Hence, we have:

$$p(I) = \sum_{i=1}^{2} P_i p(I_i) \tag{2}$$

where P_i is the proportion of pixels in each class (i=1, 2). It is assumed that the intensity values for each of the two ice facies are normally distributed with mean μ_i and standard deviation σ_i. The bias in μ_i and σ_i caused by truncation of the distribution during

thresholding was corrected following Cho et al. (1989). The optimal separation threshold (T_{opt}) was obtained by minimizing the criterion function:

$$T_{opt} = \min\left\{ J(I) = 1 + \begin{pmatrix} 2\left[P_1(I)\log\sigma_1(I) + P_2\log\sigma_2(I)\right] \\ -2\left[P_1(I)\log P_1(I) + P_2(I)\log P_2(I)\right] \end{pmatrix} \right\} \quad (3)$$

where the subscripts 1 and 2 correspond to the two ice facies. The cost function *J(I)* reflects the amount of overlap between the object and background density functions. An internal minimum in *J(I)* corresponds to the threshold that minimizes the classification error between the two components (Kittler and Illingworth, 1986). For any image, if $p(I)$ is unimodal, the criterion function has no internal minimum and no threshold is returned. The whole image is then classified as glacier ice since this facies dominates. Visual verification showed that this scheme was almost always correct. Only one small (20 cm), broken core segment consisting entirely of infiltration ice had to be reclassified.

The algorithm described above successfully identified melt features in the core (Figure 5.5 and 5.6). However, two situations sometimes confused the thresholding algorithm and required manual editing of the binary image: (1) the presence of opened, bright cracks, mostly in the top 20 m of the core; (2) micro-fractured surfaces. Cracks were mistakenly classified by the algorithm as infiltration ice and had to be edited out from the classified images. Fractures caused a third (darker) pixel population to appear in the image intensity histogram, which violated the assumption of a two-class mixed population. The core quality index, which gives the percentage of an image covered by dark micro-fractures, was used to remove the corresponding lower percentile from the image histogram and the MET algorithm was applied afterwards. This worked well for

cores with less than 60% fractures, but failed on some of the more damaged cores, which had to be thresholded manually. Noise was then removed from all classified images using morphological opening (Russ, 2002, p.410), and only objects larger than 20 pixels were retained.

The resulting classified images had a spatial resolution of 0.3 mm. An index of infiltration ice content (P_i, % mm^{-2}) was derived by averaging images across their row dimension and resampling at a 1 mm interval (Figure 5.5d and 5.6d). A fully wetted and refrozen layer has a P_i of 100% while a partially wetted/refrozen layer and discontinuous features such as ice glands have lower P_i values. Figure 5.5 shows an example where the automatic classification results matched closely those from the visual interpretation. In other cases, the thresholding procedure detected partially refrozen zones in the core (e.g. an irregular ice gland) more accurately (Figure 5.6a, b). Such features are sometimes difficult to interpret by eye, but were objectively detected by the thresholding procedure.

In Figure 5.7, the infiltration ice content index obtained from both methods was compared for each core segment. Although the two methods generally agree, there are significant differences. The optical method is more successful at detecting discontinuous features such as partially refrozen layers and ice glands. As an example, while both methods gave similar results for core 45 (triangle, Figure 5.7), the detection of the partially refrozen feature in core 27 resulted in significantly different average P_i values (star, Figure 5.7).

5.4.3. Effect of melting on glaciochemistry

The high-resolution ice content index may be used to investigate the effect of melting on glaciochemical signals in the POW ice core. Here we used the high-resolution (5 mm)

ECM record to look at the relationship between solid conductivity and ice facies. The ECM measures the acidity of the ice. In the Arctic this is mainly due to the deposition of sulphuric and nitric acids in snow, which are partly neutralized by alkaline dust (Hammer, 1980). Melting causes leaching of ions in snowpacks, and strong acids are preferentially eluted compared to other major ions such as Na^+ (Davies et al., 1982; Koerner, 1997). Thus melting can alter seasonal glaciochemical and ECM signals, and may compromise the identification of volcanic acidic horizons.

Melt features observed in the core were all thinner than ~50 cm, so the ECM record was high-pass filtered with a robust spline (Meeker et al., 1995) that removed all periodic variations longer than one meter (Figure 5.8a, b). This, for example, compensated for increased snow acidity due to anthropogenic emissions of SO_x and NO_x in the recent industrial era (Koerner and Fisher, 1982). Two methods were used to compare the filtered ECM signal with P_i. First, the P_i series was binned into 10% classes and the corresponding median ECM value was linearly regressed against the P_i classes. The data were binned because ECM values are unequally distributed over the P_i range and hence suffer from large heteroscedasticity. The median was used as an estimator of central tendency because the ECM distribution is skewed by spikes of volcanic origin. The median ECM signal was found to be linearly correlated ($r = 0.91$, $p < 0.05$) with the melting index (Figure 5.8c). Secondly, the ECM data were partitioned into two subsets, corresponding to infiltration and glacier ice, and a non-parametric Mann-Whitney test (e.g. Gibbons and Chakraborti, 2003) was used to assess whether the two subsets came from the same population (Figure 5.8d). The normal test statistic ($Z = 9.1$, $p < 0.01$) shows that the median ECM signal for infiltration ice is significantly larger than that for

glacier ice. Repeating the process by partitioning the populations with successively higher P_i thresholds shows that the best separation between populations occurs at $P_i \geq 0.6$ ($Z = 14.1$, $p < 0.01$). An Ansari-Bradley test for homogeneity of variance (Gibbons and Chakraborti, 2003) indicates that the ECM signal in infiltration ice is more variable than in glacier ice, with again the greatest variance contrast for $P_i \geq 0.6$. Non-parametric tests were used since the data is non-normally distributed. These results confirm that melting at the surface of the POW Icefield is causing elution of strong acids, which upon refreezing tend to accumulate within melt features. This finding has important implications for the interpretation of ice core glaciochemical records (Koerner, 1997), which will be discussed next. The higher ECM variance in infiltration ice also shows that only some, not all melt features have enhanced chemical concentrations. If the ECM probability distribution observed for glacier ice, $p(x)$, is assumed to be representative of ice unaffected by melt, then the probability $f(k|n, p)$ of observing more than k infiltration ice data points with an ECM value of x and probability of success $p(x)$ out of n total observations may be described by an inverse binomial cumulative distribution (Figure 5.8e). The density functions for both populations were estimated using a kernel smoothing method (Figure 5.8d). The probability f may be used to determine where the probability distributions from the two populations differ significantly. Melt features with ECM values > 0.0145 have a 95% probability of being chemically enriched due to elution (Figure 5.8e). Using the depth-time scale for the POW core, years when elution probably took place may then be identified (Figure 5.9a). The average annual melt percentage for the last 580 years is 9%. Surface melting at the coring site occurred in eight years out of

ten and elution probably occurred in ~36% of these years. Hence, elution due to melt occurred on average three years out of ten.

Using the density-corrected P_i index (defined in next section) averaged over one-year intervals, the distribution of annual melt fraction $P_i(t)$ for years with and without elution may be compared (Figure 5.9b). Although more elution events are associated with lower annual melt fractions, the probability of elution increases with the amount of melt, reaching 100% when $P_i(t) > 0.6$ (Figure 5.9c). These results give an indication of the quality of signal preservation to be expected from the amount of melting taking place at the site, and are consistent with previous studies. Grumet et al. (1998) identified pseudo-seasonal cycles in an ice core from Penny Ice Cap, Baffin Island, where the average melt percentage over the past 300 years is 40%. However during periods when melt rose above 50–60% these signals were obliterated. In an ice core from the Lomonosovfonna ice field, Svalbard, with average melt of 55%, Pohjola et al. (2002) found that strong acids were eluted and accumulated in melt features, which obliterated any obvious seasonal cycles in the glaciochemical series.

Seasonal melting on the POW Icefield also altered the volcanic signals present in the ECM record. While the acid peaks from the Katmai eruption and the 1259 AD event were clearly identified in a section of the core with low melt percentage (< 4% a^{-1}) no peak could be found for other volcanic horizons commonly found in Arctic ice caps, such as Laki (1783 AD), which according to the timescale occurred during a period with higher melt rates (~ 15% a^{-1}) (Figure 5.9a).

5.4.4. Melt history

The melt index from the POW core may be used as a proxy for past summer warmth at the site (Koerner, 1977). The ice content index P_i was first corrected for differential compaction with depth before averaging over time. The measured bulk density profile, smoothed with a robust spline, was used to convert firn to ice equivalent depths. The high-resolution proxy density profile was not used as it is only continuous above 75 m. The bias in P_i resulting from artificial compression of melt features when converting to ice depths was removed by multiplying P_i by the reciprocal of the smoothed density curve, $0.917/\rho$ (e.g. Koerner and Fisher, 1990). The corrected P_i values were then averaged into one and five-year intervals.

Over the last 1000 years the annual melt percentage shows large decadal variability and a general cooling trend until ~1850 AD, after which melting increased progressively (Figure 5.10a). The 12th century and the second half of the 20th century are the periods with the highest and most sustained melt. Sections with poor core quality may underestimate the melting percentage, for example during the 1000–1100 AD and 1700–1750 AD intervals. Melt records from other Arctic ice caps were gathered and compared with the POW record (Figure 5.10a). The POW record is noticeably different from those from the nearby Agassiz (alt. 1730 m) and Devon ice caps (alt. 1800 m). Devon and Agassiz are ~750 km apart and the correlation between these melt records over the last 1000 years is 0.53, which is similar to that observed between air temperature records from Arctic weather stations separated by this distance (Rigor et al., 2000). However the correlation between the POW record and these two sites, each ~375 km away, is close to zero. Furthermore, the lag-1 autocorrelation coefficients for the Agassiz and Devon

records are 0.61 and 0.60, which is typical of temperature series (Fisher, 2002), but it is only 0.28 for the POW record, using either the visual or optical melt indices. The autocorrelation coefficient did not change significantly when calculated for periods with good core quality, so the varying core quality may explain part, but not all of the higher-frequency character of the POW record. Hence melt events on the POW Icefield appear to be mostly asynchronous with those at neighbouring sites, and the record is also less 'persistent' (smaller lag-1 autocorrelation) than is typically expected for temperature series, suggesting that melting episodes on the POW Icefield may be associated with local, rather than regional conditions.

A principal components analysis was performed on the seven standardized Arctic melt records over their common time period 1551-1956 AD. The first principal component (PC1) explains 34% of the total variance and is significantly different from red noise at the 95% significance level. PC1 is similar ($r = 0.60$, $p < 0.05$) to the Arctic summer proxy temperature reconstruction from Overpeck et al. (1997) and may be interpreted as the common response of the seven Arctic ice caps to pan-Arctic thermal forcing (Figure 5.10b). The loadings are positive for all sites and explain between 17% and 66% of the variance of individual series, except for the POW site where PC1 only accounts for 5% of the variance (Figure 5.10b). The amount of local variance explained reflects the contribution of local climate and glaciological processes. While most melt records show a post-1850 AD melt increase in response to a pan-Arctic temperature rise, the rate of increase in the POW record was comparatively slower. Only in recent decades has melt increased abruptly at this site.

Marshall et al (2007) have shown that on the summit of POW Icefield low melt years occur together with steep surface temperature lapse rates, resembling moist adiabatic rates in free air, and enhanced cyclonic activity with a southerly flow aloft. In contrast, large melt was observed together with weak lapse rates and a northerly, anticylonic flow aloft. Intermittent decoupling of surface climate conditions between the high and low elevations of the ice cap was also reported by Wang et al. (2005, their Fig.3), who showed that inter-annual variability in the melt season length at high elevations on the POW Icefield was inverse to that at low elevations for the period 2000–2004. Alt (1987) and Gardner and Sharp (2007) showed that the shape, position and strength of the July polar vortex are determinant for mass balance conditions on Queen Elizabeth Islands (QEI) glaciers. Three main influential synoptic regimes are recognized: (1) contraction of the polar vortex and intrusion of a ridge into the QEI, bringing warm and dry air and causing extreme melting; (2) general expansion of the polar vortex, or its elongation across Ellesmere Island and down Baffin Bay, resulting in increased advection of cold/moist air from the Arctic Ocean, which suppresses melt and increases precipitation; (3) Baffin Bay low pressure center, which advects mild/moist air to the eastern QEI, overcast conditions, increased precipitation and generally negative mass balance conditions. In this last situation, melting may be enhanced at low elevations of ice caps due to rainfall, but higher elevations receive more snow and melt may be limited by overcast conditions. Increased snow accumulation in summer will also raise the albedo of the ice cap surface and reduce melting. At present, the POW Icefield appears to be affected by the mild/moist climate of Baffin Bay on its eastern flank, and the varying influence of warm/dry continental and/or cold/moist Arctic Ocean air masses on its

western side. The coring site is located near the boundary where melt anomalies at high and low elevations are of opposite signs (Wang et al., 2005) and on the boundary between the drier, colder 'Northern' region and the more maritime 'Eastern' climatic region, as defined by Maxwell (1981). The similarity of the Agassiz and Devon melt records, as well as their coherent response to pan-Arctic thermal forcing in summer, may imply that these two sites have remained in different but stable climatic zones over the past 1000 years. In contrast, the POW melt record may partly reflect the migration of the Baffin Bay climate boundary over time. The progressive shift from a more continental to a cooler, more maritime regime could explain the offset between the regional warming trend and the POW melt record.

Another factor that is likely to impact locally on the climate of the POW Icefield is the proximity of the NOW polynya in northern Baffin Bay (see Figure 5.1). With an area of 80 000 km^2, it is the largest polynya in the Canadian Arctic (Smith and Rigby, 1981). The polynya forms in winter when prevailing northerly winds push sea ice down Nares Strait, forming an ice bridge which blocks further ice advection to the South. The NOW polynya is not continually present, but nevertheless represents an important yet variable local source of heat and moisture for nearby glaciers and ice caps. This is reflected in the larger accumulation rate at the POW coring site (0.30 m-ice a^{-1}) compared to Agassiz (0.175 m-ice a^{-1}) and Devon (0.23 m-ice a^{-1}) ice caps. Heat advection from the polynya would take place in winter when temperatures on the POW Icefield are well below freezing. However, it is likely that the timing of opening/closing and the areal extent of the polynya in spring and fall exert a control on the timing and amount of snow accumulating on the POW Icefield summit. Barber et al (2001) showed that warm (cold)

years tend to be associated with positive (negative) sea ice concentration anomalies in the NOW polynya. This occurs because cold northerly winds favour ice export from, and opening of, the polynya, while warmer southerly wind restrict the advection of ice south of the polynya, limiting its extent.

We estimated the contribution of site-specific process(es) to the melt history on the POW Icefield by subtracting the PC1 signal from the standardized POW melt record (Figure 5.10d). The resulting series exhibits pulse-like fluctuations, and a gradual decrease in melt after the early 1850s relative to PC1. This could be due to a local cooling feedback from Baffin Bay during summer, but observations suggest a warming in that area over 1916–2003 (Zweng and Munnchow, 2006). In light of the previous discussion, we suggest that the slow melt increase on the POW Icefield after ~1850 when compared with the pan-Arctic trend, may reflect a growing influence of the Baffin Bay climate, and/or more open water conditions in the NOW polynya, causing increasing snow accumulation on the POW Icefield. An increase in accumulation rate while keeping the amount of seasonal melt constant would result in an apparent decreased melt percentage in the ice core (melt % = melt [cm yr^{-1}] / accumulation [cm yr^{-1}]). Accumulation typically increases with warmer temperature and decreases with cooler temperature, so that changes in accumulation rate usually attenuate the melt-temperature relationship (Koerner and Fisher, 1990). Unfortunately, long accumulation time series are not presently available for the POW Icefield to test this hypothesis, and neither are high-resolution proxy records of sea ice conditions in the NOW polynya to compare with the POW melt record. Levac et al. (2001) developed a coarse (centennial scale) reconstruction of sea-surface conditions in the NOW polynya from a sediment core from

Smith Sound. Their analysis suggests an increase in open water conditions from two to four months per year over the last ~200 years. We speculate that the post-1850 AD regional warming trend has caused a northward contraction of the mid-tropospheric summer polar vortex over the western Arctic while an elongated trough has remained over the eastern QEI (Alt, 1987; Gardner and Sharp, 2007). This synoptic pattern favours the northward movement of cyclones into Baffin Bay which cause colder summers and milder winters (Barry et al., 1975), and the concomitant opening of the NOW polynya (Barber et al., 2001). Hence colder (warmer) conditions would lead to larger (lower) precipitation on the POW Icefield due opening (closing) of the polynya. This coupling between atmospheric synoptic conditions and the wind-driven dynamic of the NOW polynya may then accentuate, and not attenuate (Koerner and Fisher, 1990), the melt-temperature relationship on the POW Icefield.

5.5. Conclusions

The optical system and image analysis techniques developed in this study have proven useful for characterizing ice core stratigraphy at a high spatial resolution. The imaging apparatus uses a low-cost CCD digital camera and is easily implemented. However the images derived suffer from various radiometric and geometric biases which need to be carefully corrected, and this work has provided methods to do so. The derived profile of transmitted light intensity is related to core density in a non-linear way, as found by others (Sjögren et al., 2007), an observation explained by the fact that light transmission depends on the total area of scattering ice-air interfaces, which vary with the densification process. The modelled relationship was used to produce a high-resolution (5 mm) proxy density profile for the core. Seasonal density variations, which are commonly found in

the dry snow zones of ice caps, were only observed in a few sections of the core with low melt, so the original depositional sequence in the POW core has been mostly obliterated by melt.

The melt features caused by infiltration and refreezing of meltwater appeared brighter in digital images, and were successfully discriminated with an automatic thresholding algorithm. Heavily fractured sections, however, confounded the algorithm and manual editing was necessary. The ice content index derived from the classified images was generally in good agreement with visual observations, but the image analysis method identified irregular melt features more accurately and is considered more objective.

The optical ice content index was used to quantify the effect of melting on the solid conductivity of the ice core. A greater and more variable ECM signal was found in melt features compared to glacier ice, suggesting that elution of strong acids occurs at the site. A critical ECM threshold was derived to identify chemically-enriched melt features and was used to identify periods in the record which probably suffered from elution. The annual probability that elution occurred was found to increase from 20% for annual melt percentages in the range >0–10%, to 100% when over 60% of the annual layer consists of infiltration ice. The alteration of glaciochemistry records by elution represents a significant problem in ice core studies. In this regard our results offer a useful estimate of the preservation of glaciochemical signals in ice cores recovered from the percolation zone of Arctic ice caps.

The POW melt history, a proxy for past summer warmth, bears little resemblance to the melt histories from neighbouring ice core sites or the common melt signal from

seven circum-Arctic ice caps. This suggests that its signal is predominantly controlled by site-specific climatic or glaciological factors that we cannot resolve from the melt record alone. We propose that the varying influence of cyclonic conditions in Baffin Bay and associated steep lapse rates, as well as the intermittent opening and closing of the adjacent NOW polynya are the major control on the POW Icefield melt history.

Acknowledgements

This paper is dedicated to Dr Roy 'Fritz' Koerner (1932–2008). Dr Koerner has led an outstanding career as a glaciologist and polar explorer. He pioneered the use of "melt layers" in Arctic ice cores to reconstruct past temperature, which contributed greatly to the field of paleoclimate science. He is remembered for his sharpness of mind, inspiring enthusiasm, and contagious humour. This project was funded by the Canadian Foundation for Climate and Atmospheric Sciences. Funding to C. Kinnard was provided by the Natural Sciences and Engineering Research Council of Canada.

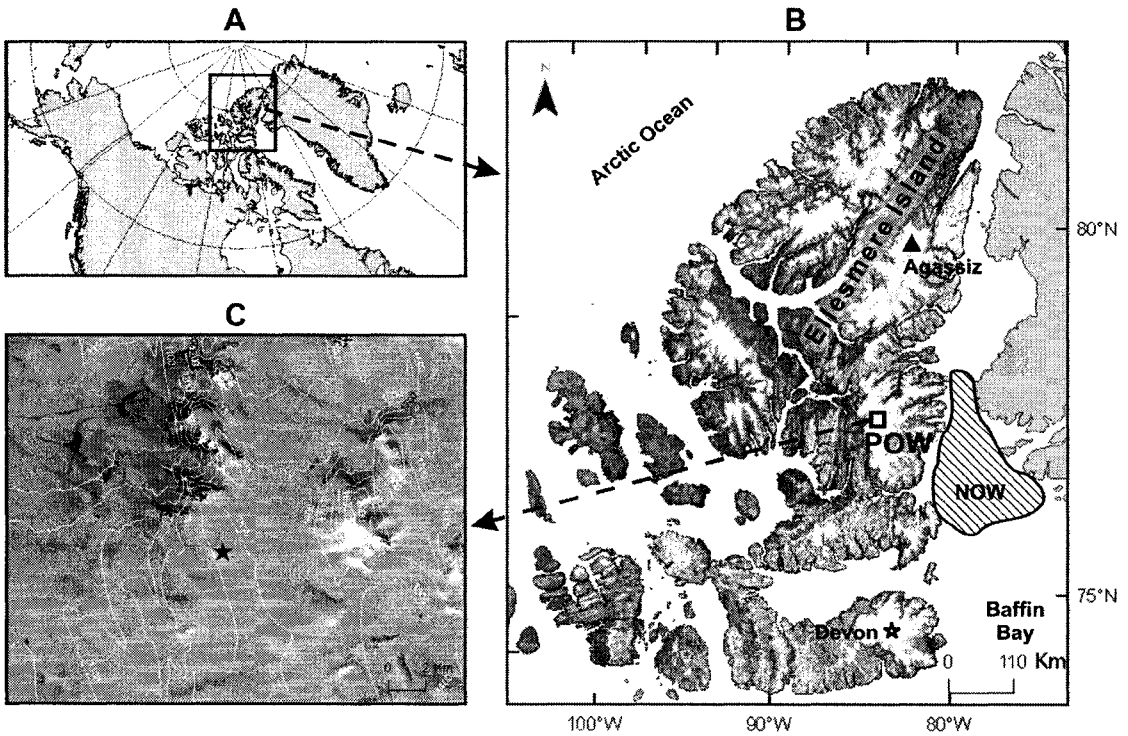

Figure 5.1. Study area. (a) Western Arctic; (b) Ellesmere Island, with Radarsat image overlay and ice core sites discussed in the text; (c) drill site (star), with Landsat image overlay. Contour interval is 100 m. Satellite image and elevation data source: Natural Resource Canada.

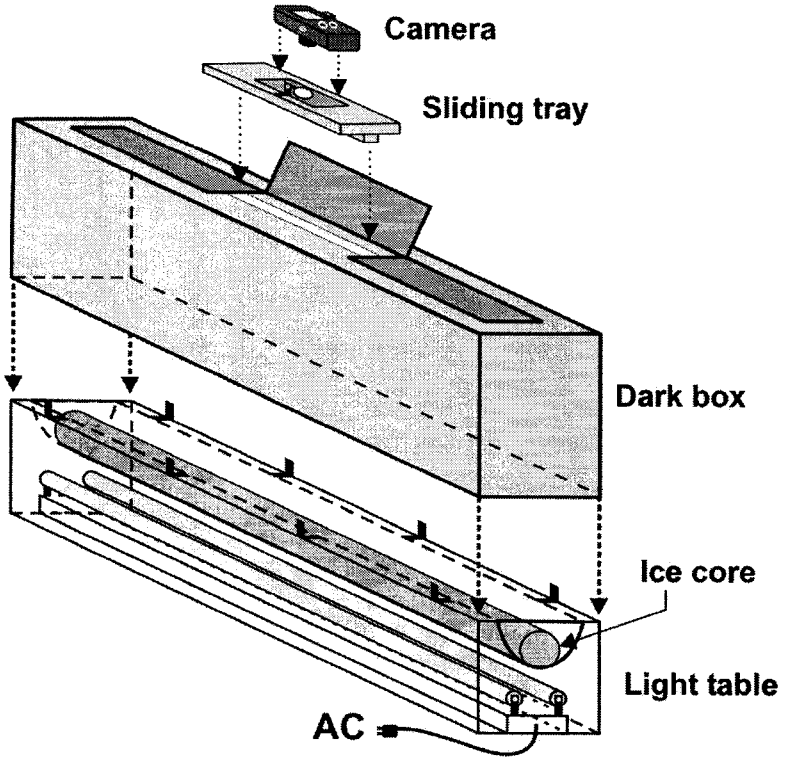

Figure 5.2. Light table and imaging apparatus.

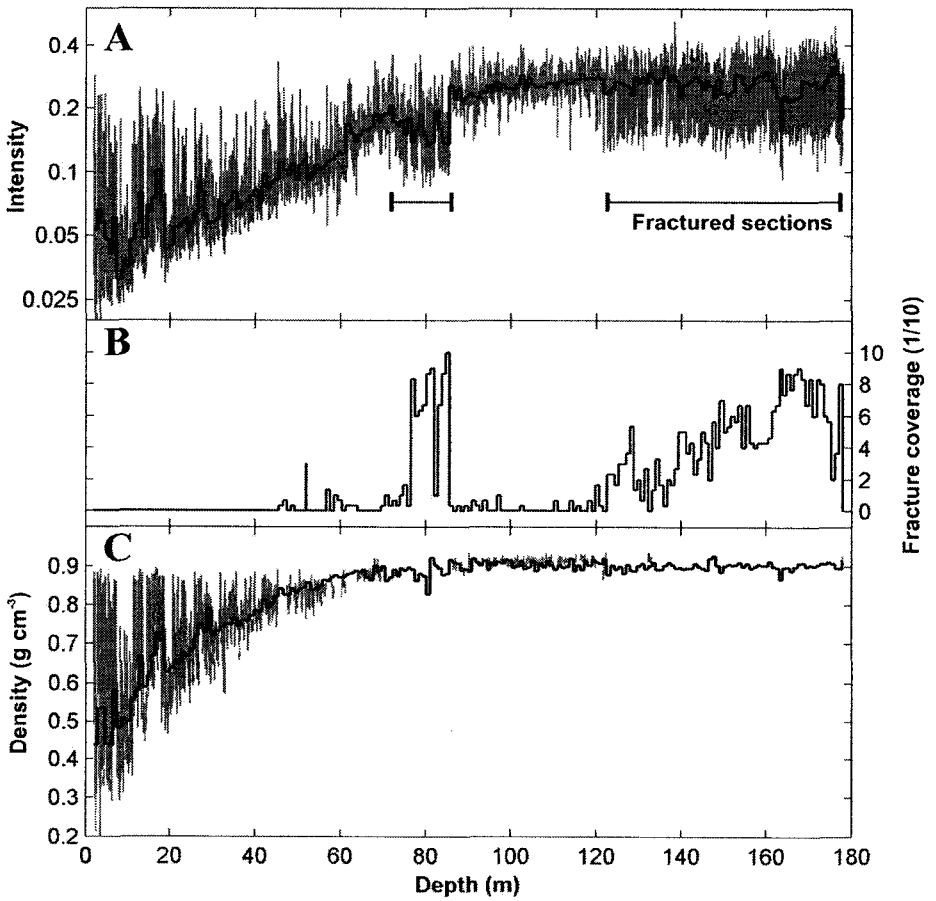

Figure 5.3. (a) Transmitted intensity profile (gray line) with core segment averages (black line). Profiles are shown on a logarithmic scale in accordance with equation 1; (b) core segment fracture coverage, an index of core quality; (c) measured bulk density profile (black line) and 5 mm-interval reconstructed proxy density profile (gray line).

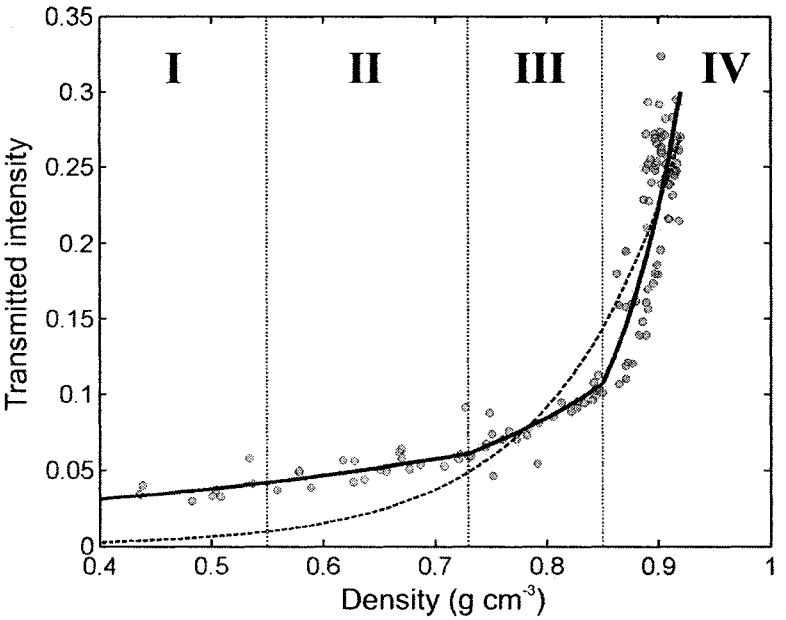

Figure 5.4. Mean transmitted light versus measured bulk density. The stippled line shows the theoretical relationship predicted by equation 1. The black line shows the piecewise exponential function with nodes at the main densification threshold values (dotted vertical lines with roman numbers).

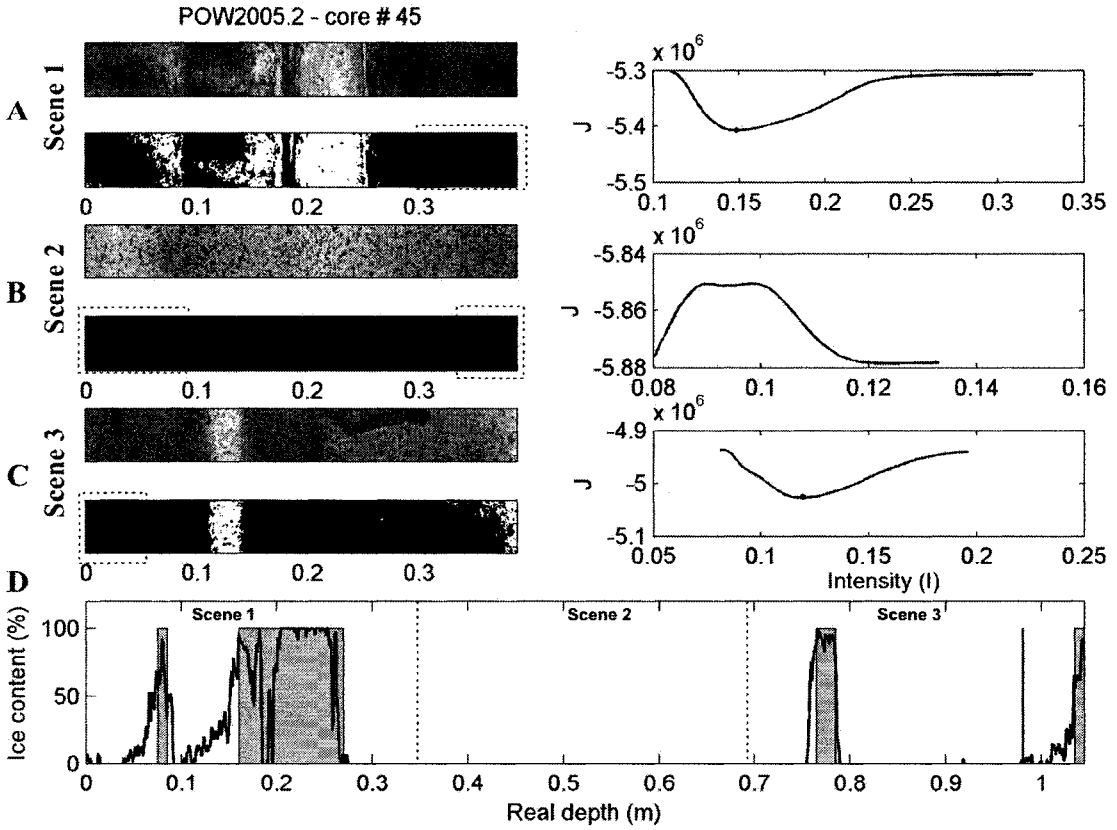

Figure 5.5. Results from the facies classification procedure for core 45 (45.5–46.5 m-depth). (a) Original and classified core image from scene 1, with associated criterion function *J(I)* and internal minimum corresponding to the optimal intensity threshold (black dot); (b) Same as Figure 5a, but for scene 2; *J(I)* has no internal minimum so the whole image is classified as glacier ice; (c) same as Figure 5a, but for scene 3. The stippled rectangles over the binary images delineate the overlapping scene areas; Note the different x-axis limits for *J(I)* functions. (d) stitched ice content index P_i (black line) and corresponding visual estimations (gray bars). Stippled vertical lines show stitching boundaries.

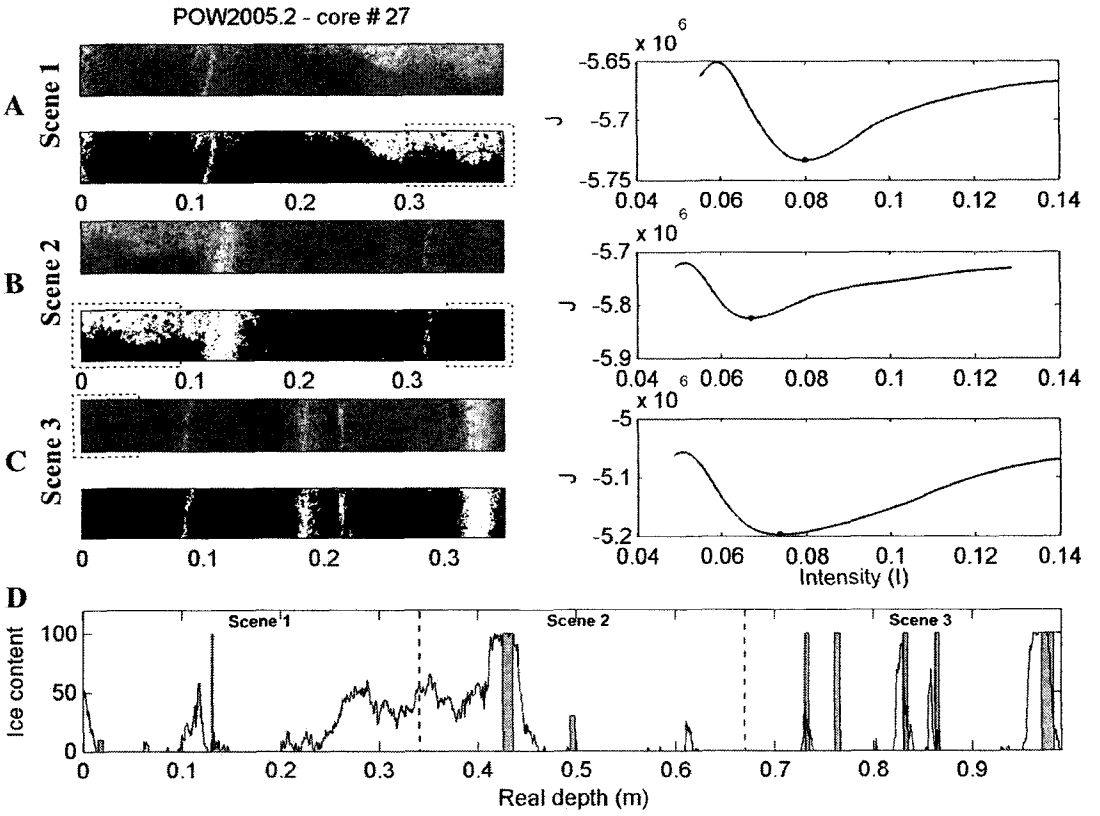

Figure 5.6. Same as Figure 5.5, but for core 27 (27.8–28.8 m-depth).

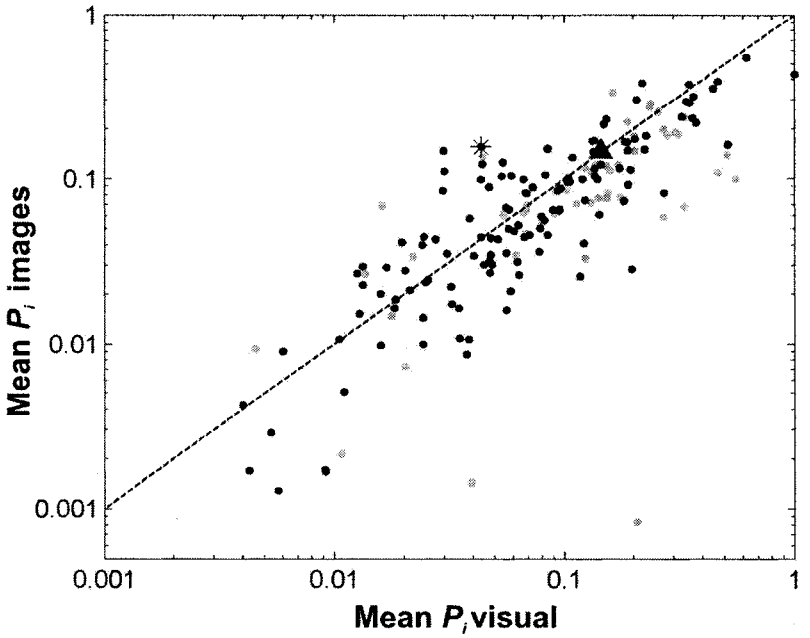

Figure 5.7. Core-wise average ice content from images versus that derived from visual interpretation. Stippled line is the 1:1 delineation. Black dots are for cores with no fractures, gray dots are for fractured cores.

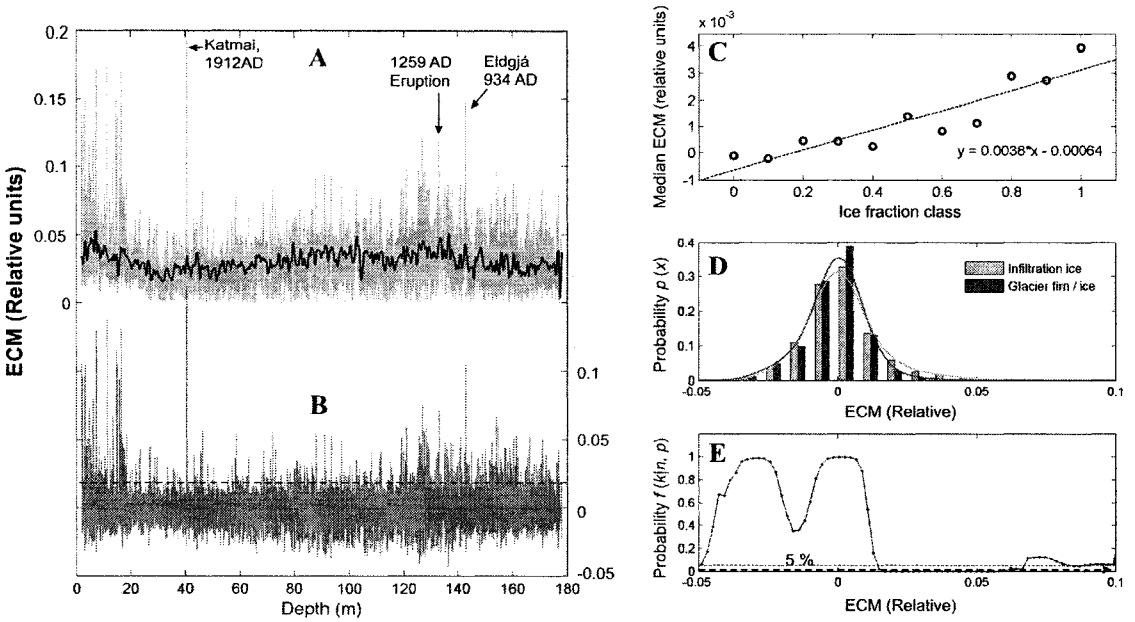

Figure 5.8. (a) 5mm-interval ECM record (gray line) with robust spline function (black line); (b) high-frequency residual ECM values, with calculated elution threshold (stippled line); (c) median residual ECM versus ice fraction class. A class of 0–0.1 includes all samples with melt above 0 and below 0.1; (d) histogram (bars) and density functions (stippled lines) of ECM values for glacier and infiltration ice; (e) probability of observing more infiltration ice than glacier ice samples with a given ECM value. ECM values below the 5% threshold (stippled line) have a 95% probability of being chemically enriched due to elution. The rise above the threshold for ECM values larger than 0.07 may be due to the strongly acidic volcanic layers and/or because of poor density estimation near the distribution tail.

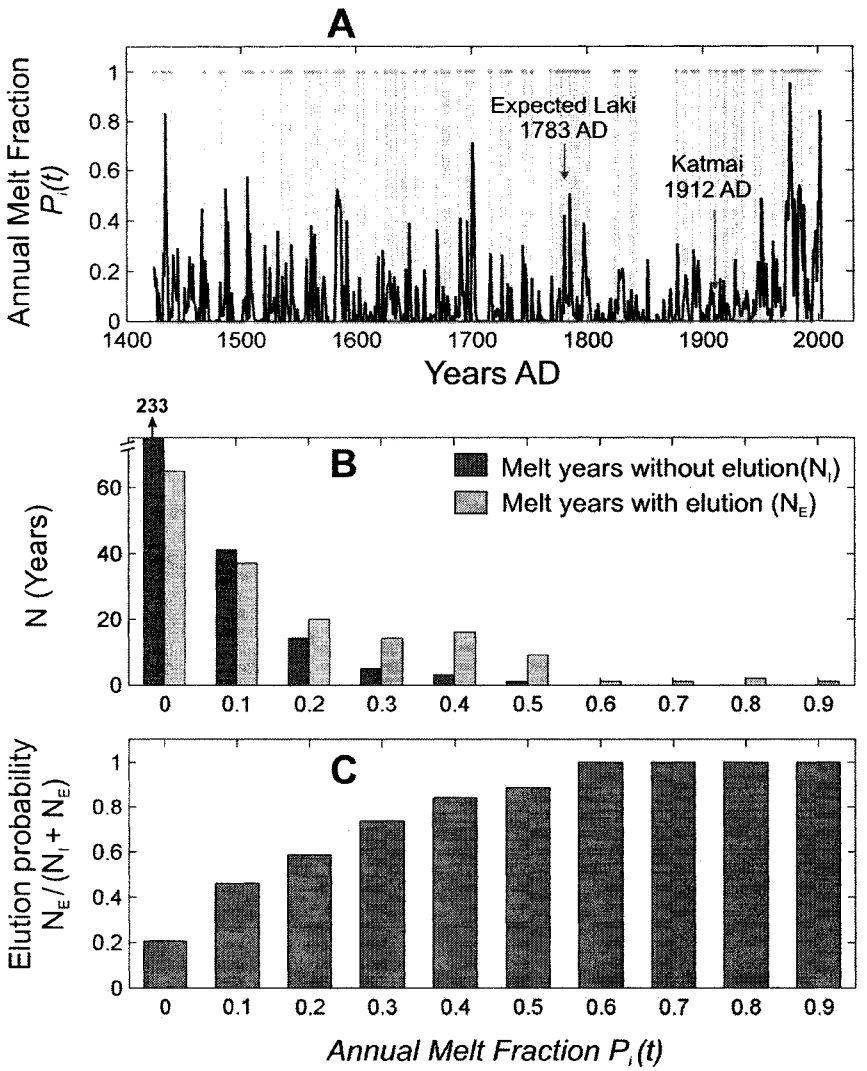

Figure 5.9. (a) Annual melt fraction for 1424–2004 AD, corresponding to the upper 120 m of the core. Gray vertical dotted lines indicate years with probable elution. Also shown are the Katmai (observed) and Laki (expected) volcanic events; (b) number of years per annual melt fraction class for years with (light gray) and without (dark gray) elution. A class of 0–0.1 includes all samples with melt above 0 and below 0.1; (c) probability of elution occurrence per annual melt class.

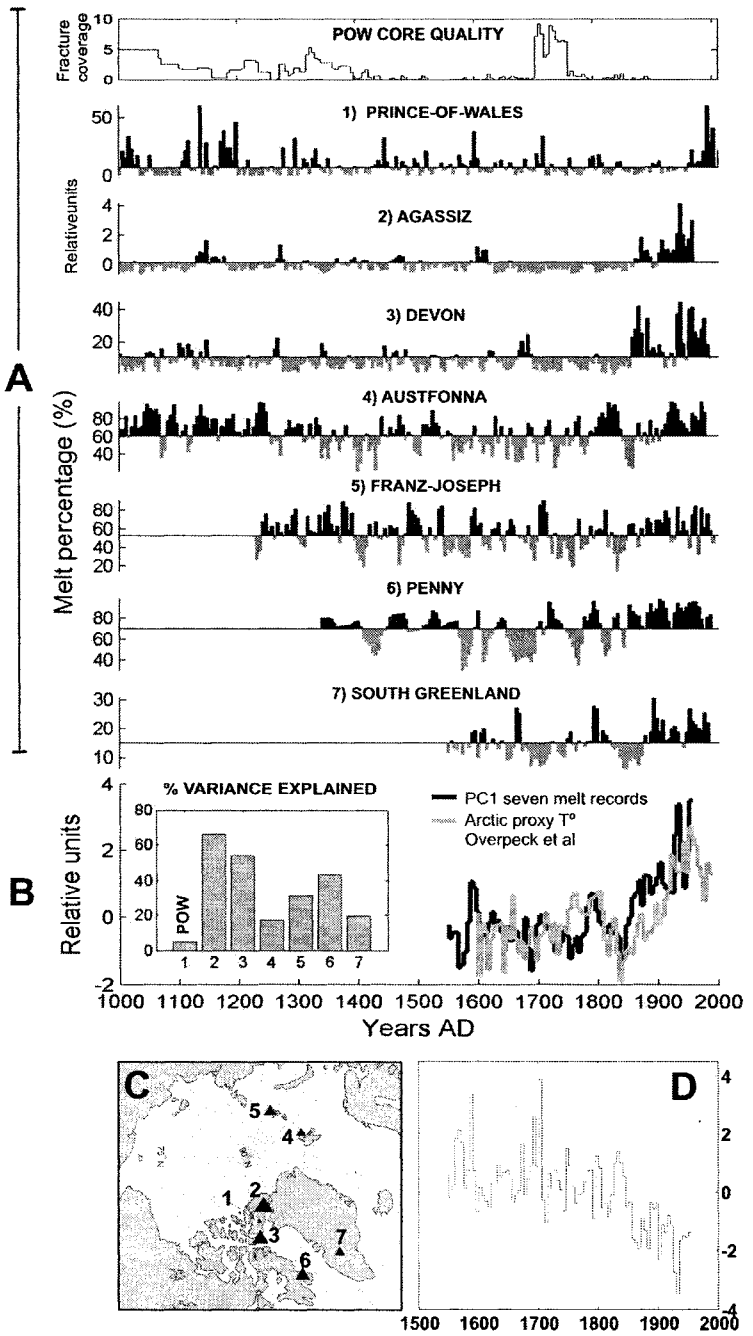

Figure 5.10. (a) Circum-Arctic melt record (five-year averages). The top panel displays the core quality index for POW. Data sources: (1) This study; (2) Fisher and Koerner, 1994; (3) Kinnard et al., 2006; (4) Tarussov, 1992; (5) Henderson, 2002; (6) Okuyama et al., 2003; (7) Kameda et al., 1995; (b) fist principal component (PC1) of the seven Arctic melt records (black line) and Arctic summer temperature reconstruction (gray line, Overpeck et al., 1997). The bar graph shows the percent variance explained in each melt record, with bar numbers referring to site numbers in Figure 10a; (c) Map of ice core sites; triangle size represent the percent variance explained by PC1; (d) difference time-series between the standardized POW melt and PC1 records.

CHAPTER 6. COUPLED ARCTIC CLIMATE AND SEA ICE EXTENT OVER THE PAST MILLENNIUM RECONSTRUCTED FROM TERRESTRIAL PROXIES

Christophe Kinnard[1, 2]

Christian M. Zdanowicz[2]

David A. Fisher[2]

Elisabeth Isaksson[3]

...

(1) Department of Geography, University of Ottawa, Ottawa, Canada

(2) Geological Survey of Canada, Ottawa, Canada

(3) Norwegian Polar Institute, Tromsø, Norway

MANUSCRIPT IN PREPARATION FOR PUBLICATION

6.1. INTRODUCTION

The Arctic sea ice cover is in a state of profound change. More than 30 years of satellite observations have shown a continuous decrease of -4% per decade in the mean annual sea ice extent, defined as the area of ocean with a fractional ice cover of at least 15% (Comiso and Nishio, 2008). The ice decline is mostly driven by the fast disappearance (-9% per decade) of thick perennial ice, i.e. ice that survives summer melt. This perennial ice is partly being replaced by seasonal ice, which is ice that forms in winter but melts in summer (Kinnard et al., 2008). Since 2002 pronounced minima have occurred in late-summer ice extent, with a record-breaking 40% reduction in September 2007 relative to the 1979-2007 average (Stroeve et al., 2008). Climate models predict that the ice cover will continue to retreat to attain summer ice-free conditions during the mid- to late 21st century, but the recent ice decline is occurring faster than forecast (Stroeve et al., 2007).

The accelerating ice decline in summer is driven by a combination of thermodynamic and dynamic processes. Longer melting seasons cause ice loss (Belchansky et al., 2004). Warmer winters decrease freezing rates, which result in thinner ice that is more vulnerable to wind stress and hence more easily advected outside the Arctic (Maslanik et al., 2007; Nghiem et al., 2007; Zhang et al., 2008). Increased advection of warm, saline North Atlantic water into the Arctic contributes to ice melting and reduced ice growth (Dickson et al., 2000). Sea ice variability also impacts on climate. The loss of highly reflective sea ice cover decreases the surface albedo and allows solar radiation to warm the ocean, promoting further ice melt and warming the atmosphere (Perovich et al., 2007). This positive feedback process is the main postulated cause for polar amplification of greenhouse gas (GHG) induced climate warming (Serreze and

Francis, 2006). The intensified seasonal sea ice freeze-thaw cycle also affects water stratification in the Arctic Ocean, which impacts the global thermohaline circulation (Aagaard and Carmack, 1989; Kinnard et al., 2008).

The recent sea ice decline has been attributed to anthropogenic climate warming (Gregory et al., 2002; Min et al., 2008; Vinnikov et al., 1999). However, sea ice variability also bears a strong imprint of natural climate variability, being closely connected with dominant modes of atmospheric circulations such as the Arctic Oscillation (Deser and Teng, 2008; Deser et al., 2000; Rigor et al., 2002) and other low-frequency atmospheric and oceanic oscillatory modes (Polyakov et al., 2003a; Polyakov and Johnson, 2000).

Because reliable Arctic-wide sea ice observations do not extend far prior to the 20th century, it is difficult to properly characterize the magnitude of natural sea ice variability and to interpret recent trends in a long-term context. Only a few documentary records from the North Atlantic region provide information on multi-centennial ice edge fluctuations. These records show the existence of substantial low-frequency (>20 years) variability that could confound the detection of an anthropogenic signal within shorter pan-Arctic records (Divine and Dick, 2006; Vinje, 1999; Wallevik and Sigurjónsson, 1998). Proxies for regional sea ice conditions during the Holocene have been developed from the distribution of ^{14}C-dated bowhead whale fossils and coastal driftwood (Dyke et al., 1996; England et al., 2008), and from ice-rafted debris and micro-organism assemblages in ocean sedimentary records (de Vernal et al., 2005; Moros et al., 2006). These records suggest a much reduced summer ice cover during the early Holocene warm period (Fisher et al., 2006). While these proxies offer valuable time slices of past sea ice

conditions over the last glacial cycle, they usually have a coarse temporal resolution (>centennial) and restricted spatial coverage. However, promising new sea ice proxies are currently being developed from sea ice algae biomarkers measured in sediment cores from continental shelves where sedimentation rates are higher (Belt et al., 2007; Massé et al., 2008). High-resolution reconstructions of Arctic sea ice conditions are critically needed for the last one to two millennia, a period during which the basic boundary conditions of Earth's climate have not changed significantly (Mann, 2007), in order to characterize the range of natural variability at timescales relevant to human populations.

In this study we use a network of high-resolution (<5 year) terrestrial climate proxies from the circum-Arctic region to reconstruct the coupled climate and sea ice extent history over the past millennia. We use a multi-proxy calibration approach, which has been used successfully before to reconstruct past temperature (D'Arrigo et al., 2006; Hegerl et al., 2006; Luterbacher et al., 2004; Mann, 2008; Mann et al., 1998; Moberg et al., 2005), sea-level pressure (Fritts, 1991; Luterbacher et al., 2002) and circulation indices (Cook et al., 2002). The reconstructed sea ice history is compared to recent temperature and atmospheric circulation reconstructions, in an effort to identify natural drivers of sea ice variability in pre-industrial times.

6.2. DATA

6.2.1. Observational data

We used the Northern Hemisphere (NH) ice concentration grids for the period 1900-2003, available from the University of Illinois (hereafter called 'WC dataset', http://arctic.atmos.uiuc.edu/SEAICE/, Walsh, 1978; Walsh and Chapman, 2001), to calibrate against the proxy network. These data represent a compilation of observations

from multiple sources integrated into a single gridded product, and constitutes the most complete sea ice dataset currently available. The source of data has changed over the years from infrequent land/sea observations, to operational charts, and to satellite data for the most recent decades. A large portion of the pre-1953 concentration data is either climatology-filled or interpolated, and only the ice edge position is reliable. The data is also most complete during summer when ship navigation occurs. For these reasons we used a measure of ice extent, defined as the total ocean area within the 15% concentration contour (Walsh and Chapman, 2001). The reliability of ice extent values increases with time as observational methods became more precise and the data coverage increased. The spatial coverage and data accuracy is most complete for the post-1972 satellite era. Observations for the period 1953-1971 are spatially complete and considered generally accurate while the pre-1953 data is the least accurate, containing both observed and interpolated data (Walsh and Chapman, 2001).

In the early 20th century ice edge observations are scarce in the Russian and Canadian Arctic, especially during the Second World War (1940-45). Polyakov et al (2003a) compiled August ice extent in Russian Arctic seas for the period 1900-2000 AD using ice charts recently released by the Arctic and Antarctic Research Institute in St. Petersburg, Russia. These data show more pronounced ice extent variations in the pre-satellite era than that observed in the WC dataset (see appendix 4). Hence in this study we reconstructed the total ice extent for the month of August, obtained by integrating the August ice extent grids from the WC dataset for every year of record, and by replacing the WC ice extent in the Chuckchi, East Siberian, Laptev and Kara seas with ice extent

values from Polyakov et al (2003a). Ice extent in August is close to the annual minimum, and is a good indicator of summer ice conditions (see Figure 6.2).

6.2.2. Proxy data

We used a multiproxy network consisting mainly of ice core records, along with a few long tree-ring chronologies, lake sediment records and documentary sea ice observations for the circum-Arctic region (Figure 6.1 and Table 6.1). Ice cores contain a wealth of proxy environmental information recorded at a high-resolution (e.g. Bradley, 1999). Parameters considered as potential sea ice proxies include stable oxygen isotopes concentrations ($\delta^{18}O$), percentage of melting ice (melt %), and sea-salt (Na^+ and Cl^-) and Methanesulfonic acid aerosol concentrations. Varve thickness from four laminated lake sediment records and tree-ring width from 11 sites located along the Arctic Ocean periphery were also included in the network. Documentary sources include the Iceland ice severity index (Wallevik and Sigurjónsson, 1998) and the Barents Sea mean August ice edge position (Vinje, 1999). All proxies have a time resolution better than 5 years (Table 1).

Many of the proxies used represent first-order indicators of air temperature ($\delta^{18}O$, melt %, tree-ring width and varve thickness). However, for $\delta^{18}O$ other factors influence the isotope fractionation process, such as such as the distance to the moisture source and the water temperature at the source (Bradley, 1999). On low-elevation ice caps, the varying distance to the sea ice edge may thus influence the $\delta^{18}O$ of snow (Isaksson et al., 2003; Isaksson et al., 2005b). Ice core sea-salt concentrations have been used as sea ice proxies in the Canadian Arctic, where more open water conditions lead to enhanced production of sea-salt aerosols (sea spray), which are then transported and deposited onto

adjacent ice caps (Grumet et al., 2001; Kinnard et al., 2006b). However in Greenland ice cores, variations in sea-salt concentrations are usually interpreted to reflect changes in atmospheric circulation (Dawson et al., 2003; Fischer and Mieding, 2005). Methanesulfonic acid (MSA), an oxydation by-product of biogenic dimethyl sulfide gas, reflects marine biogenic productivity, which in polar waters is strongly influenced by sea ice coverage. MSA has been used as a sea ice indicator in both the Arctic (Isaksson et al., 2005a; O'Dwyer et al., 2000)and the Antarctic (Curran et al., 2003). The fact that many of these proxies are biased toward the warm season, combined to the strong month-to-month persistence of sea-anomalies (Figure 6.2) make the proxy network a good candidate for capturing past August sea ice extent .

As an integral component of the global climate system, sea ice is strongly coupled with changes in climate at various timescales (Mysak and Venegas, 1998; Overland et al., 2004b; Polyakov and Johnson, 2000; Venegas and Mysak, 2000). In this study we exploit this coupling by reconstructing sea ice extent history using a combination of proxies which may be directly linked with sea ice conditions (sea salt aerosols, $\delta^{18}O$, MSA), as well as proxies for climate variables known to both drive, and respond to, sea ice variability, such as air temperature and atmospheric circulation. The recent sea ice response to changing air temperature and atmospheric circulation is well documented (Deser and Teng, 2008; Deser et al., 2000; Rigor et al., 2002; Zhang et al., 2000). The strong correlation found between the percentage of melting ice in an ice core from Devon ice cap and sea ice coverage in the surrounding Queen Elizabeth Island (Koerner, 1977) is an example of indirect sea ice proxy arising from common thermal forcing. Trees along

the boreal treeline have the same potential to exhibit a common response with sea ice to climate forcing.

Because sea ice strongly modulates the exchange of heat between the ocean and the atmosphere, changes in sea ice coverage feed back on surface air temperature and pressure patterns. A recent modelling experiment showed that simulated events of rapid sea ice loss generated a warming signal that penetrated 1500 km inland and lasted throughout the year (Lawrence et al., 2008). The strong horizontal temperature gradient at the sea ice margin also favours the development of cyclones, so that changes in ice extent influence the intensity and location of storm tracks (Hakkinen et al., 2008; Serreze et al., 1997; Singarayer et al., 2006). The proxy network used in this study offers the potential to capture past coupled climate and sea ice variability trough direct proxy connections, as well as via forcing and feedback relationships.

6.3. EXPLORATORY DATA ANALYSIS

An empirical orthogonal function (EOF) analysis (e.g. Peixoto and Oort, 1992) was first performed on the proxy network, in order to identify the dominant modes of co-variability amongst the proxies. The number of available proxies in the network increases with time (Figure 6.2) but begins to decrease after 1969. EOF was first applied on the proxies over their full overlapping period, 1844-1969, and an Expectation-Maximization algorithm (EOF-EM, Beckers and Rixen, 2003) was used to fill the missing proxy values before the 1995 endpoint. In the EOF-EM algorithm, missing values in the mean-centered data matrix are first set to zero before applying EOF, and then are iteratively substituted by their predicted values until convergence. The first two EOF components were found to be significantly different than noise and were retained for analysis and prediction of

missing values. The EOF-EM method estimates missing values in proxy series terminating before 1995 based on their mutual covariance with the other available proxy data over the period 1844-1995. This approach is similar to the regularized EM algorithm (RegEM, Schneider, 2001) used to infill proxy networks in previous paleoclimate studies (Mann et al., 2008; Rutherford et al., 2005).

6.4. RECONSTRUCTION METHODS

We used partial least-square (PLS) regression (e.g. Geladi and Kowalski, 1986; Naes et al., 2004) to calibrate the proxy network against modern sea ice observations. PLS is a multivariate regression method commonly used in analytical chemistry (Wold et al., 2001). PLS iteratively creates orthogonal scores, also called latent vectors or components, which are linear combinations of the predictor variable (the proxies) and have maximum covariance with the predictand vector (sea ice extent). A small number of PLS scores is usually retained and used to model the predictand using least-square regression. We used the NIPALS algorithm, in which PLS components are calculated one component at a time, after the previous component has been removed from the data (deflation step). While the final prediction is based on a linear combination of the proxies such as in multiple ordinary linear regression (MOLS), the PLS weights themselves are *not* determined linearly, but rather in latent variables space. PLS is ideally suited to deal with a large number of predictor variables suffering from strong collinearity and irregular spatial distribution. Spatially-clustered and/or collinear variables are grouped within the same score vector, whose rank depends solely on its covariance with the predictand. PLS is similar to principal component regression (PCR), which has been used in several paleoclimate reconstruction studies (Cook et al., 1994; Luterbacher et al., 2004;

Luterbacher et al., 2002; Mann et al., 1998; Pauling et al., 2006). However for prediction purpose PLS is a more flexible approach, because scores are calculated and ranked according to their covariance with the predictand, as opposed to PCR scores which are determined solely from the covariance between the predictors.

The number of PLS scores retained for prediction determines the model's dimensionality and must be carefully chosen so as to avoid under-, or over-fitting. Traditionally, the number of PLS components is chosen so as to minimize the prediction error, estimated by cross-validation techniques (Naes et al., 2004). In this work the number of PLS components was chosen by sequentially testing, at each deflation step, the statistical significance of the covariance between the (deflated) ice extent series and each PLS component using Monte Carlo noise simulations (see detailed method section). Surrogate noise series were created by randomizing the Fourier phases of the ice extent series and then applying the inverse Fourier transform. These surrogate series then have similar statistical properties than the original one, but their ordering is destroyed (Davison and Hinkley, 1997, p. 408). At each deflation step in the NIPALS algorithm the observed covariance and RE statistic were compared to their null distribution obtained from the noise simulation, and consecutive significant components ($p<0.05$) were retained in the model.

The shortness of the calibration interval prohibits the discarding of data for independent, external verification. Instead, we used a Monte-Carlo cross-validation procedure to test the predictive skill of the reconstruction models (Bürger, 2007; Xu and Liang, 2001). The ice extent series and proxy matrix were randomly split in a calibration subset of length 2/3N and a verification subset of length 1/3N, where N = 96, the total

number years in the calibration interval. This approach was preferred to using a single (Rutherford et al, 2005) or two alternate (Mann et al, 2008) test subsets, as the choice of one particular subset is hard to justify and the derived skill diagnostics prone to significant variability (Burger, 2007). Separate PLS models were built for each calibration subset and the reconstruction skill was estimated from the verification subset (see detailed methods). The statistical significance of the reconstruction was determined by Monte Carlo simulation, using the phase scrambling procedure previously described.

The full calibration interval 1900-1995 was used to calibrate the final model following cross-validation. Proxies with a resolution larger than one year were interpolated to annual resolution. Proxies showing pronounced skewness (>1) in their distribution were transformed to approximately normal distributions using the Box-Cox transformation (Wilks, 1995, p. 37). Both the proxies and the ice extent series were centered to have zero mean over the 1900-1995 calibration interval, and the proxies were further standardized to unit variance over the same period. We used a 'stepwise' calibration approach (Luterbacher et al, 2004; Mann et al, 2008), in which new PLS models are constructed as an increasing number of proxies becomes available with time (Figure 6.3). Forty-nine different models were calibrated and tested. As in previous climate reconstructions, it is implicitly assumed that the relationship between ice extent and the proxies is stationary over the reconstruction period (Jones and Mann, 2004). Confidence intervals (95 %) around predicted values were calculated as twice the average root-mean-squared error (RMSE) derived from Monte Carlo cross-validation.

6.5. RESULTS

6.5.1. EOF analysis

Two EOF components were found to differ significantly from noise ($p<0.01$, Figure 6.4). The first principal component time series (PC1) appears to capture a temperature signal (Figure 6.5a). The PC1 index matches quite well the annual temperature composite from Arctic coastal weather stations (Polyakov et al., 2003b), with a gradual warming trend during the early 20th century, the characteristic pronounced warming of the 1920-40s, cooling in 1940-70, and a stabilization and slight warming afterward. Eigenvector ('loading') maps were plotted for PC1 by proxy type (Figure 6.6). Most ice core $\delta^{18}O$ records have strong positive loadings, except for central Greenland, Mt Logan and Penny ice cap which have loadings around zero. The fact that high-altitude sites have small loadings implies that PC1 is a surface-based temperature signal, while the poor correlation between PC1 and the Penny $\delta^{18}O$ record may be due to the climatic influence of the cold south flowing Baffin Current on the ice cap. Ice core melt % records are all loaded positively on the PC1 index. These results are consistent with our interpretation of PC1 as a temperature signal, with glacier melting increasing, and $\delta^{18}O$ becoming less negative, with increasing air temperature. The low-frequency oscillation (LFO, Polyakov et al, 2003b) seen in both the PC1 and observed composite coastal temperature record points to a significant influence of oceanic processes, from which the higher altitudes sites of central Greenland are mostly immune. Polyakov et al (2004) have shown that during the positive phase of the LFO, there are increased advection of warm air as well as intrusion of warm Atlantic water farther into the Eastern Arctic.

Tree-ring width records, as well as three out of four lake sediment records (varve thickness), are also loaded positively on PC1. This is consistent with the documented increase in high-latitude tree growth and larger discharge and sediment delivery to lake catchment in response to warming temperature (D'Arrigo and Jacoby, 1993; Hughen et al., 2000). The Icelandic sea ice severity (Kock) index is negatively loaded, which means that there is less ice along the coast under warmer conditions, while the historical ice edge latitudinal position in the Barents Sea is positively loaded, also signifying ice retreat. The loading map for ice core sea-salt aerosol concentrations shows strong positive loadings in the eastern Arctic, negative loadings in Greenland, and positive loadings for the Davis Strait region. Variations in sea-salt concentration on Mt Logan relate to atmospheric circulation in the Pacific (Yan et al., 2005). Fischer (2001) also found that the main source for sea salt aerosols in Northern Greenland was from the Pacific Ocean. Grumet et al (2001) found that on Penny ice cap sea-salt concentration increase in response to reduced ice extent in Baffin Bay, but also in response to increased transport under a more positive NAO index. Ice caps in the Eurasian Arctic are primarily influenced by climate variability in the North Atlantic region, with greater sea-salt deposition occurring when there is increased northward penetration of cyclones from the Atlantic Ocean (Henderson, 2002; Kekonen et al., 2005; Opel et al., 2009).

MSA records are all loaded negatively on PC1. The relationship between MSA records and climate variables is not consistent: MSA in southern Greenland was found to be weakly inversely correlated with sea surface temperature (SST) (Whung et al., 1994), while in Svalbard MSA was associated with higher SST and decreased sea ice extent (O'Dwyer et al., 2000).

The low-frequency oscillation (LFO, Polyakov et al, 2003b) seen in both the PC1 and observed composite coastal temperature record points to a significant influence of oceanic processes, from which the higher altitudes sites of central Greenland are mostly immune. Overall the loading maps for EOF1 suggest an almost Arctic-wide warming pattern, with slightly enhanced warming in the eastern Arctic. This is consistent with increased heat advection from the North Atlantic area during the positive phase of the LFO and associated AO circulation indices (Polyakov et al., 2004; Polyakov et al., 2003b; Polyakov and Johnson, 2000). During the positive phase of the LFO and AO, there is increasing penetration of air masses from the North Atlantic region, which brings warm air and draw warm Atlantic water into the Eastern Arctic. In its negative phase, the Icelandic cyclone is weakened while the Beaufort anticyclone strengthens, increasing the influence of the North Pacific region on Arctic climate. The contrasting pattern of sea-salt deposition on ice caps reflects this oscillation in atmospheric mass, with increased (decreased) transport of marine aerosols to the eastern (western) Arctic during the positive (negative) phase of the oscillation.

The PC2 index (Figure 6.5b) exhibits relatively small variations before an abrupt and continuous decrease beginning in the 1950s. PC2 is compared with the total August Arctic ice extent series from the WC dataset, with early missing values in-filled by the EOF-EM method, as well as the same curve but with ice extent in the Russian Arctic replaced by the Polyakov et al (2003a) data. The two records (PC2 and ice extent) show good similarity, exhibiting a similar post-1950 downward trend. However, the correspondence between higher-frequency variations is not as good. Nonetheless, we propose that PC2 represents a coupled Arctic climate and sea ice signal. The loading

maps for PC2 (Figure 6.7) show more complicated patterns than for PC1. Ice core $\delta^{18}O$ loadings are small in the eastern Arctic and large in central-north Greenland and the Baffin Bay area. An interesting dipole occurs between Ellesmere Island and NW Greenland which may be related to the contrasting sea ice and climate regimes in that region (Barber et al., 2001). No consistent pattern emerges from the melt % loading map, with melting inversely related with PC2 in Baffin Bay, southern Greenland and Svalbard, but positively loaded in Davis Strait and the Kara / Laptev Seas. Reduced summer ice extent may increase or decrease glacier melting through different processes. More open water around ice caps may cause melting by increasing liquid precipitation or by enhancing storms bringing warm air, but may also suppress melt due to increased cloudiness or increase snow precipitation, which raises the surface albedo (Alt, 1987).

The sea-salt map shows a similar pattern than PC1: positive loadings in the western Arctic, negative over Greenland and positive in the eastern Canadian Arctic. The loadings are positive for the Devon and Penny ice cap. Hence the inverse relationship found between ice core sea salt concentration and local sea ice conditions at these two sites is not reflected on a hemispheric scale (Grumet et al., 2001; Kinnard et al., 2006b). This may be explained by the different seasonal response of sea-salt deposition to local sea-ice conditions and transport efficiency. On Devon ice cap increased sea-salt deposition occurs with reduced sea-ice concentration in northern Baffin Bay during the fall, while on Penny ice cap sea-salt variations were found to relate to sea-ice extent in Davis Strait during the spring. Hence the varying sea ice cover exerts a control on sea-spray production and the delivery of sea salt aerosols to surrounding ice caps only during periods of the year when sea ice is intermittently present or absent around the ice caps.

During the past 25 years, sea-ice was almost absent from Baffin Bay and Davis Strait in late August, so that the varying amount of open water during that time is not expected to directly influence the amount of sea-salts deposited on these ice caps. As in Baffin Bay, the positive correlation between PC2 and sea-salt records from the low-elevations Eurasian ice caps implies that a coupling between atmospheric circulation and sea ice extent, rather than the varying fraction of open water, is responsible for the reduced sea-salt delivery which parallels the ice extent decrease after ~1950. The sea-salt loading pattern may reflect the enhancement, from retreating sea ice, of the circulation pattern depicted by the EOF1 loading map, i.e., the northward displacement of storm tracks whose location partly depend on the strong temperature gradient at the ice edge (Serreze et al., 1997).

MSA shows a positive relationship with PC2 in central and southern Greenland, which corroborates previous findings of a positive relationship between MSA and sea ice at this location (Legrand et al., 1997). The relationship is negative in Svalbard, as reported by O'Dwyer et al (2000). All but one tree-ring records with large loadings are positive, which implies a cooling effect along the coast due to retreating sea ice. Lake records are all negatively loaded, which means that less sea ice is associated with larger runoff and sediment fluxes to lake catchments. This may occurs because of and increase in precipitation in response to decreased sea-ice extent (Kattsov and Walsh, 2000), or from enhanced snow and glacier melting in the lake catchment (Moore et al., 2001). The latitude of the sea ice edge in the Barents Sea increases (sea ice retreats) when PC2 decreases, but oddly, the Kock ice severity index decreases when PC2 increases. Sea ice conditions on the North coast of Iceland is influenced by ice drift from the Greenland

Sea, which is not necessarily following the trend in total ice extent. It was found previously that while Arctic sea-ice extent decreases as a whole when the AO/NAO is more positive (Rigor et al., 2002), there is also larger ice export south through Fram Strait (Kwok, 2000).

Overall there are no consistent loading patterns associated with our postulated coupled sea ice - climate proxy PC2. This does not mean that PC2 is not capturing a sea ice signal, since there was no a priory expected relationship between the *hemispheric* ice extent and the local proxies. The relationship between each proxy and the coupled climate - sea ice variability may be strongly site-specific, depending in part on the *local* ice extent anomaly and associated climate drivers and feedbacks.

The EOF analysis has shown that the proxy network contains two dominant and independent climate signals: the first one representing an Arctic wide temperature signal, and the second one, possibly, a coupled sea ice and climate signal. Because the number of proxies decreases back in time, a multivariate calibration between the proxy network and sea ice is a more promising approach for extracting the sea ice signal among the available proxies.

6.5.2. Sea ice extent reconstruction

Figure 6.8 presents the observed and reconstructed Arctic summer sea ice extent history back to 1128 AD, when the reconstruction began to fail the verification test. The reconstructed sea ice history shows a period of decreased ice extent during the early millennia, a broadly warmer climate period known as the Medieval Warm Period (MWP, e.g. Jones and Mann, 2004). The confidence interval is wide during that period, due to the restricted number of available proxies. Prolonged periods of increased ice extent are

apparent during the period 1450-1550 AD, as well as during the mid-17th century. Other punctual increases are seen throughout the record such as during the early to mid 19th century. The most striking feature of the reconstruction is the abrupt and sustained decrease in ice extent observed during the second half of the 20th century, which breached the 95% confidence interval of the MWP in 1985. This agrees with previous conclusions based on fingerprinting methods that the human influence on Arctic sea ice is detectable from the early 1990s onwards (Min et al., 2008).

The reconstruction is also punctuated by sharp increases and decreases in ice extent, on the order of 1×10^6 km^2 per decade, such as observed during the late 17th century. The magnitude of these episodes is similar to the abrupt ice extent reductions modeled by Holland et al (2006) for the 21st century. The late 20th century decline is occurring at a similar rate, although the decrease has been exceptionally sustained for the last ~50 years. The abrupt fluctuations seen in the reconstruction suggest the presence of non-linear feedbacks acting to rapidly increase / decrease ice extent in the Arctic. Holland et al (2006) suggested that such abrupt reductions predominantly result from thermodynamic processes involving a non-linear relationship between ice thinning and open water formation, and ice-albedo feedbacks. In their model, abrupt ice retreat events occurred when ocean heat transport to the Arctic increased.

6.6. TIME-FREQUENCY CHANGES IN ARCTIC ICE EXTENT

Previous studies have found that the Arctic climate system is dominated by a decadal-scale oscillation associated with the Arctic Oscillation, an index of the strength of the polar vortex, and another multi-decadal oscillation (LFO) (Delworth and Mann, 2000; Polyakov and Johnson, 2000; Venegas and Mysak, 2000). Part of the late 20th century

sea ice retreat has been associated with a sustained positive phase of the AO (Deser et al, 2002) and LFO (Polyakov and Johnson, 2000), but the AO index has gone back to a more neutral state since the mid 1990s while sea ice has continued to shrink dramatically, suggesting a growing influence of GHG-induced warming on the sea ice decline (Deser and Teng, 2008; Overland and Wang, 2005). Polyakov et al (2003a, 2004) found that during the last century the Arctic air-ice-ocean system exhibited coherent fluctuations on a multidecadal scale that could be part of an internal feedback loop. The LFO may be the manifestation of an oscillatory mode known as the Atlantic Multidecadal Oscillation (AMO), which appears to be driven by variations in the thermohaline circulation (Kerr, 2000; Polyakov et al., 2003b). The short period of climate observations (~100 years), however, makes it hard to assess the significance of the LFO.

The reconstructed Arctic sea ice extent was examined for the presence of significant cycles associated with known circulation modes such as the AO and LFO / AMO. The continuous wavelet spectrum (Figure 6.9) of the reconstructed ice extent shows multiple decadal and bi-decadal fluctuations over time. A broad band of increased power also occurs throughout the record at multidecadal timescales. In the early part of the record this band is centered at a period of ~30-60 years, but shifts to a shorter period during the 20th century (~25-35 years). However, the oscillation is only distinguishable from red noise around 1700 AD and during the 20th century. Interestingly, significant power occurs in all frequencies between 5-50 years during the 20th century. Hence the decadal behaviour observed in modern sea ice observations (e.g. Yi et al, 1999; Venegas and Mysak, 2000) and model simulations (Holland et al, 2001) is seen to persist throughout the reconstruction period, although intermittently. The presence of a clear

LFO signal remains ambiguous, as the observed low-frequency spectral peak is barely distinguishable from red noise.

6.7. CLIMATE CONTROL ON LONG-TERM SEA ICE VARIABILITY

In figure 6.10 the reconstructed ice extent history is compared to recent reconstructions of NH (Mann et al, 2008) and Arctic (Overpeck et al, 1997) surface air temperature histories as well as reconstructions of the summer AO (D'Arrigo et al., 2003) and winter NAO (Cook et al, 2002) index variations. During winter the AO and NAO are almost undistinguishable, while in summer the NAO is confined to the North Atlantic region. These reconstructions allow us to examine the influence of past thermodynamic (temperature) and dynamic (circulation) factors on sea ice extent. The reconstructed Arctic temperature history shows increased variance compared to NH temperatures, reflecting polar amplification of climate variability (Serreze and Francis, 2006). Long-term trends in both sea ice extent and temperature are similar, showing a gradual cooling / increased ice extent over the last millennia and warming / decreased ice extent during the industrial era (> 1850 AD). However, the correspondence between these variables is not obvious at centennial timescales. The same conclusion applies to the correspondence between sea ice extent and the circulation indices. The summer AO index corresponds well with the reconstructed Arctic temperature, suggesting that much of the variability in Arctic temperature arises from meridional heat advection during the positive AO phase. The previously recognized negative correlation between modern ice extent observations and the NAO/AO index (e.g. Deser et al, 2000; Dickson et al, 2000; Rigor et al, 2002) is not readily apparent from these data.

The correlation coefficient between NH temperature and ice extent is -0.47 over the full reconstruction period (-0.50 when both series are detrended with a 2nd order polynomial). The correlations between sea ice extent and the reconstructed summer AO and NAO indices are -0.10 and -0.04, respectively, and are not significantly different from zero. Several factors may explain the poor correlation between ice extent and the proxy climate drivers:

(1) While we would expect a strong correlation between sea ice volume and temperature, sea ice extent is not a good proxy for ice volume. Several non-linear relationships involving ice thickness must control the ice extent–temperature relationship (e.g. Holland et al, 2006).

(2) Dynamic and thermodynamic forcing associated with the AO/NAO variability is mostly apparent during winter (Deser et al, 2000). A more positive NAO/AO index is associated with a weakening of the Beaufort surface anticyclone and an intensification of the cyclonic circulation in the eastern Arctic Ocean. This leads to an intensification of the transpolar drift, increased ice export through Fram Strait, decreased ice concentration and thickness in the eastern Arctic, and increased concentration and thickness in the western Arctic (Zhang et al, 2000, Polyakov et al, 2004). This alternation between cyclonic-anticyclonic wind circulation regimes appears to drive a significant part of the variability in Arctic winter sea ice conditions on a decadal timescale (Polyakov and Johnson, 2000; Proshutinsky and Johnson, 1997). Summer ice conditions appear to be primarily driven by thermodynamic forcing, but with a significant 'preconditioning effect' inherited from atmospheric circulation variability during the previous winter and spring (Deser et al,

2000; Rigor et al, 2002). Hence the relationship between summer ice conditions and atmospheric circulation, strongest in winter, may be non-linear.

(3) While good correlations have been found between the NAO/AO index, sea ice extent, and ice export through Fram Strait since the late 1970s, the relationship is weaker in earlier periods (Cavalieri, 2002). The non-steady relationship between the NAO and other climate variables was also recently pointed out by Polyakova et al (2006). Hence indices such as the AO and NAO may not be ideal indicators of the complex spatio-temporal changes in atmospheric circulation (Cavalieri, 2002). An alternative hypothesis is simply that sea ice does not respond in a consistent way to circulation changes. The sea ice cover may become more responsive to wind forcing as climate warms and the ice cover becomes thinner and looser (Hakkinen et al, 2008).

6.8. Conclusions

The reconstructed Arctic summer extent shows that the pronounced late 20th century ice extent retreat is unprecedented for at least the last 900 years. It remains to be seen whether sea ice may have been more restricted during the early MWP (800-1100 AD) as compared to the reconstructed extent during the late MWP (1100-1300 AD). Ice extent shows periods of abrupt retreat and expansion similar to those simulated by models, and which point at the presence of non-linear processes governing ice extent variability.

Based on the evidence presented here, past sea ice extent shows a moderate response to past temperature variations, and no response to reconstructed atmospheric circulation indices. This again suggests that non-linear processes are responsible for much of the variability in ice extent over the past millennium, and that the same processes may be enhancing the GHG-induced decrease in ice extent currently observed.

Table 6.1. List of proxies used in the sea ice reconstruction

No.	Lat. (°)	Long. (°)	dT (yr)	T start (yr)	T range (yr)	Site name	Location	Type
1	78.0	30.0	5	1997	416	August ice extent	Barent Sea	Documentary
2	65.8	-18.7	1	1990	891	Kock Index	Iceland	Documentary
3	81.0	64.0	1	1996	772	Windy Dome	Franz Joseph Land	Ice core Cl^-
4	79.8	24.0	5	1981	756	Austfonna	Svalbard	Ice core Cl^-
5	67.2	-65.5	1	1990	655	Penny	Baffin Is.	Ice core melt %
6	80.8	-72.8	1	1971	1368	Agassiz	Ellesmere Is.	Ice core melt %
7	78.4	-80.4	1	2002	1003	Prince-of-Wales	Ellesmere Is.	Ice core melt %
8	81.0	64.0	1	1996	772	Windy Dome	Franz Joseph Land	Ice core melt %
9	66.9	-46.3	1	1989	444	site J	Greenland	Ice core melt %
10	80.5	94.8	3	1998	274	Akademii Nauk	Severnaya-Zemlya	Ice core melt %
11	79.8	24.0	5	1985	756	Austfonna	Svalbard	Ice core melt %
12	67.2	-65.5	1	1991	198	Penny	Baffin Is.	Ice core MSA
13	65.1	-44.9	1	1984	217	20D	Greenland	Ice core MSA
14	75.1	-42.3	1	1997	1811	NGRIP	Greenland	Ice core MSA
15	79.8	24.0	5	1997	695	Austfonna	Svalbard	Ice core MSA
16	78.9	17.4	5	1996	876	Lomonosofonna	Svalbard	Ice core MSA
17	67.2	-65.5	5	1994	1000	Penny	Baffin Is.	Ice core Na^+
18	75.3	-81.6	5	1997	1005	Devon	Devon Is.	Ice core Na^+
19	81.0	64.0	5	1996	770	Windy Dome	Franz Joseph Land	Ice core Na^+
20	65.1	-44.9	1	1984	218	20D	Greenland	Ice core Na^+
21	73.9	-37.6	3	1992	513	B16	Greenland	Ice core Na^+
22	76.6	-36.4	3	1992	550	B18	Greenland	Ice core Na^+
23	78.8	-36.5	1	1993	928	B20	Greenland	Ice core Na^+
24	80.0	-41.1	3	1992	596	B21	Greenland	Ice core Na^+
25	72.6	-38.5	3	1985	1248	GISP2	Greenland	Ice core Na^+
26	75.1	-42.3	1	1997	1811	NGRIP	Greenland	Ice core Na^+
27	80.5	94.8	3	1998	274	Akademii Nauk	Severnaya-Zemlya	Ice core Na^+
28	79.8	24.0	5	1998	696	Austfonna	Svalbard	Ice core Na^+
29	78.9	17.4	5	1996	876	Lomonosofonna	Svalbard	Ice core Na^+
30	60.5	139.5	1	2001	992	Eclipse	Yukon	Ice core Na^+
31	60.6	-140.5	1	2000	1441	Mt Logan	Yukon	Ice core Na^+
32	67.2	-65.5	5	1992	1271	Penny	Baffin Is.	Ice core $\delta^{18}O$
33	75.3	-81.6	5	1994	1981	Devon	Devon Is.	Ice core $\delta^{18}O$
34	80.8	-72.8	5	1987	2511	Agassiz	Ellesmere Is.	Ice core $\delta^{18}O$
35	78.4	-80.4	5	2002	2121	Prince-of-Wales	Ellesmere Is.	Ice core $\delta^{18}O$
36	81.0	64.0	1	1996	772	Windy Dome	Franz Joseph Land	Ice core $\delta^{18}O$
37	65.1	-44.9	1	1984	218	20D	Greenland	Ice core $\delta^{18}O$
38	73.9	-37.6	1	1992	515	B16	Greenland	Ice core $\delta^{18}O$
39	76.6	-36.4	1	1992	1122	B18	Greenland	Ice core $\delta^{18}O$
40	80.0	-41.1	1	1993	597	B21	Greenland	Ice core $\delta^{18}O$

41	77.3	-49.2	1	1994	493	B26	Greenland	Ice core $\delta^{18}O$
42	77.2	-61.1	1	1975	734	Camp Century	Greenland	Ice core $\delta^{18}O$
43	71.1	-37.3	1	1974	1422	Crete	Greenland	Ice core $\delta^{18}O$
44	66.5	-46.3	1	1974	233	Dye 2	Greenland	Ice core $\delta^{18}O$
45	65.2	-43.8	1	1979	2080	Dye 3	Greenland	Ice core $\delta^{18}O$
46	72.6	-38.5	1	1987	1170	GISP2	Greenland	Ice core $\delta^{18}O$
47	75.1	-42.3	1	1996	1810	NGRIP	Greenland	Ice core $\delta^{18}O$
48	71.3	-26.7	1	1986	808	Renland	Greenland	Ice core $\delta^{18}O$
49	70.6	-35.8	1	1984	363	Site A	Greenland	Ice core $\delta^{18}O$
50	80.5	94.8	3	1998	287	Akademii Nauk	Severnaya-Zemlya	Ice core $\delta^{18}O$
51	79.8	24.0	5	1998	719	Austfonna	Svalbard	Ice core $\delta^{18}O$
52	78.9	17.4	5	1996	597	Lomonosofonna	Svalbard	Ice core $\delta^{18}O$
53	60.6	-140.5	1	1999	1441	Mt Logan	Yulon	Ice core $\delta^{18}O$
54	64.4	-61.2	1	1992	1241	Donard	Baffin Is.	Lake varve t
55	62.6	-69.5	1	1992	479	Soper	Baffin Is.	Lake varve t
56	75.6	-89.3	1	1993	151	DV09	Devon Is.	Lake varve t
57	81.3	-69.5	1	1969	957	Murray	Ellesmere Is.	Lake varve t
58	-150.9	68.8	1	2000	704	NW North Alaska	Alaska	Tree ring w
59	-165.9	65.3	1	2002	863	Seward	Alaska	Tree ring w
60	13.7	64.0	1	1978	639	Jaemtland	Central Norway	Tree ring w
61	-62.5	57.6	1	2001	432	Labrador	Labrador	Tree ring w
62	-112.4	65.4	1	2003	716	Central NWT	NWT	Tree ring w
63	66.0	67.7	1	1996	1053	Polar Urals	Russia	Tree ring w
64	100.6	72.7	1	1997	1243	Taymir	Russia	Tree ring w
65	142.1	70.3	1	1994	653	Yakutia	Russia	Tree ring w
66	-137.6	67.9	1	2002	826	Yukon	Yukon	Tree ring w
67	27.1	69.2	1	1980	1234	Tornetraesk	N. Scandinavia	Tree ring w
68	68.8	15.7	1	1994	637	Forfjorddalen	NW Norway	Tree ring w

References (by site number):
(1) Vinje, 1999; (2) Wallevik and Sigurjónsson, 1998; (3, 8, 19, 36) Henderson, 2002; (4, 15, 28, 51) Motoyama et al., 2001; (5) Fisher, 2002; (6, 34) Fisher et al., 1994; (7) Kinnard et al., 2008b; (9) Kameda et al., 1995; (10, 50) Opel et al, 2009; (11, 27) Tarussov, 1992; (12) K. Goto-Azuma, pers. comm.; (13) Whung et al., 1994; (14, 26, 47) Andersen et al., 2005; (16) Isaksson et al., 2005a; (17, 32) Fisher et al., 1998; (18, 33) Kinnard et al, 2006b; (20) Yan et al., 2005; (21-24) Fischer and Mieding, 2005; (25) Mayewski et al., 1993; (29) Kekonen et al., 2005; (30) Wake et al., 2002; (31, 53) Fisher et al., 2008; (35) This study, unpublished; (37, 42-46, 49) Fisher et al., 1996; (38-41) Fischer et al., 1998; (48) Vinther et al., 2008; (51-52) Isakkson et al, 2005b; (54) Moore et al., 2001; (55) Hughen et al., 2001; (56) Gajewski et al., 1997; (57) Besonen et al., 2008; (58-66) D'Arrigo et al., 2006; (67) Grudd, 2007(Grudd, 2008); (68) Kirchhefer, 2001

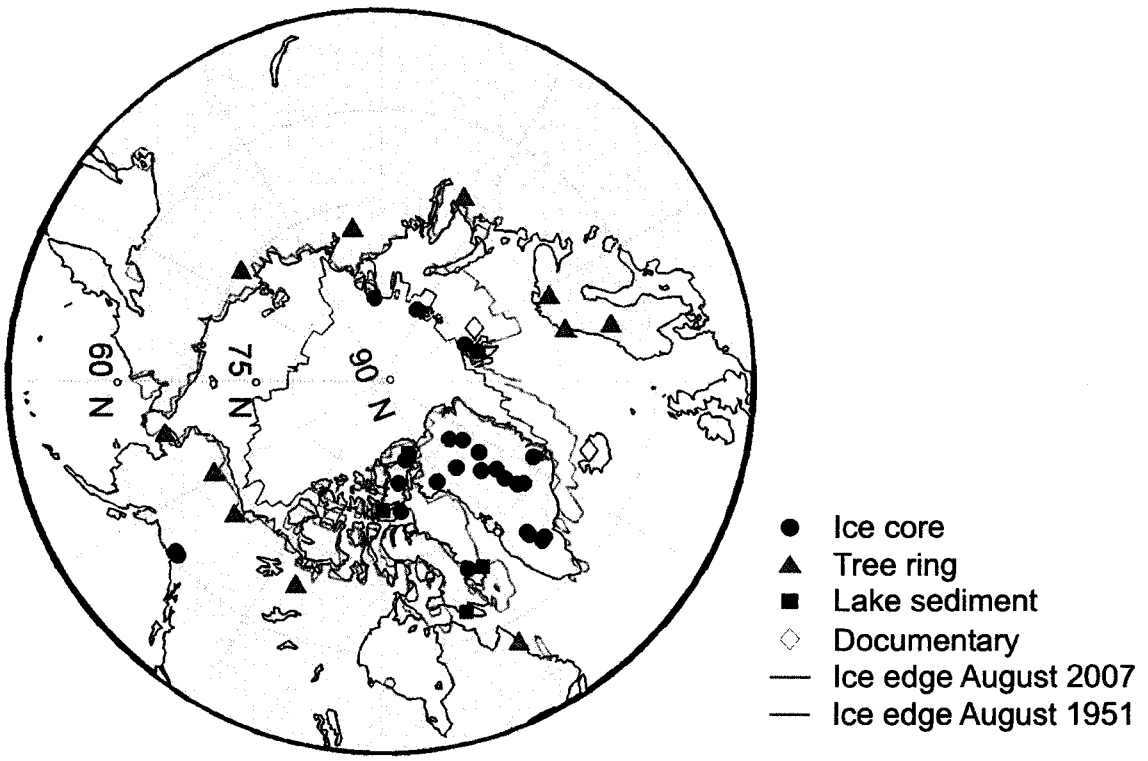

Figure 6.1. Proxy network map. The ice edge for the year of minimum (2007, red) and maximum (1951, blue) ice extent is shown.

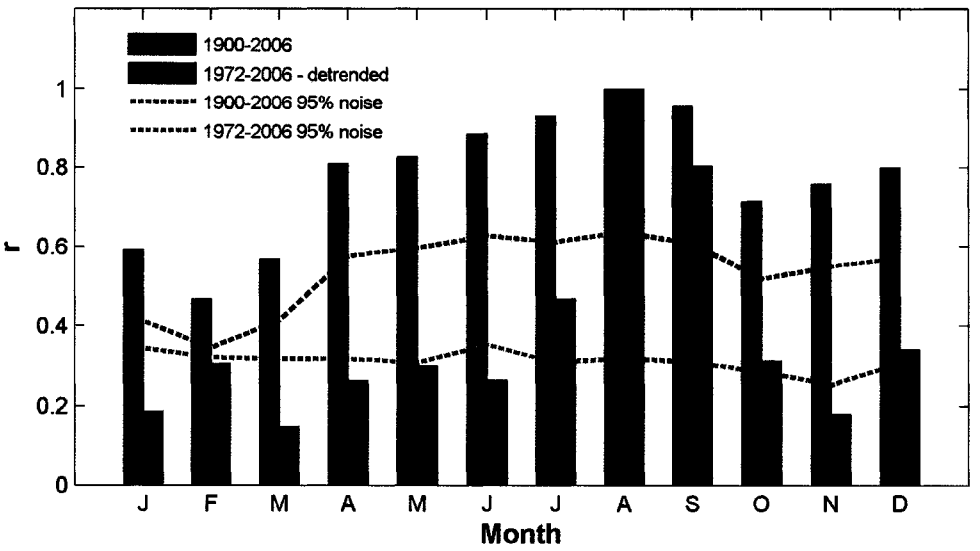

Figure 6.2. Persistence of monthly ice extent anomalies, measured by correlation between August ice extent and ice extent in other months. Blue: 1900-2006; Red: satellite era 1972-2006 with linear trend removed. Stippled lines indicate the 95% confidence level for correlation from Monte Carlo noise simulations.

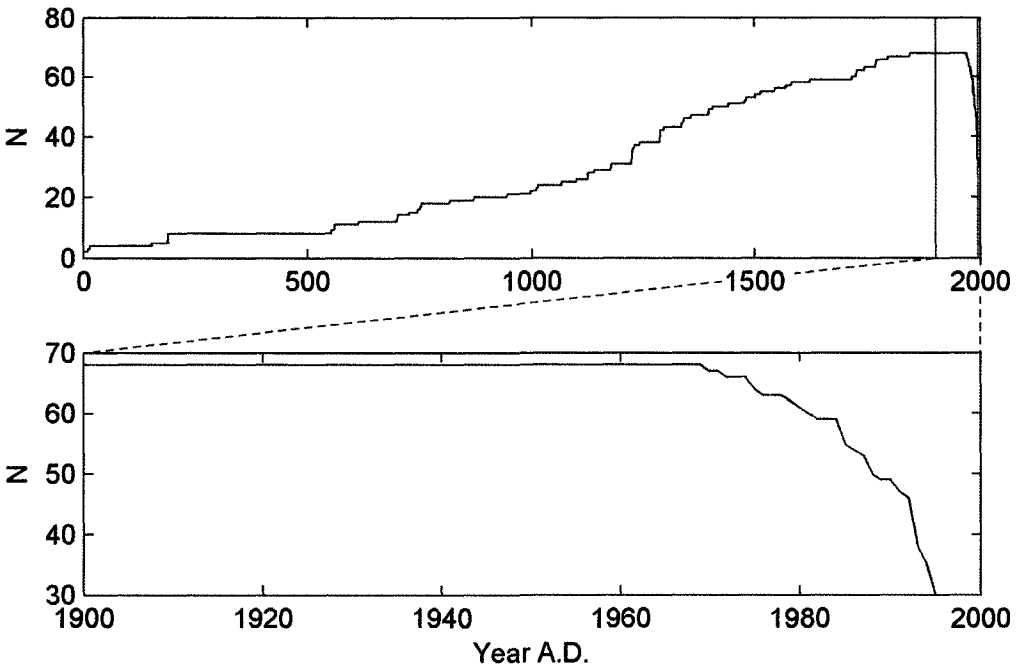

Figure 6.3. Number of proxies available from present to year 0 A.D. The red box delineates the calibration interval 1900-1995.

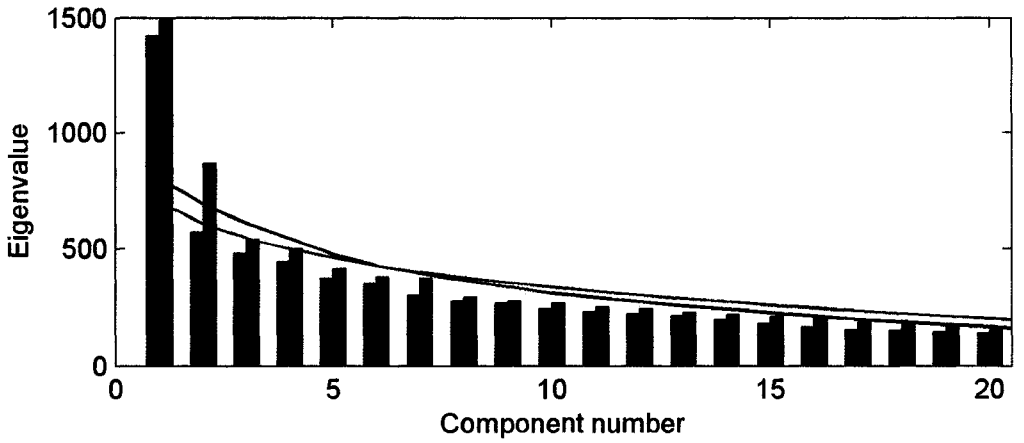

Figure 6.4. Eigenvalue spectrum of proxy network for the restricted period 1843-1969 when all proxies are available (blue bars) and for the extended period 1843-1995 (red bars) during which missing values were inputted by the EOF-EM procedure. Colored lines are the respective 95% significance levels derived from Monte Carlo noise simulations.

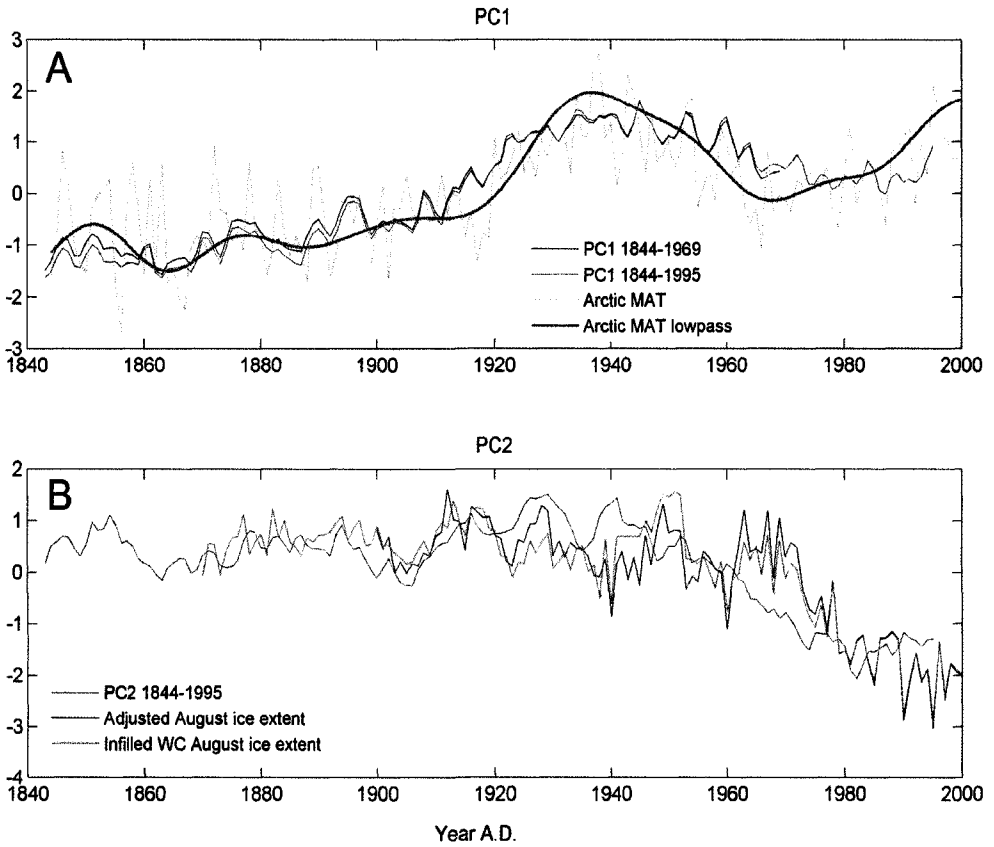

Figure 6.5. (A) Proxy network PC1 for period of full data coverage 1844-1969 (blue) and extended period 1844-1995 (red). Stippled green line: mean annual Arctic SAT from Polyakov et al (2003b), with 20 year low-pass smooth (thick green line). (B) Proxy network PC2 for period 1844-1995 (pink). Blue: Walsh and Chapman (WC) August ice extent 1901-1995 with Polyakov et al (2003a) Russian Arctic sea ice extent included; Green: WC August ice extent with missing data in early record in-filled by EOF-EM.

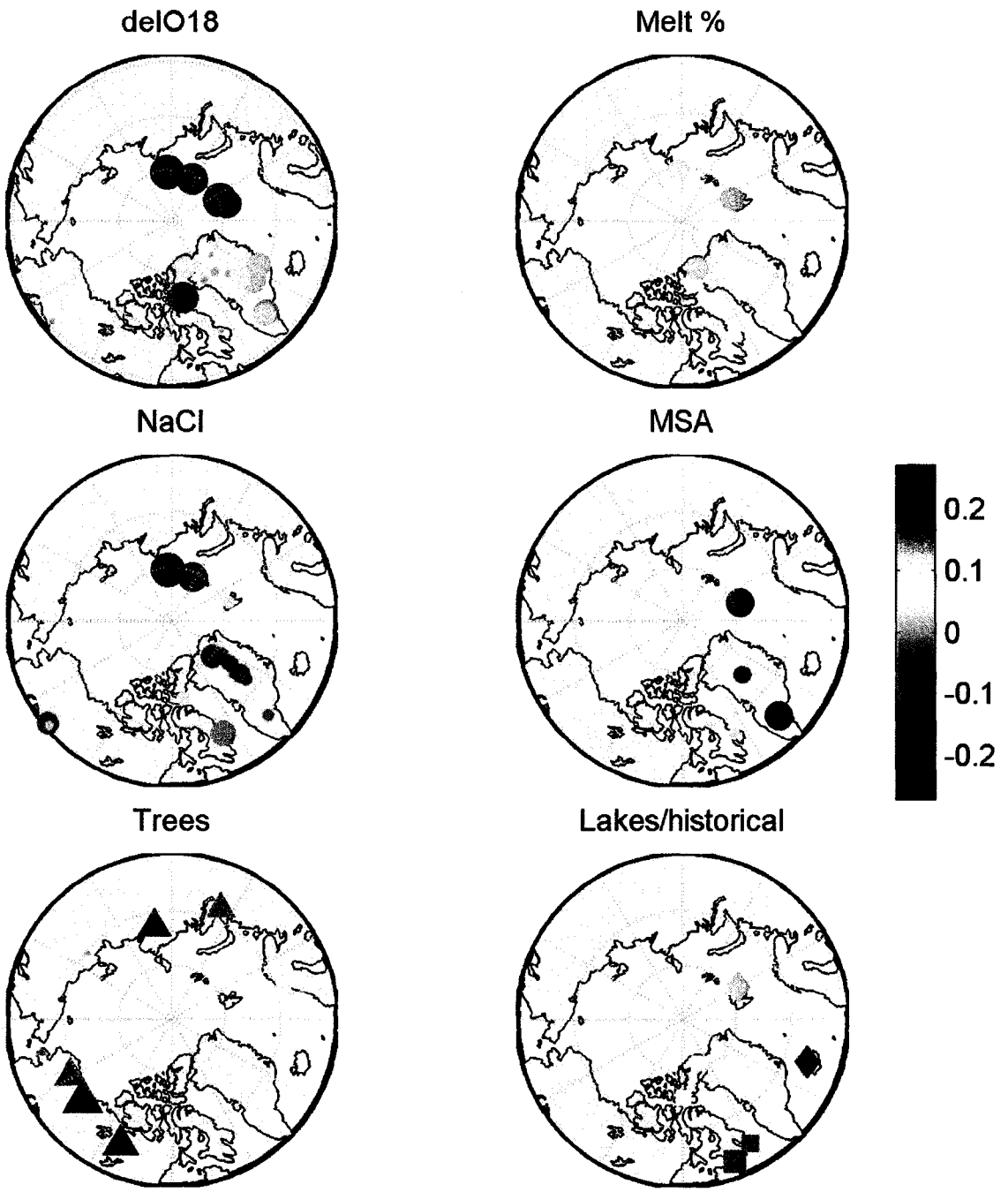

Figure 6.6. PC1 Loading maps by proxy type. Circles: ice core records; triangles: tree-ring records; squares: lake records; diamonds: historical sea ice records.

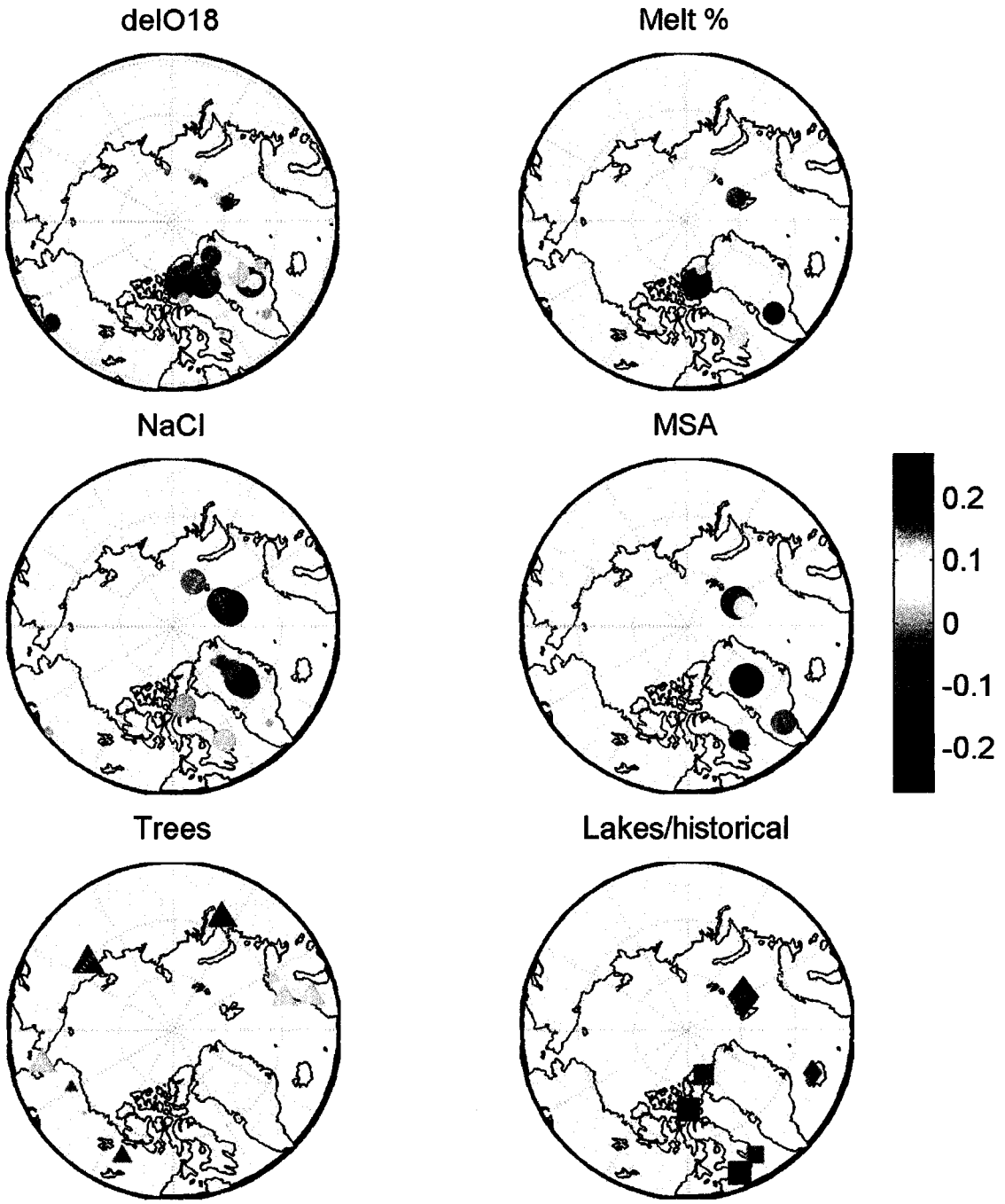

Figure 6.7. Same as Figure 6.6 but for PC2.

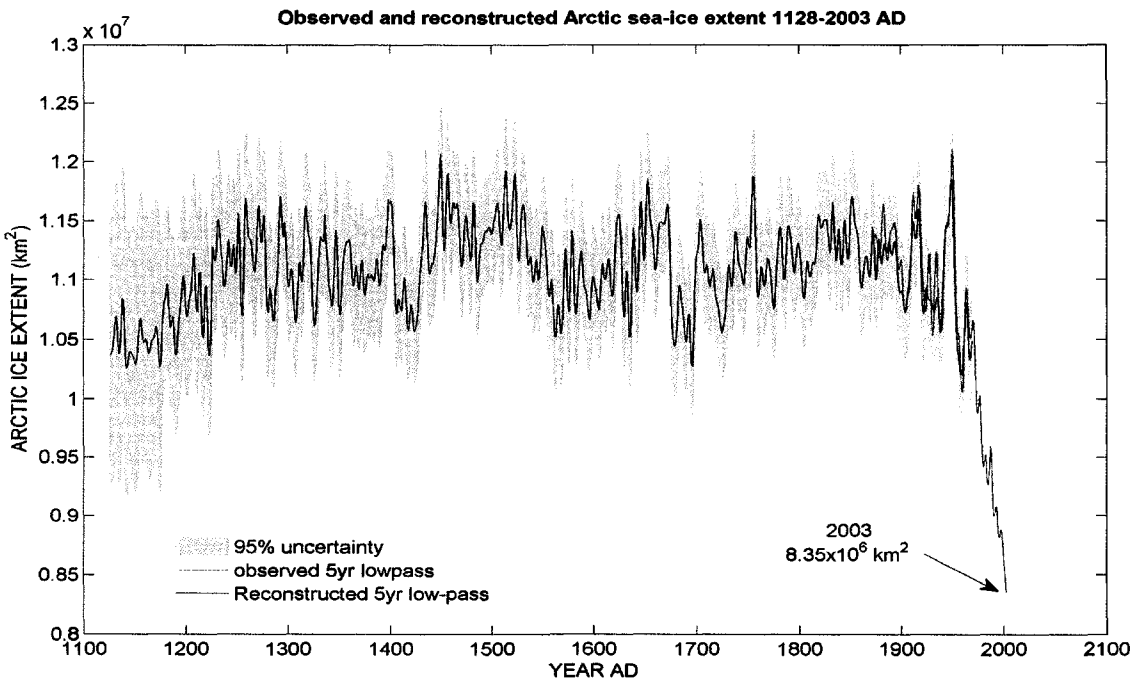

Figure 6.8. Observed (1870-2003, red) and reconstructed (1128-1995 AD) Arctic August ice extent.

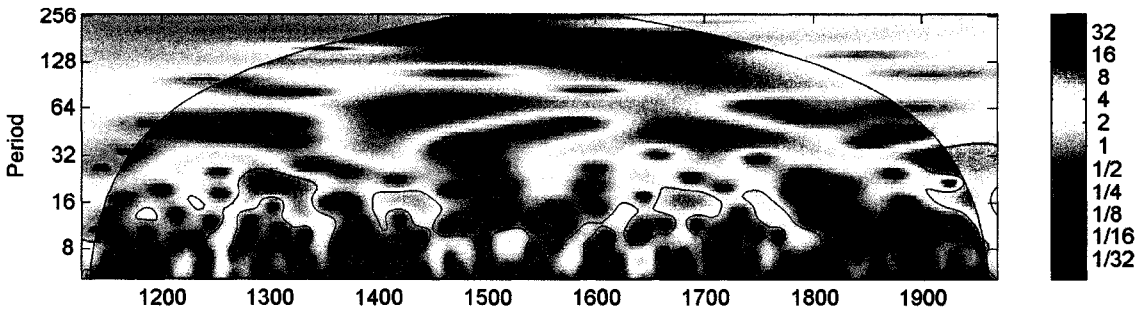

Figure 6.9. Continuous wavelet power spectrum for reconstructed sea ice extent.

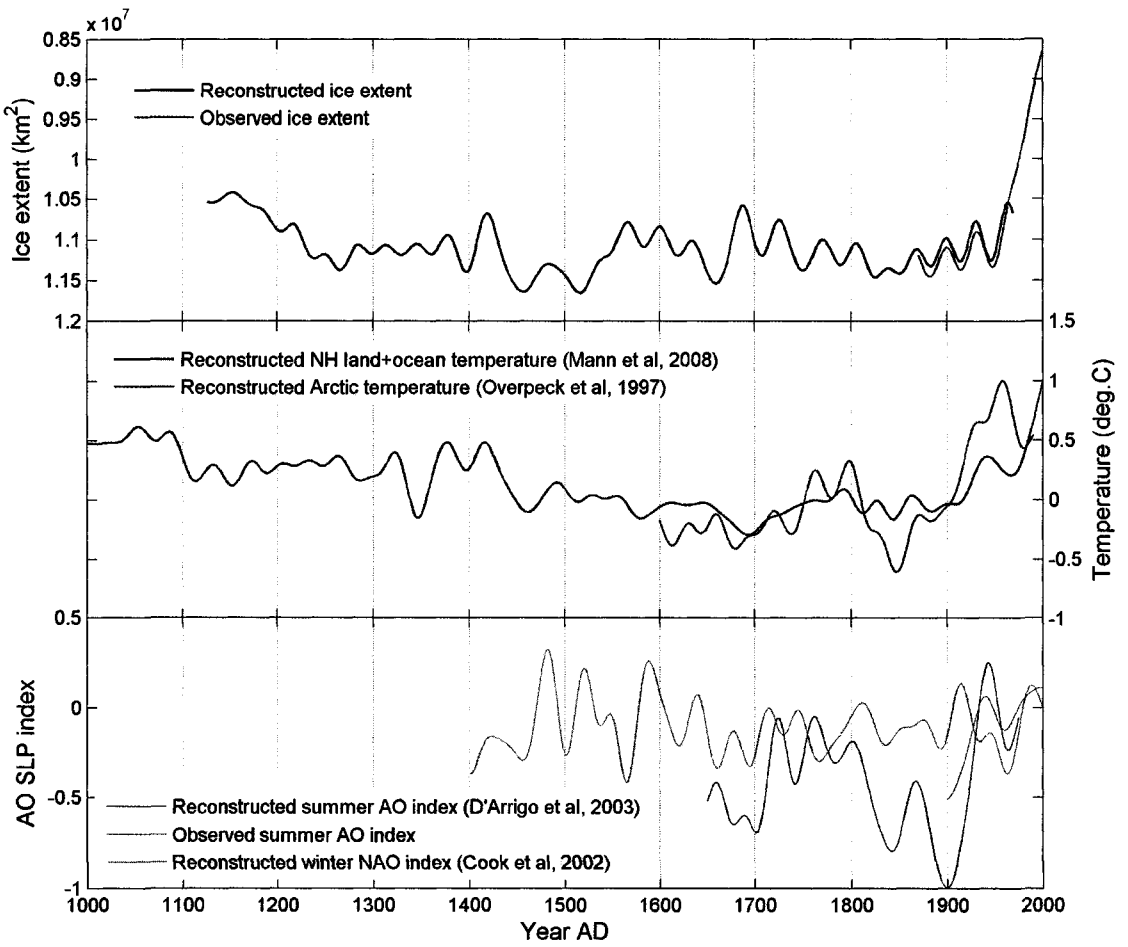

Figure 6.10. (A) Reconstructed (black) and observed (red) inverted sea ice extent record; (B) NH (blue) and Arctic (magenta) temperature reconstructions (Mann et al, 2008; Overpeck et al, 1997). (C) Observed (red) and reconstructed (blue) summer Arctic Oscillation index (D'Arrigo et al, 2003), and reconstructed winter North Atlantic Oscillation index (Cook et al, 2002). All series are 40 year low-pass filtered.

CHAPTER 7. SUMMARY AND CONCLUSIONS

7.1. INTRODUCTION

This dissertation contributes to our understanding of the coupled climate and sea ice variability in the Arctic. The Arctic climate is a complex system, in which multiple interactions and feedbacks take place between the ocean, atmosphere and cryosphere and give rise to climate variability on multiple time scales. The prospect of global warming from anthropogenic greenhouse gas emissions and its impact on the cryosphere has put the Arctic at the forefront of the climate science community. This stimulated a strong impetus for Arctic climate research over the last few decades, which led to the realization that the Arctic is not a stable climatic region as was often perceived before. Yet, there is still much to be learned about the long-term, 'natural' behavior of Arctic climate variability and its contribution to global climate change. This dissertation has put an emphasis on the coupling between climate and sea ice. Sea ice is the most dynamic feature of the last few decades in the Arctic, and its current retreat may be one of the strongest signs of human-induced climate warming. The main drivers of the recent sea ice decline, as well as the effect of sea ice variability on Arctic and global climate are the focus of intense research. This dissertation has made use of modern, historical, and proxy climate observations in order to push further our understanding of the climate-sea ice system variability.

7.2. SUMMARY OF MAJOR FINDINGS

The Arctic sea ice cover is in a state of profound change. The ice extent has decreased by 4% per decade over the past 30 years, with dramatic reductions of over 20% since 2002

(e.g. Parkinson and Cavalieri, 2008). The disappearing sea ice is causing the loss of natural habitats, the opening of new shipping routes, and the amplification of global warming due to a decreased Earth albedo. This dissertation has examined both recent (1900-2005) and long-term (last 1000 years) sea ice and climate variability using available remotely-sensed and historical sea ice observations, and trough the use of high-resolution climate and sea ice sensitive proxies from glacier ice cores, tree-rings and lake sediments.

The influence of climate variability on sea ice conditions in the Canadian Arctic was investigated by comparing detailed operational sea ice charts with surface climate observations for the past 25 years. Coherent patterns of sea ice variability were identified, and related to climate variables such as air and sea surface temperature, air pressure patterns, and winds. Ice extent in the Canadian Arctic was found to respond primarily to large-scale atmospheric circulation changes associated with the NAO and ENSO. The influence of these phenomena makes it difficult to detect meaningful trends in short records.

The varying extent of seasonal ice (i.e. that forms in winter but melts in summer) was studied using historical observations since 1870 AD. Results show that sea ice is retreating faster during summer than winter, and that the thick, 'perennial' ice cover (i.e. ice that survives summer melt) is being progressively replaced by seasonal ice. The increasing rate in seasonal ice formation over the last few decades matches that predicted by the last IPCC AR4 ensemble model simulations forced by 'worst-type' GHG emission scenarios. The accentuated sea ice freeze-thaw cycle releases more salt into the ocean, which could intensify the vertical mixing of water over shallow continental shelves, and

could strengthen the global thermohaline circulation. Hence it is hypothesized that the increasingly seasonal nature of Arctic sea ice cover will increase the contribution of Arctic Ocean waters to the global thermohaline circulation.

Sea ice conditions in the Baffin Bay region were reconstructed using an ice core sea salt record from the nearby Devon ice cap. A significant negative correlation was found between sea ice extent in Baffin Bay and the annual concentration of sea salts measured in the ice core. This is consistent with the hypothesis that more open water leads to an increased production of sea spray aerosols, which are deposited onto nearby ice caps. The reconstructed sea ice history-was compared to the ice core melt layer and $\delta^{18}O$ isotope records, both temperature proxies. The 200 year-long reconstruction suggests that sea ice concentration changes in Baffin Bay are not driven by temperature variability, but by wind fluctuations, which advect ice from the Arctic Ocean trough Nares Strait and into Baffin Bay. Open water conditions in Baffin Bay are favored when Nares Strait is congested with ice, thus blocking further influx of ice from the Arctic Ocean, and when northerly winds are pushing the ice from Baffin Bay southward. Because of these processes, variations of ice conditions in Baffin Bay may differ from the hemispheric trend.

Melt layers in ice cores are formed by seasonal melting of snow at the ice cap surface, followed by percolation and refreezing at depth. Here, a new method was developed which uses digital ice core image analysis to automatically identify these melt layers. The method was used to derive a 1000 year-long summer warmth proxy record from a new ice core drilled trough the Prince of Wales (POW) icefield on Ellesmere Island. Comparison of this new record with other Arctic melt layer records underscores

the unique character of the POW climate, which is partly controlled by the dynamics of the North Open Water Polynya, a large expense of perennially open water in Northern Baffin Bay. The POW icefield coring site also rests on the boundary between the maritime climate of Baffin Bay, and the drier, colder climate of the High Arctic (QEI). Migrations of this climatic boundary over time may explain the local nature of the POW melt history, which differs markedly from the other Arctic records. The POW melt and $\delta^{18}O$ records are strongly related with the second dominant mode of variability identified in a network of 68 sea ice-sensitive Arctic climate proxies, and which is interpreted as a pan-Arctic sea ice signal. This is in agreement with our interpretation that sea ice cover in the NOW polynya is exerting an important climatic control on the icefield.

The variability in Arctic-wide minimum (August) ice extent was reconstructed using multivariate statistical calibration the aforementioned network of sea ice proxies of against a century-long historical sea ice record. The reconstruction shows that the minimum summer ice extent observed during the last two decades is unprecedented in the last 900 years. While the general ice decline since the end of the Little Ice Age (~1850 AD) follows the temperature rise observed in previous NH temperature reconstructions, the connection between longer-term sea ice variability and reconstructed NH temperature history is weak. Reconstructions of atmospheric circulations indices, which are known to influence modern sea ice variability, show no clear relationships with the reconstructed sea ice history. Hence, we hypothesize that much of the natural sea ice variability arises from complex non-linear feedbacks mechanisms, which may be also enhancing the current GHG-induced sea ice decline.

7.3. FUTURE RESEARCH

The network of sea ice/climate proxies developed in this dissertation represents a rich source of Arctic paleoclimate data. However as shown in our EOF analysis (chapter 6), only a few dominant modes of variability stand out, which is probably due to the large amount of noise present in each of the proxy time series. One of the biggest challenges in terms of calibrating the proxies against modern observations is the dating error. The ice core records affected by melting are the worst in this respect. Hence, there is a need to improve the time scales of ice core records in the Canadian Arctic over the last 1000 years. While many records contained details at the annual to sub-annual resolution, their dating accuracy is often questionable, and limits any calibration attempts. Fine-tuning the existing records with the well-dated Greenland records over the last one to two millennia would represent a worthwhile effort.

The hemispheric sea ice dataset used for calibrating the proxy network suffers from important data quality issues in the early 20th century. Over the past years a few new datasets have been produced, especially for the Russian Arctic. An important step would be to merge these new data sources into an up-to-date and optimal pan Arctic dataset. In this study, a first step in this direction was made by incorporating ice extent information from the new Russian dataset (Polyakov et al, 2003b) into the well established dataset of Walsh and Chapman (2001), but there are still concerns that the early 20th century data are not entirely reliable. For the purpose of calibration against proxies, a longer and more realistic sea ice extent index could be created using optimal interpolation of missing values from available data, as is often done for other climatic parameters.

Lastly, the updated proxy network could be analyzed in order to derive a longer Arctic temperature history, which could then be compared against our sea ice reconstruction and NH temperature reconstructions. This could help to elucidate the role of sea ice in the polar amplification of climate change.

REFERENCES

Aagaard, K., and Carmack, E.C., 1989, The Role of Sea Ice and Other Fresh Water in the Arctic Circulation: Journal of Geophysical Research, v. 94, p. 14,485–14,498.

Aagaard, K., Fahrbach, E., Meincke, J., and Swift, J.H., 1991, Saline Outflow From the Arctic Ocean: Its Contribution to the Deep Waters of the Greenland, Norwegian, and Iceland Seas: Journal of Geophysical Research, v. 96, p. 20433-20441

Aagaard, K., Swift, J.H., and Carmack, E.C., 1985, Thermohaline Circulation in the Arctic Mediterranean Seas: J. Geophys. Res., v. 90, p. 4833-4846

Aagaard, K., and Woodgate, R.A., 2001, Some thoughts on the freezing and melting of sea ice and their effects on the ocean: Ocean Modelling, v. 3, p. 127-135.

ACIA, 2005, Arctic Climate Impact Assessment, Cambridge University Press, p. 1042 p.

Agnew, T., Alt, B., De Abreau, R., and Jeffers, S., 2001, The loss of decade old sea ice plugs in the Canadian Arctic Islands, Polar Meteorology and Oceanography Conference: San Diego, American Meteorological Society, p. 3.

Agnew, T., and Howell, S., 2003, The use of operational ice charts for evaluating passive microwave ice concentration data: Atmosphere - Ocean, v. 41, p. 317-331.

Alley, R.B., Shuman, C.A., Meese, D.A., Gow, A.J., Taylor, K.C., Cuffey, K.M., Fitzpatrick, J.J., Grootes, P.M., Zielinski, G.A., Ram, M., Spinelli, G., and Elder, B., 1997, Visual-stratigraphic dating of the GISP2 ice core: basis, reproducibility, and application: Journal of Geophysical Research, v. 102, p. 26367-26381.

Alt, B.T., 1987, Developing synoptic analogs for extreme mass balance conditions on Queen Elizabeth Island ice caps: Journal of Climate & Applied Meteorology, v. 26, p. 1605-1623.

Andersen, K.K., Siggaard-Andersen, M.-L., Clausen, H.B., Hansson, M., Strømfeldt, T.E., Steffensen, J.P., and Johnsen, S.J., 2005, A multi-proxy record of Greenland climate variability over the past two thousand years: Geophysical Research Abstracts, v. 7.

Aristarain, A.J., and Delmas, R.J., 2002, Snow chemistry measurements on James Ross Island (Antarctic Peninsula) showing sea-salt aerosol modifications: Atmospheric Environment, v. 36, p. 765-772.

Aristarain, A.J., Delmas, R.J., and Stievenard, M., 2004, Ice-core study of the link between sea-salt aerosol, sea-ice cover and climate in the Antarctic Peninsula area: Climatic Change, v. 67, p. 63-86.

Barber, D.G., Hanesiak, J.M., Chan, W., and Piwowar, J., 2001, Sea-ice and meteorological conditions in northern Baffin Bay and the North Water Polynya between 1979 and 1996: Atmosphere - Ocean, v. 39, p. 343-359.

Barnett, T., Zwiers, F., Hegerl, G., Allen, M., Crowley, T., Gillett, N., Hasselmann, K., Jones, P., Santer, B., Schnur, R., Stott, P., Taylor, K., and Tett, S., 2005, Detecting and attributing external influences on the climate system: A review of recent advances: Journal of Climate, v. 18, p. 1291-1314.

Barnston, A.G., and Livezey, R.E., 1987, Classification, seasonality and persistence of low-frequency atmospheric circulation patterns: Monthly Weather Review, v. 115, p. 1083-1126.

Barrie, L., 1985, Atmospheric particles: Their physical and chemical characteristics, and deposition processes relevant to the chemical composition of glaciers: Ann. Glaciol, v. 7, p. 100–108.

Barry, R.G., Bradley, R., and Jacobs, J.D., 1975, Synoptic climatology studies of the baffin island area, *in* Weller, G., and Bowling, S.A., eds., Climate of the Arctic: Fairbanks, Geophysical Institute of the University of Alaska, p. 82-90.

Beckers, J., and Rixen, M., 2003, EOF Calculations and Data Filling from Incomplete Oceanographic Datasets: Journal of Atmospheric and Oceanic Technology, v. 20, p. 1839-1856.

Belchansky, G., Douglas, D., and Platonov, N., 2004, Duration of the Arctic Sea Ice Melt Season: Regional and Interannual Variability, 1979–2001: Journal of Climate, v. 17, p. 67-80.

Belt, S., Massé, G., Rowland, S., Poulin, M., Michel, C., and LeBlanc, B., 2007, A novel chemical fossil of palaeo sea ice: IP25: Organic Geochemistry, v. 38, p. 16-27.

Besonen, M.R., Patridge, W., Bradley, R.S., Francus, P., Stoner, J.S., and Abbott, M.B., 2008, A record of climate over the last millennium based on varved lake sediments from the Canadian High Arctic: The Holocene, v. 18, p. 169.

Blanchard, D., and Woodcock, A., 1980, The production, concentration, and vertical distribution of the sea-salt aerosol: Annals of The New York Academy of Sciences, v. 338, p. 330-347.

Bohren, C.F., and Barkstrom, B.R., 1974, Theory of the Optical Properties of Snow: J. Geophys. Res., v. 79.

Bradley, R., 1996, Are There Optimum Sites for Global Paleotemperature Reconstruction?: NATO ASI Series I Global Environmental Change, v. 41, p. 603-624.

Bradley, R.S., 1999, Paleoclimatology–reconstructing climates of the Quaternary. Vol 64 of International Geophysics Series, Academic Press, San Diego, USA.

Bradley, R.S., Hughes, M.K., and Diaz, H.F., 2003, Climate in Medieval Time: Science, v. 302, p. 404-405.

Bretherton, C., Widmann, M., Dymnikov, V., Wallace, J., and Bladé, I., 1999, The Effective Number of Spatial Degrees of Freedom of a Time-Varying Field: Journal of Climate, v. 12, p. 1990-2009.

Bürger, G., 2007, On the verification of climate reconstructions: Climate of the Past v. 3, p. 397-409.

Cavalieri, D.J., 2002, A link between Fram Strait sea ice export and atmospheric planetary wave phase: Geophysical Research Letters, v. 29.

Cavalieri, D.J., Gloersen, P., Parkinson, C.L., Comiso, J.C., and Zwally, H.J., 1997, Observed hemispheric asymmetry in global sea ice changes: Science, v. 278, p. 1104-1106.

Cavalieri, D.J., Parkinson, C.L., Gloersen, P., Comiso, J.C., and Zwally, H.J., 1999, Deriving long-term time series of sea ice cover from satellite passive-microwave multisensor data sets: Journal of Geophysical Research C: Oceans, v. 104, p. 15803-15814.

Cavalieri, D.J., Parkinson, C.L., and Vinnikov, K.Y., 2003, 30-year satellite record reveals contrasting Arctic and Antarctic decadal sea ice variability: Geophysical Research Letters, v. 30.

Cho, S., Haralick, R., and Yi, S., 1989, Improvement of kittler and illingworth's minimum error thresholding: Pattern Recognition, v. 22, p. 609-617.

Comiso, J.C., 2002, A rapidly declining perennial sea ice cover in the Arctic: Geophysical Research Letters, v. 29, p. 17-1.

Comiso, J.C., and Nishio, F., 2008, Trends in the sea ice cover using enhanced and compatible AMSR-E, SSM/I, and SMMR data: Journal of Geophysical Research, v. 113.

Comiso, J.C., Parkinson, C.L., Gersten, R., and Stock, L., 2008, Accelerated decline in the Arctic sea ice cover: Geophysical Research Letters, v. 35.

Cook, E., Briffa, K., and Jones, P., 1994, Spatial regression methods in dendroclimatology: A review and comparison of two techniques: International Journal of Climatology, v. 14, p. 379-402.

Cook, E.R., D'Arrigo, R.D., and Mann, M.E., 2002, A well-verified, multiproxy reconstruction of the winter North Atlantic Oscillation index since A.D. 1400: Journal of Climate, v. 15, p. 1754-1764.

Cooper, M.C., 1998, The use of digital image analysis in the study of laminated sediments: Journal of Paleolimnology, v. 19, p. 33-40.

Crocker, G., and Carrieres, T., 2000, Documentation for the Canadian Ice Service Digital Sea Ice Database, p. 49p.

Crowley, T.J., and Lowery, T.S., 2000, How warm was the Medieval Warm Period?: Ambio, v. 29, p. 51-54.

Curran, M.A.J., Van Ommen, T.D., Morgan, V.I., Phillips, K.L., and Palmer, A.S., 2003, Ice Core Evidence for Antarctic Sea Ice Decline since the 1950s: Science, v. 302, p. 1203-1206.

D'Arrigo, R., Cook, E., Mann, M., and Jacoby, G., 2003, Tree-ring reconstructions of temperature and sea-level pressure variability associated with the warm-season Arctic Oscillation since AD 1650: Geophysical Research Letters, v. 30, p. 1549.

D'Arrigo, R., Mashig, E., Frank, D., Wilson, R., and Jacoby, G., 2005, Temperature variability over the past millennium inferred from Northwestern Alaska tree rings: Climate Dynamics, v. 24, p. 227-236.

D'Arrigo, R., Wilson, R., and Jacoby, G., 2006, On the long-term context for late twentieth century warming: Journal of Geophysical Research D: Atmospheres, v. 111.

D'Arrigo, R.D., and Jacoby, G.C., 1993, Secular trends in high northern latitude temperatures reconstructions based on tree rings: Climatic Changes, v. 25, p. 163-177.

Dansgaard, W., and Johnsen, S., 1969, A flow model anda time scaleforthe ice core from Camp Century, Greenland: J. Glaciol, v. 8, p. 215-223.

Davies, T.D., Vincent, C.E., and Brimblecombe, P., 1982, Preferential elution of strong acids from a Norwegian ice cap: Nature, v. 300, p. 161-163.

Davison, A., and Hinkley, D., 1997, Bootstrap methods and their application, Cambridge University Press.

Dawson, A.G., Elliott, L., Mayewski, P., Lockett, P., Noone, S., Hickey, K., Holt, T., Wadhams, P., and Foster, I., 2003, Late-Holocene North Atlantic climate 'seesaws', storminess changes and Greenland ice sheet (GISP2) palaeoclimates: Holocene, v. 13, p. 381-392.

de Vernal, A., Hillaire-Marcel, C., and Darby, D.A., 2005, Variability of sea ice cover in the Chukchi Sea (western Arctic Ocean) during the Holocene: Paleoceanography, v. 20.

Delworth, T., and Mann, M., 2000, Observed and simulated multidecadal variability in the Northern Hemisphere: Climate Dynamics, v. 16, p. 661-676.

Deser, C., Holland, M., Reverdin, G., and Timlin, M., 2002, Decadal variations in Labrador Sea ice cover and North Atlantic sea surface temperatures: Journal of Geophysical Research C: Oceans, v. 107.

Deser, C., and Teng, H., 2008, Evolution of Arctic sea ice concentration trends and the role of atmospheric circulation forcing, 1979-2007: Geophysical Research Letters, v. 35.

Deser, C., Walsh, J.E., and Timlin, M.S., 2000, Arctic sea ice variability in the context of recent atmospheric circulation trends: Journal of Climate, v. 13, p. 617-633.

Dickson, R., Osborn, T., Hurrell, J., Meincke, J., Blindheim, J., Adlandsvik, B., Vinje, T., Alekseev, G., and Maslowski, W., 2000, The Arctic Ocean Response to the North Atlantic Oscillation: Journal of Climate, v. 13, p. 2671-2696.

Divine, D.V., and Dick, C., 2006, Historical variability of sea ice edge position in the Nordic Seas: Journal of Geophysical Research C: Oceans, v. 111.

Domine, F., Albert, M., Huthwelker, T., Jacobi, H.W., Kokhanovsky, A.A., Lehning, M., Picard, G., and Simpson, W.R., 2008, Snow physics as relevant to snow photochemistry: Atmospheric Chemistry and Physics, v. 8, p. 171-208.

Dyke, A., Hooper, J., and Savelle, J., 1996, A history of sea ice in the Canadian Arctic Archipelago based on postglacial remains of the bowhead whale (Balaena mysticetus): Arctic, v. 49, p. 235-255.

England, J.H., Lakeman, T.R., Lemmen, D.S., Bednarski, J.M., Stewart, T.G., and Evans, D.J.A., 2008, A millennial-scale record of Arctic Ocean sea ice variability and the demise of the Ellesmere Island ice shelves: Geophys. Res. Lett., v. 35.

Esper, J., Cook, E.R., and Schweingruber, F.H., 2002, Low-frequency signals in long tree-ring chronologies for reconstructing past temperature variability: Science, v. 295, p. 2250-2253.

Esper, J., Frank, D., and Wilson, R., 2004, Climate Reconstructions: Low-Frequency Ambition and High-Frequency Ratification: EOS Transactions, AGU, v. 85.

Esper, J., Wilson, R.J.S., Frank, D.C., Moberg, A., Wanner, H., and Luterbacher, J., 2005, Climate: Past ranges and future changes: Quaternary Science Reviews, v. 24, p. 2164-2166.

Falkingham, J.C., Chagnon, R., and McCourt, S., 2001, Sea ice in the Canadian Arctic in the 21st Century, The State of the Arctic cryosphere during the extreme warm summer of 1998: documenting cryospheric variability in the Canadian Arctic, CCAF summer 1998 Project Team, CCAF Final Report.

Fang, Z., and Wallace, J.M., 1994, Arctic sea ice variability on a timescale of weeks and its relation to atmospheric forcing: Journal of Climate, v. 7, p. 1897-1914.

Fischer, H., 2001, Imprint of large-scale atmospheric transport patterns on sea-salt records in northern Greenland ice cores: Journal of Geophysical Research D: Atmospheres, v. 106, p. 23977-23984.

Fischer, H., and Mieding, B., 2005, A 1,000-year ice core record of interannual to multidecadal variations in atmospheric circulation over the North Atlantic: Climate Dynamics, v. 25, p. 65-74.

Fischer, H., Werner, M., Wagenbach, D., Schwager, M., Thorsteinnson, T., Wilhelms, F., Kipfstuhl, J., and Sommer, S., 1998, Little Ice Age clearly recorded in northern Greenland ice cores: Geophysical Research Letters, v. 25, p. 1749-1752.

Fisher, D., Dyke, A., Koerner, R., Bourgeois, J., Kinnard, C., Zdanowicz, C., de Vernal, A., Hillaire-Marcel, C., Savelle, J., and Rochon, A., 2006, Natural Variability of Arctic Sea Ice Over the Holocene: EOS Trans. AGU, v. 87, p. 273-275.

Fisher, D., Reeh, N., and Clausen, H., 1985, Stratigraphic noise in time series derived from ice cores: Ann. Glaciol, v. 7, p. 76–83.

Fisher, D.A., 2002, High-resolution multiproxy climatic records from ice cores, tree-rings, corals and documentary sources using eigenvector techniques and maps: Assessment of recovered signal and errors: Holocene, v. 12, p. 401-419.

Fisher, D.A., and Koerner, R.M., 1994, Signal and noise in four ice-core records from the Agassiz Ice Cap, Ellesmere Island, Canada: details of the last millennium for stable isotopes, melt and solid conductivity: Holocene, v. 4, p. 113-120.

Fisher, D.A., Koerner, R.M., Bourgeois, J.C., Zielinski, G., Wake, C., Hammer, C.U., Clausen, H.B., Gundestrup, N., Johnsen, S., and Goto-Azuma, K., 1998, Penny ice cap cores, Baffin Island, Canada, and the Wisconsinan Foxe Dome connection: two states of Hudson Bay ice cover: Science, v. 279, p. 692.

Fisher, D.A., Koerner, R.M., Kuivinen, K., Clausen, H.B., Johnsen, S.J., Steffensen, J.P., Gundestrup, N., and Hammer, C.U., 1996, Intercomparison of Ice Core d 18 O and Precipitation Records from Sites in Canada and Greenland over the last 3500 years and over the last few Centuries in detail using EOF Techniques: Climatic Variations and Forcing Mechanisms of the Last 2000 Years, p. 297–328.

Fisher, D.A., Osterberg, E., Dyke, A., Dahl-Jensen, D., Demuth, M., Zdanowicz, C., Bourgeois, J.C., Koerner, R.M., Mayewski, P.A., and Wake, C., 2008, The Mt Logan Holocene--late Wisconsinan isotope record: tropical Pacific--Yukon connections: The Holocene, v. 18, p. 667.

Fritts, H., 1991, Reconstructing large-scale climatic patterns from tree-ring data, Tucson, AZ (United States); University of Arizona Press.

Gajewski, K., Hamilton, P.B., and McNeely, R., 1997, A high resolution proxy-climate record from an arctic lake with annually-laminated sediments on Devon Island, Nunavut, Canada: Journal of Paleolimnology, v. 17, p. 215-225.

Gardner, A.S., and Sharp, M., 2007, Influence of the Arctic circumpolar vortex on the mass balance of Canadian High Arctic glaciers: Journal of Climate, v. 20, p. 4586-4598.

Geladi, P., and Kowalski, B., 1986, Partial Least Squares: A Tutorial: Analytica Chemica Acta v. 185, p. 1-17.

Gibbons, J., and Chakraborti, S., 2003, Nonparametric Statistical Inference, CRC Press.

Gildor, H., Tziperman, E., Nienow, P.W., Shepherd, J.G., Alley, R.B., Lawton, J.H., Mahadevan, A., and Lenton, T.M., 2003, Sea-ice switches and abrupt climate change: Philosophical Transactions of the Royal Society A: Mathematical, Physical and Engineering Sciences, v. 361, p. 1935-1944.

Gloersen, P., Parkinson, C.L., Cavalieri, D.J., Comiso, J.C., and Zwally, H.J., 1999, Spatial distribution of trends and seasonality in the hemispheric sea ice covers: 1978-1996: Journal of Geophysical Research C: Oceans, v. 104, p. 20827-20835.

Goto-Azuma, K., and Koerner, R.M., 2001, Ice core studies of anthropogenic sulfate and nitrate trends in the Arctic: Journal of Geophysical Research D: Atmospheres, v. 106, p. 4959-4969.

Goto-Azuma, K., Koerner, R.M., and Fisher, D.A., 2002, An ice-core record over the last two centuries from Penny Ice Cap, Baffin Island, Canada: Annals of Glaciology, v. 35, p. 29-35.

Goto-Azuma, K., Koerner, R.M., Nakawo, M., and Kudo, A., 1997, Snow chemistry of Agassiz Ice Cap, Ellesmere Island, Northwest Territories, Canada: Journal of Glaciology, v. 43, p. 199-206.

Gow, A., 1969, On the rates of growth of grains and crystals in south polar firn: J. Glaciol, v. 8, p. 241–252.

—, 1975, Time-Temperature Dependence of Sintering in Perennial Isothermal Snowpacks, *in* Sciences, I.A.o.H., ed., Proceedings of the Grindewald Symposium, AHS Publication No. 114, Volume 114: Gentbrugge, Belgium, p. 25-41.

Gregory, J.M., Stott, P.A., Cresswell, D.J., Rayner, N.A., Gordon, C., and Sexton, D.M.H., 2002, Recent and future changes in Arctic sea ice simulated by the HadCM3 AOGCM: Geophys. Res. Lett., v. 29.

Groisman, P.Y., Karl, T.R., and Knight, R.W., 1994, Observed impact of snow cover on the heat balance and the rise of continental spring temperatures: Science, v. 263, p. 198-200.

Grudd, H., 2008, Torneträsk tree-ring width and density ad 500–2004: a test of climatic sensitivity and a new 1500-year reconstruction of north Fennoscandian summers: Climate Dynamics, v. 31, p. 843-857.

Grumet, N.S., Wake, C.P., Mayewski, P.A., Zielinski, G.A., Whitlow, S.I., Koerner, R.M., Fisher, D.A., and Woollett, J.M., 2001, Variability of sea-ice extent in Baffin Bay over the last millennium: Climatic Change, v. 49, p. 129-145.

Grumet, N.S., Wake, C.P., Zielinski, G.A., Fisher, D., Koerner, R., and Jacobs, J.D., 1998, Preservation of glaciochemical time-series in snow and ice from the Penny Ice Cap, Baffin Island: Geophysical Research Letters, v. 25, p. 357-360.

Hakkinen, S., Proshutinsky, A., and Ashik, I., 2008, Sea ice drift in the Arctic since the 1950s: Geophysical Research Letters, v. 35.

Hammer, C.U., 1980, Acidity of polar ice cores in relation to absolute dating, past volcanism, and radio echoes: Journal of Glaciology, v. 25, p. 359-372.

Hansson, M.E., 1995, Are changes in atmospheric cleansing responsible for observed variations of impurity concentrations in ice cores?: Annals of Glaciology, v. 21, p. 219-224.

Hawley, R.L., and Morris, E.M., 2006, Borehole optical stratigraphy and neutron-scattering density measurements at Summit, Greenland: Journal of Glaciology, v. 52, p. 491-496.

Hawley, R.L., Waddington, E.D., Alley, R.B., and Taylor, K.C., 2003, Annual layers in polar firn detected by Borehole Optical Stratigraphy: Geophysical Research Letters, v. 30.

Hegerl, G.C., Crowley, T.J., Hyde, W.T., and Frame, D.J., 2006, Climate sensitivity constrained by temperature reconstructions over the past seven centuries: Nature, v. 440, p. 1029-1032.

Henderson, K.A., 2002, An ice core paleoclimate study of Windy Dome, Franz Josef Land (Russia): Development of a recent climate history for the Barents Sea: Columbus, Ohio State University.

Herron, M.M., Herron, S.L., and Langway, C.C., 1981, Climatic signal of ice melt features in southern Greenland: Nature, v. 293, p. 389-391.

Holland, M.M., Bitz, C.M., Eby, M., and Weaver, A.J., 2001, The role of ice-ocean interactions in the variability of the North Atlantic thermohaline circulation: Journal of Climate, v. 14, p. 656-675.

Holland, M.M., Bitz, C.M., and Tremblay, B., 2006, Future abrupt reductions in the summer Arctic sea ice: Geophysical Research Letters, v. 33.

Hori, A., Tayuki, K., Narita, H., Hondoh, T., Fujita, S., Kameda, T., Shoji, H., Azuma, N., Kamiyama, K., Fujii, Y., Motoyama, H., and Watanabe, O., 1999, A detailed density profile of the Dome Fuji (Antarctica) shallow ice core by X-ray transmission method: Annals of Glaciology, v. 29, p. 211-214.

Hu, A., Rooth, C., Bleck, R., and Deser, C., 2002, NAO influence on sea ice extent in the Eurasian coastal region: Geophysical Research Letters, v. 29, p. 10-1.

Hughen, K.A., Overpeck, J.T., and Anderson, R.F., 2000, Recent warming in a 500-year palaeotemperature record from varved sediments, Upper Soper Lake, Baffin Island, Canada: Holocene, v. 10, p. 9-19.

Hurrell, J.W., 1995, Decadal trends in the North Atlantic Oscillation: Regional temperatures and precipitation: Science, v. 269, p. 676-679.

Isaksson, E., Hermanson, M., Hicks, S., Igarashi, M., Kamiyama, K., Moore, J., Motoyama, H., Muir, D., Pohjola, V., Vaikmäe, R., van de Wal, R.S.W., and Watanabe, O., 2003, Ice cores from Svalbard - Useful archives of past climate and pollution history: Physics and Chemistry of the Earth, v. 28, p. 1217-1228.

Isaksson, E., Kekonen, T., Moore, J., and Mulvaney, R., 2005a, The methanesulfonic acid (MSA) record in a Svalbard ice core: Annals of Glaciology, v. 42, p. 345-351.

Isaksson, E., Kohler, J., Pohjola, V., Moore, J., Igarashi, M., Karlöf, L., Martma, T., Meijer, H., Motoyama, H., Vaikmäe, R., and Van De Wal, R.S.W., 2005b, Two ice-core δ18O records from Svalbard illustrating climate and sea-ice variability over the last 400 years Holocene, v. 15, p. 501-509.

Jeffers, S., Agnew, T.A., Alt, B.T., de Abreu, R., and McCourt, S., 2001, Investigating the anomalous sea-ice conditions in the Canadian High Arctic (Queen Elizabeth Islands) during summer 1998: Annals of Glaciology, v. 33, p. 507-512.

Jensen, K.G., Kuijpers, A., Koç, N., and Heinemeier, J., 2004, Diatom evidence of hydrographic changes and ice conditions in Igaliku Fjord, South Greenland, during the past 1500 years: Holocene, v. 14, p. 152-164.

Johannessen, O.M., Bengtsson, L., Miles, M.W., Kuzmina, S.I., Semenov, V.A., Alekseev, G.V., Nagurnyi, A.P., Zakharov, V.F., Bobylev, L.P., Pettersson, L.H., Hasselmann, K., and Cattle, H.P., 2004, Arctic climate change: Observed and modelled temperature and sea-ice variability: Tellus, Series A: Dynamic Meteorology and Oceanography, v. 56, p. 559-560.

Johnson, M.A., and Polyakov, I.V., 2001, The Laptev Sea as a source for recent Arctic Ocean salinity changes: Geophysical Research Letters, v. 28, p. 2017-2020.

Jones, P.D., Briffa, K.R., Barnett, T.P., and Tett, S.F.B., 1998, High-resolution palaeoclimatic records for the last millennium: Interpretation, integration and comparison with General Circulation Model control-run temperatures: Holocene, v. 8, p. 455-471.

Jones, P.D., and Mann, M.E., 2004, Climate over past millennia: Reviews of Geophysics, v. 42.

Kaczmarska, M., Isaksson, E., Karlöf, L., Brandt, O., Winther, J.G., Van De Wal, R.S.W., Van Den Broeke, M., and Johnsen, S.J., 2006, Ice core melt features in relation to Antarctic coastal climate: Antarctic Science, v. 18, p. 271-278.

Kalnay, E., Kanamitsu, M., Kistler, R., Collins, W., Deaven, D., Gandin, L., Iredell, M., Saha, S., White, G., Woollen, J., Zhu, Y., Chelliah, M., Ebisuzaki, W., Higgins, W., Janowiak, J., Mo, K.C., Ropelewski, C., Wang, J., Leetmaa, A., Reynolds, R., Jenne, R., and Joseph, D., 1996, The NCEP/NCAR 40-year reanalysis project: Bulletin of the American Meteorological Society, v. 77, p. 437-471.

Kameda, T., Narita, H., Shoji, H., Nishio, F., Fujii, Y., and Watanabe, O., 1995, Melt features in ice cores from Site J, southern Greenland: Some implications for summer climate since AD 1550: Ann. Glaciol, v. 21, p. 51–58.

Kattsov, V., and Walsh, J., 2000, Twentieth-century trends of Arctic precipitation from observational data and a climate model simulation: Journal of Climate, v. 13, p. 1362-1370.

Kawamura, T., 1990, Nondestructive, three-dimensional density measurements of ice core samples by X-ray computed tomography: Journal of Geophysical Research, v. 95.

Keene, W.C., Pszenny, A.A.P., Galloway, J.N., and Hawley, M.E., 1986, Sea-Salt Corrections and Interpretation of Constituent Ratios in Marine Precipitation: J. Geophys. Res., v. 91.

Kekonen, T., Moore, J., Perämäki, P., Mulvaney, R., Isaksson, E., Pohjola, V., and van de Wal, R.S.W., 2005, The 800 year long ion record from the Lomonosovfonna (Svalbard) ice core: Journal of Geophysical Research, v. 110.

Kelly, P., Goodess, C., and Cherry, B., 1987, The interpretation of the Icelandic Sea ice record: Journal of Geophysical Research, v. 92, p. 10835-10844.

Kerr, R.A., 2000, A North Atlantic Climate Pacemaker for the Centuries: Science, v. 288, p. 1984-1985.

Kinnard, C., Zdanowicz, C.M., Fisher, D.A., Alt, B., and McCourt, S., 2006a, Climatic analysis of sea-ice variability in the Canadian Arctic from operational charts, 1980-2004: Annals of Glaciology, v. 44, p. 391-402.

Kinnard, C., Zdanowicz, C.M., Fisher, D.A., and Wake, C.P., 2006b, Calibration of an ice-core glaciochemical (sea-salt) record with sea-ice variability in the Canadian Arctic: Annals of Glaciology, v. 44, p. 383-390.

Kinnard, C., Zdanowicz, C.M., Koerner, R.M., and Fisher, D.A., 2008, A changing Arctic seasonal ice zone: Observations from 1870-2003 and possible oceanographic consequences: Geophysical Research Letters, v. 35.

Kirchhefer, A., 2001, Reconstruction of summer temperatures from tree-rings of Scots pine (Pinus sylvestris L.) in coastal northern Norway: The Holocene, v. 11, p. 41.

Kittler, J., and Illingworth, J., 1986, Minimum error thresholding: Pattern Recognition, v. 19, p. 41-47.

Koerner, R., 1973, The mass balance of the sea ice of the Arctic Ocean: Journal of Glaciology, v. 12, p. 173-185.

Koerner, R., and Fisher, D., 1982, Acid snow in the Canadian high Arctic: Nature, v. 295, p. 137-140.

Koerner, R.M., 1977, Devon island ice cap: Core stratigraphy and paleoclimate: Science, v. 196, p. 15-18.

—, 1997, Some comments on climatic reconstructions from ice cores drilled in areas of high melt: Journal of Glaciology, v. 43, p. 90-97.

Koerner, R.M., and Fisher, D.A., 1990, A record of Holocene summer climate from a Canadian high-Arctic ice core: Nature, v. 343, p. 630-631.

Koerner, R.M., Fisher, D.A., and Goto-Azuma, K., 1999, A 100 year record of ion chemistry from Agassiz Ice Cap Northern Ellesmere Island NWT, Canada: Atmospheric Environment, v. 33, p. 347-357.

Kokhanovsky, A.A., and Zege, E.P., 2004, Scattering optics of snow: Applied Optics, v. 43, p. 1589-1602.

Kwok, R., 2000, Recent changes in Arctic Ocean sea ice motion associated with the North Atlantic Oscillation: Geophysical Research Letters, v. 27, p. 775-778.

Langway, C.C., 1970, Stratigraphic analysis of a deep ice core from Greenland: Special Paper of the Geological Society of America, v. 125, p. 186 p.

Lawrence, D.M., Slater, A.G., Tomas, R.A., Holland, M.M., and Deser, C., 2008, Accelerated Arctic land warming and permafrost degradation during rapid sea ice loss: Geophys. Res. Lett., v. 35.

Legrand, M., Hammer, C., De Angelis, M., Savarino, J., Delmas, R., Clausen, H., and Johnsen, S., 1997, Sulfur-containing species (methanesulfonate and SO 4) over the last climatic cycle in the Greenland Ice Core Project (central Greenland) ice core: Journal of Geophysical Research, v. 102, p. 26-26.

Legrand, M., and Mayewski, P., 1997, Glaciochemistry of polar ice cores: A review: Reviews of Geophysics, v. 35, p. 219-243.

Legrand, M.R., and Delmas, R.J., 1988, Formation of HCl in the Antarctic atmosphere: Journal of Geophysical Research, v. 93, p. 7153-7168.

Levac, E., De Vernal, A., and Blake Jr, W., 2001, Sea-surface conditions in northernmost Baffin Bay during the Holocene: Palynological evidence: Journal of Quaternary Science, v. 16, p. 353-363.

Livezey, R.E., and Chen, W.Y., 1983, Statistical field significance and its determination by Monte Carlo techniques: Monthly Weather Review, v. 111, p. 46-59.

Luterbacher, J., Dietrich, D., Xoplaki, E., Grosjean, M., and Wanner, H., 2004, European Seasonal and Annual Temperature Variability, Trends, and Extremes since 1500: Science, v. 303, p. 1499-1503.

Luterbacher, J., Xoplaki, E., Dietrich, D., Rickli, R., Jacobeit, J., Beck, C., Gyalistras, D., Schmutz, C., and Wanner, H., 2002, Reconstruction of sea level pressure fields over the Eastern North Atlantic and Europe back to 1500: Climate Dynamics, v. 18, p. 545-562.

Macdonald, R., Harner, T., Fyfe, J., Loeng, H., and Weingartner, T., 2003, The Influence of Global Change on Contaminant Pathways to, within, and from the Arctic, *in* Macdonald, R., ed.: Oslo, Arctic Monitoring and Assessment Programme, p. 65.

Macdonald, R.W., and Bewers, J.M., 1996, Contaminants in the arctic marine environment: Priorities for protection: ICES Journal of Marine Science, v. 53, p. 537-563.

Mann, M.E., 2002, Climate reconstruction: The value of multiple proxies: Science, v. 297, p. 1481-1482.

—, 2007, Climate over the past two millennia, Annual Review of Earth and Planetary Sciences, Volume 35, p. 111-136.

—, 2008, Smoothing of climate time series revisited: Geophysical Research Letters, v. 35.

Mann, M.E., Bradley, R.S., and Hughes, M.K., 1998, Global-scale temperature patterns and climate forcing over the past six centuries: Nature, v. 392, p. 779-787.

—, 1999, Northern hemisphere temperatures during the past millennium: Inferences, uncertainties, and limitations: Geophysical Research Letters, v. 26, p. 759-762.

Mann, M.E., and Rutherford, S., 2002, Climate reconstruction using Pseudoproxies: Geophysical Research Letters, v. 29.

Mann, M.E., Rutherford, S., Wahl, E., and Ammann, C., 2005, Testing the fidelity of methods used in proxy-based reconstructions of past climate: Journal of Climate, v. 18, p. 4097-4107.

Mann, M.E., Zhang, Z., Hughes, M.K., Bradley, R.S., Miller, S.K., Rutherford, S., and Ni, F., 2008, Proxy-based reconstructions of hemispheric and global surface temperature variations over the past two millennia: Proceedings of the National Academy of Sciences of the United States of America, v. 105, p. 13252-13257.

Mantua, N., and Hare, S., 2002, The Pacific Decadal Oscillation: Journal of Oceanography, v. 58, p. 35-44.

Marshall, J., Kushnir, Y., Battisti, D., Chang, P., Czaja, A., Dickson, R., Hurrell, J., McCartney, M., Saravanan, R., and Visbeck, M., 2001, North Atlantic climate variability: Phenomena, impacts and mechanisms: International Journal of Climatology, v. 21, p. 1863-1898.

Marshall, S.J., Sharp, M.J., Burgess, D.O., and Anslow, F.S., 2007, Near-surface-temperature lapse rates on the Prince of Wales Icefield, Ellesmere Island, Canada: Implications for regional downscaling of temperature: International Journal of Climatology, v. 27, p. 385-398.

Maslanik, J.A., Fowler, C., Stroeve, J., Drobot, S., Zwally, J., Yi, D., and Emery, W., 2007, A younger, thinner Arctic ice cover: Increased potential for rapid, extensive sea-ice loss: Geophysical Research Letters, v. 34.

Maslanik, J.A., Serreze, M.C., and Agnew, T., 1999, On the record reduction in 1998 Western Arctic sea-ice cover: Geophysical Research Letters, v. 26, p. 1905-1908.

Massé, G., Rowland, S.J., Sicre, M.-A., Jacob, J., Jansen, E., and Belt, S.T., 2008, Abrupt climate changes for Iceland during the last millennium: Evidence from high resolution sea ice reconstructions: Earth and Planetary Science Letters, v. 269, p. 565-569.

Maxwell, J., 1981, Climatic regions of the Canadian Arctic Islands: Arctic, v. 34, p. 225-240.

Mayewski, P.A., Meeker, L.D., Morrison, M.C., Twickler, M.S., Whitlow, S.I., Ferland, K.K., Meese, D.A., Legrand, M.R., and Steffensen, J.P., 1993, Greenland Ice Core "Signal" Characteristics: An Expanded View of Climate Change: Journal of Geophysical Research, v. 98.

Meeker, L., and Mayewski, P., 2002, A 1400-year high-resolution record of atmospheric circulation over the North Atlantic and Asia: The Holocene, v. 12, p. 257.

Meeker, L.D., Mayewski, P.A., and Bloomfield, P., 1995, A new approachto glaciochemical time series analysis, *in* Delmas, R.J., ed., Ice Core Studies of Global Biogeochemical Cycles: Berlin, Springer, p. 383-400.

Meese, D.A., Gow, A.J., Alley, R.B., Zielinski, G.A., Grootes, P.M., Ram, M., Taylor, K.C., Mayewski, P.A., and Bolzan, J.F., 1997, The Greenland Ice Sheet Project 2 depth-age scale: methods and results: Journal of Geophysical Research, v. 102, p. 26411-26423.

Meincke, J., Rudels, B., and Friedrich, H.J., 1997, The Arctic Ocean-Nordic Seas thermohaline system: ICES Journal of Marine Science, v. 54, p. 283-299.

Mellor, M., 1978, Engineering properties of snow: Journal of Glaciology, v. 19, p. 15-66.

Min, S.-K., Zhang, X., Zwiers, F.W., and Agnew, T., 2008, Human influence on Arctic sea ice detectable from early 1990s onwards: Geophys. Res. Lett., v. 35.

Moberg, A., Sonechkin, D.M., Holmgren, K., Datsenko, M.H., and Karle?n, W., 2005, Highly variable Northern Hemisphere temperatures reconstructed from low- and high-resolution proxy data: Nature, v. 433, p. 613-617.

Moore, J.J., Hughen, K.A., Miller, G.H., and Overpeck, J.T., 2001, Little Ice Age recorded in summer temperature reconstruction from varved sediments of Donard Lake, Baffin Island, Canada: Journal of Paleolimnology, v. 25, p. 503-517.

Morison, J., Aagaard, K., and Steele, M., 2000, Recent environmental changes in the Arctic: A review: Arctic, v. 53, p. 359-371.

Moritz, R., Bitz, C., and Steig, E., 2002, Dynamics of Recent Climate Change in the Arctic: Science, v. 297, p. 1497.

Moros, M., Andrews, J.T., Eberl, D.D., and Jansen, E., 2006, Holocene history of drift ice in the northern North Atlantic: Evidence for different spatial and temporal modes: Paleoceanography, v. 21.

Motoyama, H., Watanabe, O., Goto-Azuma, K., Igarashi, M., Miyahara, H., Nagasaki, T., Karlöf, L., and Isaksson, E., 2001, Activities of the Japanese Arctic Glaciological Expedition in 1999 (JAGE 1999): Memoirs of National Institute of Polar Research, v. 54, p. 253-260.

Murphy, A.M., 2000, A glaciochemical record from the Devon Ice Cap and Late-Holocene reconstruction of past sea ice extent in the North Water Polynya, Eastern Canadian Arctic, University of New Hampshire.

Mysak, L.A., Ingram, R.G., Wang, J., and Van Der Baaren, A., 1996, The anomalous sea-ice extent in Hudson Bay, Baffin Bay and the Labrador Sea during three simultaneous NAO and ENSO episodes: Atmosphere - Ocean, v. 34, p. 313-343.

Mysak, L.A., and Venegas, S.A., 1998, Decadal climate oscillations in the Arctic: a new feedback loop for atmosphere-ice-ocean interactions: Geophysical Research Letters, v. 25, p. 3607-3610.

Naes, T., Isaksson, T., Fearn, T., and Davies, T., 2004, Multivariate Calibration and Classification, NIR, Chichester, UK, 344 p.

Nederbragt, A., and Thurow, J., 2004, Digital sediment colour analysis as a method to obtain high resolution climate proxy records, *in* Francus, P., ed., Image Analysis, Sediments, and Paleoenviroments, Volume 7: Dordrecht, Netherlands, Kluwer Academic, p. 105-124.

Nghiem, S.V., Rigor, I.G., Perovich, D.K., Clemente-Colón, P., Weatherly, J.W., and Neumann, G., 2007, Rapid reduction of Arctic perennial sea ice: Geophys. Res. Lett., v. 34.

North, G., Bell, T., Cahalan, R., and Moeng, F., 1982, Sampling Errors in the Estimation of Empirical Orthogonal Functions: Monthly Weather Review, v. 110, p. 699-706.

North, G., Biondi, F., Bloomfield, P., Christy, J., Cuffey, K., Dickinson, R., Druffel, E., Nychka, D., Otto-Bliesner, B., and Roberts, N., 2006, Surface Temperature Reconstructions for the Last 2,000 Years: Washington DC, The National Academy Press, 145 p.

O'Brien, S.R., Mayewski, P.A., Meeker, L.D., Meese, D.A., Twickler, M.S., and Whitlow, S.I., 1995, Complexity of Holocene climate as reconstructed from a Greenland Ice Core: Science, v. 270, p. 1962-1964.

O'Dwyer, J., Isaksson, E., Vinje, T., Jauhiainen, T., Moore, J., Pohjola, V., Vaikmäe, R., and Van De Wal, R.S.W., 2000, Methanesulfonic acid in a Svalbard ice core as an indicator of ocean climate: Geophysical Research Letters, v. 27, p. 1159-1162.

Opel, T., Fritzsche, D., Meyer, H., Schütt, R., Weiler, K., Ruth, U., Wilhelms, F., and Fischer, H., 2009, 115 year ice-core data from Akademii Nauk ice cap, Severnaya Zemlya: high-resolution record of Eurasian Arctic climate change: Journal of Glaciology, v. 55, p. 21-31.

Osborn, T.J., and Briffa, K.R., 2006, The Spatial Extent of 20th-Century Warmth in the Context of the Past 1200 Years: Science, v. 311, p. 841-844.

Osterberg, E.C., Handley, M.J., Sneed, S.B., Mayewski, P.A., and Kreutz, K.J., 2006, Continuous ice core melter system with discrete sampling for major ion, trace element, and stable isotope analyses: Environmental Science and Technology, v. 40, p. 3355-3361.

Overland, J., and Wang, M., 2005, The Arctic climate paradox: The recent decrease of the Arctic Oscillation: Geophysical Research Letters, v. 32.

Overland, J.E., Spillane, M.C., Percival, D.B., Wang, M., and Mofjeld, H.O., 2004a, Seasonal and regional variation of pan-Arctic surface air temperature over the instrumental record: Journal of Climate, v. 17, p. 3263-3282.

Overland, J.E., Spillane, M.C., and Soreide, N.N., 2004b, Integrated analysis of physical and biological pan-arctic change: Climatic Change, v. 63, p. 291-322.

Overpeck, J., Hughen, K., Hardy, D., Bradley, R., Case, R., Douglas, M., Finney, B., Gajewski, K., Jacoby, G., Jennings, A., Lamoureux, S., Lasca, A., MacDonald, G., Moore, J., Retelle, M., Smith, S., Wolfe, A., and Zielinski, G., 1997, Arctic environmental change of the last four centuries: Science, v. 278, p. 1251-1256.

Parkinson, C.L., and Cavalieri, D.J., 2008, Arctic sea ice variability and trends, 1979-2006: Journal of Geophysical Research C: Oceans, v. 113.

Parkinson, C.L., Cavalieri, D.J., Gloersen, P., Zwally, H.J., and Comiso, J.C., 1999, Arctic sea ice extents, areas, and trends, 1978-1996: Journal of Geophysical Research C: Oceans, v. 104, p. 20837-20856.

Partington, K., Flynn, T., Lamb, D., Bertoia, C., and Dedrick, K., 2003, Late twentieth century Northern Hemisphere sea-ice record from U.S. National Ice Center ice charts: Journal of Geophysical Research C: Oceans, v. 108, p. 7-1.

Paterson, W., 1994, The Physics of Glaciers, 3rd Edition: UK, Pergamon, 480 p.

Pauling, A., Luterbacher, J., Casty, C., and Wanner, H., 2006, Five hundred years of gridded high-resolution precipitation reconstructions over Europe and the connection to large-scale circulation: Climate Dynamics, v. 26, p. 387-405.

Peixoto, J., and Oort, A., 1992, Physics of Climate: New York, Am. Inst. of Phys., 520 p.

Perovich, D.K., Light, B., Eicken, H., Jones, K.F., Runciman, K., and Nghiem, S.V., 2007, Increasing solar heating of the Arctic Ocean and adjacent seas, 1979â€"2005: Attribution and role in the ice-albedo feedback: Geophys. Res. Lett., v. 34.

Peterson, B.J., McClelland, J., Curry, R., Holmes, R.M., Walsh, J.E., and Aagaard, K., 2006, Trajectory shifts in the arctic and subarctic freshwater cycle: Science, v. 313, p. 1061-1066.

Pohjola, V.A., Moore, J.C., Isaksson, E., Jauhiainen, T., Van De Wal, R.S.W., Martma, T., Meijer, H.A.J., and Vaikma?e, R., 2002, Effect of periodic melting on geochemical and isotopic signals in an ice core from Lomonosovfonna, Svalbard: Journal of Geophysical Research D: Atmospheres, v. 107.

Polyakov, I., Alekseev, G., Timokhov, L., Bhatt, U., Colony, R., Simmons, H., Walsh, D., Walsh, J., and Zakharov, V., 2004, Variability of the Intermediate Atlantic Water of the Arctic Ocean over the Last 100 Years: Journal of Climate, v. 17, p. 4485-4497.

Polyakov, I.V., Alekseev, G.V., Bekryaev, R.V., Bhatt, U.S., Colony, R., Johnson, M.A., Karklin, V.P., Walsh, D., and Yulin, A.V., 2003a, Long-term ice variability in Arctic marginal seas: Journal of Climate, v. 16, p. 2078-2085.

Polyakov, I.V., Bekryaev, R.V., Alekseev, G.V., Bhatt, U.S., Colony, R.L., Johnson, M.A., Maskshtas, A.P., and Walsh, D., 2003b, Variability and trends of air temperature and pressure in the maritime Arctic, 1875-2000: Journal of Climate, v. 16, p. 2067-2077.

Polyakov, I.V., and Johnson, M.A., 2000, Arctic decadal and interdecadal variability: Geophysical Research Letters, v. 27, p. 4097-4100.

Polyakova, E.I., Journel, A.G., Polyakov, I.V., and Bhatt, U.S., 2006, Changing relationship between the North Atlantic Oscillation and key North Atlantic climate parameters: Geophys. Res. Lett., v. 33.

Prinsenberg, S., Peterson, I., Narayanan, S., and Umoh, J., 1997, Interaction between atmosphere, ice cover, and ocean off Labrador and Newfoundland from 1962 to 1992: Can. J. Fish. Aquat. Sci, v. 54, p. 30-39.

Proshutinsky, A., and Johnson, M., 1997, Two circulation regimes of the wind-driven Arctic Ocean: Journal of Geophysical Research, v. 102.

Rankin, A.M., Wolff, E.W., and Martin, S., 2002, Frost flowers: Implications for tropospheric chemistry and ice core interpretation: Journal of Geophysical Research D: Atmospheres, v. 107.

Ribera, P., Gimeno, L., Garcia, R., Hernandez, E., and Venegas. , S.A., 2001, Statistical Methods for Field Analysis used in Climatology, *in* Mateu, J., and Montes, F., eds., Spatial Statistics Through Applications. , Volume 13: Advances in Ecological Sciences Series: Southampton, Witpress, p. 300 p.

Rigor, I.G., Colony, R.L., and Martin, S., 2000, Variations in surface air temperature observations in the Arctic, 1979-97: Journal of Climate, v. 13, p. 896-914.

Rigor, I.G., Wallace, J.M., and Colony, R.L., 2002, Response of sea ice to the Arctic Oscillation: Journal of Climate, v. 15, p. 2648-2663.

Rogers, J.C., Wang, C.C., and McHugh, M.J., 1998, Persistent cold climatic episodes around Greenland and Baffin Island: Links to decadal-scale sea surface temperature anomalies: Geophysical Research Letters, v. 25, p. 3971-3974.

Rudels, B., 1995, The thermohaline circulation of the Arctic Ocean and the Greenland Sea: Philosophical Transactions - Royal Society of London, A, v. 352, p. 287-299.

Russ, J., 2002, The Image Processing Handbook, 4th Edition: London, CRC Press, 744 p.

Rutherford, S., Mann, M., Osborn, T., Bradley, R., Briffa, K., Hughes, M., and Jones, P., 2005, Proxy-Based Northern Hemisphere Surface Temperature Reconstructions: Sensitivity to Method, Predictor Network, Target Season, and Target Domain: Journal of Climate, v. 18, p. 2308-2329.

Schneider, T., 2001, Analysis of Incomplete Climate Data: Estimation of Mean Values and Covariance Matrices and Imputation of Missing Values: Journal of Climate, v. 14, p. 853-871.

Sciremammano, F., 1979, A Suggestion for the Presentation of Correlations and Their Significance Levels: Journal of Physical Oceanography, v. 9, p. 1273-1276.

Serreze, M., 1995, Climatological Aspects of Cyclone Development and Decay in the Arctic: Atmosphere-Ocean v. 33, p. 1-1.

Serreze, M.C., Carse, F., Barry, R.G., and Rogers, J.C., 1997, Icelandic low cyclone activity: Climatological features, linkages with the NAO, and relationships with recent changes in the Northern Hemisphere circulation: Journal of Climate, v. 10, p. 453-464.

Serreze, M.C., and Francis, J.A., 2006, The arctic amplification debate: Climatic Change, v. 76, p. 241-264.

Serreze, M.C., Holland, M.M., and Stroeve, J., 2007, Perspectives on the Arctic's shrinking sea-ice cover: Science, v. 315, p. 1533-1536.

Serreze, M.C., Walsh, J.E., Chapin Iii, F.S., Osterkamp, T., Dyurgerov, M., Romanovsky, V., Oechel, W.C., Morison, J., Zhang, T., and Barry, R.G., 2000, Observational evidence of recent change in the northern high-latitude environment: Climatic Change, v. 46, p. 159-207.

Canadian Ice Service, 2002, Sea Ice Climatic Atlas, Northern Canadian Waters, 1971-2000, Minister of Public Works and Government Services of Canada, p. 200.

Sezgin, M., and Sankur, B., 2004, Survey over image thresholding techniques and quantitative performance evaluation: Journal of Electronic Imaging, v. 13, p. 146-168.

Sharp, M., Skidmore, M., and Nienow, P., 2002, Seasonal and spatial variations in the chemistry of a High Arctic supraglacial snow cover: Journal of Glaciology, v. 48, p. 149-158.

Singarayer, J., Bamber, J., and Valdes, P., 2006, Twenty-First-Century Climate Impacts from a Declining Arctic Sea Ice Cover: Journal of Climate, v. 19, p. 1109-1125.

Singarayer, J.S., and Bamber, J.L., 2003, EOF analysis of three records of sea-ice concentration spanning the last 30 years: Geophysical Research Letters, v. 30, p. 55-1.

Sjögren, B., Brandt, O., Nuth, C., Isaksson, E., Pohjola, V., Kohler, J., and Van de Wal, R.S.W., 2007, Determination of firn density in ice cores using image analysis: Journal of Glaciology, v. 53, p. 413-419.

Smith, M., and Rigby, B., 1981, Distribution of polynyas in the Canadian Arctic: Polynyas in the Canadian Arctic. Can. Wildl. Serv. Occas. Pap, p. 7–28.

Smith, T.M., and Reynolds, R.W., 2004, Improved extended reconstruction of SST (1854-1997): Journal of Climate, v. 17, p. 2466-2477.

Solomon, S., Qin, D., Manning, M., Chen, Z., Marquis, M., Averyt, K., Tignor, M., and Miller, H., 2007, IPCC, 2007: Climate Change 2007: The Physical Science Basis. Contribution of Working Group I to the Fourth Assessment Report of the Intergovernmental Panel on Climate Change, Cambridge University Press, Cambridge, UK.

Soon, W., and Baliunas, S., 2003, Proxy climatic and environmental changes of the past 1000 years: Climate Research, v. 23, p. 89-110.

Steele, M., and Boyd, T., 1998, Retreat of the cold halocline layer in the Arctic Ocean: Journal of Geophysical Research C: Oceans, v. 103, p. 10419-10435.

Steele, M., and Flato, G., 2000, Sea ice growth, melt, and modeling: A survey: The Freshwater Budget of the Arctic Ocean, p. 549–587.

Stroeve, J., Holland, M.M., Meier, W., Scambos, T., and Serreze, M., 2007, Arctic sea ice decline: Faster than forecast: Geophysical Research Letters, v. 34.

Stroeve, J., Serreze, M., Drobot, S., Gearheard, S., Holland, M., Maslanik, J., Meier, W., and Scambos, T., 2008, Arctic sea ice extent plummets in 2007: Eos, v. 89, p. 13-14.

Svensson, A., Nielsen, S.W., Kipfstuhl, S., Johnsen, S.J., Steffensen, J.P., Bigler, M., Ruth, U., and Ro?thlisberger, R., 2005, Visual stratigraphy of the North Greenland Ice Core Project (NorthGRIP) ice core during the last glacial period: Journal of Geophysical Research D: Atmospheres, v. 110, p. 1-11.

Swift, J.H., Aagaard, K., Timokhov, L., and Nikiforov, E.G., 2005, Long-term variability of Arctic Ocean waters: Evidence from a reanalysis of the EWG data set: Journal of Geophysical Research C: Oceans, v. 110, p. 1-14.

Takata, M., Iizuka, Y., Hondoh, T., Fujita, S., Fujii, Y., and Shoji, H., 2004, Stratigraphic analysis of Dome Fuji Antarctic ice core using an optical scanner: Annals of Glaciology, v. 39, p. 467-472.

Tarussov, A., 1992, The Arctic from Svalbard to Severnaya Zemlya: Climatic reconstructions from ice cores, *in* Bradley, R.S., and Jones, P.D., eds., Climate Since AD 1500: London, Routledge, p. 505-516.

Thompson, D.W.J., and Wallace, J.M., 1998, The Arctic oscillation signature in the wintertime geopotential height and temperature fields: Geophysical Research Letters, v. 25, p. 1297-1300.

Thorndike, A., and Colony, R., 1982, Sea ice motion in response to geostropic winds: Journal of Geophysical Research, v. 87.

Venegas, S.A., and Mysak, L.A., 2000, Is there a dominant timescale of natural climate variability in the Arctic?: Journal of Climate, v. 13, p. 3412-3434.

Vinje, T., 1999, Barents Sea ice edge variations over the past 400 years, Workshop on Sea-Ice Charts of the Arctic: Seattle, Washington, World Meteorological Organization, p. 4-6.

—, 2001, Anomalies and trends of sea-ice extent and atmospheric circulation in the Nordic Seas during the period 1864-1998: Journal of Climate, v. 14, p. 255-267.

Vinnikov, K.Y., Robock, A., Stouffer, R.J., Walsh, J.E., Parkinson, C.L., Cavalieri, D.J., Mitchell, J.F.B., Garrett, D., and Zakharov, V.F., 1999, Global warming and Northern Hemisphere sea ice extent: Science, v. 286, p. 1934-1937.

Vinther, B.M., Clausen, H.B., Fisher, D.A., Koerner, R.M., Johnsen, S.J., Andersen, K.K., Dahl-Jensen, D., Rasmussen, S.O., Steffensen, J.P., and Svensson, A.M., 2008, Synchronizing ice cores from the Renland and Agassiz ice caps to the Greenland Ice Core Chronology: Journal of Geophysical Research-Atmospheres, v. 113, p. D08115.

Vinther, B.M., Clausen, H.B., Johnsen, S.J., Rasmussen, S.O., Andersen, K.K., Buchardt, S.L., Dahl-Jensen, D., Seierstad, I.K., Siggaard-Andersen, M.L., Steffensen, J.P., Svensson, A., Olsen, J., and Heinemeier, J., 2006, A synchronized dating of three Greenland ice cores throughout the Holocene: Journal of Geophysical Research D: Atmospheres, v. 111.

von Storch, H., Zorita, E., Jones, J.M., Dimitriev, Y., Gonzalez-Rouco, F., and Tett, S.F.B., 2004, Reconstructing Past Climate from Noisy Data: Science, v. 306, p. 679-682.

Wake, C., Yalcin, K., and Gundestrup, N., 2002, The climate signal recorded in the oxygen-isotope, accumulation and major-ion time series from the Eclipse ice core,YukonTerritory, Canada: Annals of Glaciology, v. 35, p. 416-422.

Wallevik, J., and Sigurjónsson, H., 1998, The Koch Index: Formulation, corrections and extension. Icelandic Meteorological Office Rep, VÍ-G98035-ÚR28, 14 pp.

Walsh, J.E., 1978, A data set on Northen Hemisphere sea ice extent, World Data Center-A for Glaciology: Glaciological Data, Report GD-2 part1, p. 49-51.

Walsh, J.E., and Chapman, W.L., 2001, 20th-century sea-ice variations from observational data: Annals of Glaciology, v. 33, p. 444-448.

Walsh, J.E., Chapman, W.L., and Shy, T.L., 1996, Recent decrease of sea level pressure in the central Arctic: Journal of Climate, v. 9, p. 480-486.

Wang, J., Mysak, L.A., and Ingram, R.G., 1994, Interannual variability of sea-ice cover in Hudson Bay, Baffin Bay and the Labrador Sea: Atmosphere-ocean. Toronto ON, v. 32, p. 421-447.

Wang, L., Sharp, M.J., Rivard, B., Marshall, S., and Burgess, D., 2005, Melt season duration on Canadian Arctic ice caps, 2000-2004: Geophysical Research Letters, v. 32, p. 1-4.

Warren, S.G., 1982, Optical properties of snow: Reviews of Geophysics and Space Physics, v. 20, p. 67-89.

Weatherhead, E.C., Reinsel, G.C., Tiao, G.C., Meng, X.L., Choi, D., Cheang, W.K., Keller, T., DeLuisi, J., Wuebbles, D.J., Kerr, J.B., Miller, A.J., Oltmans, S.J., and Frederick, J.E., 1998, Factors affecting the detection of trends: Statistical considerations and applications to environmental data: Journal of Geophysical Research D: Atmospheres, v. 103, p. 17149-17161.

Welch, K.A., Mayewski, P.A., and Whitlow, S.I., 1993, Methanesulfonic acid in coastal Antarctic snow related to sea-ice extent: Geophysical Research Letters, v. 20, p. 443-446.

Whung, P.Y., Saltzman, E.S., Spencer, M.J., Mayewski, P.A., and Gundestrup, N., 1994, Two-hundred-year record of biogenic sulfur in a south Greenland ice core (20D): Journal of Geophysical Research, v. 99.

Wilks, D.S., 1995, Statistical Methods in the Atmospheric Sciences: An Introduction, Academic Press.

Wilson, K.J., Falkingham, J., Melling, H., and De Abreu, R., 2004, Shipping in the Canadian Arctic: other possible climate change scenarios, Proceedings from IEEE International Geoscience and Remote Sensing Symposium: Anchorage, Alaska, p. 1-4.

Wold, S., Sjöström, M., and Eriksson, L., 2001, PLS-regression: a basic tool of chemometrics: Chemometrics and Intelligent Laboratory Systems, v. 58, p. 109-130.

Wolff, E.W., Rankin, A.M., and Röthlisberger, R., 2003, An ice core indicator of Antarctic sea ice production?: Geophysical Research Letters, v. 30.

Xu, Q., and Liang, Y., 2001, Monte Carlo cross validation: Chemometrics and Intelligent Laboratory Systems, v. 56, p. 1-11.

Yan, Y., Kang, S., Sun, J., Mayewski, P.A., and Qin, D., 2005, Sea-salt aerosol transport patterns over the Northern Hemisphere inferred from two subarctic ice core records: Science in China Serie D: Earth Sciences, v. 48, p. 576-584.

Yi, D., Mysak, L.A., and Venegas, S.A., 1999, Decadal-to-interdecadal fluctuations of arctic sea-ice cover and the atmospheric circulation during 1954- 1994: Atmosphere - Ocean, v. 37, p. 389-415.

Zhang, J., Rothrock, D., and Steele, M., 2000, Recent changes in Arctic Sea ice: The interplay between ice dynamics and thermodynamics: Journal of Climate, v. 13, p. 3099-3114.

Zhang, X., Sorteberg, A., Zhang, J., Gerdes, R.d., and Comiso, J.C., 2008, Recent radical shifts of atmospheric circulations and rapid changes in Arctic climate system: Geophys. Res. Lett., v. 35.

Zhang, X., and Walsh, J.E., 2006, Toward a seasonally ice-covered Arctic Ocean: Scenarios from the IPCC AR4 model simulations: Journal of Climate, v. 19, p. 1730-1747.

Zhang, X., Walsh, J.E., Zhang, J., Bhatt, U.S., and Ikeda, M., 2004, Climatology and interannual variability of Arctic cyclone activity: 1948-2002: Journal of Climate, v. 17, p. 2300-2317.

Zheng, J., Kudo, A., Fisher, D.A., Blake, E.W., and Gerasimoff, M., 1998, Solid electrical conductivity (ECM) from four Agassiz ice cores, Ellesmere island NWT, Canada: High-resolution signal and noise over the last millennium and low resolution over the Holocene: Holocene, v. 8, p. 413-421.

Zielinski, G.A., Mayewski, P.A., Meeker, L.D., Whitlow, S., Twickler, M.S., Morrison, M., Meese, D.A., Gow, A.J., and Alley, R.B., 1994, Record of volcanism since 7000 B.C. from the GISP2 Greenland ice core and implications for the volcano-climate system: Science, v. 264, p. 948-952.

Zweng, M.M., and Munnchow, A., 2006, Warming and freshening of Baffin Bay, 1916-2003: Journal of Geophysical Research C: Oceans, v. 111.

APPENDICES

APPENDIX 1

Fisher, D., Dyke, A., Koerner, R., Bourgeois, J., Kinnard, C., Zdanowicz, C., de Vernal, A., Hillaire-Marcel, C., Savelle, J., and Rochon, A., 2006, Natural Variability of Arctic Sea Ice Over the Holocene: EOS Trans. AGU, v. 87, p. 273-275.

APPENDIX 2

Ice core drilling on the Prince of Wales Icefield, April-May 2005

APPENDIX 3

Description of the ice core melting system

APPENDIX 4

Comparison between Polyakov (2003a) and Walsh and Chapman (2001) ice extent

APPENDIX 5

Theoretical estimate of time scale error for the Devon 98 ice core

APPENDIX 6.

Ice core image processing steps

APPENDIX 7.

Coupled Arctic climate and sea ice extent over the past millennium reconstructed from terrestrial proxies: *supplementary material*

APPENDIX 1. NATURAL VARIABILITY OF HOLOCENE SEA ICE

Eos, Vol. 87, No. 28, 11 July 2006

EOS

EOS, TRANSACTIONS, AMERICAN GEOPHYSICAL UNION

VOLUME 87 NUMBER 28
11 JULY 2006
PAGES 273–280

Natural Variability of Arctic Sea Ice Over the Holocene

PAGES 273, 275

The area and volume of sea ice in the Arctic Ocean is decreasing, with some predicting ice-free summers by 2100 A.D. [*Johannessen et al.*, 2004]. The implications of these trends for transportation and ecosystems are profound; for example, summer shipping through the Northwest Passage could be possible, while loss of sea ice could cause stress for polar bears. Moreover, global climate may be affected through albedo feedbacks and increased sea ice production and export. With more open water, more new sea ice forms in winter, which melts and/or gets exported out of the Arctic.

The recent decrease in summer sea ice (Figure 1a) may result from radiative forcing, possibly due to increased greenhouse gas concentrations, and/or from reduced winter ice cover which allows greater atmospheric warming [*Rigor et al.*, 2002]. While several studies predict a continuous decline in ice cover, the timing, magnitude, and regional expression vary between models [e.g., *Johannessen et al.*, 2004]. For example, the Canadian Arctic Archipelago (CAA) may remain encumbered with summer ice, because multi-year ice accumulates along its coastline and invades the channels [*Agnew et al.*, 2001].

Interestingly, the Holocene sea ice history of the CAA indicates less summer sea ice 10,500–9000 years before present (B.P.), perhaps similar to current trends. All sea ice proxies point to an early Holocene ice cover minimum, but regional differences characterize later times.

A consortium of Canadian groups is using ocean cores, ice cores, and mammalian and archeological histories to build a Holocene sea ice history; preliminary results are reported here. By the end of International Polar Year activities in 2008, more will be known about the natural variability of sea ice during past times. Although sea level changed over the Holocene, tracing sea ice history across the Arctic can lead to a better assessment of the underlying dynamics that govern sea ice extent, which may help distinguish anthropogenic from natural forcing.

BY D. FISHER, A. DYKE, R. KOERNER, J. BOURGEOIS, C. KINNARD, C. ZDANOWICZ, A. DE VERNAL, C. HILLAIRE-MARCEL, J. SAVELLE, AND A. ROCHON

Marine Mammals

The establishment of perennial Arctic sea ice cover in the late Tertiary led to the evolution of ice-adapted mammals, including the bearded seal, ring seal, walrus, polar bear, narwhal, beluga, and bowhead whale. Continued existence of this community is evidence that the sea ice cap has not disappeared during the Quaternary.

The remains of over 1200 bowheads have been recorded in the CAA, and more than 500 have been radiocarbon dated. The annual migration of bowheads follows the seasonal expansion and contraction of the sea ice front, as the animals prefer to remain close to the ice edge. As the sea ice retreats, Bering Sea as well as Davis Strait stocks of bowheads converge upon the CAA. The two are prevented from intermingling today by a persistent sea ice barrier that plugs the central part of the archipelago.

The distribution and radiocarbon ages of whale remains indicate that during at least one interval of the Holocene, Bering Sea and Davis Strait bowheads could intermingle, (Figure 1b). The Bering Sea bowhead was the first to reach the CAA about 10,000 carbon-14 (^{14}C) years ago (11,450 calendar years B.P.). Bowheads entered via the Beaufort Sea about 1000 years after submergence of the Bering Strait, and they ranged up to the fronts of receding continental ice sheets [*Dyke et al.*, 1996; *Dyke and Savelle*, 2001]. Until about 9500 ^{14}C years B.P. (10,700 calendar years B.P.), by which time the Davis Strait bowhead ranged into the eastern Northwest Passage, the Bering Sea and Davis Strait stocks were separated by a glacier ice barrier. With dissipation of this barrier, the two stocks were able to intermingle, ranging well beyond historical limits. About 8000 ^{14}C years B.P. (8900 calendar years B.P.), the Bering Sea and Davis Strait stocks were separated, as they are today. Thus, a year-round sea ice barrier must have become established at that time in the central part of the Northwest Passage.

Holocene Ice Cores

The melt layers in summit cores from Agassiz (82°N) and Penny (65°N) ice caps are records of summer warmth (Figure 2a). Some melting occurs in 90% of summers atop the Agassiz ice cap. Refreezing after infiltration forms air-bubble-free 'melt layers.' Temperature can be interpreted based on the correlation between measured summer warmth and the percentage of the annual layer thickness consisting of refrozen meltwater. However, this melt layer/temperature transfer function has a limited range as the coldest summers leave no melt record, and the warmest summers, after complete infiltration of the annual layer, generate runoff from the site. Thus a 100% melt layer does not represent maximum warmth, and temporal discontinuities may occur in long intervals of the ice core with 100% melt replacement.

The Agassiz record in Figure 2a is from a core that reached bedrock at 135 meters. With this core, the Holocene melt record is complete, extending over 10,000 years back to the large oxygen-18 (^{18}O) increase at the termination of the Younger Dryas cooling period. Oxygen-18 in ice is a paleothermometer that mimics the air temperature of the past. During the early Holocene, some annual layers were formed entirely by refrozen meltwater. Because runoff may then have occurred from the core site, temperature reconstructions are minima. After about 9500 years B.P., the record shows high centennial-scale variability superimposed on a progressive summer cooling (of about 2.5°C) from that warmest period until today.

The Agassiz melt record is rather invariant over the last 2000 years, except for twentieth-century warming. Here the relationship between summer temperature and melt percent (the transfer function) is at the cold (low) end of its sensitivity range. The Penny record, from a warmer location, is more sensitive for this period and shows substantial variability in intensity of summer snowmelt through the last two millenia.

Summer wind direction may also influence sea ice clearance. If sea ice is exported by wind, it need not melt in situ. Paleowind proxies in the Arctic are difficult to obtain. However, pollen records indicate variable transport of tree pollen to the Arctic throughout the Holocene [*Bourgeois et al.*, 2000]. If the northwest mainland was the source of tree pollen, then early Holocene winds were

Eos, Vol. 87, No. 28, 11 July 2006

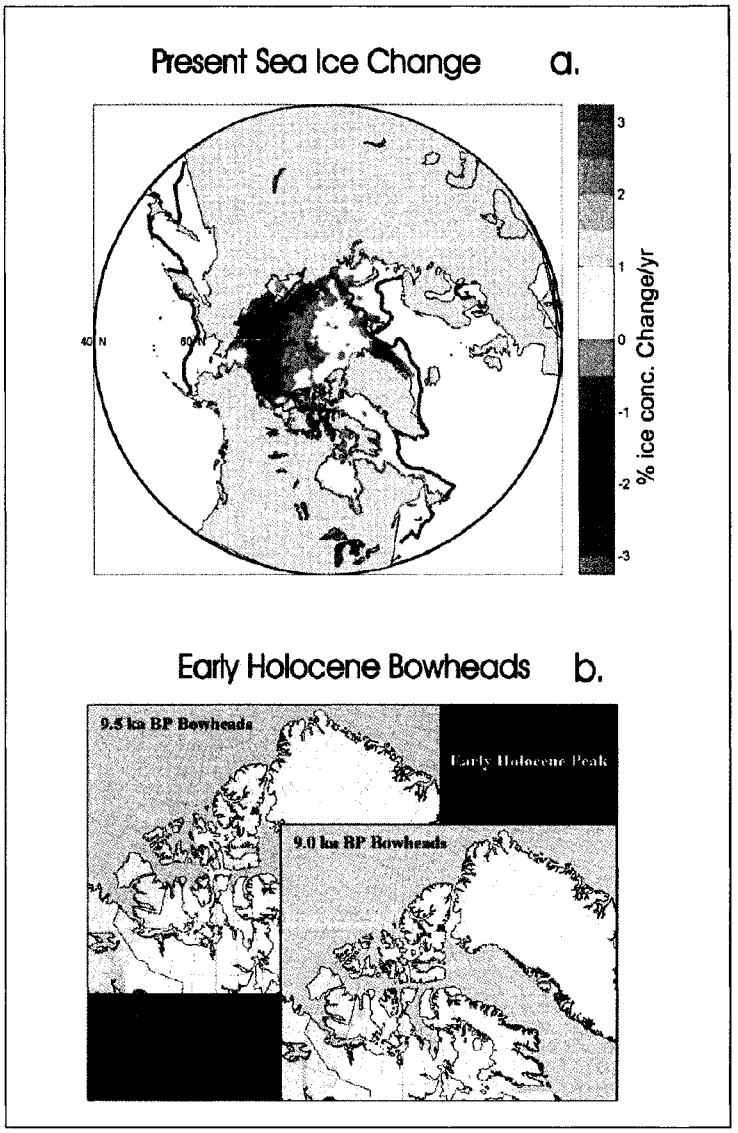

*Fig. 1. (a) September ice trends and average minimum (September, red line) and maximum (March, green line) ice extents, 1979–2003 [*Cavalieri et al., *2004]. (b) Distribution of bowhead whale bones dated 9.5 ± 0.25 and 9.0 ± 0.25 ^{14}C kiloyears B.P. White areas are ice sheets.*

more frequently from the southwest during spring and early summer.

Ocean Core Dinoflagellates and Isotopes

Dinoflagellate cyst assemblages reflect sea surface temperature, salinity, and ice cover. Inferences of sea ice cover, temperature, and salinity rely on the best analogues among modern assemblages from sites throughout northern oceans [*de Vernal et al.*, 2005]. Results from the eastern and western Arctic indicate opposite trends in sea ice cover: increasing in the east while decreasing in the west (Figure 2b). Both regions experienced successions of warm and cold intervals. Changes in regional fresh water input in conjunction with millennial-scale extraterrestrial cycles (e.g., the 1800-year lunar cycle) may explain such trends. Long sediment cores collected in 2004 and 2005 in the Beaufort Sea, the Northwest Passage, and Chukchi-Siberian seas will better define the regionalism of Holocene sea ice history.

Foraminiferal Isotopes

Neogloboquadrina pachyderma left-coiled (Npl) foraminifera grow along the pycnocline, where water density switches from cold, dilute, surface water to warmer, saline North Atlantic Water (NAW) in the Arctic Ocean. The $\delta^{18}O$ values in their shells have negative offsets from isotopic equilibrium values ranging from -1‰ (Arctic Seas) to -3‰ (Canada Basin), although temperature gradients still result in predictable isotopic shifts [*Hillaire-Marcel et al.*, 2004]. The offset could be linked to rate of sea ice formation [*Bauch et al.*, 1997]. Freezing isotopically light seawater produces ice and isotopically light brines that sink to the pycnocline. Mixing of these brines into NAW and export of surface water and sea ice to the North Atlantic maintain steady state conditions, thus resulting in an asymptotic isotopic offset value near -2.5 to 3‰ in Npl. From this view, the greater modern offsets in the western than in the eastern Arctic Ocean would reflect the differences in sea ice formation rates along the shelves.

These offsets were maintained in the Chukchi Sea during most of the Holocene (Figure 2b), with possibly larger offsets early on, which can be inferred as continuous sea ice formation and the greatest brine production in the early Holocene. The record illustrates some decoupling between surface-water conditions, as reconstructed from dinoflagellate cyst assemblages, and conditions prevailing in the NAW, as indicated by the size-dependent ^{18}O-gradients in Npl (Figure 2b). The 9000–8000 year interval depicts a large offset between small and large specimens, suggesting much warmer conditions in the NAW than in the surface water [see *Hillaire-Marcel et al.*, 2004]. However, between 7000 and 6000 years B.P., these size-dependent gradients nearly vanished, suggesting a weakening of the pycnocline. This likely resulted from a higher surface salinity and less sea ice, as also indicated by the dinoflagellate cysts.

Implications for Future Warming

The history of sea ice shows strong regionalism. Marine animals that depend on sea ice survived the early Holocene by adapting and migrating. At the height of the warmth, which was but three degrees warmer than now, the Pacific and Atlantic bowhead whales could visit each other through the Northwest Passage. Future Arctic warming is expected to be considerably warmer than this, and the free passage of biota and ships is certain.

More open water in summer means more area for freezing winter sea ice. Hence, less summer ice can increase the rate of winter brine expulsion. North Atlantic bottom-water formation rates feed back into the climate system. Since climate feedbacks are often not linear, one could expect surprises. This research suggests that hints about these surprises and their explanations may be found in the past.

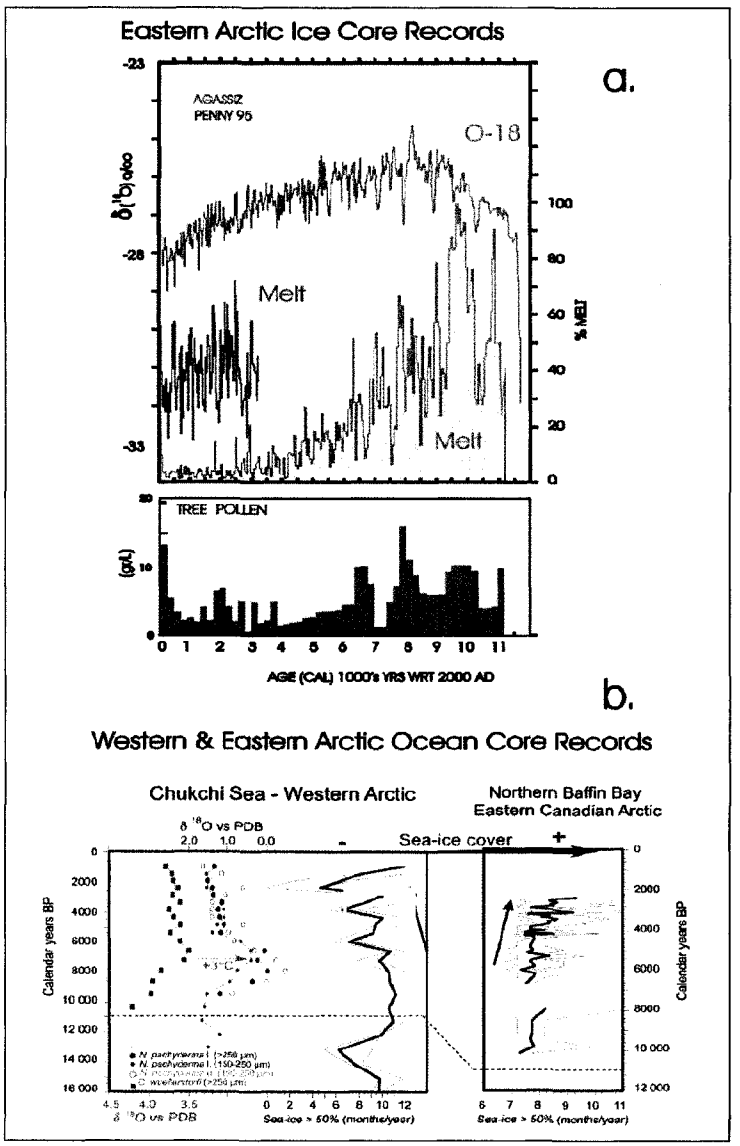

*Fig. 2. (a) Melt layer percent, Agassiz and Penny ice caps, Canadian Arctic. Ages based on annual layering and volcanic acid horizons; estimated accuracies ±5% [*Fisher et al., *1995]. (b) Opposite trends of sea ice cover in western and eastern Arctic. Chukchi core B15 is from Northwind Basin (Holocene, 10 centimeters thick) [*de Vernal et al., *2005]. Baffin Bay data are from cores P008 and P012 (10 meters of Holocene).*

References

Agnew, T., B. Alt, R. De Abreau, and S. Jeffers (2001), The loss of decade old sea ice plugs in the Canadian Arctic Islands, paper presented at the Sixth Polar Meteorology and Oceanography Conference, Am Meteorol Soc., San Diego, Calif., 14–18 May

Bauch, D., J. Carstens, and G. Wefer (1997), Oxygen isotope composition of living *Neogloboquadrina pachyderma* (sin.) in the Arctic Ocean, *Earth Planet. Sci. Lett., 146*, 47–58.

Bourgeois, J. C., R. M. Koerner, K. Gajewski, and D. A. Fisher (2000), A Holocene ice-core pollen record from Ellesmere Island, Nunavut, Canada, *Quat. Res., 54*, 275–283.

Cavalieri, D., C. Parkinson, P. Gloerson, and H. J. Zwally (2004), Sea ice concentrations from Nimbus-7 SMMR and DMSP SSM/I passive microwave data, June to September 2001, NOAA Natl. Snow and Ice Data Cent., Boulder, Colo.

de Vernal, A., C. Hillaire-Marcel, and D. Darby (2005a), Variability of sea ice cover in the Chukchi Sea (western Arctic Ocean) during the Holocene, *Paleoceanography, 20*, PA4018, doi: 10.1029/2005PA001157.

de Vernal, A., et al. (2005b), Reconstruction of sea-surface conditions at middle to high latitudes of the Northern Hemisphere during the Last Glacial Maximum (LGM) based on dinoflagellate cyst assemblages, *Quat. Sci. Rev., 24*, 897–924.

Dyke, A. S., and J. M. Savelle (2001), Holocene history of the Bering Sea bowhead whale (*Balaena mysticetus*) in its Beaufort Sea summer grounds off southwestern Victoria Island, western Canadian Arctic, *Quat. Res., 55*, 371–379.

Dyke, A. S., J. Hooper, and J. M. Savelle (1996), A history of sea ice in the Canadian Arctic Archipelago based on postglacial remains of the bowhead whale (*Balaena mysticetus*), *Arctic, 49*, 235–255.

Fisher, D. A., R. M. Koerner, and N. Reeh (1995), Holocene climatic records from Agassiz Ice Cap, Ellesmere Island, NWT, Canada, *Holocene, 5*, 19–24.

Hillaire-Marcel, C., A. de Vernal, L. Polyak, and D. Darby (2004), Size-dependent isotopic composition of planktic foraminifers from Chukchi Sea vs. NW Atlantic sediments—Implications for the Holocene paleoceanography of the western Arctic, *Quat. Sci. Rev., 23*, 245–260.

Johannessen, O. M., et al. (2004), Arctic climate change: Observed and modelled temperature and sea-ice variability, *Tellus, Ser. A, 56*, 328–341.

Rigor, I. G., J. M. Wallace, and R. L. Colony (2002), Response of sea ice to the Arctic Oscillation, *J. Clim., 15*, 2648–2663.

Author Information

David Fisher, Art Dyke, Roy Koerner, Jocelyne Bourgeois, Christophe Kinnard, and Christian Zdanowicz, Geological Survey of Canada, Ottawa, Ontario; Anne de Vernal and Claude Hillaire-Marcel, Universite du Québec a Montreal, Canada; James Savelle, McGill University, Montreal, Quebec, Canada; and André Rochon, Université du Québec à Rimouski, Canada. E-mail: David.Fisher@nrcan.gc.ca

APPENDIX 2. ICE CORE DRILLING ON THE PRINCE OF WALES ICEFIELD, APRIL-MAY 2005

Ice drilling camp

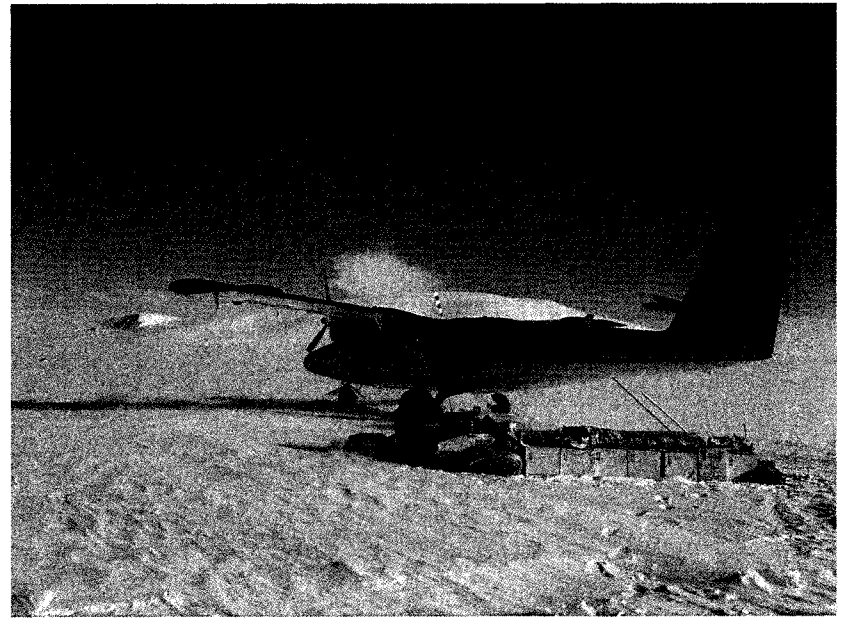

Twin Otter with ice core boxes

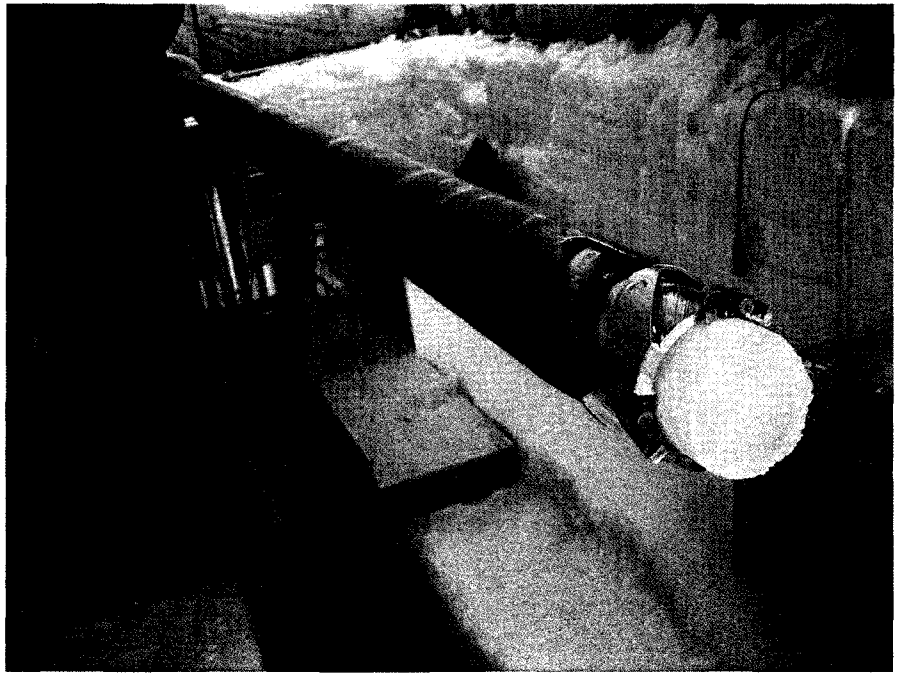

Electro-mechanical drill and drill trench

Ice core photography

ECM measurement

Visual stratigraphy

APPENDIX 3. DESCRIPTION OF THE ICE CORE MELTING SYSTEM

Schematic operational diagram of ice-core melter-sampler system set up at GSC laboratory.
Modified from Osterberg *et al. (2006) ES&T* 40: 3355-336.

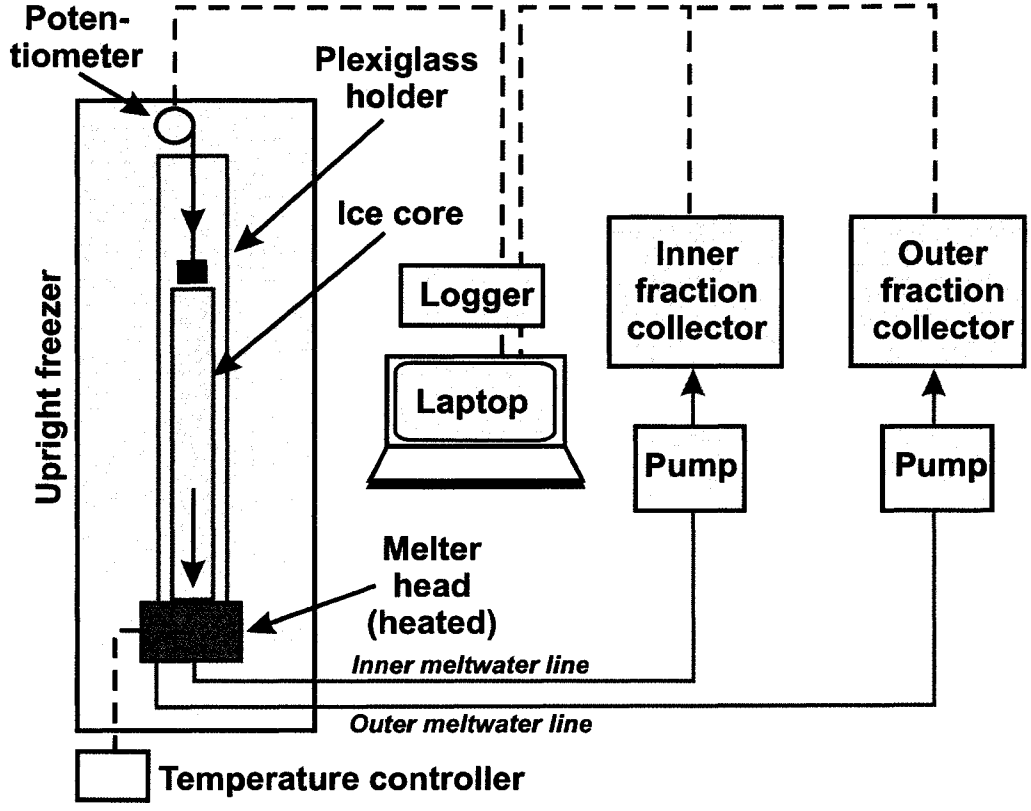

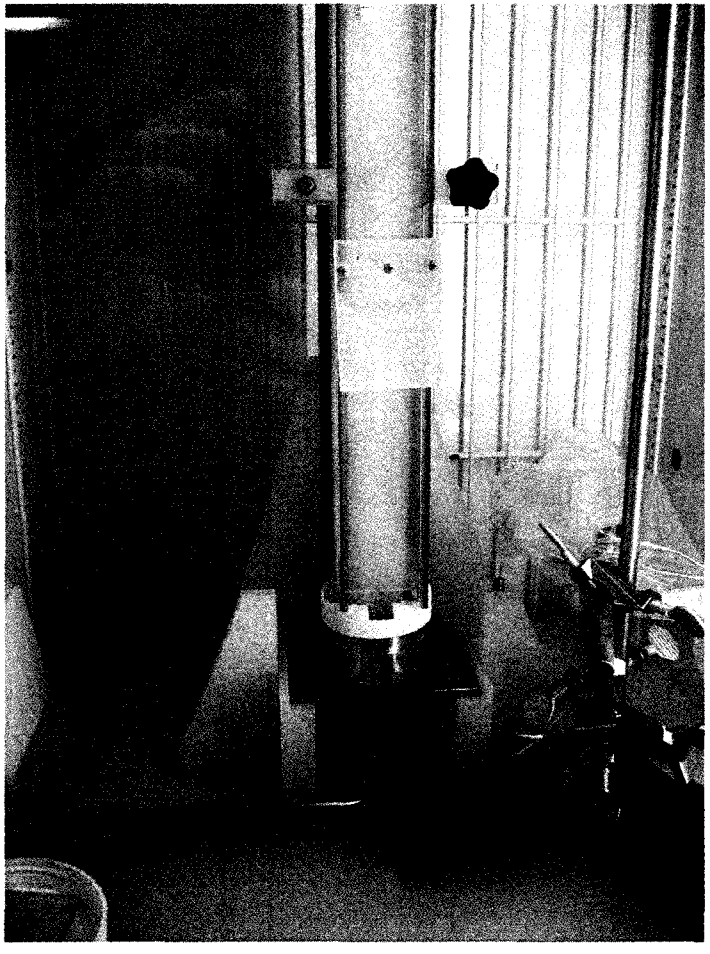

Melting ice core in the Plexiglas holder resting on top of the melter head.

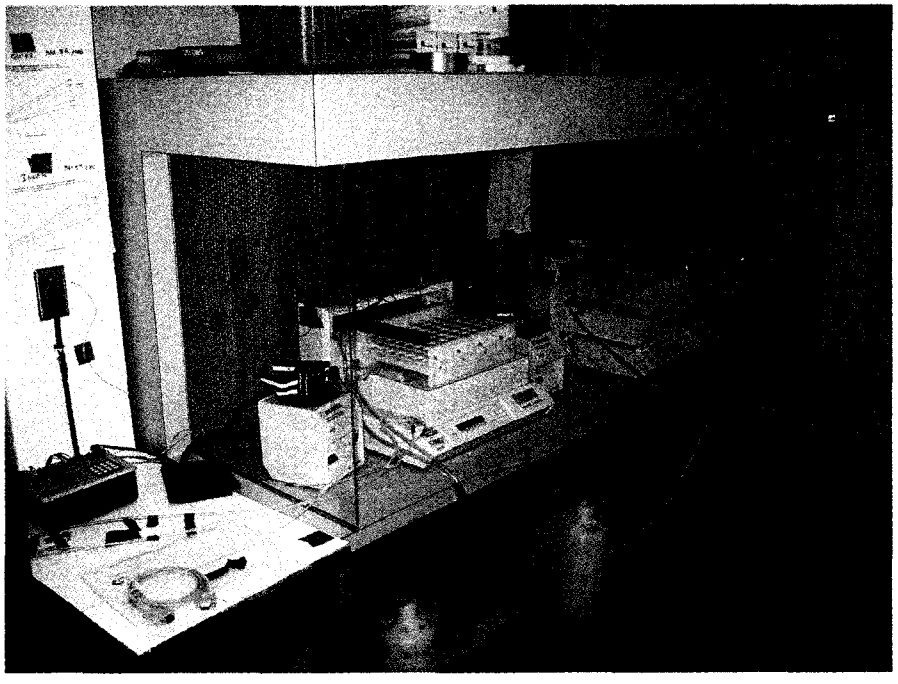

Fractional collectors, peristaltic pumps and data logger

APPENDIX 4. COMPARISON BETWEEN POLYAKOV (2003A) AND WALSH AND CHAPMAN (2001) ICE EXTENT

Longitudinal bins used to derive regional ice extent time series

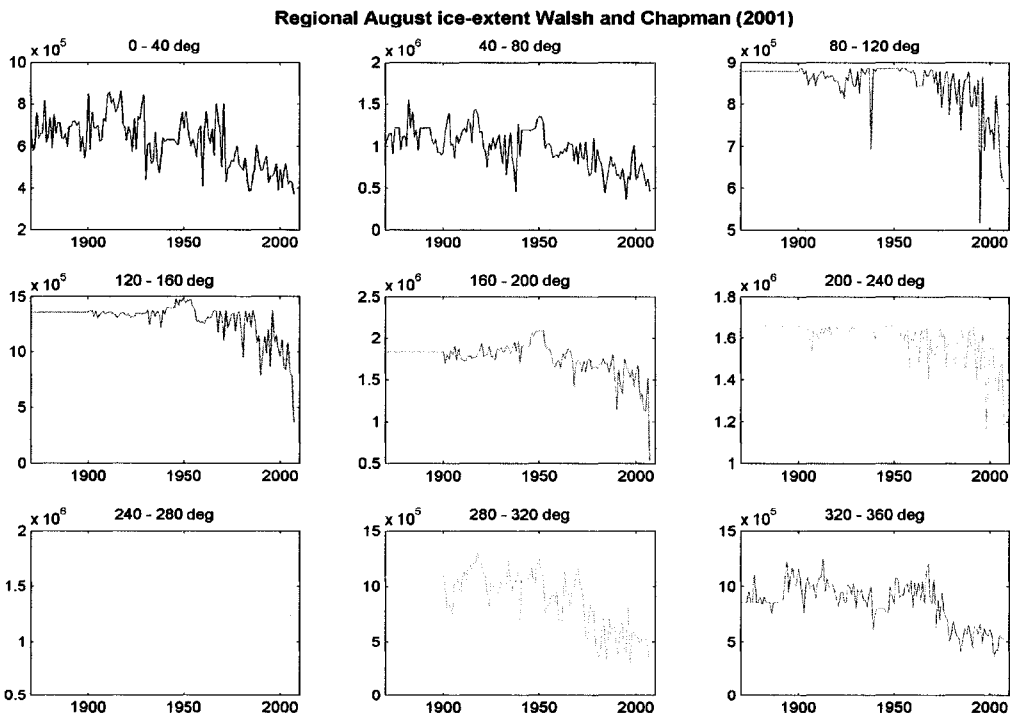

Total August ice extent time series from Walsh and Chapman dataset for each longitudinal bin. Line colors refer to the color of the map sectors. Note the absence of data in the late 19th and early 20th century in the Russian and Canadian Arctic

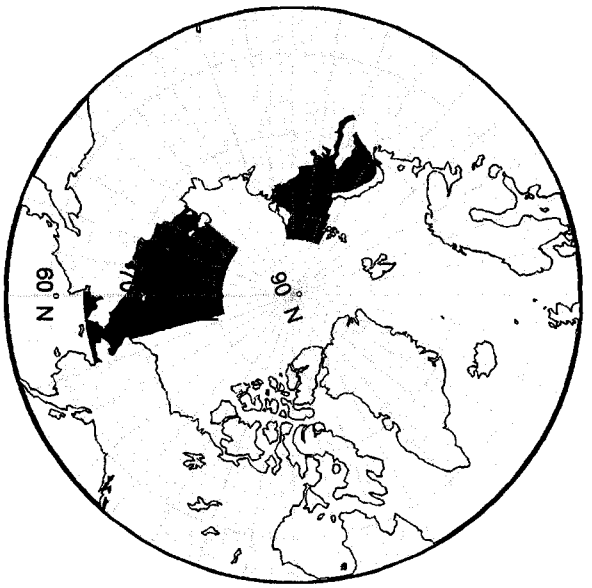

Russian Arctic marginal seas for which total ice extent was derived from Russian ice charts (after Polyakov et al, 2003b). Blue = Chuckchi Sea; Cyan = East Siberian Sea; Yellow = Laptev Sea; Red = Kara Sea.

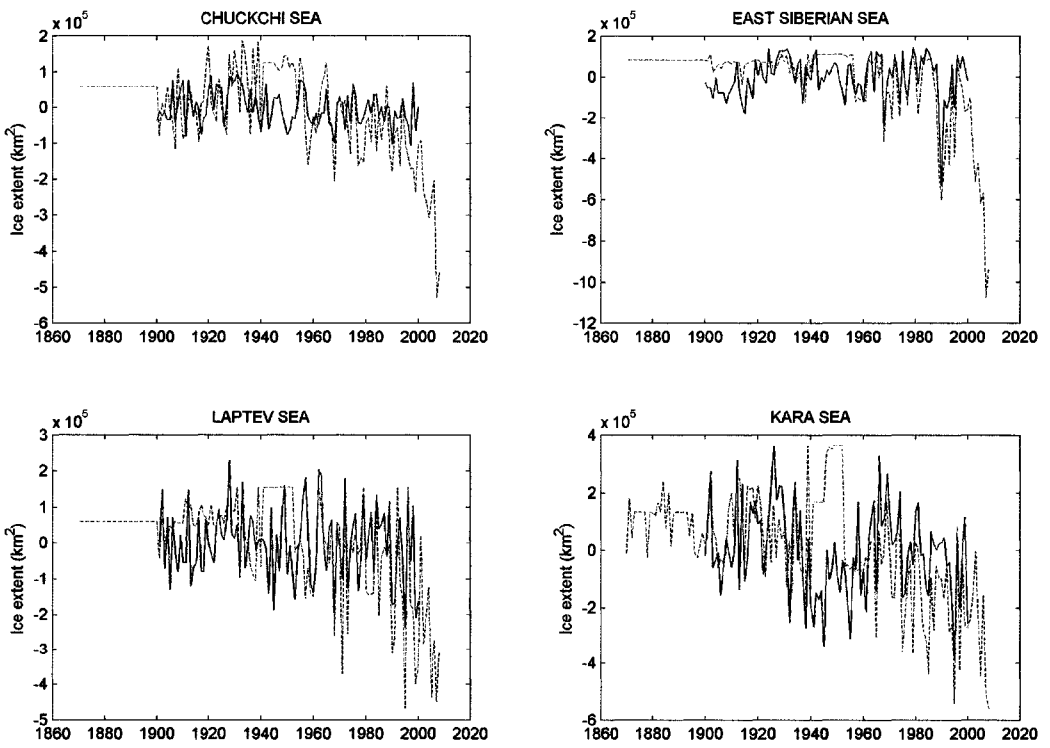

Total August ice extent in Russian Arctic seas from the Walsh and Chapman (red) and Polyakov (black) dataset.

APPENDIX 5. THEORETICAL ESTIMATE OF TIME SCALE ERROR FOR THE DEVON 98 ICE CORE

The cumulative error between the theoretical time scale, which assumes constant accumulation rate $\overline{\lambda}$, and the true unknown accumulation rate function $\lambda_{(t)}$ is:

$$Y_{(t)} = \sum_{t=0}^{t=N} \lambda_{(t)} - \sum_{t=0}^{t=N} \overline{\lambda}_{(t)} \qquad (1)$$

where t=1:N is the number of years between two well-dated points (e.g. the Katmai and Laki volcanic horizons). The function $\lambda_{(t)}$ is assumed to be a white or blue stationary noise process with a mean $\overline{\lambda}$ and standard deviation σ. The white noise model is a more conservative assumption and is used here. Attenuation of ice layers is assumed to be negligible in the firn section of the D98 core. $\overline{\lambda}$ is calculated as the ice thickness between the two fixed points divided by N years. σ must be estimated from known accumulation series. σ is 30% of $\overline{\lambda}$ for the upper 11 m of the D98 core but values between 20 and 25% are more common from the literature and from mass balance measurements. The maximum error in units of depth (m ice) is: E_{max} = max ($Y_{(t)}$). In time units (years), E_{max} = max ($Y_{(t)}$) / $\overline{\lambda}$. E_{max} is computed for n=5000 surrogate $\lambda_{(t)}$ series and the 95% percentile of the distribution is taken as a conservative estimate of the maximum error expected in the theoretical time scale. For a white noise model with σ = 30% and N = 146 years, this gives an E_{max} of 4.5 years. This is in good agreement with the <5 yr error estimated by Zheng and others (1998) for an ice core from Agassiz ice cap over the past 1000 years.

APPENDIX 6. ICE CORE IMAGE PROCESSING STEPS

1. Greyscale conversion

The original RGB images were converted to a single greyscale channel by eliminating the hue and saturation information while retaining the luminance (Russ, 2002 p.40).

$$I = 0.299R + 0.587G + 0.114B \quad (1)$$

where I is a photoquantity expressing the relative light intensity (greyscale, or luminance) and is scaled between 0 and 1.

2. Image linearization

Because the output images were in a JPEG format, they were not linear with respect to the voltage received by the CCD sensors. Unless images are shot in a RAW format, the built-in camera processor applies a non-linear response function to the input voltage which compresses the dynamic range and renders images that are better perceived by human viewers (Mann, 2002, p.107; Russ, 2002, p.8). There are two main reasons for using a photoquantity that is linear: (1) to adjust images to a common exposure, which is a linear operation and thus requires a linear variable; (2) to facilitate comparison between optical and physical properties of the ice cores. The JPEG format was used because the RAW (linear) format was not available using the stitch-assist mode. Since the camera can generate RAW images in the manual mode, the camera response function was determined by comparing the light intensity of a Kodak 20-steps greyscale chart JPEG image against its RAW counterparts, over a range of exposures (Manders and Mann, 2004). A

comparametric function (Mann, 2002) was fitted to the empirical data, and the inverse camera response function was then used to convert the images back to a linear output (Figure S1).

3. Exposure correction

The exposure time varied between pictures due to the automatic setting of the stitch-assist mode. While this insured that the light intensity extended over the full dynamic range of the camera and that minimum saturation occurred (clipping of bright pixels), it also introduced an exposure bias between pictures. Because images have been converted to a linear format, exposure correction (brightening or darkening) is a simple multiplicative operation which allows an image to be tonally adjusted to another (Mann, 2002, p.151).

$$I_{REF} = kI_{IMG} \tag{2}$$

Where I_{IMG} and I_{REF} are images with different exposure and k is the exposure ratio, in this case equal to t_{IMG}/t_{REF}, the ratio of exposure times (see Figures S1d and S2). This operation holds providing that the image to be corrected is not saturated. Because the maximum light intensity in every image was caused by direct illumination around the ice core and the exposure was adjusted by the camera accordingly, the light transmitted through the core itself never saturated. The exposure of individual images was adjusted to that of an image chosen for reference in each scene. Two reasons precluded simply using the ratios of exposure time to correct the exposure: (1) the fluorescent light source flickers at twice the frequency of the input AC current (60 Hz), which is enough for two similar pictures taken with the same exposure time to have different light intensities; (2)

the power was provided by a generator and may have been fluctuating, causing further differences in intensity between pictures. Instead, we used the light intensity transmitted through reference holes drilled into the light table surface, alongside the ice core receptacle, which provided a direct comparative measure of image exposure. The sub-scene was identified in each image by cross-correlation, and its intensity values regressed against those of the reference image. Because the images are in linear units, the slope of the regression gives the exposure ratio, which was then used to tonally align both images using equation 2 (Figure S2).

4. Uneven background illumination

Three factors resulted in uneven background illumination of the ice core images: (1) vignetting, a common optical defect of camera lenses, caused a gradual light falloff from the center of the images; (2) The walls at the box extremities resulted in boundary effects which caused a steeper light falloff than that attributable to vignetting; (3) because of the cylindrical shape of the cores, the core thickness decreased away from the central transverse axis, which increased light transmission. The combination of these three factors produced a significant but systematic bias in the background light distribution, which needed to be removed. A background illumination image was derived by averaging all images within the same box scene, and smoothing the results with a second-order polynomial surface (Russ, 2002, p.174).

$$B(x,y) = a_0 + a_1 x + a_2 y + a_3 x^2 + a_4 y^2 + a_5 xy \qquad (3)$$

Because the images have been converted to linear units, the uneven background can be removed by dividing each image by the background (Russ, 2002, p.173). However, slight tilts of the camera tray sometimes occurred between images, causing small deviations from the mean background pattern. Image division could amplify these small deviations and result in spurious corrections. Instead, a four steps data-adaptive procedure was used to remove the uneven background from each image. (1) The mean background image was divided by its central value, near the optical axis where no illumination bias occurs. This yielded a matrix of weights representing the fraction of light falloff from the center of the image.

$$W(x,y) = \frac{B}{B(x_i, y_i)} \tag{4}$$

(2) A preliminary background surface was created by multiplying W by the median intensity of the target image I, and then centering the results on the target image median value.

$$B_2 = W \cdot median(I), \text{ and } B_3 = B_2 - median(B_2) + median(I) \tag{5a, b}$$

Medians are used instead of averages because several images had skewed distributions. (3) B_3 was subtracted from the target image and residual values above and below one median absolute deviation (MAD) were discarded.

$$R(x,y) = I - B_3, \text{ and } R_2(x,y) = -MAD(R) \le R \le MAD(R) \quad (6a, b)$$

(4) B_3 was added back to the "clean" data R_2, and the results fitted with equation 3 to produce a new estimate of the background for the target image.

$$B_{IMG} = f(x_{R_2+B_3}, y_{R_2+B_3}) \quad (7)$$

where f is the polynomial function in equation 3. The procedure insures that only the image data close to the expected background pattern is fitted by the trend surface, and that large intensity deviations such as those caused by bright ice layers do not influence the fitting process. The procedure was verified by checking how well the overlapping segments of adjacent scenes matched after the backgrounds were removed, and was found to work successfully on various types of images (Figures S3 and S4).

An additional radiometric bias arose from photographing overlapping image segments from different camera position (hence different viewing angles). Because ice is anisotropic, overlapping segments had slightly different intensity values in each image. However, as shown from the overlapping light profiles (Figures S3 and S4), the differences were too small to affect the image analysis results.

5. Geometric correction

Barrel distortion is another common optical defect affecting camera lenses. Image magnification decreases away from the optical axis, causing a spherical deformation of image features. A radial pincushion function was used to correct the geometric distortion (Sjörgren et al., 2007). 'Perspective distortion' also arises when a three-dimensional

object is projected on a flat plane. This geometric effect can be removed by specifying a new camera projection model and performing careful calibration. In this study the cylindrical shape of the ice cores caused the thickest, central part of the core to be closer to the camera than the thinner, outer portion of the core. This caused: (1) a slight decrease in melt feature size away from the transverse (horizontal) core axis, and (2) a slight bending of vertical ice layers away from the transverse axis and toward the image center (optical axis). The distortion effect was small, however, and its consequence on the image analysis results judged to be too negligible to apply a projective correction.

References

Manders, C., and S. Mann (2004), Determining camera response functions from comparagrams of images with their raw datafile counterparts, Proceedings of the 2004 IEEE International Symposium on Intelligent Multimedia, Oct. 20-22 2004, Hong Kong, p. 418–421.

Mann, S. (2002), Comparametric equations, quantigraphic image processing, and comparagraphic rendering, in *Intelligent Image Processing*, edited by S. Mann, pp. 103–176, John Wiley and Sons, New-York.

Russ, J.C. (2002), *The Image Processing Handbook, Fourth Edition*, CRC Press, London, UK.

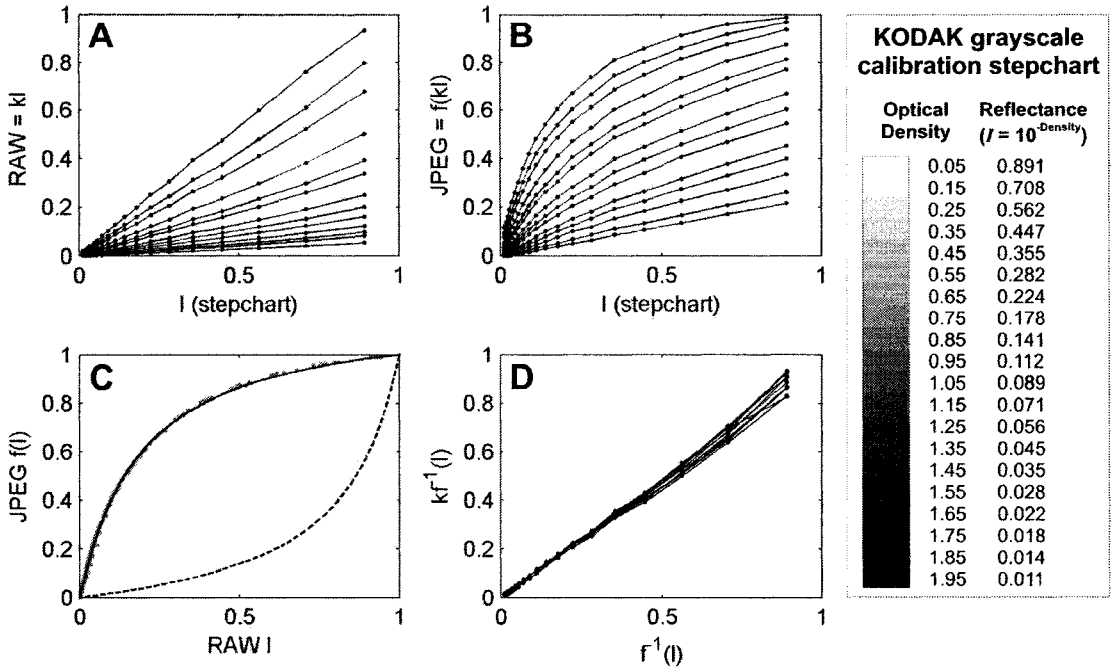

Figure S1. Determination of the camera response function, image linearization and exposure correction. (a) Known reflectance values from the calibration chart (see inset) versus those returned by the camera RAW images. Each line represents an image taken at a different exposure time, and each point represents the RAW image brightness I averaged over a 25 × 25 pixels area centered on each patch of the stepchart. The linear relationships confirm that the RAW images have a linear output. The top line is close to the 1:1 ratio and hence represents the optimal exposure settings for the lighting conditions. Varying the exposure time amounts to multiplying the intensity values by an exposure ratio k, equal to the ratio of exposure times between two images; (b) same as Figure S1a but for JPEG images, showing the non-linear nature of JPEG greyscale values; (c) JPEG versus RAW stepchart intensity values for different exposure times (gray points) along with the camera response function fitted to the data (black line). The dotted black line is the inverse camera response function used to convert JPEG images back to linear units; (d) example of image linearization and exposure correction: the JPEG stepchart greyscale data was converted back to linear units using the inverse camera response function and tonally aligned to the best-exposed image using the exposure time ratios k. The linearization and exposure correction is successful, although the very under-exposed images deviate slightly from linearity in the high intensity values, due to increasing noise. The range of exposure times used in the ice core images is much less than that used for the calibration, which reduces errors in the exposure correction procedure.

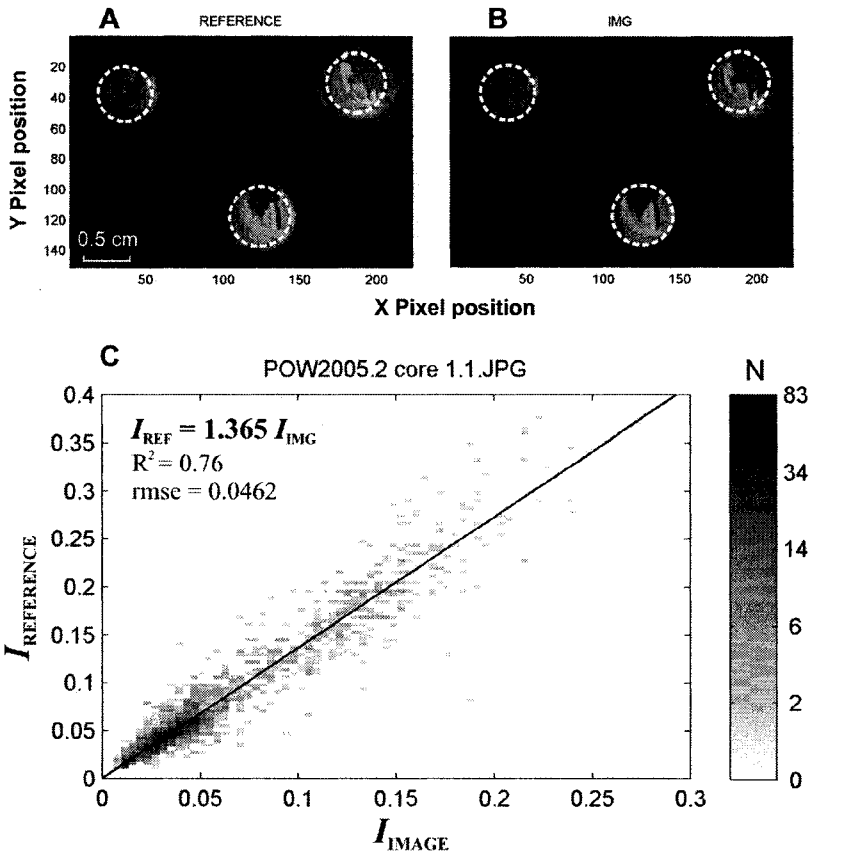

Figure S2. Example of exposure correction. The core image 1.1, with exposure time 1/60 sec., was tonally adjusted to the reference core image 15.1 with exposure time 1/40 sec. The sub-scene containing the holes in the reference image (a) is found within the target image (b) by cross-correlation and the pixel values inside the holes (dotted white circles) are used to calculate the exposure ratio k using linear regression through the origin (c). A robust fitting procedure with bisquare weights, implemented in matlab®, was used in order to reduce the influence of outliers. k is then used in equation 2 to tonally adjust image 1.1 to image 15.1, and all the other core images from scene 1 were tonally adjusted to core 15.1 in the same way. The greyscale in Figure S2c represents the number of data points.

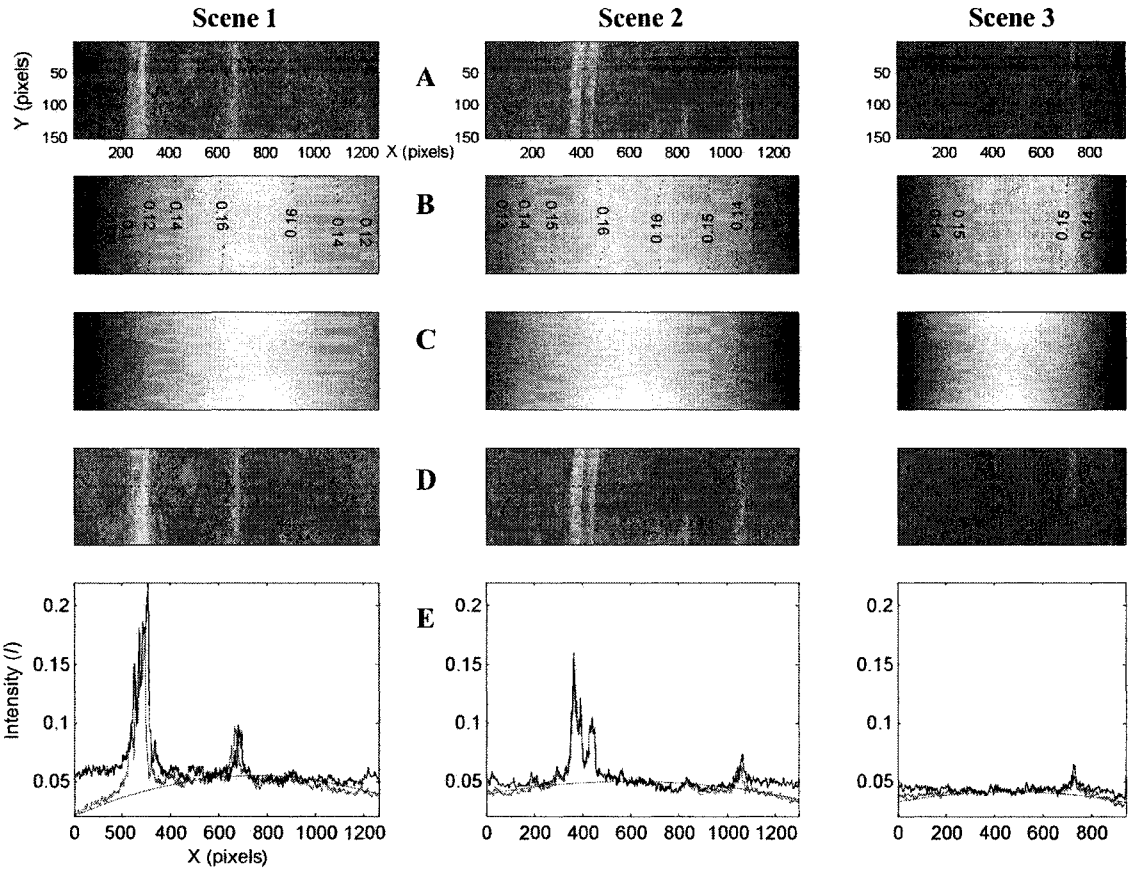

Figure S3. Example of uneven background illumination correction for core 20 (firn, 20.7–21.7 m-depth). Each column in the figure corresponds to one of the three overlapping camera scenes; (a) original core images, corrected for exposure bias; (b) mean background surfaces with polynomial trend surfaces (contours); (c) image-specific background images calculated using data-adaptive procedure; (d) cores images with uneven backgrounds removed. Stippled lines represent the intensity profile averaging area; (e) transverse intensity profiles for original (grey line) and corrected images (black line).

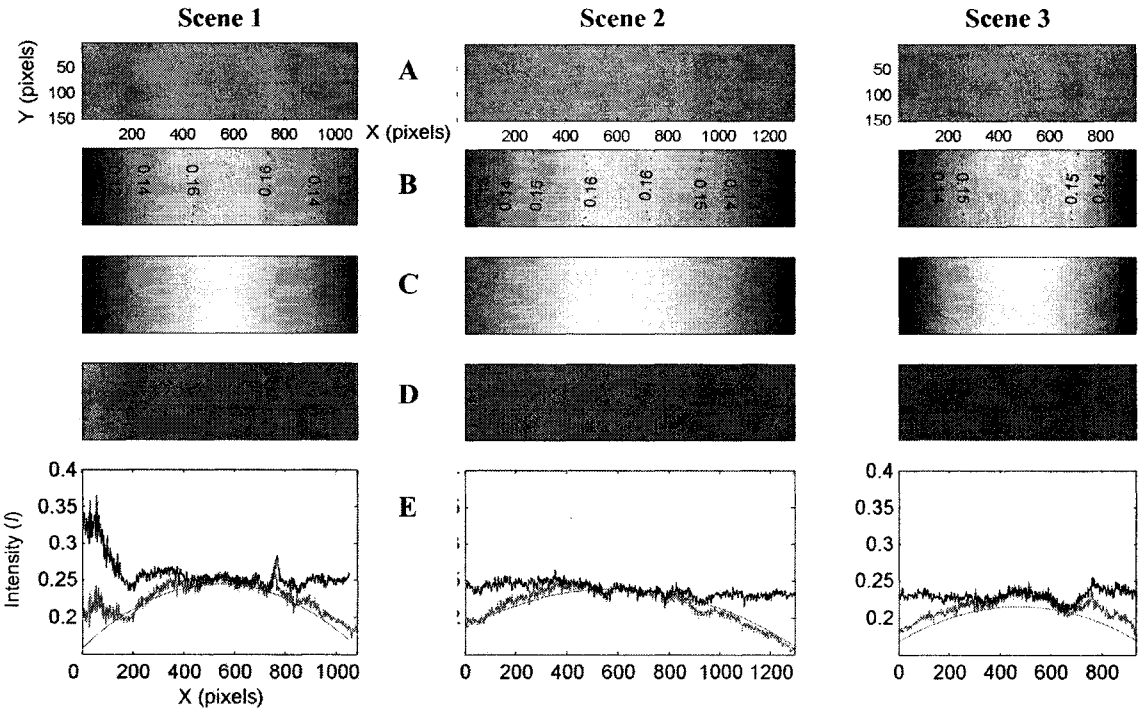

Figure S4. Same as Figure S3 but for core 109 (ice, 103–103.9 m-depth)

APPENDIX 7. COUPLED ARCTIC CLIMATE AND SEA ICE EXTENT OVER THE PAST MILLENNIUM RECONSTRUCTED FROM TERRESTRIAL PROXIES: *SUPPLEMENTARY MATERIAL*

1. Calibration methods

Partial least square regression (PLS) was used to calibrate modern sea ice extent observations with the proxy network. The calibration was performed over the period 1900-1995 (N = 96 years) with the number of proxies K decreasing back in time, from 68 in the most recent period to 22 in the last model. PLS projects the predictor matrix X (the proxies) into a set of orthogonal score vectors t which successively maximizes the covariance with the dependent variable Y (sea ice extent). The PLS model for a single predictor variable is expressed by:

$$X = TP^{\mathrm{T}} + E$$

$$y = Tq^{\mathrm{T}} + f$$

Where T $[N \times A]$ is the score matrix; P $[K \times A]$ is the loading matrix of X; E $[N \times K]$ is the residual matrix of X; q is the loading matrix of y and f $[N \times 1]$ is the vector of y residuals. The matrix inverse is expressed by the uppercase Tau symbol. A reduced number of scores A, smaller than K, is retained for prediction of y. The PLS scores and loading are calculated successively using the Non-linear Iterative Partial Least Square (NIPALS) algorithm (e.g. Geladi and Kowalski, 1986). For s single y vector, the NIPALS algorithm is:

1) $w = X^{\mathrm{T}} y / \left(y^{\mathrm{T}} y\right)$

2) $w = w / \|w\|$

3) $t = Xw$

4) $q = y^{\mathrm{T}} t / \left(t^{\mathrm{T}} t\right)$

5) $p = X^{\mathrm{T}} t / \left(t^{\mathrm{T}} t\right)$

6) $E = X - tp^{\mathrm{T}}$, $f = y - tq^{\mathrm{T}}$

For additional components, use $X = E$ and $y = f$ and return to Step (1).

Once the desired number of components has been calculated, the final model can be expressed by:

$$Y = XB + F$$

$$B = W\left(P^{\mathrm{T}} W\right)^{-1} P^{\mathrm{T}}$$

Where B is the vector of regression coefficients for a PLS model with A components and W $[K \times A]$ is the weight matrix of X.

2. Model dimensionality

The number of PLS components A retained for prediction of y determines the dimensionality of the final regression model. Including too many components will lead to statistical over-fitting (modelling noise), while too few components will cause under-fitting, which means that the model does not capture all the variability in the data. A is usually determined by cross-validation procedures (CV). Many variants exist, such as leave-one-out (LOO) or k-fold CV where either one, or a contiguous block of k values, are left out from the model calibration and used for validation. LOO-CV tends to under-estimate the true prediction error and result in over-fitting (Xu and Liang, 2001). We then used a Monte Carlo cross-validation procedure (Xu and Liang, 2001) to evaluate the prediction skill as well as guide the selection of the number of PLS components. Both the predictor X matrix and y vector is randomly split into calibration samples y_c and X_c of length n_c years and validation samples y_v and X_v of length n_v years. A PLS model is

developed on [y_c, X_c] and the prediction skill is measured on [y_v, X_v]. The procedure is repeated N times (i = 1, 2, ... N).

$$CV(a) = \frac{1}{Nn_v} \sum_{i=1}^{N} (SKILL)$$

CV(a) is calculated for every *a* component as it is added to the model. The component *a* which gives a minimum value of *CV(a)* determines the model dimensionality *A*. The Reduction of error statistic (*RE*), coefficient of efficiency (*CE*), and squared correlation coefficient (r^2) were used to evaluate prediction skill, as in previous studies (Cook et al, 1994; Mann et al, 2005; 2008). See North et al (2006) for an in-depth discussion of these measures. As a second dimensionality test, the significance of the covariance between the predictand *y* and successive score vector *t* was tested by Monte Carlo noise simulation, by randomizing the Fourier phase of *y* 1000 times and calculating the product $y^T t$ at each iteration. Components that were significantly different from noise ($p < 0.1$) were retained in the model. See Faber and Rajkó (2007) for more details.

3. Model verification and confidence intervals

The statistical significance of the prediction skill of the final PLS model was tested against noise using the same randomization technique. 1000 surrogate ice extent series were created and predicted from the proxies, and the skill metrics calculated each time. Models with skill significantly different ($p<0.05$) than noise were considered to have valid predictive skill. 95% confidence intervals around predicted values were then estimated from the cross-validated residual variance.